

# Catalytic conversion of carbon dioxide to hydrocarbons

Mohan, Ojus

2020

Mohan, O. (2020). Catalytic conversion of carbon dioxide to hydrocarbons. Doctoral thesis, Nanyang Technological University, Singapore.

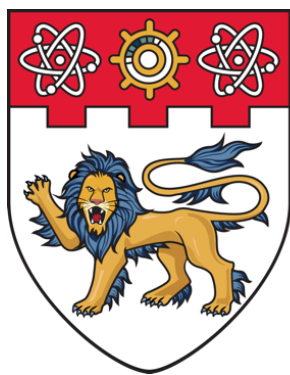
<https://hdl.handle.net/10356/146544>

<https://doi.org/10.32657/10356/146544>

---

This work is licensed under a Creative Commons Attribution-NonCommercial 4.0 International License (CC BY-NC 4.0).

*Downloaded on 09 Apr 2024 13:08:59 SGT*



**NANYANG  
TECHNOLOGICAL  
UNIVERSITY**

---

**SINGAPORE**

**CATALYTIC CONVERSION OF CARBON DIOXIDE TO  
HYDROCARBONS**

**OJUS MOHAN**

**Interdisciplinary Graduate School  
Energy Research Institute @ NTU**

**2020**



# **CATALYTIC CONVERSION OF CARBON DIOXIDE TO HYDROCARBONS**

**OJUS MOHAN**

INTERDISCIPLINARY GRADUATE SCHOOL

A thesis submitted to the Nanyang Technological University  
in partial fulfillment of the requirement for the degree of  
Doctor of Philosophy

**2020**





## Statement of Originality

I hereby certify that the work embodied in this thesis is the result of original research, is free of plagiarised materials, and has not been submitted for a higher degree to any other University or Institution.

27 July 2020

.....

Date

A handwritten signature in black ink, appearing to read 'Ojus Mohan', with a long horizontal flourish extending to the right.

.....

Ojus Mohan



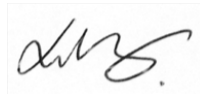
## Supervisor Declaration Statement

I have reviewed the content and presentation style of this thesis and declare it is free of plagiarism and of sufficient grammatical clarity to be examined. To the best of my knowledge, the research and writing are those of the candidate except as acknowledged in the Author Attribution Statement. I confirm that the investigations were conducted in accord with the ethics policies and integrity standards of Nanyang Technological University and that the research data are presented honestly and without prejudice.

27 July 2020

.....

Date



.....

Prof Xu Rong



## Authorship Attribution Statement

This thesis contains material from one paper published in the following peer-reviewed journal in which I am listed as an author.

Chapter 3 is published as O. Mohan, Q.T. Trinh, A. Banerjee, S.H. Mushrif. Predicting CO<sub>2</sub> adsorption and reactivity on transition metal surfaces using popular density functional theory methods. *Molecular Simulation* **45**, 1163-1172 (2019). DOI: 10.1080/08927022.2019.1632448.

The contributions of the co-authors are as follows:

- Assoc/Prof Mushrif provided the initial project direction and edited the manuscript drafts.
- I prepared the manuscript drafts. The manuscript was revised by Dr. Banerjee and Dr. Trinh.
- I designed the study and performed all the computational simulations on resources of the National Supercomputing Centre (NSCC), Singapore, West Grid, Canada, and Compute Canada. I also analyzed the data.
- Dr. Banerjee helped in establishing the initial computational system and understanding the procedure of molecular simulation calculations for geometry optimization and transition state search.
- Dr. Trinh helped in understanding the procedure for DFT-XPS and projected density of state calculations.
- Assoc/Prof Mushrif provided guidance in the interpretation of the simulation results.

Chapter 4 is published as O. Mohan, Shambhawi, A.A. Lapkin, S.H. Mushrif. Investigating methane dry reforming on Ni and B promoted Ni surfaces: DFT assisted microkinetic analysis and addressing the coking problem

The contributions of the co-authors are as follows:

- Assoc/Prof Mushrif and Prof Alexei provided the initial project direction and edited the manuscript drafts.
- I prepared the manuscript drafts. The manuscript was revised by Prof. Alexei and Assoc/Prof. Samir.
- I designed the study and performed all the DFT simulations on resources of the National Supercomputing Centre (NSCC), Singapore, West Grid, Canada, and Compute Canada. I also analyzed the data.
- Shambhawi performed the microkinetic modeling calculations. Shambhawi also contributed in writing the microkinetic results and discussion.
- Assoc/Prof Mushrif provided guidance in the interpretation of the simulation results.

27 July 2020

.....  
Date



.....  
Ojus Mohan

## Abstract

CO<sub>2</sub> methanation and dry reforming of methane (DRM) are promising routes for CO<sub>2</sub> utilization. Ni-based catalysts are widely employed for these reactions. However, these are less active and are prone to deactivation due to carbon deposition. Gaining mechanistic insights is pivotal in developing more active and coke resistant Ni-based catalysts. This work combines Density Functional Theory (DFT) calculations with microkinetic modeling (MKM), to provide mechanistic insights into CO<sub>2</sub> methanation (on Ni and Ru) and DRM reactions (on Ni and boron-doped Ni (NiB)). Based on the computed energetics, this work predicts a novel catalyst (Mn-NiB single atom alloy (SAA)) for these reactions.

The choice of correct DFT functional is crucial to accurately predict the reaction energetics. Hence, a benchmarking study was performed for the first time to identify a DFT functional for studying CO<sub>2</sub> conversion reactions. A functional screening was performed based on CO<sub>2</sub> and CO adsorption energies, DFT-XPS, and density of state calculations. rPBE-vdW functional with a correction of 28 kJ/mol for gas-phase CO<sub>2</sub> energy, was proposed to be the best available functional for studying CO<sub>2</sub> conversion reactions. The inability of a functional to accurately predict energetics was typically attributed to the wrong description of adsorbate-surface interactions. However, for rPBE-vdW functional, we found that this is due to the erroneous treatment of C=O double bonds in gas phase CO<sub>2</sub>.

Employing the benchmarked functional, CO<sub>2</sub> methanation (46 elementary reactions) and DRM (38 elementary reactions) reactions were studied by combined DFT and MKM. CO<sub>2</sub> methanation reaction mechanism is debated and the reaction mechanism elucidation is crucial in developing efficient catalysts based on a bottom-up approach. The most debated step is the activation routes of CO<sub>2</sub> and CO and whether the reaction proceeds with/without forming CO\* intermediate. The current study resolved the discrepancy in the CO<sub>2</sub> methanation reaction mechanism on Ru (most active noble metal catalyst) and Ni surfaces. We identified that the dominant reaction pathways are CO<sub>2</sub>\*→CO\*→HCO\*→CH\*→CH<sub>2</sub>\*→CH<sub>3</sub>\*→CH<sub>4</sub> and CO<sub>2</sub>\*→CO\*→COH\*→C\*→HC\*→CH<sub>2</sub>\*→CH<sub>3</sub>\*→CH<sub>4</sub> on Ni (111) and Ru (001) respectively. On comparing Ni (111) and Ru (001), Ni (111) was more



selective towards methane formation. Therefore, CO<sub>2</sub> methanation proceeds via CO\* intermediate and this study resolves the contradictions in CO<sub>2</sub> methanation reaction mechanisms on Ni and Ru surfaces. For DRM reaction, the deactivation of Ni-based catalyst is a key challenge, and this impedes commercializing the DRM process. Doping boron at the sub-surface interstitial sites in Ni prevents the diffusion of carbon. Hence, we investigated NiB as a potential catalyst. The effect of doping is evaluated by comparing the dominant pathway with that on Ni (111). The dominant reaction pathway is CO<sub>2</sub>\*→CO\*+O\*; CH<sub>4</sub>→CH<sub>3</sub>\*→CH<sub>2</sub>\*→C\*→CO\* and CO<sub>2</sub>\*→CO\*+O\*; CH<sub>4</sub>→CH<sub>3</sub>\*→CH<sub>2</sub>\*→CH<sub>2</sub>O\*→CHO\*→CO\* on Ni (111) and NiB surfaces respectively. We reveal that boron doping alters the dominant reaction pathway (via CH<sub>2</sub>\* oxidation route) to kinetically hinder carbon formation (no C\* intermediate). In contrast to Ni, the barriers in CH<sub>4</sub> activation routes and Boudouard reaction are significantly lower on NiB but the CO<sub>2</sub> activation barrier (124 kJ/mol) is high resulting in reduced conversion.

The strategy is to reduce the CO<sub>2</sub> activation barrier selectively to improve the activity of NiB without compromising the stability. A computational screening was performed to identify thermodynamically stable NiB-based SAA that selectively reduces the CO<sub>2</sub> activation barrier. The thermodynamic stability was evaluated against clustering and Mn-NiB SAA was identified as the only candidate on which there is a significant reduction in the CO<sub>2</sub> activation barrier (68 kJ/mol). Subsequently, CO<sub>2</sub> methanation and DRM reactions were studied on Mn-NiB SAA. The barriers for key reactions (CO<sub>2</sub> and CO activation, CH\* hydrogenation) are low on Mn-NiB SAA compared to Ni and Ru making it a suitable catalyst for CO<sub>2</sub> methanation reaction. For the DRM reaction, Mn-NiB SAA has a significantly lower barrier for CH<sub>4</sub> (compared to Ni) and CO<sub>2</sub> (compared to NiB) activation. Additionally, the high endergonicity for CH<sub>4</sub> stepwise dehydrogenation to form C\* combined with a low barrier for Boudouard reaction prevents the catalyst deactivation.

Employing an appropriate DFT functional, the combined DFT and MKM approach adopted in this investigation predicted the CO<sub>2</sub> methanation and DRM reaction mechanisms. The gained insights from SAA would serve as guidelines for the development of alloy catalysts which can prevent carbon deposition without compromising the catalytic activity.

## Acknowledgments

Foremost, I express my sincere gratitude to Prof. Samir H. Mushrif for his guidance, encouragement, and support throughout my Ph.D. program. His guidance was critical for me to develop independent and fundamental thinking and improve my scientific communication skills. His passion for research and quick and efficient responses to challenging scientific problems have inspired me throughout my Ph.D. journey. I sincerely thank my main supervisor, Prof. Xu Rong, for her support and good advice from time to time during my Ph.D. Besides my advisor, I express my gratitude to the rest of my thesis advisory committee Prof. Claude Guet and Prof. Paul Liu for their insightful comments and advice.

I thank Dr. Arghya Banerjee for the help in performing simulations during the initial stage of my Ph.D. I sincerely thank Dr. Thang for his involvement in one of the projects and his guidance in the interpretation of critical results. I am most grateful to Dr. Jithin John Varghese for the innumerable discussions and guidance throughout my Ph.D. I thank my fellow lab mates in NTU: Mr. Spandan Gautam, Dr. Sukriti Gupta, Dr. Jyotsna Arora and Dr. Khursheed Ansari for the constructive discussions and for all the fun we have had. Also, I thank my fellow lab mates at the University of Alberta: Mr. Arul Padmanathan, Mr. Nilesh Orupattur, Mr. Jose Carlos Velasco Calderon, Ms. Katherine Hassan-Legault and Mr. Sagar Bathla for the support and friendship during my academic visit.

In particular, I thank Dr. Kartavya Bhola for all the discussions and brainstorming sessions with him during my Ph.D. journey which has prevented several wrong turns. I would like to extend my heartfelt gratitude to my friends and flatmates in Singapore: Mr. Abhijith Surendran, Mr. Govind Harikumar, Mr. Riyas Ahmad, Mr. Sujith Kunniniyil and Mr. Vishal Jose for the invaluable emotional support.

I extend my gratitude to IGS, SCBE, and NTU for providing funding, facilities and resources for my project. I also thank the Department of Chemical and Materials Engineering at the University of Alberta for giving me an opportunity to work as a research

award recipient. I would like to acknowledge the National Supercomputing Centre Singapore and Compute Canada for providing the resources to perform all the computational simulations.

Finally, I thank my parents Mr. D.S. Mohanan and Ms. Sunila Mohan and my brother Mr. Omex Mohan, for their unconditional love and emotional support during my Ph.D. journey. I appreciate my wife Ms. Akshara Soman for her unambiguous support and for writing a few codes that have speed up my pre and post calculation steps.

---

## Table of Contents

<b>Abstract .....</b>	<b>i</b>
<b>Acknowledgments.....</b>	<b>iii</b>
<b>Table of Contents.....</b>	<b>v</b>
<b>Table Captions .....</b>	<b>ix</b>
<b>Figure Captions.....</b>	<b>xi</b>
<b>Abbreviations .....</b>	<b>xvii</b>
<b>Chapter 1 Introduction .....</b>	<b>1</b>
1.1 CO <sub>2</sub> : Problems and mitigation.....	2
1.2 CO <sub>2</sub> to value-added products.....	3
1.2.1 CO <sub>2</sub> Methanation .....	5
1.2.2 Dry Reforming of Methane.....	10
1.3 Challenges in catalytic conversion of CO <sub>2</sub> .....	13
1.4 DFT for studying CO <sub>2</sub> conversion reactions .....	15
1.4.1 Challenges in DFT .....	16
1.5 Objectives.....	17
1.5.1 Key objectives of Chapter 3.....	18
1.5.2 Key objectives of Chapter 4.....	18
1.5.3 Key objectives of Chapter 5.....	18
1.5.4 Key objectives of Chapter 6.....	19
1.6 Dissertation overview.....	19

<b>Chapter 2 Computational Methods .....</b>	<b>23</b>
2.1 Molecular modeling .....	24
2.2 Density Functional Theory (DFT).....	26
2.3 Exchange-Correlation functional .....	28
2.3.1 Local Density Approximation (LDA).....	29
2.3.2 Generalized Gradient Approximation (GGA).....	29
2.4 Simulation system .....	30
<b>Chapter 3 Benchmarking popular density functional theory methods for predicting CO<sub>2</sub> adsorption and reactivity on transition metal .....</b>	<b>31</b>
3.1 Introduction .....	32
3.1.1 Need for functional benchmarking .....	32
3.2. Computational methods and simulation system.....	35
3.3 Results and Discussions .....	37
3.3.1 Adsorption of CO <sub>2</sub> and CO on Ni (110).....	37
3.3.2 Reasons for the difference in CO <sub>2</sub> binding energy prediction by rPBE-vdW and optPBE-vdW .....	41
3.3.3 Evaluating the difference in activation barrier and DFT-XPS calculations .....	46
3.3.4 CO <sub>2</sub> adsorption on different transition metals .....	50
3.4 Summary and Conclusions.....	51
<b>Chapter 4 Investigating CO<sub>2</sub> methanation on Ni and Ru: DFT assisted microkinetic analysis.....</b>	<b>53</b>
4.1 Introduction .....	54
4.1.1 CO <sub>2</sub> methanation reaction mechanisms .....	55
4.1.2 Challenges in CO <sub>2</sub> methanation .....	56

---

4.2. Computational details.....	58
4.2.1 DFT calculations.....	58
4.2.2 Microkinetic model.....	59
4.2.3. Reaction pathway analysis.....	61
4.3. Results and Discussions .....	62
4.3.1 DFT study of CO <sub>2</sub> methanation on Ni (111) and Ru (001).....	62
4.3.2 Microkinetic Analysis .....	73
4.4. Summary and Conclusions.....	79
<b>Chapter 5 Investigating methane dry reforming on Ni and B promoted Ni surfaces: DFT assisted microkinetic analysis and addressing the coking problem .....</b>	<b>81</b>
5.1 Introduction .....	82
5.1.1 Dry reforming of methane and potential catalysts.....	82
5.1.2 Effect of promoters on Ni catalyst performance for DRM .....	82
5.1.3 DRM reaction mechanism .....	83
5.1.4 Challenges in DRM .....	84
5.2. Computational details.....	86
5.2.1 DFT calculations.....	86
5.2.2 Microkinetic model.....	88
5.2.3 Rate determining step .....	91
5.3 Results and Discussion.....	92
5.3.1 DFT study of DRM on Ni (111) and NiB .....	92
5.3.2 Microkinetic Analysis .....	106
5.3.3 Sensitivity analysis .....	111
5.4 Summary and Conclusions.....	117

<b>Chapter 6 Prediction of NiB based single atom alloy as a novel catalyst for CO<sub>2</sub> conversion reactions: computational screening and reaction mechanism analysis.</b>	<b>119</b>
6.1 Introduction .....	120
6.1.1 CO <sub>2</sub> methanation: effect of promoters and reaction mechanism .....	120
6.1.2 DRM: effect of promoters and reaction mechanism.....	123
6.1.3 NiB based single atom alloy (SAA) .....	125
6.2 Computational details.....	127
6.3 Results and Discussions .....	129
6.3.1 Screening of NiB-based SAA .....	129
6.3.2 CO <sub>2</sub> methanation on Mn-NiB SAA .....	132
6.3.3 DRM on Mn-NiB SAA.....	143
6.4 Conclusions .....	152
<b>Chapter 7 Conclusions and perspectives .....</b>	<b>153</b>
<b>APPENDIX.....</b>	<b>159</b>
8.1 Appendix to chapter 3 .....	159
8.2 Appendix to chapter 4 .....	167
8.3 Appendix to chapter 5 .....	185
<b>REFERENCES .....</b>	<b>211</b>

## Table Captions

<b>Table 3. 1</b> Most stable adsorption configurations and calculated adsorption energies (kJ/mol) of CO <sub>2</sub> (chemisorbed and physisorbed) and CO on Ni (110) using different functionals..	39
<b>Table 3. 2</b> The difference in binding energies calculated using optPBE-vdW and rPBE-vdW	45
<b>Table 3. 3</b> Comparison of CO <sub>2</sub> vibrational frequencies between calculated and experimental values	46
<b>Table 3. 4</b> XPS C1s and O1s chemical shifts relative to C1s and O1s binding energy of chemisorbed CO <sub>2</sub> on Ni (110) surface.	49
<b>Table 3. 5</b> Binding energies (kJ/mol) calculated using optPBE-vdW and rPBE-vdW for different CO <sub>2</sub> hydrogenation transition metals	51
<b>Table 4. 1</b> Calculated free energy barriers and reaction free energies (550K and 10 atm pressure) of all elementary reactions for CO <sub>2</sub> methanation on Ni (111) and Ru (001) surfaces.	63
<b>Table 4. 2</b> Fractional surface coverages of most abundant surface species and fractional conversion of CO <sub>2</sub> computed by the model at a reaction temperature of 550 K, 10 bar pressure and an inlet feed composition of 20% volume fraction CO <sub>2</sub> and 80% volume fraction of H <sub>2</sub> .	74
<b>Table 5. 1</b> Different model specifications based on the values of DFT functionals, corrections, elementary reactions, and standard pressure.	90



<b>Table 5. 2</b> Calculated free energy barriers and reaction free energies (973K and 10 bar pressure) of all elementary reactions for DRM on Ni (111) and NiB surfaces..	93
<b>Table 5. 3</b> Fractional surface coverages of surface species computed by the model at a reaction temperature of 973.15 K, 10 bar pressure and an inlet feed composition of 50% volume fraction CH <sub>4</sub> and 50% volume fraction of CO <sub>2</sub> .	107
<b>Table 6. 1.</b> Summary of key results for CO <sub>2</sub> methanation on modified Ni catalysts.....	120
<b>Table 6. 2</b> Comparison of CO <sub>2</sub> methanation reaction mechanism on Ni and modified Ni catalysts .....	122
<b>Table 6. 3</b> Summary of key results for DRM on modified Ni catalysts .....	124
<b>Table 6. 4</b> CO <sub>2</sub> *, CO* and O* adsorption energies (electronic energies) and CO <sub>2</sub> activation barriers (electronic energies) on Ni (111), NiB and Pt, Pd, Rh, Cu, and Mn-based NiB SAA surfaces .....	131
<b>Table 6. 5</b> Calculated free energy barriers and reaction free energies (550K and 10 atm pressure) of all elementary reactions for CO <sub>2</sub> methanation on Ni (111), Ru (001), and Mn-NiB SAA surfaces .....	133
<b>Table 6. 6</b> Calculated free energy barriers and reaction free energies of all elementary reactions for DRM on Ni (111), NiB, and Mn-NiB SAA surfaces. ....	144

## Figure Captions

<b>Figure 1. 1</b> Schematic diagram showing CO <sub>2</sub> conversion to different value-added products via hydrogenation and dry reforming routes .....	4
<b>Figure 1. 2</b> Schematic showing possible products and potential catalysts for CO <sub>2</sub> hydrogenation .....	5
<b>Figure 1. 3</b> Schematic diagram of power to methane technology showing the utilization of surplus renewable energy to produce methane .....	7
<b>Figure 1. 4</b> Schematic showing the possible reaction pathways for CO <sub>2</sub> methanation .....	9
<b>Figure 1. 5</b> Schematic showing the possible reaction pathways for CO <sub>2</sub> and CH <sub>4</sub> activation routes in DRM reaction .....	12
<b>Figure 1. 6</b> Organization of the thesis.....	22
<b>Figure 2. 1</b> Molecular modeling methods.....	26
<b>Figure 2. 2</b> The algorithm for solving Kohn-Sham DFT formulation .....	28
<b>Figure 3. 1</b> The density of states (DOS) projected on d-band for surface Ni site that coordinates with chemisorbed CO <sub>2</sub> molecule using rPBE-vdW and optPBE-vdW functionals. ....	42
<b>Figure 3. 2</b> Alternate CO <sub>2</sub> binding energy calculation schemes based on methane (system 1), methanol (system 2) and formic acid (system 3) .....	44
<b>Figure 3. 3</b> Structure of the initial state (IS), final state (FS) and transition state (TS) for CO <sub>2</sub> activation on Ni (110).....	47

<b>Figure 4. 1</b> CO <sub>2</sub> direct dissociation and hydrogenation with/without CO* intermediate routes. ....	63
<b>Figure 4. 2</b> CO <sub>2</sub> activation and dissociation on Ni (111) and Ru (001).....	66
<b>Figure 4. 3</b> Free energy barriers and reaction free energies for CO* dissociation routes on Ni (111) and Ru (001) surfaces. ....	68
<b>Figure 4. 4</b> Free energy barriers and reaction free energies for CO <sub>2</sub> * dissociation routes without forming CO* as an intermediate on Ni (111) and Ru (001).....	71
<b>Figure 4. 5</b> Free energy barriers and reaction free energies for sequential hydrogenation of C* on Ni (111) and Ru (001).....	72
<b>Figure 4. 6</b> (a) Relative sensitivity coefficients (b) Partial equilibrium coefficient $\phi$ analysis of CO <sub>2</sub> methanation reaction steps ( $k$ ) reported over Ni (111) at space-time value of 0.01 gcat·h·mol <sup>-1</sup> at reaction temperature 550 K and 10 atm pressure. ....	76
<b>Figure 4. 7</b> (a) Relative sensitivity coefficients and (b) Partial equilibrium coefficient $\phi$ analysis of CO <sub>2</sub> methanation reaction steps ( $k$ ) reported over Ru (001) at space-time value of 0.01 gcat·h·mol <sup>-1</sup> at reaction temperature 550 K and 10 atm pressure. ....	77
<b>Figure 4. 8</b> Dominant reaction pathway and rate determining steps for CO <sub>2</sub> methanation reaction on (a) Ni (111) and (b) Ru (001) as identified from the algorithm.....	78
<b>Figure 5. 1</b> Structure of Ni (111) and Ni with subsurface B after reconstruction .....	87
<b>Figure 5. 2</b> (a) CO <sub>2</sub> dissociation routes and (b) CH <sub>4</sub> sequential dehydrogenation routes and CH <sub>x</sub> (x = 0 to 3) oxidation by OH* and O* routes. ....	93

**Figure 5. 3** Methane dissociation on Ni (111) and NiB. (a) Free energy barriers and reaction free energies (inside brackets) and (b) free energy profile for sequential dehydrogenation of CH<sub>4</sub> to C\*. ..... 96

**Figure 5. 4** CO<sub>2</sub> activation and dissociation on Ni (111) and NiB. (a) Free energy barriers and reaction free energies (inside brackets), (b) free energy profile for different CO<sub>2</sub> activation routes..... 98

**Figure 5. 5** Most stable chemisorption configuration of CO<sub>2</sub> on a) Ni (111) and b) NiB. .... 99

**Figure 5. 6** Free energy barriers and reaction free energies for CH<sub>x</sub> oxidation by O\*/OH\* routes. .... 103

**Figure 5. 7** Fractional surface coverages of CO\*, H\* (a) and H<sub>2</sub>O\*, CO<sub>2</sub>\* (b) vs space-time over Ni (111) at reaction temperature 973.15 K and 10 bar pressure. .... 109

**Figure 5. 8** Fractional surface coverages of CO\*, H\*(a) and H<sub>2</sub>O\*, CO<sub>2</sub>\*(b) vs space-time over B-doped Ni at reaction temperature 973.15 K and 10 bar pressure. .... 110

**Figure 5. 9** Partial equilibrium coefficient  $\phi$  analysis of RWGS reaction steps over Ni (111) and NiB surfaces at space-time value of  $1 \times 10^{-3} \text{ g}_{\text{cat}} \cdot \text{h} \cdot \text{mol}^{-1}$  at reaction temperature 973.15 K and 10 bar pressure ..... 111

**Figure 5. 10** Partial equilibrium coefficient  $\phi$  analysis of DRM reaction steps over Ni (111) and NiB surfaces at space-time value of  $0.01 \text{ g}_{\text{cat}} \cdot \text{h} \cdot \text{mol}^{-1}$  at reaction temperature 973.15 K and 10 bar pressure. .... 112

<b>Figure 5. 11</b> Sensitivity analysis of DRM reaction steps over Ni (111) and NiB surfaces at space-time value of $0.01 \text{ g}_{\text{cat}}\cdot\text{h}\cdot\text{mol}^{-1}$ at reaction temperature 973.15 K and 10 bar pressure. ....	113
<b>Figure 5. 12</b> Dominant reaction pathway on Ni (111) (a) and NiB (b) based on sensitivity analysis and reaction rates .....	114
<b>Figure 5. 13</b> Forward reaction rates of R1 and R25 vs space-time at a reaction temperature of 973.15 K and 10 bar pressure (a) and zoomed-in image (b). ....	116
<b>Figure 6. 1</b> The energy of aggregation relative to the SAA for the clustering of dopant atoms into dimers and trimers .....	129
<b>Figure 6. 2</b> The most stable chemisorption configuration of $\text{CO}_2$ on Mn-NiB SAA. ...	131
<b>Figure 6. 3</b> $\text{CO}_2$ direct dissociation and hydrogenation with/without $\text{CO}^*$ intermediate routes. ....	133
<b>Figure 6. 4</b> Free energy barriers and reaction free energies $\text{CO}_2$ activation and dissociation on Mn-NiB SAA. ....	136
<b>Figure 6. 5</b> Free energy barriers and reaction free energies for $\text{CO}^*$ dissociation routes. ....	137
<b>Figure 6. 6</b> Free energy barriers and reaction free energies for $\text{CO}_2^*$ dissociation routes without forming $\text{CO}^*$ as an intermediate. ....	138
<b>Figure 6. 7</b> Free energy barriers and reaction free energies for sequential hydrogenation of $\text{C}^*$ . ....	139

<b>Figure 6. 8</b> The free energy diagram of the CO <sub>2</sub> activation route on Ni (111), Ru (001), and Mn-NiB SAA.....	140
<b>Figure 6. 9</b> The free energy diagram of the CO activation route on Ni (111), Ru (001), and Mn-NiB SAA .....	141
<b>Figure 6. 10</b> The free energy diagram of CH* stepwise hydrogenation on Ni (111), Ru (001), and Mn-NiB SAA.....	142
<b>Figure 6. 11</b> CO <sub>2</sub> dissociation routes and CH <sub>4</sub> sequential dehydrogenation routes and CH <sub>x</sub> (x = 0 to 3) oxidation by OH* and O* routes.....	143
<b>Figure 6. 12</b> Free energy barriers and reaction free energies form methane dissociation on Mn-NiB SAA. ....	146
<b>Figure 6. 13</b> Free energy barriers and reaction free energies for CO <sub>2</sub> activation and dissociation on Mn-NiB SAA. ....	146
<b>Figure 6. 14</b> Free energy barriers and reaction free energies for CH <sub>x</sub> oxidation by O*/OH* routes. ....	147
<b>Figure 6. 15</b> The free energy diagram of CO <sub>2</sub> direct dissociation on Ni (111), NiB, and Mn-NiB SAA .....	149
<b>Figure 6. 16</b> The free energy profile for sequential dehydrogenation of CH <sub>4</sub> to C* on Ni (111), NiB and Mn-NiB SAA .....	150
<b>Figure 6. 17</b> The free energy profile for Boudouard reaction on Ni (111), NiB and Mn-NiB SAA .....	151



**Abbreviations**

DFT	Density Functional Theory
MKM	Microkinetic Model
RDS	Rate-determining Step
DRM	Dry Reforming of Methane
SEM	Scanning Electron Microscopy
TEM	Transmission Electron Microscopy
STM	Scanning Tunneling Microscopy
FTIR	Fourier Transform Infrared Spectroscopy
HRTEM	High-Resolution Transmission Electron Microscopy
SAED	Selected Area Electron Diffraction
XRD	X-ray Diffraction
SA	Sensitivity Analysis
PEA	Partial Equilibrium Analysis





## Chapter 1 Introduction

*Catalytic Conversion of CO<sub>2</sub> to value-added products is a promising strategy for CO<sub>2</sub> utilization. Two prominent reaction routes in this strategy are CO<sub>2</sub> methanation and dry reforming of methane reactions. Even though noble metal based catalysts are active for these reactions, nickel-based catalysts are widely employed considering its high selectivity, low cost, and ease of availability. An overview of the CO<sub>2</sub> methanation and dry reforming of methane reactions including the reaction mechanisms reported on nickel are presented here. Challenges and knowledge gaps were identified and summarized and based on these, objectives were formulated and presented in this chapter.*

## 1.1 CO<sub>2</sub>: Problems and mitigation

Carbon dioxide is formed by the combustion and fermentation of carbon-containing substances like wood, sugar, grapes, etc. and also by the burning of carbon-rich fuels like coal, oil, and natural gas<sup>1,2</sup>. Although CO<sub>2</sub> has always been essential for life on earth, it constitutes only 0.04% by volume of the atmosphere<sup>3,4</sup>. However, this tiny percentage plays a huge role in greenhouse effect<sup>5</sup>. Greenhouse effect is the natural phenomenon that traps solar heat in the atmosphere and keeps the temperature warm enough for all forms of life to survive. However, today the greenhouse effect that inured to protect us has become a threat<sup>1,2,6</sup>. Industrial production, mass consumption, and modern comforts have led to a steady rise in the use of fossil fuels that release CO<sub>2</sub> into the atmosphere causing global warming<sup>7</sup>. The effects of rising temperatures are spreading fast worldwide and are difficult to control if no measures are taken to control its level. The temperature could climb by 6 degrees by the end of the century sparking to a series of events such as melting ice at the poles, swelling oceans, submerging coastal regions with consequences that could be irreversible<sup>8</sup>. Climate change is one of society's biggest problems at present bringing about the rising temperatures that are causing species to go extinct, rising sea levels, longer periods of droughts for some areas of the world, increased number of more intense storms in other areas<sup>4,6</sup>. By now, scientists have revealed that it is extremely likely that the warming of the atmosphere is due to human influence<sup>9</sup>. Humans generate most of the total emitted greenhouse gases in the form of CO<sub>2</sub> and most of that is generated from fossil fuel usage. The constant addition of CO<sub>2</sub> to the atmosphere has caused the atmospheric concentration of CO<sub>2</sub> to increase beyond 400 ppm over the last several decades<sup>10</sup>. This increase is perturbing as the currently accepted maximum level at which we can hold CO<sub>2</sub> concentration in the atmosphere without perceiving severe effects of climate change is 350 ppm<sup>10</sup>. The current carbon cycle is inadequate to keep the CO<sub>2</sub> levels in the atmosphere under control<sup>3</sup>. This seems that we not only have to stop putting CO<sub>2</sub> into the atmosphere we also must start pulling it out somehow. Also, in light of the Paris agreement<sup>11,12</sup>, there is a significant pressure on countries to control CO<sub>2</sub> emissions into the atmosphere<sup>5,10,13</sup>. For instance, the Singapore government has pledged to reduce emissions by 36% from 2005 levels by 2030<sup>14</sup>.

Increasing CO<sub>2</sub> emissions worldwide and its negative impact on climate change has led to a notable academic and industrial interest in various strategies for CO<sub>2</sub> reduction. Predominantly three strategies are employed to control the level of CO<sub>2</sub> in the atmosphere<sup>15,16</sup>: i) decrease in fossil fuel consumption and other activities that result in CO<sub>2</sub> emission, ii) capture CO<sub>2</sub> and dump it in geologic or oceanic reservoirs and iii) utilize CO<sub>2</sub> by converting it to either fuels or some other value-added products. The first strategy can be employed by utilizing energy sources that do not release CO<sub>2</sub> such as hydropower, wind power, solar energy, biomass, marine energy, geothermal energy, and nuclear energy<sup>16</sup>. This strategy involves developing intelligent solutions for storing these forms of energy and connecting them to existing transmission networks. CO<sub>2</sub> capture and sequestration is the second option to prevent more CO<sub>2</sub> from being released into the atmosphere<sup>17,18</sup>. This is done by trapping CO<sub>2</sub> and then pump it deep underground. However, sequestration comes with several downfalls including concern for leaks (even though it is pumped very deeply underground), increasing the monetary cost of sequestering CO<sub>2</sub>, and increasing and very large to begin with energy costs of transporting CO<sub>2</sub> and pumping it underground. However, importantly this technique can only be applied to stationary sources of CO<sub>2</sub> like power plants and does nothing to address the CO<sub>2</sub> that is already in the atmosphere. Also, the separation of CO<sub>2</sub> from the gas stream is an energy-intensive process. Taking one big step forward, the CO<sub>2</sub> can be used to make fuels/chemicals giving it value and eliminating the cost needed to store it. This is the third strategy in which CO<sub>2</sub> is converted to a value-added chemical that can be stored easily<sup>16–18</sup>. Employing this strategy results in the two-fold advantage of reducing CO<sub>2</sub> emissions and producing beneficial chemicals such as methane, methanol, formic acid, etc. that can be stored without difficulty<sup>16,17,19–21</sup>.

## 1.2 CO<sub>2</sub> to value-added products

CO<sub>2</sub> being a relatively inert and highly stable molecule, its activation is the crucial step in utilizing CO<sub>2</sub> as a chemical feedstock<sup>22</sup>. Two of the feasible routes for this conversion are CO<sub>2</sub> hydrogenation and CO<sub>2</sub> dry reforming of methane (DRM), as shown in Figure 1. 1. In the CO<sub>2</sub> hydrogenation route, hydrogen is employed as a reagent to transform CO<sub>2</sub> into other valuable chemicals<sup>23,24</sup>. The hydrogen required for this reaction can be supplied via

water electrolysis. To achieve an overall CO<sub>2</sub> reduction, the electricity needed for water electrolysis must be produced from renewable sources of energy such as wind or solar and not from fossil hydrocarbons<sup>25–27</sup>. Additionally, hydrogen can also be produced by natural gas reforming using steam or via biomass gasification process<sup>28,29</sup>.

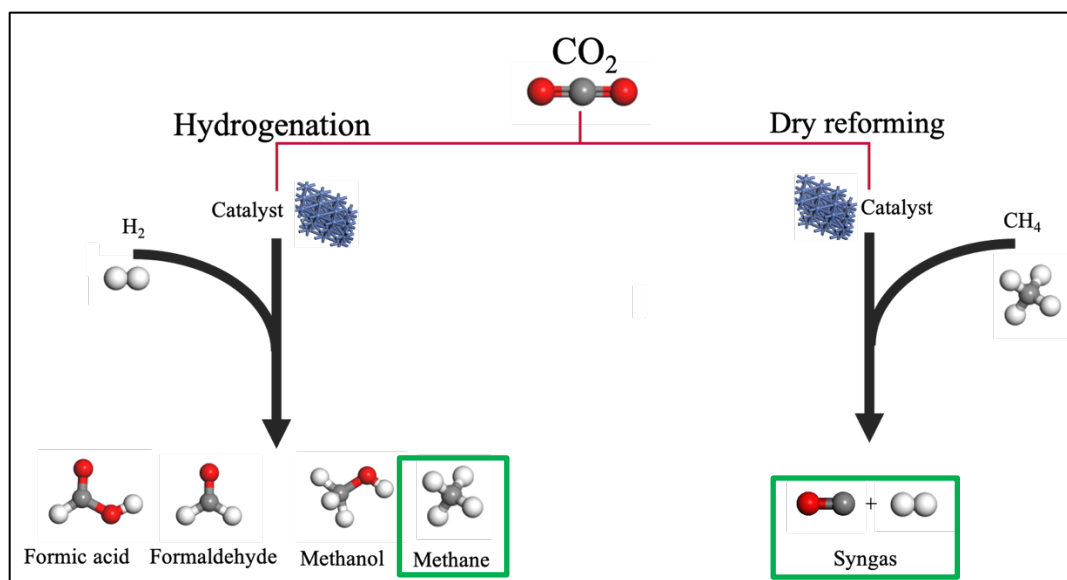


**Figure 1. 1** Schematic diagram showing CO<sub>2</sub> conversion to different value-added products via hydrogenation and dry reforming routes. The current work focuses on CO<sub>2</sub> hydrogenation to form methane and CO<sub>2</sub> dry reforming of methane to form syngas (shown inside green box).

Metal-based heterogeneous catalysts can activate CO<sub>2</sub> and its hydrogenation leads to various valuable products, as shown in Figure 1. 1 and Figure 1. 2<sup>30–35</sup>. Noble metals such as Ru, Rh, Pt, Pd, etc. have shown excellent selectivity and catalytic activity for CO<sub>2</sub> hydrogenation, compared to cheap transition metals such as Ni, Cu, etc. However, the high cost of such metals limits their use in large-scale applications. The low cost and ease of availability of metals like Ni, Cu, Fe make them extremely relevant for CO<sub>2</sub> activation. Among the different hydrogenation reactions, the current work focuses on CO<sub>2</sub> methanation. Notably, Ru and Ni (*cf* Figure 1. 2) have shown good catalytic activity for CO<sub>2</sub> methanation<sup>36–38</sup>. Methane is the main constituent of natural gas, which is the cleanest fossil fuel for electricity production<sup>25</sup>. Using natural gas helps to meet the ever-growing energy needs and its worth mentioning that 95% of Singapore’s electricity is generated

using natural gas<sup>39</sup>. The product methane could benefit from the existing infrastructure for storage and transport of natural gas<sup>40</sup>. It is also a promising candidate for use in direct methane fuel cells that could generate energy more efficiently than other combustion methods<sup>41,42</sup>. Additionally, CO<sub>2</sub> methanation is a promising approach for biogas upgrading<sup>17,43</sup>. Biogas, a mixture of CO<sub>2</sub> and CH<sub>4</sub>, can be used directly as a feedstock for CO<sub>2</sub> methanation resulting in the production of high purity CH<sub>4</sub> that can be directly fed to the existing natural gas pipelines. The CH<sub>4</sub> present in biogas could act as a diluent and can be useful for temperature control during the process<sup>39</sup>.

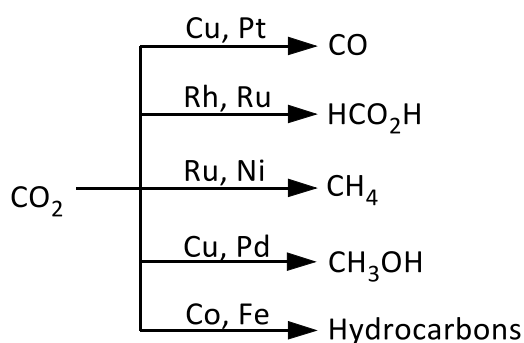


**Figure 1. 2** Schematic showing possible products and potential catalysts for CO<sub>2</sub> hydrogenation

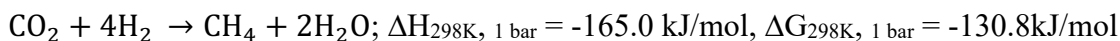
Another prominent reaction route for CO<sub>2</sub> conversion is the dry reforming of methane (DRM) (*cf* Figure 1. 1). This reaction converts two greenhouse gases, CH<sub>4</sub> and CO<sub>2</sub>, to produce synthesis gas (syngas), an important chemical precursor for liquid fuels and commodity chemicals<sup>44</sup>. Syngas, which is a mixture of CO and H<sub>2</sub>, can further be used in Fischer-Tropsch synthesis to produce long-chain hydrocarbons<sup>45</sup>.

The current thesis focuses on CO<sub>2</sub> methanation and CO<sub>2</sub> dry reforming of methane reactions. Interestingly, Ni-based catalysts are well suited for both these reactions.

### 1.2.1 CO<sub>2</sub> Methanation

This reaction also called as Sabatier reaction or Sabatier process was discovered by the French chemist Paul Sabatier in 1910s<sup>46</sup>. It involves the reaction of hydrogen with carbon

dioxide at temperatures in the range of 300–400 °C and atmospheric pressures in the presence of a catalyst to produce methane and water.



The hydrogen required for this conversion can be produced by electrolysis of water using surplus energy available from renewable sources<sup>25–27</sup>. The renewable energy sources being intermittent, could lead to a dip in energy generation or a surplus in energy generation. Currently, the surplus generation goes to waste because of the lack of technology to store the electricity in a very large quantity. However, this problem can be solved by utilizing this excess energy to produce fuels that can be easily stored. This technology of converting electrical power to gaseous fuel is called power to gas (P2G) technology<sup>25,47</sup>. The surplus electricity is passed through water and the electrical current breaks apart the water molecule separating oxygen from hydrogen. Hydrogen can be directly used as a fuel, but storage and transportation of hydrogen have been a challenge in this technology. We are still not technologically advanced to use hydrogen as a fuel and this can be avoided if hydrogen is spent to produce other value-added products like methane<sup>46</sup>.

In the power to methane technology (*cf* Figure 1. 3), CO<sub>2</sub> is reduced by hydrogen in power to gas plants to produce methane, and the hydrogen comes from the surplus renewable energy and not from fossil fuels<sup>46</sup>. Methane is then introduced into the existing gas grid which can intermediately store energy for a longer period compared to a power grid before its transported and used as needed. This way the methane can be used as a substitute for petrol/diesel which subsequently decreases the dependence on fossil fuels. The gas can even be converted back to electrical power in case of storage. The power to methane technology is extremely relevant from Singapore's perspective as 95% of total electricity in Singapore is produced from natural gas<sup>39</sup>. Notably, the majority of natural gas used in Singapore is imported from Malaysia and Indonesia via pipelines (Piped natural gas (PNG))<sup>14,48,49</sup>. Additionally, more focus is given on solar energy, Singapore's most potential renewable source of energy<sup>50,51</sup>. As mentioned before (*cf* Figure 1. 3), the excess solar energy could be used to produce hydrogen and expended in power to methane plants. Thus, the power to methane technology helps in utilizing CO<sub>2</sub> to produce methane and reduces

the wastage of surplus renewable energy produced. However, activation of stable the  $\text{CO}_2$  molecule is a challenge in using it as a chemical feedstock and a catalyst must be employed.

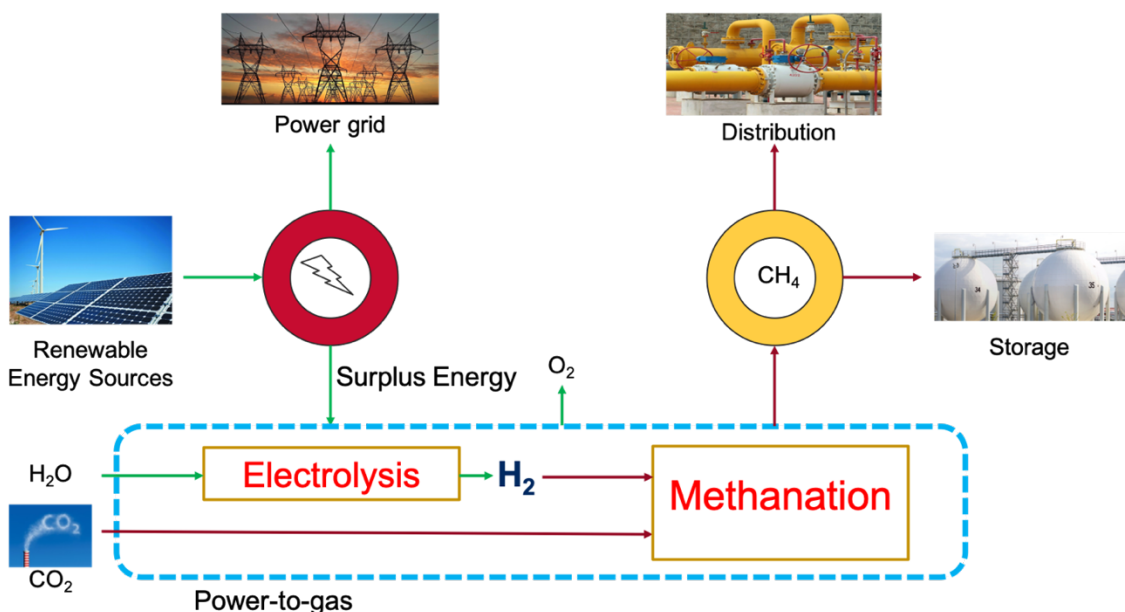


**Figure 1. 3** Schematic diagram of power to methane technology showing the utilization of surplus renewable energy to produce methane

#### 1.2.1.1 Catalysts for $\text{CO}_2$ methanation

The reduction of the fully oxidized carbon,  $\text{CO}_2$ , to methane is an eight-electron process with significant kinetic limitations, which requires a catalyst to achieve acceptable rates and selectivity for potential industrial use<sup>16,18,38</sup>. Ni and Ru based catalysts exclusively produce methane, while less reactive metal constituents Pd, Pt, Rh, Mo, Re, and Au catalyze simultaneously  $\text{CH}_4$ ,  $\text{CH}_3\text{OH}$ , and CO (by reverse water-gas shift reaction). Comparing the  $\text{CO}_2$  methanation reaction on alumina supported Ni and Ru catalyst, it was found that the apparent activation energy on Ni is 45 kJ/mol higher than that on Ru, effecting the higher activity of Ru<sup>52</sup>. But its high cost is a challenge in using Ru in the industry. Nickel is the most widely used catalyst for  $\text{CO}_2$  methanation because it shows good selectivity towards methane and it has low cost. Most of the work performed to enhance the activity of Ni is done by modifying supports. Nickel catalysts along with different supports have been used and studied widely. Usually metal oxides such as  $\text{Al}_2\text{O}_3$ ,



TiO<sub>2</sub>, MgO, etc. are preferred as supports due to their high surface area. Numerous researchers have mentioned the effects of electronic interaction between support and adsorbing species through the metal<sup>53</sup>. When a metal oxide is used as a support, charge transfer takes place from support to metal and thus the metal has the potential of transferring more charge to the adsorbing species leading to higher activation of the adsorbing species. It can be comprehended that researchers concentrated much on improving the support material rather than the catalyst. Support helps in the dispersion of metal and has little effect in methanation reaction. Different supports were tried and tested out but didn't result in a breakthrough since the fundamental reason behind their role is not explained. Also, the different supports proposed in different works cannot be directly compared since the experiments were performed at dissimilar conditions. Much work hasn't been done to modify the metal catalyst and majority of the improvements were suggested for the support. So, if we must design a novel catalyst using a bottom-up approach, these studies don't help much, and a detailed understanding of the underlying reaction mechanism is essential.

#### 1.2.1.2 CO<sub>2</sub> methanation reaction mechanism

On a catalyst surface, the CO<sub>2</sub> methanation reaction doesn't take place in a single step. First, the reactants adsorb onto the surface. Adsorbed intermediates are produced and destroyed through a series of bonds being formed and being broken. Then the final product(s) is produced, and it desorbs from the catalyst surface. Understanding the elementary reaction steps and rate-determining step (RDS) will lead to effective catalyst design and development by modifying the reaction route/reducing the barrier for RDS. Many studies have been carried out to understand the mechanism of CO<sub>2</sub> methanation on Ni and Ru surfaces. Even then, there is a difference in opinion exists among researchers regarding the reaction mechanism on both Ni and Ru. The most debated step in CO<sub>2</sub> methanation is the hydrogenation step. The hydrogen could react with CO<sub>2</sub>, CO and/or C as shown in Figure 1. 4. In addition, the reaction could proceed with/without forming a CO intermediate. Understanding the exact pathway is essential for experimentalists to improve the ability of catalysts for methanation. For instance, if methanation takes place via CO

intermediate route, the catalyst should have both carbon-oxygen bond cleavage ability and hydrogenation ability. But if the reaction proceeds without forming CO intermediate (via formate pathway), carbon-oxygen bond cleavage takes place in a hydrogenated species ( $\text{HCOO}$ )<sup>54</sup>. Also, for the methanation reaction mechanism through the CO pathway, the activation of this stable intermediate stands as a challenge. Hence, knowing the reaction mechanism is required to tailor the catalyst for it.

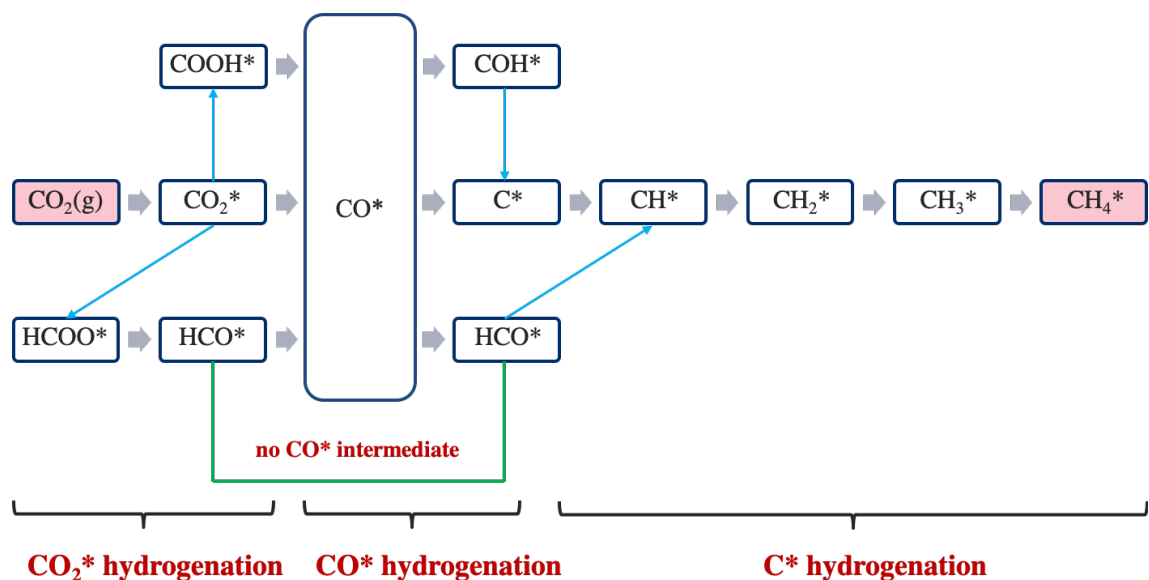


**Figure 1. 4** Schematic showing the possible reaction pathways for  $\text{CO}_2$  methanation. The pathways include  $\text{CO}_2$  direct dissociation and hydrogenation with/without  $\text{CO}^*$  intermediate routes,  $\text{CO}^*$  hydrogenation, and  $\text{C}^*$  hydrogenation.

Hence, understanding the  $\text{CO}_2$  methanation reaction mechanism has a crucial significance in designing better catalyst and it still remains a challenging task since the reaction mechanism on both Ru and Ni is debated and remains unsettled<sup>37,38</sup>. The major reaction routes studied for  $\text{CO}_2$  methanation are discussed here (*cf* Figure 1. 4).  $\text{CO}_2$  activation routes include direct decomposition to  $\text{CO}^*$  and  $\text{O}^*$  and  $\text{CO}_2$  hydrogenation via  $\text{HCOO}^*$  or  $\text{COOH}^*$  intermediate. The different  $\text{CO}_2$  transformation routes lead to  $\text{CO}^*$  formation and the activation route of  $\text{CO}^*$  is often debated. This step is extremely relevant as  $\text{CO}^*$  activation is typically regarded as the rate-determining step (RDS). In addition,  $\text{CO}^*$  coverages are reported to be high and this leads to catalyst poisoning by blocking the active

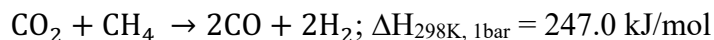
sites<sup>55,56</sup>. CO\* can transform via C-O bond cleavage ( $\text{CO}^* \rightarrow \text{C}^*$ ) or undergoes further hydrogenation and dissociation via COH\* ( $\text{CO}^* \rightarrow \text{COH}^* \rightarrow \text{C}^*$ ) or HCO\* ( $\text{CO}^* \rightarrow \text{HCO}^* \rightarrow \text{CH}^*$ ) route to form C\*/CH\*. In contrast to the CO\* intermediate routes discussed above, the CO<sub>2</sub> methanation pathway without forming CO\* as an intermediate is also possible ( $\text{CO}_2 \rightarrow \text{HCOO}^* \rightarrow \text{HCO}^* \rightarrow \text{CH}^*$ ) (*cf* Figure 1. 4). The C\*/CH\* thus formed (with/without CO\* intermediate route) undergoes sequential hydrogenation to form methane. It is worthy to mention that the methane formation via CH<sub>x</sub>OH/CH<sub>x</sub>O (x = 1 – 3) (formed from the hydrogenation of HCO\*/COH\*) routes are hardly explored.

There is a discrepancy in the CO<sub>2</sub> methanation reaction mechanism on Ni (111) and Ru (001) surfaces. It is essential to have a fundamental understanding of CO<sub>2</sub> methanation reaction on both Ru and Ni to rationally develop better catalysts based on Ni. The key step is the hydrogenation reaction, and this may happen to adsorbed CO<sub>2</sub>\*, CO\*, and/or C\* depending on which the RDS also differs. The complexity of the methanation reaction network results in the inconsistent prediction of reaction pathways and RDS reported in different studies, causing the experimental/computational predictions extremely challenging on both Ni and Ru surfaces. Even though CO<sub>2</sub> direct dissociation to CO\* is thermodynamically and kinetically favorable on both Ni and Ru surfaces, CO\* activation has a high barrier. Hence, it is crucial to investigate CO<sub>2</sub> hydrogenation routes with/without CO\* intermediate to ascertain the dominant reaction pathway.

### 1.2.2 Dry Reforming of Methane

Methane is an alternative feedstock to produce fuels, chemicals, and electricity<sup>57,58</sup>. It is the smallest hydrocarbon and the most abundant organic gas present in the Earth's atmosphere. It is the primary component of natural gas and constitutes about 80-95% of the volume<sup>57,58</sup>. The natural gas reserve on Earth is reported to be 196.03 trillion cubic meters<sup>59</sup>. Despite these immense reserves, the use of natural gas/methane to produce value-added chemicals remain underutilized. Increasing natural gas (rich in methane) infrastructure due to its newly found availability and resources, as well as depleting crude oil reserves, has intensified interest in methane conversion processes to produce alternative

fuels, chemicals and electricity<sup>60,61</sup>. Synthesis gas, an important chemical precursor for liquid fuels and commodity chemicals, is a mixture of CO and H<sub>2</sub> that is produced through catalytic indirect methane conversion processes, viz. the partial oxidation of methane (POM) and methane steam reforming (SRM)<sup>60–63</sup>. There is also notable research interest in novel methane dry reforming (DRM) processes as they use CO<sub>2</sub> as the oxidant<sup>62,64–66</sup>. In addition, the produced syngas from DRM has H<sub>2</sub>/CO ratio of 1:1 that can be preferentially used in Fischer-Tropsch synthesis to produce long-chain hydrocarbons. Most importantly DRM converts two greenhouse gases, CH<sub>4</sub> and CO<sub>2</sub><sup>67</sup>. It involves the reaction of methane with carbon dioxide at temperatures in the range of 700–900 °C and atmospheric pressures in the presence of a catalyst to produce syngas.



Aggressive operating conditions are required to activate the highly stable and non-polar methane C–H and carbon dioxide C=O bonds, which favors undesired reactions and decreases catalyst activity, as well as product selectivity and yield<sup>60,61,68</sup>. With a hostile environment, the perfect catalytic materials require high temperature, oxidation, and corrosion resistance, as well as excellent catalytic activity, which are all characteristics of transition metals<sup>69</sup>.

#### 1.2.2.1 Catalysts for DRM

Transition metals such as Pt, Pd, Ru, Rh, Ir, and Ni have shown good catalytic activity for this reaction<sup>66,70</sup>. DRM turnover rates were found to be higher on noble metals such as Pt, Ru, Rh and Ir compared to Ni catalyst<sup>71</sup>. Even though noble metals are more active and selective, Ni-based catalysts are viable, considering their low cost and availability<sup>62,66,72</sup>. However, nickel catalysts suffer from deactivation from coking (surface carbon formation), which leads to fouling and high pressure drops across reactors<sup>73,74</sup>. Developing coke resistant catalysts for DRM is the current bottleneck in commercializing the process. For improving the stability of Ni catalysts, several strategies were proposed, including doping by other metals and metalloids<sup>75–79</sup>. However, in many cases, the addition of promoters leads to a trade-off between catalyst activity and stability. Hardly any breakthrough has come in improving the stability of Ni because it was done more or less arbitrarily without

a clear molecular level understanding. Interestingly, microstructure modifications like boron-promoted Ni are reported to have enhanced coke resistance<sup>80–82</sup> without downgrading activity. Thus, NiB can be a potential catalyst for DRM. However, for employing NiB to study DRM necessitates the fundamental understanding of the elementary reaction steps and reaction energetics in the conversion of CO<sub>2</sub> and CH<sub>4</sub> to syngas to assess the activity, stability and selectivity of the catalyst. To the best of our knowledge, there are no studies reported in the literature that employs NiB and gives mechanistic insights into the DRM reaction. To evaluate the effects due to B doping, it is essential to comprehensively study DRM reaction on clean Ni first and then compare the changes in the reaction pathways and energetics due to B doping.

### 1.2.2.1 DRM Reaction mechanism

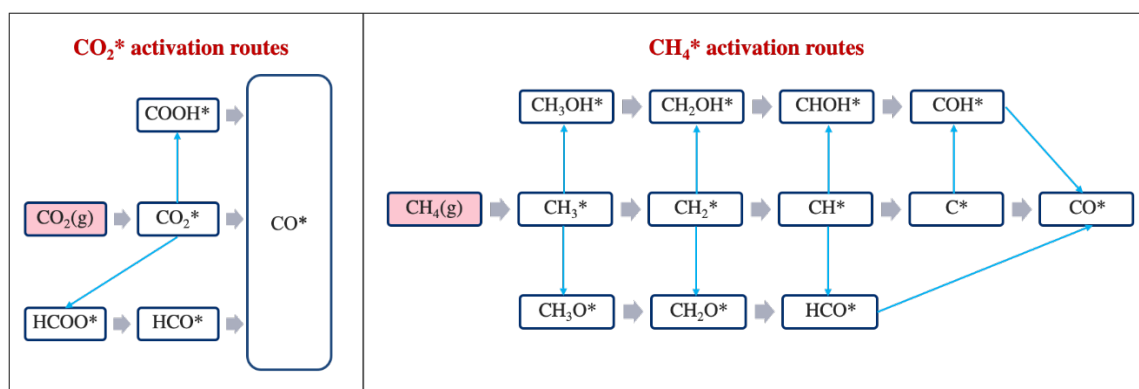


**Figure 1. 5** Schematic showing the possible reaction pathways for CO<sub>2</sub> and CH<sub>4</sub> activation routes in DRM reaction. CO<sub>2</sub> activation includes direct dissociation and hydrogenation routes. CH<sub>4</sub> activation includes sequential dehydrogenation and O\*/OH\* oxidation routes

The DRM reaction network is complex as it involves a large number of elementary reactions that can be grouped under three reaction categories (*cf* Figure 1. 5): i) CH<sub>4</sub> stepwise dehydrogenation, ii) formation of surface oxidants (O\*/OH\*), and iii) CH<sub>x</sub> oxidation<sup>83</sup>. Typically, on Ni (111), the computed activation barriers for the dissociation of CH<sub>4</sub> to CH<sub>3</sub>\* and CH\* to C\* were substantially higher compared to other steps<sup>84–86</sup>. Importantly, the sequential dehydrogenation of CH<sub>4</sub> was favored (both thermodynamically and kinetically) over bimolecular reactions, and the production of gas-phase C<sub>2</sub>

hydrocarbon species was highly unlikely<sup>85</sup>. The sequential dehydrogenation of CH<sub>4</sub> leads to the formation of surface carbon that deactivates nickel catalysts by blocking reactive sites and also diffusing into Ni, forming nickel carbide<sup>73,74</sup>.

Very little is known about the subsequent oxidation of CH<sub>x</sub> by surface O\*/OH\*. The oxidants can also be the key decoking media via reactions with surface carbon. In DRM, these oxidants are generated from the dissociation of CO<sub>2</sub>. Various CO<sub>2</sub> dissociation routes (direct dissociation and H-assisted transformation via COOH\*/HCOO\* intermediate) are studied and the direct decomposition of CO<sub>2</sub>\* to CO\* and O\* is proposed to be the dominant CO<sub>2</sub> conversion route on Ni (111)<sup>87,88</sup>. Hence, O\* is suggested to be the major oxidizing agent generated from CO<sub>2</sub>.

Among the different CH<sub>x</sub>\* oxidation routes by O\* and OH\*, CH<sub>3</sub>\* and CH<sub>2</sub>\* oxidation reactions are kinetically and thermodynamically impeded and only CH\* and C\* oxidation steps are kinetically feasible reactions<sup>64,84,86,87</sup>. It is interesting to note that often the CH\*/C\* oxidation step is described as the rate-determining step.

In short, the methane reforming pathway involves the decomposition of CH<sub>4</sub> to form CH\* or C\* followed by O\*/OH\* oxidation and finally decompose to form CO\*. However, the RDS in DRM is still debated. Some literature describes CH<sub>4</sub> dissociation as the RDS<sup>71</sup> whereas other studies have shown that C\*/CH\* oxidation by O\*/OH\* as the RDS<sup>64</sup>. This inconsistency in the RDS reported in various studies appears to result from the intricacy of the DRM reaction network making the experimental/computational predictions extremely challenging.

### 1.3 Challenges in catalytic conversion of CO<sub>2</sub>

In CO<sub>2</sub> methanation and DRM reactions, the preferred catalyst is Ni due to its high selectivity and low cost, despite its poor activity (for methanation) and stability (for DRM). Interestingly, microstructure modifications (including doping by metals and metalloids) are reported to have enhanced the activity and coke resistance of Ni-based catalysts<sup>75,89–92</sup>.

Therefore, it is imperative to modify the Ni surface to improve its activity for methanation and kinetically hinder carbon formation and favor carbon destruction for the DRM reaction. As discussed before, it is crucial to have a thorough understanding of the complex reaction network on the catalyst, active sites, as well as reaction energetics and kinetics and rate-determining step (RDS) for effective catalyst design and development by modifying the reaction route/reducing the barrier for RDS<sup>93</sup>.

Even though CO<sub>2</sub> methanation is widely studied, there is a discrepancy in the reaction mechanism on both Ni and Ru surfaces. The insights gained from the methanation reaction mechanism on Ru could aid in designing efficient catalysts based on Ni. However, the number of reactions and the modeling systems considered for Ni and Ru in various studies are different making the direct comparison of selectivity and activity between Ni and Ru extremely challenging. Additionally, it is essential to understand and compare the CO<sub>2</sub> methanation reaction on Ru and Ni. However, the reaction mechanism on both Ru and Ni is debated and remains unsettled<sup>37,38</sup>. The most debated steps are the activation routes of CO<sub>2</sub> and CO\*. This includes direct dissociation routes and different hydrogenation pathways for CO<sub>2</sub> and CO\* activation. In addition, another key argument is whether the reaction proceeds by forming a CO\* intermediate. The complexity of the methanation reaction network results in the inconsistent prediction of reaction pathways and RDS reported in different studies on both Ni and Ru surfaces. Moreover, methanation involves large and complex reaction network and hence the accuracy of the model is affected by the number and type of possible reactions selected for the study. Additionally, methane formation via CH<sub>x</sub>OH/CH<sub>x</sub>O (x = 1 – 3) (formed from the hydrogenation of HCO\*/COH\*) routes are hardly explored and intermediates such as HCO\* (formed via HCOO\* route), HCOH\*, HCOOH\*, H<sub>2</sub>COO\*, H<sub>2</sub>COOH\* and C(OH)<sub>2</sub>\* were not considered in many studies.

For the DRM reaction, Ni-based catalysts suffer from deactivation due to carbon deposition. One of the techniques for improving catalyst stability involves doping of metals and metalloids. However, in many cases, this doping is accompanied by a decrease in the conversion rates of CH<sub>4</sub> and CO<sub>2</sub>. We identified B doped Ni as a potential catalyst for DRM

that can improve catalyst stability without compromising activity. However, no studies are reported in the literature that employs NiB as a catalyst for DRM, to the best of our knowledge. Additionally, DRM involves large and complex reaction network and the accuracy of the model is affected by the number and type of possible reactions selected for the study. Understanding and mastering methane activation and C-H bond dissociation continues to be one of the biggest challenges for chemists and reaction engineering practitioners to date. In addition, less is known about the subsequent oxidation steps and Boudouard reaction (identified as a potential carbon source) has not been considered in the majority of studies.

In addition, single-atom alloys for selective catalysis are now gaining traction to develop catalysts with high stability and activity. However, these catalysts were not explored for studying different CO<sub>2</sub> conversion reactions including methanation and DRM reactions.

From the above discussion, it is clear that there are discrepancies in the RDS and reaction mechanisms of CO<sub>2</sub> methanation and DRM reactions on Ni. Understanding atomic and molecular level phenomena through experiments can be extremely challenging as this involves sophisticated measuring techniques like *in situ* Fourier Transform Infrared Spectroscopy and extreme temperatures and pressures and also since the intermediates are short-lived it is more challenging to identify them in experiments. Hence, getting mechanistic details from experiments is extremely challenging. Accordingly, computational tools need to be implemented to gain fundamental, molecular level insights. Molecular modeling techniques such as Density Functional Theory (DFT) can be employed as a predictive tool to understand the reaction mechanism.

#### **1.4 DFT for studying CO<sub>2</sub> conversion reactions**

Computational techniques such as DFT are established research tools that can not only be used to interpret and explain experimental findings but also can act as a predictive tool to guide catalyst design and development<sup>94-99</sup>. DFT-guided catalyst design models in heterogeneous catalyst based reactions have been proposed by many researchers<sup>96,97</sup>. This



approach eliminates the need for prerequisite knowledge of all kinetic parameters pertaining to the reaction by employing suitable descriptors controlling the activity and selectivity of catalysts. These descriptors could be adsorption energies (of reactant or product or intermediates) or activation barriers, based on experiments and/or quantum mechanical calculations. DFT can be used to examine the electronic structure of the catalysts, adsorbate geometries, reaction energetics, and provide structural and mechanistic insights into adsorbate-surface interactions<sup>100–102</sup>.

In DFT, the energy of the system expressed as a function of electron density. In this approach, the total energy of the system can be represented as a sum of non-interacting kinetic energy, the Coulomb interaction between electrons and nuclei, the Coulomb interaction between electrons, the Coulomb interaction between pair of nuclei and the exchange-correlation energy. One of the major challenges in DFT is that the exact form of exchange-correlation functional is not known<sup>103,104</sup>. Many approximations are available for the exchange-correlation functional, among which more widely accepted class of functionals for studying molecules interacting with metal surfaces is the Generalized Gradient Approximation (GGA)<sup>105</sup>. A detailed explanation of functionals and its types are provided in Chapter 2, section 2.2 and 2.3.

#### 1.4.1 Challenges in DFT

As discussed above, an accurate exchange-correlation functional must be chosen for a DFT based catalyst design procedure. However, the popular and widely employed functionals such as PBE and PW-91 have limitations in predicting CO<sub>2</sub> methanation and DRM energetics. There are some inconsistencies in the calculated values using these functionals. For example, CO<sub>2</sub> binding energies on metal surfaces calculated by these functionals do not match with experimental values<sup>106–111</sup>. Besides this, for weakly bound systems (e.g. CO<sub>2</sub> adsorption system) GGA functionals are inadequate for the description of dispersion interactions (non-local electron-electron correlation). Hence, several schemes are developed to incorporate van der Waals (vdW) interaction and thereby improving the energies of dispersion-bonded systems. The significance of vdW interactions in studying

CO<sub>2</sub> conversions is ignored in many studies<sup>108</sup>. It is essential to include the contribution of vdW interactions in studying CO<sub>2</sub> binding energies and activation.

To provide a quantitative prediction of conversion and coverages of the complex reaction network, DFT studies need to be extended to a microkinetic model. However, only a few DFT studies reported in the literature are extended to develop a microkinetic model for CO<sub>2</sub> conversion reactions. This is possibly because it involves a large number of elementary reactions making it extremely difficult to calculate the reaction energetics using DFT. Importantly, in the catalyst design model proposed by Rangarajan et al.<sup>106,112</sup>, a small deviation in binding energy (which is a descriptor) prediction was shown to affect the microkinetic model and hence the design procedure. It was shown that for the fitting of model to experimental data, DFT predicted binding energies of different adsorbing species (including CO<sub>2</sub>) on Cu (111) had to be altered by more than 50 kJ/mol.

Hence, the functional selection is not given much importance and the need for benchmarking the functionals before studying the reactions is ignored in the majority of works reported to date. Functional benchmarking is very essential to ensure the accuracy of DFT predicted energetics. It is essential to employ correct functional that can predict the interactions of reactants, products, and intermediates with the metal surface.

## 1.5 Objectives

The unifying theme of the thesis is to investigate the catalytic conversion of CO<sub>2</sub> to hydrocarbons (methane and syngas) using DFT based computational studies by employing an accurate functional choice. The primary objectives of the present thesis are 1) to identify a correct DFT functional for accurately predicting CO<sub>2</sub> conversion reaction energetics 2) to perform a combined DFT and microkinetic analysis for predicting the CO<sub>2</sub> methanation reaction mechanism and RDS on Ni (111) and Ru (001) surfaces 3) to perform a combined DFT and microkinetic analysis and predict DRM reaction mechanism and RDS on Ni (111) and NiB surfaces and addresses the coking problem on Ni (111) and 4) to perform a computational catalyst screening and predict novel catalyst (more active and stable) for the

CO<sub>2</sub> methanation and DRM reactions. The specific objectives for each chapter are given below:

### 1.5.1 Key objectives of Chapter 3

- To identify a suitable DFT functional that can be used to study CO<sub>2</sub> conversion reactions on different metals.
- To benchmark different DFT functionals via CO and CO<sub>2</sub> adsorption on Ni as a model catalyst surface.
- To identify the source of error in predicting CO<sub>2</sub> binding energy by the rPBE-vdW functional.
- To compare the change in CO<sub>2</sub> adsorption energy prediction by rPBE-vdW functional on different metal surfaces.

### 1.5.2 Key objectives of Chapter 4

- To provide mechanistic insights into the reaction pathway of CO<sub>2</sub> methanation reaction on Ni (111) and Ru (001) surfaces.
- To develop a MKM based on DFT energetics and predict the reaction rates and fractional coverages under reaction conditions.
- To perform sensitivity analysis and partial equilibrium analysis for identifying the rate-determining step.
- To compare the reaction mechanism and conversions on Ni and Ru surfaces.

### 1.5.3 Key objectives of Chapter 5

- To provide mechanistic insights into the reaction pathway of DRM reaction on Ni (111) surface
- To propose a Ni-based catalyst (NiB) that addresses the coke formation problem on Ni (111) surface.
- To study the DRM reaction mechanism on NiB and compare the mechanistic differences with that on Ni (111) surface.
- To develop a MKM based on DFT energetics and predict the reaction rates and fractional coverages under reaction conditions.

- To perform sensitivity analysis and partial equilibrium analysis for identifying the rate-determining step.

#### 1.5.4 Key objectives of Chapter 6

- To perform a thorough computational screening to identify a NiB based single atom alloy catalyst that is more active and coke resistant for CO<sub>2</sub> methanation and DRM reactions.
- To evaluate the thermodynamic stability of NiB-Mn single atom alloy catalyst surface.
- To provide mechanistic insights into the reaction pathway of CO<sub>2</sub> methanation reaction on NiB-Mn (111) single atom alloy catalyst surface.
- To provide mechanistic insights into the reaction pathway of DRM reaction on NiB-Mn (111) single atom alloy catalyst surface.

#### 1.6 Dissertation overview

The main findings of the thesis are organized into 4 chapters. Each of these chapters has a brief introduction covering the background, challenges, and relevant literature on the topic addressed in the chapter. In each of these chapters, following the introduction, a brief discussion on the computational system and methodology employed is presented. Afterward, the results are presented and discussed in detail. Subsequently, each chapter is concluded with a summary of the key findings. Following the introduction, challenges and objectives presented in *Chapter 1*, *Chapter 2* of this thesis discusses the methodology used for the current study. The specific topic addressed in the different chapters of the thesis and the broad outline of the contents of each of the chapters, along with key outcomes are presented in this section (*cf* Figure 1. 6).

*Chapter 3* focuses on the DFT functional benchmarking study. Using Ni as a model catalyst surface, studies based on CO<sub>2</sub> and CO binding energies are performed to identify a functional that can be used for studying catalytic CO<sub>2</sub> conversion reactions. The binding energies of CO<sub>2</sub> and CO were calculated on the Ni surface using different DFT functionals and compared with experimental values from the literature to identify the functional that

accurately captures the metal adsorbate interactions correctly. Interestingly, the functional that predicted CO<sub>2</sub> binding energy failed to predict CO binding energy and vice-versa. The sources of error in predicting CO<sub>2</sub> binding energy by the DFT functionals are identified and studied by the density of states (DOS) analysis, activation barrier calculations, DFT simulated XPS results, and using an alternate reaction system. Finally, rPBE-vdW functional, with the inclusion of 28 kJ/mol for the calculation of gas-phase energy of CO<sub>2</sub> is suggested for studying CO<sub>2</sub> conversion reactions. The generality of the proposed functional in predicting CO<sub>2</sub> hydrogenation reaction on different hydrogenation metals such as Cu, Ru, Co and Pt are also tested and verified.

*Chapter 4* deals with the elucidation of the CO<sub>2</sub> methanation reaction mechanism on Ni (111) and Ru (001) surfaces. A detailed reaction network of 46 elementary reactions involving multiple CO<sub>2</sub>, CO and C activation routes (including dissociation and hydrogenation), side reactions (H<sub>2</sub>O formation, Boudouard reaction) and desorption of products were considered for studying CO<sub>2</sub> methanation reaction on Ni and Ru surfaces. Importantly, the DFT-calculated energies are fed to the MKM to calculate conversions and coverages under reaction conditions. Additionally, sensitivity and partial equilibrium analysis were performed to uncover the RDS and the reaction pathway.

The reaction mechanism of DRM on Ni (111) and NiB surfaces are presented in *Chapter 5*. DFT calculations (with an accurate and benchmarked functional choice), together with microkinetic modeling was employed to provide mechanistic insights into the DRM reaction network on Ni and boron promoted Ni catalysts. Notably, the coke formation problem on Ni is addressed by doping it with boron. A comprehensive reaction network of 38 elementary reactions involving multiple CO<sub>2</sub> dissociation routes, CH<sub>4</sub> dissociation routes, side reactions (H<sub>2</sub>O formation, Boudouard reaction) and desorption of products were considered for DRM reaction. Boron doping alters the dominant reaction pathway to kinetically hinder carbon formation and favor carbon destruction. Hence, NiB is proposed to be a potential catalyst for the DRM reaction.

*Chapter 6* deals with the computational investigations into single atom alloy's (SAA) for DRM and CO<sub>2</sub> methanation reactions. Based on the ability to break the C-O bond, 15 SAA's based on NiB was considered and a thorough computational screening was performed to identify the SAA's that are thermodynamically stable under the reaction conditions. Mn SAA of NiB was identified as a potential catalyst for both CO<sub>2</sub> methanation and DRM reactions based on its ability to activate CO<sub>2</sub>. Subsequently, both these reactions were simulated on Mn-NiB SAA alloy.

*Chapter 7* summarises the conclusions drawn from this thesis and perspectives on these. Additional supporting data pertaining to each chapter is listed as appendices to different chapters.

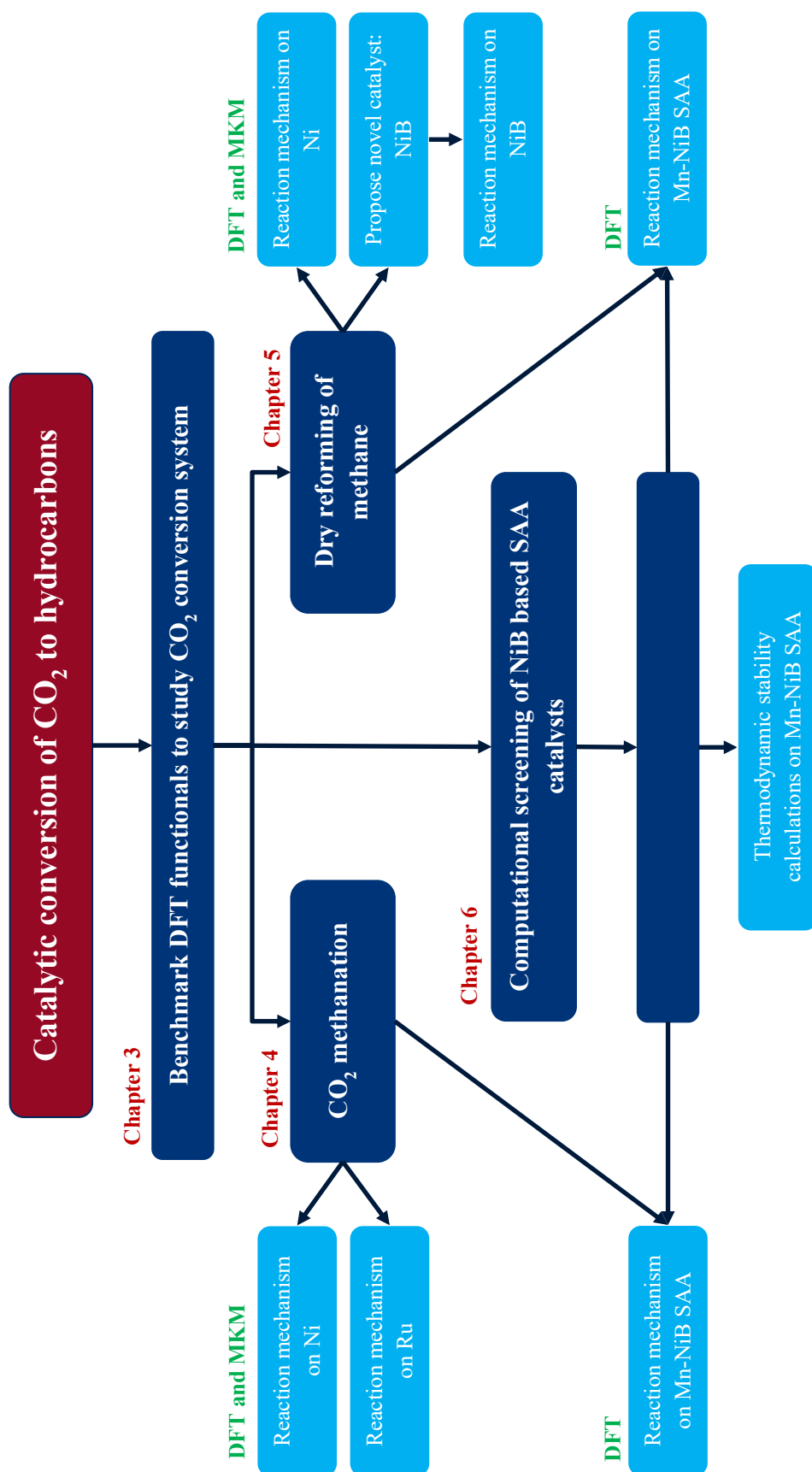


Figure 1. 6 Organization of the thesis

## Chapter 2 Computational Methods

*First principle calculations were performed based on density functional theory. An overview of density functional theory formulations is presented in sections 1 and 2 of this chapter. The accuracy of density functional theory predictions depends on the selection of appropriate exchange-correlation functional. It is essential to understand the differences between various functionals in order to select an apt functional for studying a reaction on a metal surface. An overview of different functionals and the physics behind these functionals are presented in section 3 of this chapter.*



## 2.1 Molecular modeling

Theoretical methods and computational techniques used to explain the behavior of molecules and molecular systems are termed as molecular modeling methods. Atomic and molecular level phenomena that are extremely challenging to be explored using experimental methods can be studied theoretically using molecular modeling. The two popular methods of modeling the molecules are force field method or molecular mechanics and electronic structure calculation or quantum method or *ab initio* method (*cf* Figure 2.1)<sup>113</sup>. If an individual atom is treated as the basic particle and the potential energy is calculated as a parametric function of the atomic coordinates, then the method is called force field method or molecular mechanics<sup>114</sup>. The dynamics of atoms in this method are modeled using Newton's laws of motions. In the electronic structure calculation or *ab initio* method, the positively charged nuclei and the negatively charged electrons are the fundamental particles and the interaction between these charged particles give rise to the potential energy<sup>115</sup>. Since the mass of electrons is lower than the borderline mass for Newtonian mechanics, electrons cannot be treated classically and quantum mechanics is needed. Electronic structure or quantum calculations must be employed for simulating/modeling chemical reactions such as methanation or DRM on different catalyst surfaces at an atomic level. These calculations take into account the electronic structures and also probes and predict the bonding and changes in electronic structures<sup>116,117</sup>.

In Quantum mechanics, the energy of a system is calculated by the Schrödinger equation, a second-order partial differential equation, which is a wave equation in terms of wave function  $\Psi$ <sup>118,119</sup>. It can describe the spatial and temporal evolution of the wave function of a particle in each potential. The time-independent Schrödinger equation is given by

$$H\psi = E\psi \quad (2.1)$$

where  $H$  is the Hamiltonian operator,  $\psi$  is the wave function which is a function of spatial coordinates of each of the electrons and  $E$  the energy of the system<sup>118</sup>. The wave function  $\Psi$ , determines everything that can be known about the particle. However, there are only a few simple cases (eg. Hydrogen atom, particle in a box) where the analytical solution of the Schrödinger equation is possible<sup>105</sup>. In real systems, multiple electrons interact with

many nuclei which makes the Schrödinger equation and its solution more complicated. Different methods are employed to find the solution of polyelectronic systems in electronic structure calculations. Two prominent approaches in these calculations are wave function approach and electron density approach.

In the wave function approach, the wave function is evaluated which is a function of each of the spatial coordinates of all electrons (polyelectronic) in the system. According to the molecular orbital theory, these wavefunction (molecular orbitals) can be expressed as a linear combination of atomic orbitals (LCAO). The atomic orbitals can be expressed as basis functions (eg. Gaussian, polynomial, planewaves). The total wavefunction is then expressed as a Slater determinant, in order to satisfy the Pauli exclusion principle. In the wave function approach (eg. Hartree-Fock methods), the aim is to calculate the molecular orbitals (wavefunction). The first step is to decide the type and number of basis set. Once it is decided, the molecular orbitals are formed as LCAO and the overall wavefunction is expressed in a Slater determinant form. Variational principle (energy calculated from an approximate wavefunction will always be bigger than the actual energy of the system) is used to calculate the set of coefficients in LCAO that minimises the overall energy of the system (in an iterative fashion). The accuracy of these calculations can be improved by using more number of basis functions. However, these calculations are computationally very expensive. For instance, the wave function (for a time-independent system) is a 66-dimensional function (3 spatial coordinates for 22 electrons) for a single CO<sub>2</sub> molecule. As the number of electrons increases (eg. 64 Ni (28 electrons) atom slab), these calculations become extremely difficult. Another major problem with this approach is that the electron-electron interactions are not accurately captured. Even though these interactions (electron-electron) are taken into account, the electron correlation part of the energy is not accurately captured. This is because each electron experiences the effect of an average field of all other electrons and the electron motion is not correlated. There are several methods (known as Post Hartree-Fock methods or electron correlation methods) that can improve the electron correlation energy. One of the most promising approaches is the electron density-based method in which the density of electrons determines the ground state properties of the system. This approach is called density functional theory (DFT) and is proposed by

Pierre Hohenberg and Walter Kohn in 1964. They proved that all the information of the system is contained in the electron density, and the total ground state energy of a many-electron system is a function of the density. (Detailed description of DFT method is given in Section 2.2).

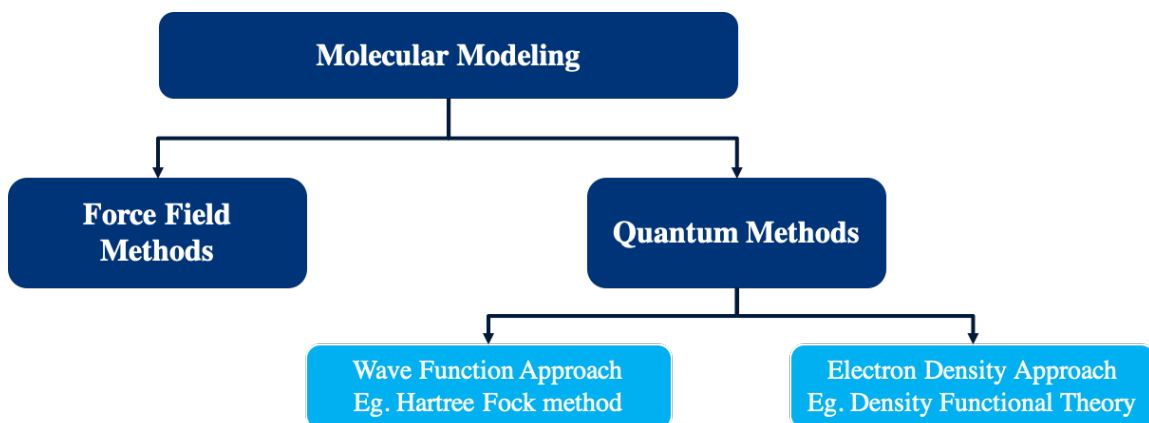


**Figure 2. 1** Schematic showing the different molecular modeling methods

## 2.2 Density Functional Theory (DFT)

It is possible to calculate the ground state density for a given potential through wave function. However, Kohn and Hohenberg showed that an inverse mapping is possible to obtain external potential from ground state density<sup>120,121</sup>. Based on this idea they proposed two fundamental theorems in DFT. The first theorem is proof for the existence of a relation between wave function and electron density of the system. It states that *the ground-state energy from Schrödinger's equation is a unique functional of the electron density*<sup>105,120,121</sup>.

$$E = E[\rho(r)] \quad (2.2)$$

where  $E$  is the ground state energy and  $\rho(r)$  is the electron density. However, the first theorem doesn't state how the density is calculated. The second theorem shows that the density obeys the variational principle. It states that *the electron density that minimizes the energy of the overall functional is the true electron density corresponding to the full solution of the Schrödinger equation*<sup>105,120,121</sup>.

$$E[\rho(r)] > E[\rho_0(r)] \quad (2.3)$$

The energy functional can be represented as:

$$E[\rho(r)] = T[\rho(r)] + E_{ne}[\rho(r)] + E_{ee}[\rho(r)] + E_{ion}[\rho(r)] + E_{xc}[\rho(r)] \quad (2.4)$$

where  $E[\rho(r)]$  is the total energy of the system,  $T[\rho(r)]$  is the kinetic energy,  $E_{ne}[\rho(r)]$  is the potential energy due to electron-nuclei interaction,  $E_{ee}[\rho(r)]$  is the potential energy due to Coulomb interaction between electrons,  $E_{ion}[\rho(r)]$  is the potential energy due to the Coulomb interaction between pair of nuclei and  $E_{xc}[\rho(r)]$  is the exchange-correlation energy. The exchange-correlation energy includes a) effects of quantum mechanical exchange and correlation b) correction for classical self-interaction energy c) difference in kinetic energy between the non-interacting system and real system.

To solve the equation, the electron density has to be varied (trial density) until energy obtained from the functional is minimized. However, the true form of the energy functional is not known because of the complex exchange-correlation energy functional term. Kohn Sham self-consistent field approach broke the problem of finding trial density and determining energy from trial densities. A novel technique is proposed by taking a fictitious system of non-interacting electrons where ground state density is the same density as a real system where electrons interact. This novel technique uses both the electron density and wave function approaches to calculate the total energy of the system. In Kohn Sham formulation, the energy is calculated using a series of one electron Kohn-sham equations:

$$\varepsilon_i \phi_i(r) = \left[ -\frac{\nabla^2}{2} + V_{KS}(r) \right] \phi_i(r) \quad (2.5)$$

where the first term on the right of equation (2.5), represents the kinetic energy of the electron,  $\phi_i(r)$  are the KS single-particle orbitals,  $\varepsilon_i$  are the KS eigenvalues,  $\rho$  is the electron density and  $V_{KS}$  is defined as

$$V_{KS}(r) = V(r) + V_H(r) + V_{XC}(r) \quad (2.6)$$

$$V_H(r) = e^2 \int \frac{n(r')}{|r-r'|} d^3r' \quad (2.7)$$

$$V_{XC}(r) = \frac{\partial E_{XC}}{\partial n(r)} \quad (2.8)$$

where  $V(r)$  is the external potential of electron-nuclei interaction,  $V_H(r)$  is the potential of electron-electron Coulomb interaction known as Hartree potential.  $V_{XC}(r)$  and  $E_{XC}(r)$  are the exchange-correlation potential and energy respectively. The solution of one electron Kohn-Sham equation (Eq. 2.5) is single electron wave functions. The algorithm for solving Kohn-Sham DFT formulation is shown in Figure 2. 2. The only unknown term in the

energy functional is the exchange-correlation energy part (Eq. 2.5 to 2.8). Therefore, to solve the Kohn-Sham equation, the exchange-correlation energy part should be specified accurately. The existence of exchange-correlation functional is guaranteed but unfortunately, its true form is not known<sup>105</sup>.

In this work, we are using the Kohn-Sham formulation of DFT. However, to use this theory the exchange-correlation functional should be properly defined. The following section describes various approaches to define it.

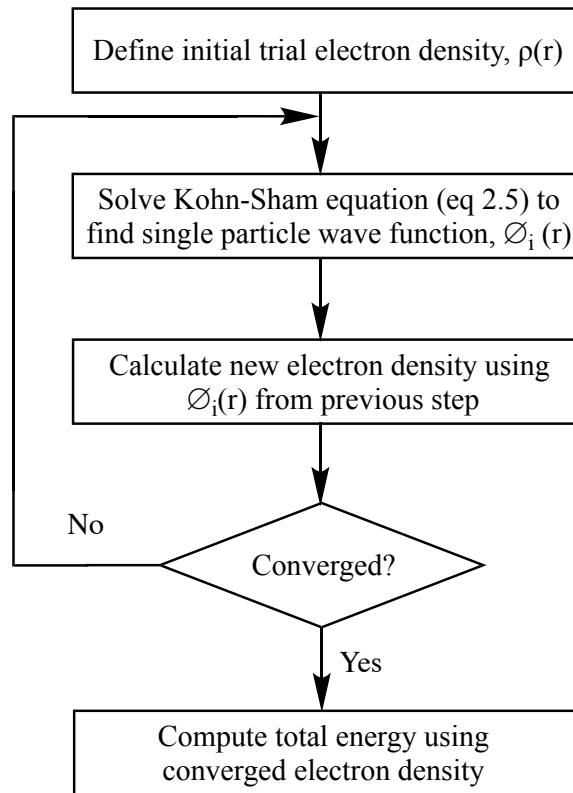


**Figure 2. 2** The algorithm for solving Kohn-Sham DFT formulation

### 2.3 Exchange-Correlation functional

The selection of apt functional, based on the system under consideration, is crucial in DFT calculations for minimizing the errors and computational cost in the calculation. The true mathematical form of the functional term is not known, and approximations are required. Many approximations are available for the exchange-correlation functional. Two

commonly employed approximations are local density approximation (LDA) and generalized gradient approximation (GGA).

### 2.3.1 Local Density Approximation (LDA)

LDA is associated with DFT calculations where the value of energy density at some position  $r$ , can be computed exclusively from the value of density at that position i.e. the ‘local value of density’<sup>122</sup>. Most of the LDA functionals are derived from the considerations of the uniform electron gas. LDA implies that it is the uniform electron gas exchange and correlation functionals that are employed for molecular calculations. It can be extended to spin-polarized calculations also. The exchange-correlation functional with LDA can be expressed as:

$$E_{xc}[\rho(r)] = \int \rho(r) \epsilon_{xc}[\rho(r)] dr \quad (2.9)$$

where  $\epsilon_{xc}$  is the energy density and  $\rho(r)$  is the electron density. Eq. 2.9 shows the functional dependence of exchange-correlation functional on density expressed as an interaction between density and an energy density that is itself dependent on electron density. Energy density,  $\epsilon_{xc}$  is treated as a sum of individual exchange and correlation contribution. LDA might give poor results when the electron density is changing drastically<sup>123</sup>. In those cases, the gradient in density should also be taken into consideration.

### 2.3.2 Generalized Gradient Approximation (GGA)

LDA has serious limitations by considering the electron density to be spatially uniform whereas in an actual molecule, the electron density is not spatially uniform. LDA can be modified by making them dependent on the extent to which the density is locally changing i.e. the gradient of the density. GGA functionals thus depend on both density and the gradient of the density<sup>105</sup>. The general form of exchange-correlation functional with GGA can be expressed as:

$$E_{xc}[\rho(r)] = \int \rho(r) \epsilon_{xc}[\rho(r)] F_x(s) dr \quad (2.10)$$

where  $F_x(s)$  is called enhancement factor and  $s$  is the reduced density gradient given as  $|\nabla\rho(r)|/2k_F\rho(r)$  in which  $k_F$  is the local Fermi wave vector. The enhancement factor

accounts for the deviation of LDA from GGA by considering the variation of density. There can be many types of GGA functionals based on the description of the enhancement factor. GGA functionals are widely employed for studying metal-gas interactions and hence these are extremely relevant for the current study. However, many GGA functionals are inadequate for the description of dispersion interactions (non-local electron-electron correlation). Hence many schemes are developed to incorporate van der Waals interaction and thereby improving the energies of dispersion bonded systems.

It is important for the functional to capture the surface adsorbate interactions correctly. Therefore, a screening of different functional needs to be carried out to select the correct functional and it is important to understand the physics behind these functionals in this regard. PBE, PW91, rPBE, optPBE-vdW, rPBE-vdW, optB88-vdW, opt86b-vdW etc. are some of the commonly used GGA functionals for DFT based calculations<sup>124-128</sup>. These functionals either have a different description of enhancement factor term or have different values for the parameters appearing in the enhancement factor term. For instance, the  $F_x(s)$  of PBE functional is defined as

$$F_x(s) = 1 + \kappa - \frac{\kappa}{1 + \frac{\mu s^2}{\kappa}} \quad (2.11)$$

where  $\kappa$  and  $\mu$  are parameters<sup>124</sup>. Becke<sup>129</sup> proposes the form given in eq. 2.11 so that it satisfies a number of criteria required for the functional. PBE and revPBE have same  $\mu$  value (0.219) and differ only in the value of  $\kappa$  ( $\kappa_{\text{PBE}} = 0.804$  and  $\kappa_{\text{revPBE}} = 1.245$ <sup>124</sup>). Another functional, optPBE, use the same form of enhancement factor but has  $\kappa$  and  $\mu$  values of 1.04804 and 0.175519 respectively<sup>130</sup>.

## 2.4 Simulation system

Vienna ab-initio simulation package (VASP)<sup>120,121</sup> developed at the Fakultät für Physik of the Universität Wien<sup>131,132</sup> is used to perform the DFT calculations. The computational parameters are selected based on the system under study (Ni or Ru based system). Hence, all the computational and modeling details including calculation and unit cell parameters and convergence criteria employed are given in each chapter. The details of thermodynamic corrections (enthalpic and entropic) are also given in each chapter.

### Chapter 3 Benchmarking popular density functional theory methods for predicting CO<sub>2</sub> adsorption and reactivity on transition metal

*With Ni (110) as a model catalyst surface and CO<sub>2</sub> as an adsorbate, a performance study of Density Functional Theory methods (functionals) is performed. CO being a possible intermediate in CO<sub>2</sub> conversion reactions, binding energies of both, CO<sub>2</sub> and CO, are calculated on the Ni surface and are compared with experimental data. OptPBE-vdW functional correctly predicts CO<sub>2</sub> binding energy on Ni (-62 kJ/mol); whereas CO binding energy is correctly predicted by the rPBE-vdW functional (-138 kJ/mol). The difference in computed adsorption energies by different functionals is attributed to the calculation of gas-phase CO<sub>2</sub>. Three alternate reaction systems based on different number of C=O double bonds present in the gas phase molecule are considered to replace CO<sub>2</sub>. The error in computed adsorption energy is directly proportional to the number of C=O double bonds present in the gas phase molecule. Additionally, both functionals predict similar carbon-oxygen activation barrier (40 kJ/mol) and equivalent Cls shifts for probe species (-2.6 eV for CCH<sub>3</sub> and +1.5 eV CO<sub>3</sub><sup>-</sup>), with respect to adsorbed CO<sub>2</sub>. Thus, by including a correction factor of 28 kJ/mol for the computed CO<sub>2</sub> gas-phase energy, we identified rPBE-vdW functional for investigating CO<sub>2</sub> conversion reactions on different metals.*



### 3.1 Introduction

Computational techniques such as Density Functional Theory (DFT) are established research tools that can not only be used to interpret and explain experimental findings but also can act as a predictive tool to guide catalyst design and development<sup>94–99</sup>. As mentioned in *Chapter 1 and Chapter 2*, one of the major challenges in DFT is that the exact form of exchange-correlation functional is not known<sup>103,104</sup>. Many approximations are available for the exchange-correlation functional, among which a more widely accepted class of functionals for studying molecules interacting with metal surfaces is the Generalized Gradient Approximation (GGA)<sup>105</sup>. PBE, PW91, rPBE, optPBE-vdW, rPBE-vdW, optB88-vdW, opt86b-vdW are some of the frequently employed GGA functionals for DFT based calculations<sup>124,127,128,130,133</sup>. The accuracy of DFT predictions highly depends on the choice of approximated exchange-correlation functional. For example, functionals such as PBE and PW91 are known to overestimate adsorption energies of O, CO, and NO on transition metals<sup>128</sup>. However, revPBE functional that has the same construction logic as that of PBE estimated the binding energies more accurately<sup>128</sup>.

#### 3.1.1 Need for functional benchmarking

As discussed before, an accurate exchange-correlation functional must be chosen for a DFT based catalyst design procedure. Different CO<sub>2</sub> conversion reactions on solid catalysts studied using DFT are presented in the review article by Cheng et.al.<sup>134</sup>. As per this extensive review, it is evident that more than 90% of the reviewed articles employ GGA based PBE and PW-91 functionals for studying CO<sub>2</sub> conversion reactions. However, there are some inconsistencies in the calculated values using these functionals. For example, CO<sub>2</sub> binding energies on metal surfaces calculated by these functionals do not match with experimental values<sup>106–111</sup>. The DFT calculated CO<sub>2</sub> binding energies on Cu (111) using PW-91 functional are reported to be -7.68 kJ/mol<sup>106</sup> and -4.80 kJ/mol<sup>107</sup>, whereas the experimental value is -20 kJ/mol<sup>108</sup>. Also, the CO<sub>2</sub> binding energy reported on Ni (110) surface using PBE functional is -40.32 kJ/mol<sup>109</sup> and -31.68 kJ/mol<sup>110</sup>, compared to an experimental value of -57.6 kJ/mol<sup>111</sup>. Besides this, for weakly bound systems (e.g. CO<sub>2</sub>

adsorption system) GGA functionals are inadequate for the description of dispersion interactions (non-local electron-electron correlation). Hence, several schemes are developed to incorporate van der Waals (vdW) interaction and thereby improving the energies of dispersion-bonded systems. The significance of vdW interactions in studying CO<sub>2</sub> conversions is ignored in the majority of studies. For instance, CO<sub>2</sub> adsorption on Cu (111) was studied by Fahdz et al.<sup>108</sup> using PBE functional and different vdW correlation functionals such as PBE-D2, vdW-DF, rev-vdW-DF2, and opt86b-vdW functionals. They found that the binding energy calculated using vdW correlation functionals predicted CO<sub>2</sub> binding energy in the range of -16 kJ/mol to -21 kJ/mol compared to an experimental value of -20 kJ/mol, whereas PBE functional underpredicted it (-2 kJ/mol).

It is also important that the chosen functional should predict the interaction of all the reaction intermediates with the metal correctly. For instance, CO has been proposed to be a possible intermediate in most of the CO<sub>2</sub> activation reactions<sup>135–137</sup>. Investigating CO adsorption on transition metals using DFT is a challenge as many DFT functionals fail to account for the HOMO-LUMO gap correctly, resulting in the incorrect prediction of CO-metal interactions present in the system<sup>111,138,139</sup>. For example, the DFT calculated CO binding energies on Ni (111) using PBE and PW-91 functionals are reported to be -175 kJ/mol and -177 kJ/mol<sup>140</sup> respectively, whereas the experimental value is -122 kJ/mol<sup>141</sup>. In several CO<sub>2</sub> conversion reactions, CO is converted to other intermediates such as C or COH or CHO. Therefore, incorrect representation of the CO-metal interaction would lead to errors in the prediction of CO activation energies to form other intermediates.

The accuracy of energetics obtained from DFT is crucial. In the catalyst design model proposed by Rangarajan et al.<sup>112,106</sup>, a small deviation in binding energy (which is a descriptor) prediction was shown to affect the microkinetic model and hence the design procedure. It was shown that for the fitting of the model to experimental data, DFT predicted binding energies of different adsorbing species (including CO<sub>2</sub>) on Cu (111) had to be altered by more than 50 kJ/mol. Tameh et.al.<sup>103</sup> studied the kinetics of methanol synthesis on Cu surface employing different exchange-correlation functionals. The study revealed that the predicted kinetics depend strongly on the employed functional choice.

The methanol turnover frequencies were predicted about 30 times higher by PBE compared to RPA, unveiling the immense effect that functionals have on predicting the reaction kinetics. Hence, it is important to choose a functional that represents reaction energetics for CO<sub>2</sub> conversion reactions correctly.

Drawing conclusive inferences from the above-mentioned literature on CO<sub>2</sub> conversion reactions are difficult because of the following limitations i) Despite the fact that functional selection is critical for the accuracy of DFT calculation, functionals are selected without much rationale. PBE and PW-91 functionals being the most extensively used functionals for studying CO<sub>2</sub> conversion reactions, no proper benchmarking studies (for CO<sub>2</sub> conversion reactions) are reported to the best of our knowledge. ii) The significance of vdW interactions in studying CO<sub>2</sub> conversions is ignored in many studies<sup>108</sup>. It is essential to include the contribution of vdW interactions in studying CO<sub>2</sub> binding energies and activation. iii) It is critical to choose a functional that predicts both, CO<sub>2</sub> and CO interactions with the metal surface and describes the reaction energetics correctly since CO is an essential intermediate in CO<sub>2</sub> conversion reaction.

In this study, the performance of different exchange-correlation functionals in predicting CO and CO<sub>2</sub> binding energies on Ni (110) surface is evaluated and compared with experimental data. From our calculations, we find that no single functional is able to accurately predict both CO<sub>2</sub> and CO binding energies on the Ni (110) surface. We investigated the source of error in predicting CO<sub>2</sub> binding energy. Further validation is then performed by computing the C-O activation barrier and XPS shifts (C 1s chemical shifts calculations). To uphold the findings, CO<sub>2</sub> binding energies are calculated for other hydrogenation catalysts such as Cu, Ru, Co, and Pt. Finally, we propose a functional that should be employed to study CO<sub>2</sub> conversion reaction pathways.

In section 3.2, computational methods and the simulation system are discussed. The benchmarking study is presented in section 3.3 for which Ni is used as a model catalyst, owing to its low cost and relatively good selectivity towards methane (one of the CO<sub>2</sub> hydrogenation products). Ni (110) facet is selected for the study, as experimental binding

energies of CO and CO<sub>2</sub> are available for this surface. The key findings from this study are summarized in section 3.4.

### 3.2. Computational methods and simulation system

First-principles calculations are performed based on periodic boundary conditions and plane-wave pseudopotential implementation of DFT. Vienna ab-initio simulation package (VASP) <sup>120,121</sup> developed at the Fakultät für Physik of the Universität Wien <sup>131,132</sup> is used to determine the electronic ground state, transition state, and the core level binding energy shifts. Projector augmented wave (PAW) <sup>142</sup> method is used to describe the interaction between valence electrons and ions with a plane wave cut-off energy of 450eV. A high level of accuracy is ensured by employing energy convergence criteria of 10<sup>-6</sup> eV per unit cell and a maximum force tolerance of 0.05 eV/Å. We used a k-points sampling of 3x3x1 with Monkhorst-pack scheme for integration over the Brillouin zone in reciprocal space and spin polarization is turned on for all simulations. The simulation system consists of six-layer Ni (110) slab with the top two layers allowed to be fully relaxed while four bottom layers are kept fixed at an optimized bulk lattice constant. A vacuum space of 12 Å is added above the top layer to avoid interaction with the adjacent unit cell in the z-direction. The number of slab layers and the density of k point grids are chosen to ensure the adsorption energies are well converged with respect to the computational setup discussed here (see appendix to chapter 3). The reported desorption energies (both CO<sub>2</sub> and CO) include thermodynamics corrections, zero-point energy (ZPE) and enthalpy corrections for gas-phase molecules, which were obtained from thermodynamic tables ZPE and enthalpic corrections calculated using different functionals are given in the appendix to chapter 3. For the adsorbed system, these are calculated by employing statistical thermodynamics using vibrational partition function <sup>143</sup>. For the model reaction (Eq. 3.2)



adsorption energy,  $E_{\text{ads}}$ , is calculated as follows:

$$E_{\text{ads}} = E_{\text{CO}_2/\text{M}} - (E_{\text{M}} + E_{\text{CO}_2 (\text{g})}) \quad (3.3)$$

In this work, we have employed PBE, rPBE, PW91, vdW-DF2, opt86b-vdW, PBE D2, rPBE-vdW and optPBE-vdW functionals. These functionals either have a different

description of enhancement factor term or have different values for the parameters appearing in the enhancement factor term. For instance,  $F_x(s)$  of PBE and revPBE functionals has the same mathematical form and is defined as

$$F_x(s) = 1 + \kappa - \frac{\kappa}{1 + \frac{\mu s^2}{\kappa}} \quad (3.4)$$

where  $\kappa$  and  $\mu$  are parameters. PBE and revPBE have same  $\mu$  value (0.219) and differ only in the value of  $\kappa$  ( $\kappa_{\text{PBE}} = 0.804$  and  $\kappa_{\text{revPBE}} = 1.245$ <sup>124</sup>). Another functional, optPBE, use the same form of enhancement factor but has  $\kappa$  and  $\mu$  values of 1.04804 and 0.175519 respectively<sup>130</sup>.

The electronic interaction between Ni and CO<sub>2</sub> is analyzed by the Density of states (DOS) projected on the d-band for surface Ni site that coordinates with the adsorbed CO<sub>2</sub> molecule. The DOS calculations are performed via the two-step procedure implemented in VASP: the first step is a self-consistent calculation to generate the charge density, and the second step is the non-self-consistent calculation using the pre-calculated charge density from the first step. The observed DOS data is then analyzed and visualized by the software p4vasp. Projected DOS analysis is widely used in the literature to compare the activities of different sites on the metal surface<sup>102, 144</sup>. This is based on the band model proposed by Hammer and Nørskov<sup>97,145</sup>. According to this model, the adsorption is stronger if the d-band center ( $\epsilon_d$ ) is closer to the Fermi level. In order to compare the performance of DFT functionals in predicting the metal adsorbate interactions, we plot the DOS projected on the d-band for surface metal atom against the energy relative to the Fermi level.

The transition state for CO<sub>2</sub> dissociation to CO and O is calculated using the Nudged Elastic Band (NEB) method. In this method, a minimum energy path is defined between known reactant (initial state) and product (final state)<sup>146</sup>. Twelve intermediate images are generated using linear interpolation. The transition state is confirmed by a vibration frequency analysis where only one negative frequency confirming the transition state is observed, corresponding to carbon-oxygen bond breaking.

To further investigate the metal-adsorbate, DFT simulated XPS study is carried out to calculate the C 1s and O 1s core-level binding energies for adsorbed CO<sub>2</sub> and different

intermediates on Ni(110) surface using the final state approximation<sup>147,148</sup>. Since only the XPS core-level binding energy shift could be captured accurately by DFT simulation<sup>147</sup>, the XPS C 1s and O 1s chemical shifts of probe molecules, relative to the C 1s and O 1s binding energy of the adsorbed CO<sub>2</sub> on Ni (110) surface for different structures are calculated, reported and compared with experimental values by Roiaz et. al.<sup>111</sup>.

### 3.3 Results and Discussions

Benchmarking the DFT functionals using binding energy as a parameter is a common practice in the literature. For example, Wellendorff et al.<sup>140</sup> benchmarked six DFT functionals for predicting the adsorption energies over ten different metal surfaces by considering 39 adsorption reactions. The capability of individual functionals has also been studied using binding energy as a descriptor. Hammer et al.<sup>128</sup> studied the performance of revPBE functional by calculating chemisorption energies of O, CO, and NO on Ni, Rh, and Pd surfaces. Hence, in this work, the binding energy of adsorbate on the metal surface is selected as an initial parameter for benchmarking the functionals. To find the correct functional, binding energies of CO<sub>2</sub> and CO on Ni surface are calculated using different GGA and vdW correlation functionals and are compared with experimental values from the literature. In the current work, we have employed PBE, rPBE, PW91, vdW-DF2, opt86b-vdW, PBE D2, rPBE-vdW and optPBE-vdW functionals that are widely accepted for studying molecules interacting with solid catalyst surface<sup>124,125,127,128,130</sup>.

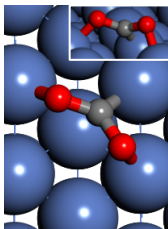
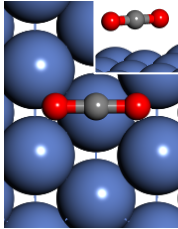
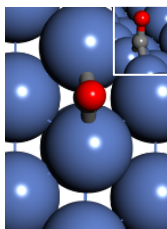
#### 3.3.1 Adsorption of CO<sub>2</sub> and CO on Ni (110)

As mentioned in the previous section, we have selected (110) facet of Ni, since experimental CO<sub>2</sub> and CO binding energies on Ni (110) surface are available in the literature. Ding et al.<sup>111</sup> performed Temperature-programmed desorption (TPD) analysis in the UHV chamber to obtain CO<sub>2</sub> binding energy on Ni (110). Two distinct peaks were obtained in the TPD spectra at 100K and 220K. The low-temperature peak corresponded to physisorbed CO<sub>2</sub> and the high-temperature peak corresponded to chemisorbed CO<sub>2</sub>. For lower exposures (<0.3L), the desorption energies (note that for non-dissociative

chemisorption the desorption barrier and desorption energy are comparable <sup>149,150</sup>) were  $57.6 \pm 10$  kJ/mol and  $25 \pm 5$  kJ/mol for the chemisorbed and physisorbed species, respectively. The CO<sub>2</sub> chemisorption geometry was also identified using low-temperature scanning tunneling microscopy combined with DFT calculations <sup>151</sup>. CO binding energy on Ni (110) was reported by Madden et al. <sup>152</sup>. They performed Low-energy electron diffraction (LEED) to determine the surface structure of CO adsorbed on Ni (110). The isosteric heat of adsorption, calculated from Clausius-Clapeyron plots for the LEED structure, at low coverages (less than 0.7 monolayer) was reported to be 125 kJ/mol.

In this study, all possible orientations of CO<sub>2</sub> and CO on Ni (110) are considered and binding energies are calculated using different GGA and vdW correlation functionals (see appendix to chapter 3). The most stable adsorption configuration remained the same irrespective of the type of functional used. These configurations are also in excellent agreement with the experimentally observed geometries for CO<sub>2</sub> and CO, reported by Ding et al. <sup>111</sup> and Madden et al. <sup>152</sup>, respectively, on Ni (110) surface. The most stable CO<sub>2</sub> and CO adsorption configurations along with binding energies calculated using different functionals are presented in Table 3. 1. The bond length and bond angle of CO<sub>2</sub> and CO calculated using different functionals are given in the appendix to chapter 3.

**Table 3. 1** Most stable adsorption configurations and calculated adsorption energies (kJ/mol) of CO<sub>2</sub> (chemisorbed and physisorbed) and CO on Ni (110) using different functionals. Blue balls represent Ni atoms, red balls represent oxygen atoms and grey balls represent carbon atoms.

Functional	Chemisorbed CO <sub>2</sub>	Physisorbed CO <sub>2</sub>	Chemisorbed CO
			
PBE	-41	-6	-179
rPBE	-5	-1	-151
PW91	-45	-8	-183
vdW-DF2	-22	-18	-144
opt86b-vdW	-88	-30	-198
PBE D2	-81	-28	-201
rPBE-vdW	-29	-20	-137
optPBE-vdW	-62	-26	-175
Experiment <sup>111</sup>	-57	-25	-125

CO<sub>2</sub> prefers the hollow up site binding with three Ni atoms present in the top layer forming two Ni-O bonds and one Ni-C bond. The two C-O bonds are elongated compared to gas-phase CO<sub>2</sub> (1.279 Å, 1.278 Å vs 1.163 Å) suggesting chemisorption. CO<sub>2</sub> is found to be bonded to the metal surface with a “V” shaped bent geometry (O-C-O bond angle of 126.704°) altering its linear structure. From Table 3. 1, it can be seen that the CO<sub>2</sub> binding energy changed significantly (-5 kJ/mol to -89 kJ/mol) with a change in functional and it is correctly predicted only by optPBE-vdW functional (-62 kJ/mol vs experimental value -57 kJ/mol). GGA functionals such as PBE and PW91 slightly underpredicted (-41 kJ/mol and -45 kJ/mol respectively) it. These values are in excellent agreement with previously



reported CO<sub>2</sub> binding energies on Ni (110) surface using PBE (-40 kJ/mol<sup>109</sup>) and PW-91 (-45 kJ/mol<sup>153</sup>) functionals. rPBE functional performed the worst in predicting CO<sub>2</sub> binding energies (-5 kJ/mol) whereas opt86b-vdW and PBE-D2 functionals overpredicted it (-88 kJ/mol and -81 kJ/mol) and vdW-DF2 and rPBE-vdW (-22 kJ/mol and -29 kJ/mol respectively) functionals under predicted it.

The physisorbed configuration of CO<sub>2</sub> on Ni (110) is determined in a systematic manner by placing CO<sub>2</sub> at variable heights above different possible adsorption sites present on the Ni (110) surface. Physisorption configuration is identified to be the one in which CO<sub>2</sub> is closest to the surface, with bond lengths same as that in the gas phase CO<sub>2</sub>. In the case of CO<sub>2</sub> physisorption, CO<sub>2</sub> retained its linear geometry (C-O bond length 1.163 Å and O-C-O bond angle 180°), implying that CO<sub>2</sub> is weakly bound to the surface through van der Waals forces. Hence, van der Waals correction terms are essential in the exchange-correlation functional. From Table 3. 1 we can infer that the functionals opt86b-vdW, PBE D2, rPBE-vdW, and optPBE-vdW that consider the van der Waals correction are correctly predicting CO<sub>2</sub> physisorption binding energy. Thus, optPBE-vdW functional is the only functional that predicted both physisorption and chemisorption binding energies of CO<sub>2</sub> on Ni (110) correctly. However, for employing optPBE-vdW functional for studying the entire reaction pathway of CO<sub>2</sub> conversion reactions, it must predict CO interaction with metal correctly too.

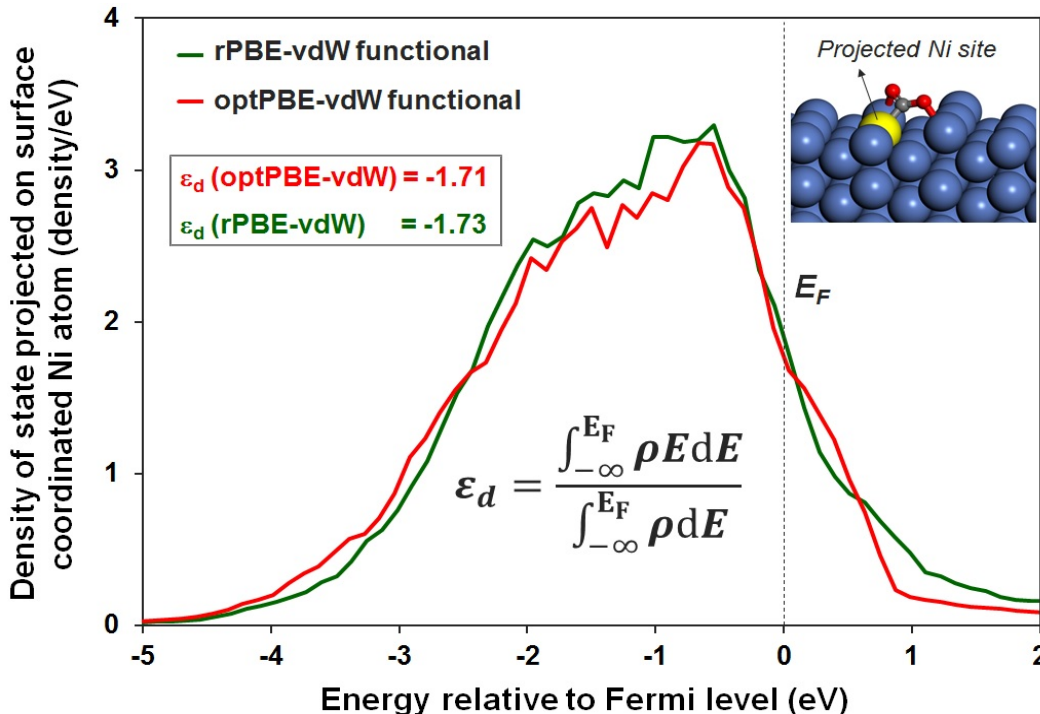
For CO adsorption on Ni (110), it is found that CO prefers to adsorb vertically, with the carbon atom binding to the surface Ni on all sites. The most stable adsorption configuration is the one in which CO sits vertically in the bridge site between two-nickel atoms. Compared to CO<sub>2</sub>, CO adsorption is stronger on the Ni surface because CO binds primarily through the C atom, whereas CO<sub>2</sub> has both, carbon and oxygen metal interactions. The carbon atom in CO is *sp* hybridized and the electron density on carbon is high due to the back donation of electrons from oxygen to the carbon atom. The carbon atom in CO<sub>2</sub> is *sp*<sup>2</sup> hybridized and is relatively electron deficient compared to that in CO.

It can be seen from Table 3. 1 that the functional that predicts CO<sub>2</sub> adsorption on Ni (110) correctly (optPBE-vdW functional) overpredicts CO adsorption by 50 kJ/mol (computed value is -175 kJ/mol vs experimental value of -125 kJ/mol). All the GGA and vdW correlation functionals over predicted CO binding energy on Ni (110). Previous studies have shown that CO binding energies on metals such as Pt, Pd, Rh, Ir, Cu, Ru, and Co are also overpredicted by GGA functionals such as PBE, PW-91, RPBE<sup>154,140,155</sup>. GGA functionals are known to overpredict CO interactions with metal due to the smaller HOMO-LUMO gap. To understand this, the bonding of CO on Co (0001) was studied by Gunasooriya et al. using Natural Bond Orbitals (NBO) theory<sup>156</sup>. This study showed that rPBE-vdW functional predicted the interaction of CO with metal surface correctly. Thus, rPBE-vdW functional is widely accepted for studying CO interactions with metals<sup>147,156,157</sup>. In our study too, rPBE-vdW functional is the closest (computed value is ~ -137 kJ/mol vs experimental value of -125 kJ/mol) in predicting CO binding energy on Ni (110) surface.

From the above discussion, it is concluded that no single choice of DFT functional could predict both CO and CO<sub>2</sub> adsorption on Ni (110) correctly. Since rPBE-vdW functional is an established functional for studying CO adsorption, we evaluated possible reasons behind the difference in the CO<sub>2</sub> binding energy calculation by rPBE-vdW and optPBE-vdW.

### **3.3.2 Reasons for the difference in CO<sub>2</sub> binding energy prediction by rPBE-vdW and optPBE-vdW**

rPBE-vdW underpredicts the CO<sub>2</sub> chemisorption binding energy by 33 kJ/mol (compared to optPBE-vdW), whereas it correctly predicts CO<sub>2</sub> physisorption energy and CO adsorption energy. Hence, we investigate the reason behind rPBE-vdW's inability to predict CO<sub>2</sub> chemisorption energy. For binding energy calculations, the error in calculating the energy of the slab<sup>130</sup> (appearing on reactant and product side) cancels out. Thus, the error in predicting chemisorption energy of CO<sub>2</sub> on Ni (110) by rPBE-vdW functional could be either due to the error in predicting the Ni-CO<sub>2</sub> interaction or due to the error in the gas phase description of CO<sub>2</sub>.

3.3.2.1 Ni-CO<sub>2</sub> interaction

**Figure 3. 1** The density of states (DOS) projected on d-band for surface Ni site that coordinates with chemisorbed CO<sub>2</sub> molecule using rPBE-vdW and optPBE-vdW functionals. The d-band center( $\epsilon_d$ ) values (eV) relative to the Fermi level ( $E_F$ ) are also shown for the two functionals. The formula to calculate  $\epsilon_d$  is also shown. Blue balls represent Ni atoms, red balls represent oxygen atoms, grey balls represent carbon atoms and yellow ball represent projected Ni site.

As discussed in the previous section (*cf* Table 3. 1), CO<sub>2</sub> adsorbs on Ni (110) surface forming two Ni-O bonds and one Ni-C bond. The projected DOS analysis is employed to study the interaction between Ni and CO<sub>2</sub> since these calculations involve only adsorbed CO<sub>2</sub>. We plotted DOS projected on d-band for the surface Ni site (that coordinates with the chemisorbed CO<sub>2</sub> molecule) against the energy relative to the Fermi level. The d-band center values, which reflect the affinity of the chemisorbed CO<sub>2</sub> on the Ni surface<sup>97,145</sup>, are also calculated. Since optPBE-vdW functional correctly predicted CO<sub>2</sub> binding energy (both chemisorption and physisorption), we compare the projected DOS plots computed with rPBE-vdW and optPBE-vdW functionals. Plots of projected DOS for Ni that

coordinates with CO<sub>2</sub> vs energy relative to Fermi level for structures optimized by optPBE-vdW and rPBE-vdW functionals are shown in Figure 3. 1. The calculated d-band centre for the Ni atom is also shown in the figure.

From Figure 3. 1, it can be seen that the projected DOS using optPBE-vdW and rPBE-vdW functionals are similar. The corresponding d-band center values are -1.71 eV and -1.73 eV for optPBE-vdW and rPBE-vdW functionals, respectively. The position of the d-band center gives a measure of how strongly the adsorbate binds to the surface <sup>100,102</sup>. However, we found that the d-band centers calculated using the two functionals are similar. Hence, we believe that both functionals capture the metal-CO<sub>2</sub> interaction similarly.

### 3.3.2.2 Gas-phase CO<sub>2</sub>

Since optPBE-vdW and rPBE-vdW functionals predict the Ni-CO<sub>2</sub> interaction (based on DOS analysis) similarly, we investigate how these functionals describe the gas phase CO<sub>2</sub> molecule. Christensen <sup>158</sup> explored several CO<sub>2</sub> reduction reactions in the gas phase and calculated reaction energies using different DFT functionals. The reaction energies are found to be highly dependent on the functional choice suggesting that carbon-oxygen double bonds present in the reaction affect the performance of the functional. The inability of certain functionals to accurately describe double and triple bonds present in gas-phase molecules in the system is also reported by Wellendorff et al. <sup>140</sup>. DFT studies performed on gas-phase reactions that have double or triple bonded species (such as NO, O<sub>2</sub>, and N<sub>2</sub>) have shown errors in calculated reaction enthalpies. This is tackled by employing an alternate binding energy calculation method to avoid the calculation of double or triple bonded species by DFT (H<sub>2</sub>O replaced  $\frac{1}{2}$  O<sub>2</sub>, NH<sub>3</sub>, and H<sub>2</sub>O replaced NO and 2NH<sub>3</sub> is used in place of N<sub>2</sub>) and consequently the reaction enthalpies improved <sup>140</sup>.

A similar approach is used in this study to analyze the performance of optPBE-vdW and rPBE-vdW functionals in describing the gas phase CO<sub>2</sub> molecule. In this approach, the net reaction is split into two reactions (*cf* Figure 3. 2). The first reaction (R1) is a gas-phase reaction and the reaction enthalpy is obtained from thermodynamic tables. The second

reaction (R2) does not involve a gas phase  $\text{CO}_2$  molecule and the reaction enthalpy is calculated using both optPBE-vdW and rPBE-vdW functionals. The net  $\text{CO}_2$  binding energy is calculated as the difference in the enthalpies of R1 and R2. In this work, three alternate reaction systems are used to replace the calculation of gas-phase  $\text{CO}_2$  using DFT, as shown in Figure 3. 2. In all three reaction systems, the first reaction involves the formation of gas-phase  $\text{CO}_2$  and the second reaction involves the formation of adsorbed  $\text{CO}_2$ , from an alternate C1 moiety.

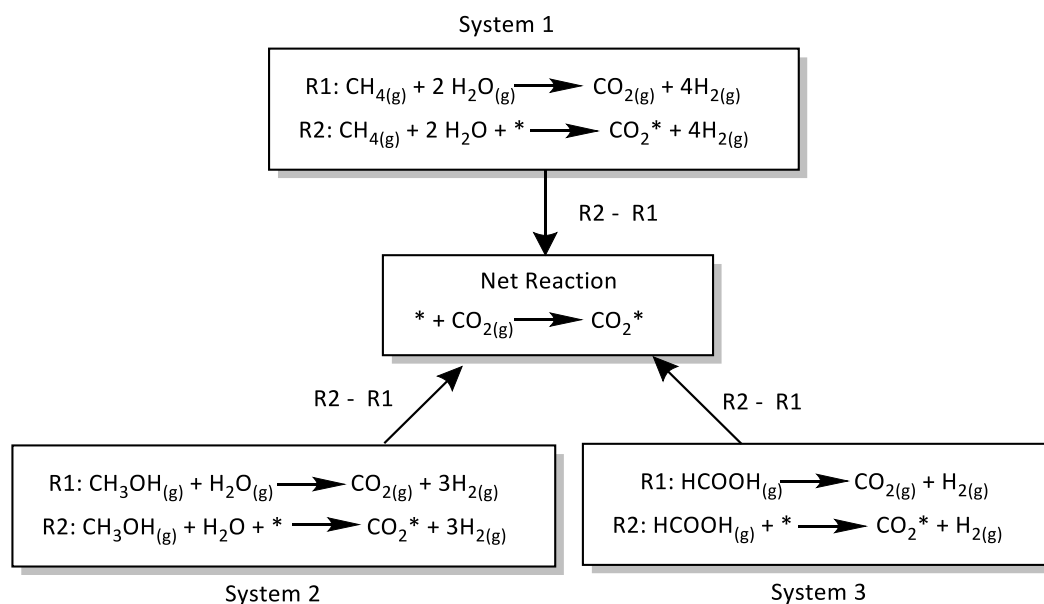


**Figure 3. 2** Alternate  $\text{CO}_2$  binding energy calculation schemes based on methane (system 1), methanol (system 2) and formic acid (system 3)

The three alternate reaction systems considered here are based on methane, methanol and formic acid (named as system 1, system 2 and system 3, respectively) for which DFT is used to calculate the gas-phase energy of a  $\text{CH}_4$ ,  $\text{CH}_3\text{OH}$ , and  $\text{HCOOH}$  in lieu of  $\text{CO}_2$ . Note that carbon-oxygen double bonds are absent in systems 1 and 2, while a single carbon-oxygen single bond exists for system 2. The third system based on formic acid has one carbon-oxygen double bond. These three systems are considered to explore the influence of carbon-oxygen bonds (single or double bond present in the system) in the gas phase on the performance of optPBE-vdW and rPBE-vdW functionals.

Table 3. 2 summarises the difference between binding energies calculated using optPBE-vdW and rPBE-vdW functionals for all three alternate reaction systems. For methane and methanol-based systems (systems 1 and 2), the difference between the energies calculated by both functionals is only 6-7 kJ/mol. However, for the formic acid system (system 3), the difference between energies calculated by the two functionals is 18 kJ/mol, which is almost half the difference when gas-phase CO<sub>2</sub> was directly employed in the DFT calculation (Table 3. 1). This clearly suggests that the difference lies in the description of double bonds of the gas-phase CO<sub>2</sub> molecule. From Table 3. 2 it can be seen that the error in the prediction increases proportionally with the number of C=O bonds present in the gas phase molecule. Hence, it can be said that the difference in binding energy prediction is due to the incorrect treatment of double bonds in gas-phase CO<sub>2</sub> by rPBE-vdW functional.

**Table 3. 2** The difference in binding energies calculated using optPBE-vdW and rPBE-vdW for the alternate reaction system shown in Figure 3.2

System number	Species	No. of C=O bonds	BE <sub>optPBE-vdW</sub> - BE <sub>rPBE-vdW</sub> (kJ.mol <sup>-1</sup> )
1	CH <sub>4</sub>	0	-6
2	CH <sub>3</sub> OH	0	-7
3	HCOOH	1	-18
-	CO <sub>2</sub>	2	-33

To further understand the contrasting behavior of both the functionals in treating gas-phase CO<sub>2</sub>, we calculated the vibrational frequencies of gas-phase CO<sub>2</sub> (employing optPBE-vdW and rPBE-vdW functionals) and compared with corresponding experimental values (Table 3. 3). CO<sub>2</sub>, being a linear triatomic molecule, has four normal vibrational modes. Since two modes are degenerate<sup>159</sup> it has only three fundamental vibration frequencies corresponding to asymmetric stretching (f1), symmetric stretching (f2) and degenerate bending (f3) vibrations. optPBE-vdW functional predicted both asymmetric stretching (2347 cm<sup>-1</sup> vs experimental value 2349 cm<sup>-1</sup>) and symmetric stretching (1311 cm<sup>-1</sup> vs experimental value

1333  $\text{cm}^{-1}$ ) accurately compared to rPBE-vdW functional ( $f1 = 2319 \text{ cm}^{-1}$  and  $f2 = 1298 \text{ cm}^{-1}$ ). This highlights the difference between optPBE-vdW and rPBE-vdW functionals in treating gas-phase  $\text{CO}_2$ .

**Table 3. 3** Comparison of  $\text{CO}_2$  vibrational frequencies between calculated and experimental values

Functional	Frequency ( $\text{cm}^{-1}$ )		
	f1	f2	f3
optPBE-vdW	2347	1311	624
rPBE-vdW	2319	1298	623
Experiment <sup>160</sup>	2349	1333	667

In the case of physisorption, as explained earlier, there is only weak physical interaction between the adsorbed  $\text{CO}_2$  and the surface; whereas in chemisorption, the double bonds in  $\text{CO}_2$  are weakened due to the relatively stronger interaction with the metal. Notably, in  $\text{CO}_2$  physisorption, the gas phase  $\text{CO}_2$  and the adsorbed  $\text{CO}_2$  have the same geometrical and electronic structure. Hence, the difference in the description of double bonds of gas-phase  $\text{CO}_2$  cancels out. This explains why the physisorption energy is predicted similarly by both optPBE-vdW and rPBE-vdW functionals (the difference the energies by these functionals is only 5 kJ/mol).

### 3.3.3 Evaluating the difference in activation barrier and DFT-XPS calculations

To confirm that both these functionals predict the  $\text{CO}_2$  interaction with the metal similarly, the  $\text{CO}_2$  activation barrier and XPS shifts are calculated using DFT. These calculations start with the chemisorbed  $\text{CO}_2$  configuration and hence gas-phase  $\text{CO}_2$  is not present.

### 3.3.3.1 First activation energy of CO<sub>2</sub>

The transition state and activation barrier are calculated using the NEB method employing optPBE-vdW and rPBE-vdW functionals. Initial and final states of CO<sub>2</sub> activation, along with the transition states, are shown in Figure 3. 3.

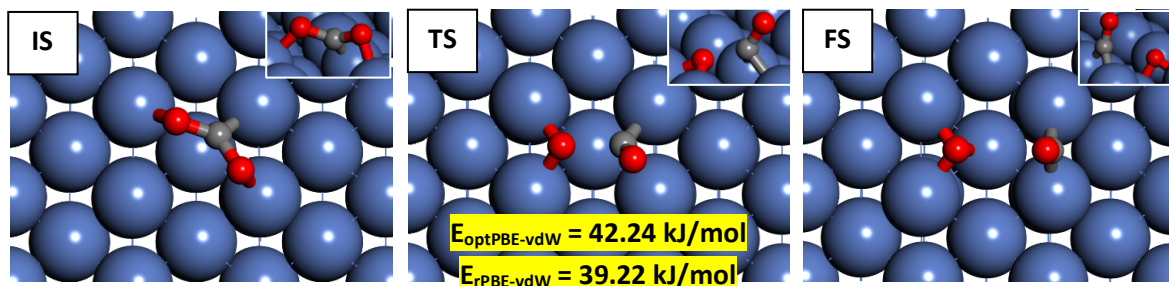


**Figure 3. 3** Structure of the initial state (IS), final state (FS), and transition state (TS) for CO<sub>2</sub> activation on Ni (110). The activation barrier calculated by optPBE-vdW and rPBE-vdW functionals is also stated in the figure. Colour code for the atoms is the same as in Figure 3.1

In the transition state (TS), the carbon atom and one of the oxygen atoms of CO<sub>2</sub> are bound to the surface Ni atoms and the other oxygen atom is not bonded to Ni. The optimized structure of the TS remained the same irrespective of the functional choice. One of the carbon-oxygen bonds in CO<sub>2</sub> elongates (1.278 Å in IS vs 1.723 Å in TS) and breaks to form CO and O in the FS, while the other carbon-oxygen bond shortens (1.279 Å in IS vs 1.203 Å in TS). The energy barrier for CO<sub>2</sub> activation is found to be 42.21 kJ/mol and 39.22 kJ/mol for optPBE-vdW and rPBE-vdW functionals, respectively. The small difference of ~3 kJ/mol between optPBE-vdW and rPBE-vdW in calculating the CO<sub>2</sub> activation barrier further strengthens our claim in the previous section that the difference lies in the description of gas-phase CO<sub>2</sub>.

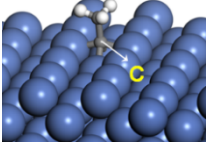
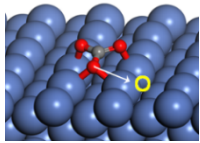
### 3.3.3.2 DFT simulated XPS shift

The C1s and O1s chemical shifts are calculated using DFT simulated XPS, employing optPBE-vdW and rPBE-vdW functionals. We used ethylidyne (CCH<sub>3</sub>) and carbonate (CO<sub>3</sub><sup>-</sup>



) adsorbed on Ni (110) as two distinct probe structures since they both are identified as stable surface species during the hydrogenation of CO<sub>2</sub> on Ni(110) by the combination of infrared-visible sum frequency generation (IR-vis SFG) vibrational spectroscopy and near-ambient pressure X-ray photoelectron spectroscopy (NAP-XPS) techniques in the study of Roiaz et al.<sup>161</sup>. We compared the C1s and O1s chemical shifts for ethylidyne (CCH<sub>3</sub>) and carbonate (CO<sub>3</sub><sup>-</sup>) adsorbed on Ni (110) with the corresponding values of chemisorbed CO<sub>2</sub>. Adsorbed CCH<sub>3</sub> is a stable intermediate that does not have C=O bond and adsorbed CO<sub>3</sub><sup>-</sup> has carbon-oxygen bonds present. The XPS peaks at 286.6 eV, 283.9 eV, and 288.3 eV correspond to experimental C 1s core level binding energies of chemisorbed CO<sub>2</sub>, CCH<sub>3</sub>, and CO<sub>3</sub><sup>-</sup> on Ni (110), respectively and are taken from the literature<sup>161</sup>. As mentioned in section 3.2, for XPS simulation we calculated chemical shifts rather than calculating absolute core binding energies. If the interaction between chemisorbed CO<sub>2</sub> and Ni (110) surface is described similarly by both optPBE-vdW and rPBE-vdW functionals then the computed XPS C 1s and O 1s chemical shift of adsorbed CCH<sub>3</sub> and CO<sub>3</sub> referenced to chemisorbed CO<sub>2</sub> are expected to be similar. DFT calculated core-level shifts are also compared with experimental reference values reported by Roiaz et al.<sup>161</sup>. The optimized structures and core-level shifts calculated between adsorbed CO<sub>2</sub> and probe species are listed in Table 3. 4.

**Table 3. 4** XPS C1s and O1s chemical shifts relative to C1s and O1s binding energy<sup>[a]</sup> of chemisorbed CO<sub>2</sub> on Ni (110) surface. White balls represent Hydrogen atoms and colour codes for all other atoms are the same as in Table 3.1

Functional	Adsorbed CCH <sub>3</sub>	Adsorbed CO <sub>3</sub>	
			
	C1s	C1s	O1s
optPBE-vdW	-2.55	+1.46	+0.19
rPBE-vdW	-2.61	+1.47	+0.14
Experiment	-2.70	+1.70	-

[a] All values in eV

The experimental C 1s chemical shifts relative to the C 1s core level binding energy of chemisorbed CO<sub>2</sub> for adsorbed CCH<sub>3</sub> and adsorbed CO<sub>3</sub><sup>-</sup> are -2.7 eV and +1.7 eV, respectively. optPBE-vdW functional predicted C 1s chemical shift values of -2.55 eV and +1.46 eV referenced to chemisorbed CO<sub>2</sub> for adsorbed CCH<sub>3</sub> and CO<sub>3</sub><sup>-</sup>, respectively, and is in excellent agreement with the experimental observation. As expected, C 1s chemical shifts values referenced to chemisorbed CO<sub>2</sub> predicted for CCH<sub>3</sub> and CO<sub>3</sub><sup>-</sup> by rPBE-vdW functional are -2.61 eV and +1.47 eV, respectively which are very close to the prediction by optPBE-vdW functional. Even the O 1s chemical shift for CO<sub>3</sub><sup>-</sup>, for which experimental data is not available, is also predicted similarly by both the functionals. Thus, from the XPS study, we can comprehend that both optPBE-vdW and rPBE-vdW functionals predicted the shifts without much difference and are comparable with experimental shifts.

Both optPBE-vdW and rPBE-vdW functionals come under the same class of PBE functionals, i.e., both these functionals use the same form of enhancement factor ( $F_x$ ). The contrasting performance of optPBE-vdW and rPBE-vdW functionals are due to the differences in the parameter,  $\kappa$ , appearing in the description of exchange energy density.

As mentioned in *Chapter 2*, the variation of  $F_x$  and hence the difference between the functionals is more apparent at higher values of RDG. In the  $\text{CO}_2$  gas-phase molecule, due to the relative diffuse region of higher electron density, the density gradient is large and hence the difference between the functionals becomes more evident.

As mentioned earlier, the functional dependence of double bonds present in  $\text{CO}_2$  is studied by Christensen et al.<sup>158</sup>, for gas-phase reduction reactions and is in good agreement with our findings. Since the difference lies only in the gas phase description of  $\text{CO}_2$ , we suggest incorporating a correction of 28 kJ/mol<sup>158</sup> for  $\text{CO}_2$  gas-phase calculations using rPBE-vdW functional. Consequently,  $\text{CO}_2$  chemisorption binding energy calculated by rPBE-vdW improved and matched with experimental results (computed value with correction is  $\sim -57.4$  kJ/mol vs experimental value of -57.6 kJ/mol). Thus, rPBE-vdW functional with a correction of 28 kJ/mol for  $\text{CO}_2$  gas-phase energy (which now predicts  $\text{CO}_2$  binding energy,  $\text{CO}_2$  activation energy, and CO binding energy accurately) can be used to predict  $\text{CO}_2$  hydrogenation reaction pathways on Ni. The generality of the proposed functional in predicting  $\text{CO}_2$  hydrogenation reaction on different metals is tested in the following section.

### 3.3.4 $\text{CO}_2$ adsorption on different transition metals

Since the source of error lies in predicting the energy of gas-phase  $\text{CO}_2$  and not in the metal-adsorbate interaction, the difference between the binding energies of  $\text{CO}_2$  calculated using optPBE-vdW and rPBE-vdW should not change (and should be equal to the difference on Ni (110)) on different metals surfaces. To establish this,  $\text{CO}_2$  binding energies on different hydrogenation metals surfaces are calculated using both the functionals and are presented in Table 3. 5. We have considered Cu (111), Cu (100), Ru (111), Co (111), and Pt (111) surfaces that are known to be employed for studying  $\text{CO}_2$  hydrogenation reactions<sup>162,163</sup>. All the stable  $\text{CO}_2$  adsorption configurations are given in the appendix to chapter 3. The difference between binding energies calculated by optPBE-vdW and rPBE-vdW functionals lies in the range of 28 - 33 kJ/mol (except for Cu), which is consistent with the corresponding difference on Ni (110) surface. In the case of Cu, there is only weak physical interaction between the adsorbed  $\text{CO}_2$  and the surface, which is similar to  $\text{CO}_2$

physisorption on Ni. Hence, the difference in the description of double bonds of gas-phase CO<sub>2</sub> cancels out and binding energy is predicted similarly by both optPBE-vdW and rPBE-vdW functionals (similar to Ni (110) physisorption). Thus, the proposed correction factor for gas-phase CO<sub>2</sub> is applicable to other metals while calculating binding energy by employing the rPBE-vdW functional.

**Table 3. 5** Binding energies (kJ/mol) calculated using optPBE-vdW and rPBE-vdW for different CO<sub>2</sub> hydrogenation transition metals

Functional	Cu		Ru	Co	Pt
	111	100	111	111	111
experiment	-20 <sup>164</sup>	-25 <sup>165</sup>	-	-	-
optPBE-vdW	-22	-23	-150	-104	9
rPBE-vdW	-21	-20	-117	-73	37
optPBE-vdW – rPBE-vdW	1	3	33	31	28

### 3.4 Summary and Conclusions

In summary, benchmarking of DFT functionals is performed on Ni (110) as a model catalyst surface. Binding energies of CO<sub>2</sub> and CO (being an essential intermediate in CO<sub>2</sub> conversion reactions) on the Ni surface are calculated using different DFT functionals and are compared with experimental binding energies from the literature. We found that none of the DFT functionals could predict both CO<sub>2</sub> and CO binding energies the Ni surface correctly. CO<sub>2</sub> binding energy on Ni surface is correctly predicted by optPBE-vdW functional (~ -62 kJ/mol). rPBE-vdW functional underpredicted CO<sub>2</sub> binding energy by 33 kJ/mol while it correctly predicted CO binding energy on Ni (~ -138 kJ/mol). The DOS analysis showed that the Ni-CO<sub>2</sub> interaction is captured similarly by both the functionals. We used three alternate reaction systems based on methane (no carbon-oxygen bond),

methanol (no carbon-oxygen double bond) and formic acid (one carbon-oxygen double bond) in the place of gas-phase CO<sub>2</sub> (two carbon-oxygen double bonds) to reveal that the error in the prediction increased proportionally with the number of C=O bonds present in the gas phase molecule. Hence the error in prediction of CO<sub>2</sub> binding energy by rPBE-vdW functional is due to the treatment of carbon-oxygen double bonds in gas phase CO<sub>2</sub>. This is further confirmed by calculating the CO<sub>2</sub> activation barrier and XPS shifts, as these calculations involve chemisorbed CO<sub>2</sub> as the reference state. The C = O activation barrier (~40 kJ/mol) and C 1s chemical shifts for probe species (~ -2.6 eV for CCH<sub>3</sub> and ~ +1.5 eV CO<sub>3</sub><sup>-</sup>) with respect to the adsorbed CO<sub>2</sub> are predicted similarly by both the functionals. Finally, we propose that rPBE-vdW functional with a correction of 28 kJ/mol for gas-phase CO<sub>2</sub> should be employed to study CO<sub>2</sub> conversion reaction pathways. This study and the proposed correction factor is applicable to other metals since the source of error lies in predicting the energy of gas-phase CO<sub>2</sub> and not in the metal-adsorbate interaction.

## Chapter 4 Investigating CO<sub>2</sub> methanation on Ni and Ru: DFT assisted microkinetic analysis

*In this work, the aim is to resolve the uncertainty in CO<sub>2</sub> methanation reaction mechanisms on both Ni and Ru surfaces. The most debated step is the activation routes of CO<sub>2</sub> and CO and whether the reaction proceeds with/without forming CO\* intermediate. A comprehensive reaction network of 46 elementary on Ni (111) and Ru (001) surfaces are considered and a benchmarked functional is employed in the study. The DFT-calculated energies are fed to the microkinetic model to perform a reaction mechanism analysis over both catalyst surfaces separately at 550 K and 10 atm pressure. The DFT calculations predicted that the CO<sub>2</sub> direct dissociation to form CO\* and O\* is kinetically and thermodynamically favorable on both Ni and Ru surfaces. However, CO\* activation (hydrogenation via HCO\*) has the highest activation barrier on both the surfaces. Interestingly, both CO<sub>2</sub> and CO activation barriers are slightly lower on Ru compared to Ni. In contrast, CH\* sequential hydrogenation barriers are higher on Ru compared to Ni. The MKM predicted that the direct dissociation of CO<sub>2</sub>\* to CO\* is favored on both Ni (111) and Ru (001) and methane is formed via CO\* hydrogenation. However, the CO\* hydrogenation routes are different on the two surfaces. On Ru (001), CO\* undergoes hydrogenation to form COH\* that further dissociates to C\*, whereas on Ni (111), CHO\* is formed that gives CH\* upon dissociation. The RDS on Ni (111) and Ru (001) surfaces are CHO\* dissociation to CH\* and O\* and CH<sub>3</sub>\* hydrogenation to CH<sub>4</sub>\* respectively. Therefore, this combined DFT and MKM study resolves the contradictions in CO<sub>2</sub> methanation reaction mechanisms on Ni and Ru surfaces.*

## 4.1 Introduction

As discussed in the introduction chapter, using hydrogen as a reagent to transform CO<sub>2</sub> to methane is one of the feasible routes for CO<sub>2</sub> utilization<sup>25–27</sup>. Transition metals such as Ru and Ni have shown good catalytic activity for CO<sub>2</sub> methanation<sup>36–38</sup>. Quindimil et al.<sup>52</sup> compared the CO<sub>2</sub> methanation reaction on alumina supported Ni and Ru catalyst and found that the apparent activation energy on Ni is 45 kJ/mol higher than that on Ru, effecting in the higher activity of Ru. However, the high cost of Ru makes its use limited. Understanding the CO<sub>2</sub> methanation reaction mechanism and rate-determining step (RDS) has a crucial significance in effective catalyst design and development by modifying the reaction route/reducing the barrier for RDS. It also helps in tuning the reaction conditions to enhance the reaction rates/selectivity<sup>93</sup>. The insights gained from the methanation reaction mechanism on Ru could aid in designing efficient catalysts based on Ni. Therefore, it is essential to understand and compare the CO<sub>2</sub> methanation reaction on Ru and Ni. However, the direct comparison of reaction energetics reported in different works is improper as there are disparities in the computational/experimental systems considered in different work. For instance, the computational study performed by Ren et al.<sup>166</sup> and Huang et al.<sup>167</sup> predicted the CO<sub>2</sub> direct dissociation barriers (electronic energy) on Ni (111) surface to be 93.7 kJ/mol and 43.2 kJ/mol respectively. This difference in barriers is attributed to the difference in the functional (PW-91<sup>166</sup> and PBE<sup>167</sup> functionals) and the computational parameters employed. Therefore, elucidating conclusive evidence by comparing the reaction mechanism on Ni and Ru from literature is inappropriate. Moreover, the reaction mechanism on both Ru and Ni is debated and remains unsettled<sup>37,38</sup>. The most debated steps are the activation routes of CO<sub>2</sub> and CO \*. This includes direct dissociation routes and different hydrogenation pathways for CO<sub>2</sub> and CO\* activation. In addition, it is not sure whether CO\* is a reactive intermediate in the methanation reaction. The complexity of the methanation reaction network results in the inconsistent prediction of reaction pathways and RDS reported in different studies on both Ni and Ru surfaces.

### 4.1.1 CO<sub>2</sub> methanation reaction mechanisms

CO<sub>2</sub> dissociation via CO\* intermediate had been studied extensively on Ni and Ru surfaces. CO<sub>2</sub> adsorbs with a bent configuration on both Ni and Ru surfaces<sup>56,166,168</sup>. Notably, the binding energy of CO<sub>2</sub> was reported to be higher on Ru (001) (~50 kJ/mol<sup>168</sup>) compared to Ni (111) (~10 kJ/mol<sup>169</sup>). Several CO<sub>2</sub> dissociation routes, including direct dissociation to CO\* and O\* and H-assisted transformation via COOH\* (CO<sub>2</sub> → COOH\* → CO\*) or HCOO\* (CO<sub>2</sub> → HCOO\* → HCO\* → CO\*) were investigated. Typically, the direct decomposition of CO<sub>2</sub> to CO\* and O\* and CO<sub>2</sub> hydrogenation via HCOO\* are kinetically more favored compared to COOH\* route<sup>167,170</sup>. For instance, Huang et al.<sup>167</sup> predicted the activation barriers for CO<sub>2</sub> transformation to CO\*, HCOO\*, and COOH\* to be 43 kJ/mol, 52 kJ/mol and 99 kJ/mol respectively on Ni (111) surface. Similarly on Ru (001) surface, Chiorescu et al.<sup>170</sup> predicted the free energy barriers for these steps to be 24 kJ/mol, 81 kJ/mol and 126 kJ/mol respectively. In contrast, Zhang et al.<sup>168</sup> predicted the barrier for CO<sub>2</sub> to CO\* dissociation to be substantially higher (115 kJ/mol) than the HCOO\* route (35 kJ/mol) on Ru (001) surface. Marwood et al.<sup>171</sup> employed in-situ measurements using Diffuse Reflectance Infrared Fourier Transform (DRIFT) Spectroscopy and studied CO<sub>2</sub> methanation on 2% Ru/TiO<sub>2</sub>. They identified both CO\* and HCOO\* intermediates and proposed that CO\* was formed from HCOO\* and further hydrogenation of CO\* leads to the formation of methane. Despite these findings, the hydrogenation routes (both COOH\* and HCOO\* routes) were eluded in some of the studies<sup>167,169</sup>.

The different CO<sub>2</sub> transformation routes lead to CO\* formation and the activation route of CO\* is often debated. This step is extremely relevant as CO\* activation is typically regarded as the RDS. In addition, CO\* coverages are reported to be high and this leads to catalyst poisoning by blocking the active sites<sup>55,56</sup>. CO\* can transform via C-O bond cleavage (CO\* → C\*) or undergoes further hydrogenation and dissociation via COH\* (CO\* → COH\* → C\*) or HCO\* (CO\* → HCO\* → CH\*) route to form C\*/CH\* intermediate. Ren et al.<sup>166</sup> used DFT calculations to give mechanistic insights into CO<sub>2</sub> methanation reaction on Ni (111). They proposed that CO\* (formed from CO<sub>2</sub> direct dissociation) dissociates to C\* and O\* species and the C\* hydrogenates to form methane,



and CO\* dissociation was the rate-limiting step. However, recent computational studies have shown that CO\* direct dissociation to C\* is kinetically and thermodynamically not feasible on both Ni and Ru surfaces<sup>168,170</sup>. For instance, the CO\* dissociation barrier and reaction energy were predicted to be 253 kJ/mol and 104 kJ/mol on Ru (001) surface<sup>168</sup>. Additionally, this was supported by the experimental observation that carbon formation was not an issue on Ni and Ru surfaces<sup>172,173</sup>. In comparison, CO\* transformation via the hydrogenation route is kinetically more favorable. Yet, Avanesian et al.<sup>174</sup> only considered 18 elementary reactions, and the HCOO\* route was not included in their study. Even though CO<sub>2</sub> direct dissociation to CO\* is thermodynamically and kinetically favorable on both Ni and Ru surfaces, CO\* activation has a high barrier. Hence, it is crucial to investigate CO<sub>2</sub> hydrogenation routes without CO\* intermediate to ascertain the dominant reaction pathway. In contrast to the CO\* intermediate routes discussed above, the CO<sub>2</sub> methanation pathway without forming CO\* as an intermediate was also proposed. For instance, Huang et al.<sup>167</sup> suggested that, on Ni (111) surface, HCO\* formation from HCOO\* was kinetically and thermodynamically more favorable compared to HCO\* formation via CO\* hydrogenation. It must be noted though that these routes (without CO\* intermediate) were not considered in many studies<sup>166,169,174</sup>.

The C\*/CH\* intermediate thus formed (with/without CO\* intermediate route) undergoes sequential hydrogenation to form methane. Typically, the CH<sub>x</sub>\* (x = 0 – 3) hydrogenation steps were kinetically favorable on both Ni (111) and Ru (001) surfaces<sup>167,169,174</sup>. In addition, based on DFT studies, Li et al.<sup>175</sup> and Zhang et al.<sup>168</sup> reported that the production of C<sub>2</sub> hydrocarbon species was highly unlikely on Ni and Ru surfaces respectively. It is worthy to mention that the methane formation via CH<sub>x</sub>OH/CH<sub>x</sub>O (x = 1 – 3) (formed from the hydrogenation of HCO\*/COH\*) routes is not included in majority of the studies.

#### 4.1.2 Challenges in CO<sub>2</sub> methanation

The existing studies on CO<sub>2</sub> methanation on Ni (111) and Ru (001) surfaces have the following limitations i) There is a discrepancy in the CO<sub>2</sub> methanation reaction mechanism on Ni (111) and Ru (001) surfaces. The key step is the hydrogenation reaction, and this

may happen to adsorbed CO<sub>2</sub>\*, CO\*, or C\*. Additionally, whether the reaction proceeds with/without forming CO\* intermediate is also debated. ii) The direct comparison of the performance (activity and selectivity) of Ni and Ru surfaces are extremely difficult. This is because the computational system (functional and modeling parameters) and the number of reactions considered on Ni and Ru in various studies are different. iii) Many key intermediates like HCO\* (formed via HCOO\* route), HCOH\*, HCOOH\*, H<sub>2</sub>COO\*, H<sub>2</sub>COOH\* and C(OH)<sub>2</sub>\*, CH<sub>x</sub>\*OH/CH<sub>x</sub>O (x = 1 - 3) routes (formed via COH\*/HCO\* hydrogenation) and other side reactions had not been considered in the majority of DFT studies reported. In addition, many of the studies are limited to a fewer number of reactions. iv) Only a few DFT studies reported in the literature are extended to develop a microkinetic model. This is extremely important to predict the reaction pathways that influence catalyst performance at any given reaction operating condition. v) Popular functionals such as PBE and PW-91 are employed for studying CO<sub>2</sub> methanation, without proper benchmarking studies. These functionals are known to underestimate CO<sub>2</sub> binding energy<sup>111,176,177</sup> and fail to predict CO-metal interactions present in the system<sup>104,139,140</sup>. Since CO is a possible intermediate in CO<sub>2</sub> methanation, this would lead to an incorrect prediction of the CO\* activation barrier and subsequently results in incorrect CO\* coverage prediction. Thus, the DFT studies prior to this work are questionable (details are specified in Page 57) based on the number of reactions considered and the functional choice. Hence, corrections must be applied before employing the results of DFT simulations in microkinetic modelling.

In this study, we combined DFT and microkinetic modeling to explore the dominant reaction pathways and kinetically relevant steps of the CO<sub>2</sub> methanation reaction system on Ni (111) and Ru (001) surfaces. We resolved the discrepancies in the reaction mechanism on both Ni and Ru surfaces by considering a comprehensive reaction network of 46 elementary reactions on each surface. Most importantly, based on the benchmarking studies<sup>178</sup>, we employed rPBE-vdW functional with a correction of 28 kJ/mol for gas-phase CO<sub>2</sub> energy for studying this reaction. This functional was identified as the only functional that predicts the adsorption of both CO<sub>2</sub> and CO correctly<sup>178</sup>. The (111) and (001) facet of Ni and Ru were selected respectively as these are the lowest energy facets and usually dominates the surface<sup>179</sup>. We compared the performance (activity and selectivity) of Ni

(111) and Ru (001) and the dominant reaction pathways were identified on both the surfaces. Given that relative rates between different catalysts are better described than absolute rates by microkinetic models<sup>180</sup>, their relative rates for methane formation were also compared.

Details of computational methods and the simulation system are discussed in section 4.2. Multiple pathways for activation of CO<sub>2</sub> and its hydrogenation are presented on Ni (111) and Ru (001) surfaces. In section 4.3, the DFT calculated activation barriers and free energy values along with the results from the microkinetic study are reported. The key findings from this study are summarized in Section 4.4.

## 4.2. Computational details

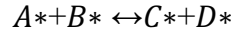
### 4.2.1 DFT calculations

All DFT calculations were performed using the Vienna *ab initio* Simulation Package (VASP) with a plane wave cut-off energy of 450 eV. Spin polarization was turned on for all calculations and a k-points sampling of 3x3x1 with Monkhorst-pack scheme was employed. The projector augmented wave (PAW) method was used to describe the interaction between the valence electron and ions. The energy convergence criteria and force tolerance were set as 10<sup>-6</sup> eV/Å per unit cell and 0.05 eV/Å respectively to ensure a high level of accuracy. Based on the previous benchmarking studies (*chapter 3*), Generalized gradient approximation (GGA) based rPBE-vdW exchange-correlation functional is employed for studying CO<sub>2</sub> methanation reaction on both Ni (111) and Ru (001) surfaces<sup>178</sup>. The rPBE-vdW functional, with a correction of 28 kJ/mol for gas-phase CO<sub>2</sub>, was identified as the best available choice of functional for studying CO<sub>2</sub> conversion reactions<sup>178</sup>. The most stable facet was selected for modeling Ni and Ru surfaces using 4-layer, p (4x4) unit cell. The bottom two layers were fixed and an inter-slab distance of 12 Å was added to avoid interaction with the adjacent cell in the z-direction. Nudged Elastic Band (NEB) method was used to identify the transition state (TS) for all reactions by considering 8-12 images and the NEB image closest to TS was optimized using the quasi-

Newton algorithm. Additionally, the TS was confirmed by performing vibrational frequency analysis. The zero-point energy and thermodynamic corrections were calculated at appropriate experimental conditions. For gas-phase molecules, the enthalpy corrections were taken from thermodynamic tables while statistical thermodynamics using vibrational partition function is employed for the adsorbed system. All the reaction energies and activation barriers are reported as Gibbs free energy change. Reactants/products are taken in separate unit cell and reaction free energy,  $G_r$ , is calculated as  $G_r = G_{\text{tot}}(\text{FS}) - G_{\text{tot}}(\text{IS})$ , with FS and IS referring to final and initial state structures. The corresponding activation barrier,  $G_a$ , is calculated as  $G_a = G_{\text{tot}}(\text{TS}) - G_{\text{tot}}(\text{IS})$ , with TS referring to transition state structure.

#### 4.2.2 Microkinetic model

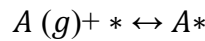
The simulations are based on a previously proposed model of the dry reforming process over Ni surface<sup>64</sup>. We employed the same methodology to generate values of rate constants for each elementary reaction step. Consider the surface reaction



The forward rates are computed for the given reaction condition using the following equation

$$r_f = (k_f \theta_A \theta_B) \times N_{\text{site,total}} \quad (4.1)$$

where,  $r_f$  is the forward reaction rate in mol/gcat.s,  $k_{f,ri}$  is the forward/backward reaction rate constant in s<sup>-1</sup>,  $\theta_A$ , and  $\theta_B$  are the fractional coverages of species A and B,  $N_{\text{site,total}}$  is the total number of active sites in mol/gcat. If the reacting species is in gas phase



then the forward rates are given as

$$r_{f,\text{ads}} = k_{f,\text{ads},ri} \times \frac{P_A}{P_{\text{std}}} \times \theta^* \times N_{\text{site,total}} \quad (4.2)$$

where,  $\theta^*$  is the fractional surface coverage of the free site,  $P_A$  is the partial pressure of A and  $P_{\text{std}}$  1 bar. The backward reaction rates are also written in a similar fashion as equation (4.1) for surface reactants and equation (4.2) for gas phase reactants. The rate constants in

equation (4.1) and (4.2) respectively are computed using transition state theory (equation 4.3)

$$k_f = k_B T/h \exp \left[ \frac{-\Delta G_{act,f}}{RT} \right] \quad (4.3)$$

where,  $k_B$  is the Boltzmann constant,  $h$  is the Planck's constant,  $R$  is the universal gas constant,  $T$  is the reaction temperature and  $\Delta G_{act,f}$  is the Gibbs free energy of activation step computed after adding temperature and entropic corrections to the DFT generated energies. Further details on evaluating these rate constants and Gibbs energies are mentioned in the appendix to chapter 4.

Once the rate constants are computed, the rate equations are evaluated and are then assembled for each species to generate differential equations of species balance. Considering an ideal PFR reactor as a reasonable simplification for a typical fixed-bed reactor, the reactant conversions are also written from the differential equations of reactant balance.

$$\frac{d\theta_j}{d\left(\frac{W}{F_0}\right)} = \sum_i^{\text{\# of reactions}} \sigma_{i,j} r_i \quad (4.4)$$

where  $W$  is the weight of catalyst in g,  $F_0$  is the total molar flow rate of gases in mol·h<sup>-1</sup>,  $\sigma_{i,j}$  is the stoichiometric coefficient of species  $j$  in reaction  $i$ ,  $r_i$  is the rate of reaction  $i$  and  $\theta_j$  is the fractional surface coverage of surface species  $j$  or mole fraction of gas-phase species. The fractional surface coverages/mole fractions are obtained as a function of space-time by solving the above system of differential equations; the solution was obtained using the MATLAB-implemented ode-solver ode15s.

Following assumptions were made while constructing the microkinetic models

1. Each site can be occupied by at most one adsorbate. This is referred to as the "exclusion principle".
2. All catalytic sites are equivalent, and any surface species has the same "stability" (quantified by the binding energy) at any site on the surface. Consequently, the probability of finding any site occupied by a species is equal to its fractional surface coverage.
3. No spatial correlations are observed between adsorbates.

4. Kinetic constants are independent of coverage
5. The gradient of species coverages, temperature and pressure along the catalyst bed is negligible.

#### 4.2.3. Reaction pathway analysis

After developing the microkinetic model for the methanation process, further analysis is performed using this model to identify the rate-determining step (RDS). The previously reported studies<sup>181,182</sup> have employed sensitivity analysis and partial equilibrium analysis on their respective microkinetic models to identify the RDS and the kinetically relevant steps for the WGS reaction on Pt<sup>39</sup> and Ni<sup>38</sup>, and for the WGS, steam and dry reforming reactions over Rh<sup>183</sup>. Here a similar strategy is applied, sensitivity analysis (SA) and partial equilibrium analysis (PEA) is performed on the microkinetic model to identify kinetically relevant reaction steps over Ni (111) and Ru (001). The partial equilibrium (PE) coefficient ( $\varphi_j$ ) of each reaction  $j$  is evaluated using the following expression

$$\varphi_j = \frac{r_j^f}{r_j^f + r_j^b} \quad (4.5)$$

where,  $r_j^f$ ,  $r_j^b$  are the forward and backward rates of the  $j^{\text{th}}$  elementary reaction. And, sensitivity coefficients of each reaction step are computed by applying a small perturbation of 5% to the rate constant of each step separately, and a series of simulations are carried out to observe the influence on a selected model response ( $M$ ), e.g. the reactant fractional conversion. Given that the rate constant of elementary steps is over several orders of magnitude higher than the model responses, a sensitivity coefficient is defined for each reaction  $j$  using the following expression (4.6),

$$S_{k,j} = \frac{\partial \ln M_k}{\partial \ln k_j} \approx \frac{\Delta M_k k_j}{M_k \Delta k_j} \quad (4.6)$$

where  $S_{k,j}$  is the sensitivity coefficient and  $M_k$  is the model response for the  $k^{\text{th}}$  variable. This analysis is carried out to identify and compare the kinetically relevant steps of the reaction on Ni (111) and Ru (001) catalyst surfaces.

An alternate sensitivity analysis approach, first proposed by Charles T Campbell, is the Degree of Rate Control (DoRC) method<sup>184–187</sup>. The DoRC simplifies complex reactions to

identify a few elementary reaction steps that are crucial to catalyst performance. The DoRC of each elementary step is calculated as the ratio of the change in apparent activation free energy of the overall reaction system over the change in activation free energy of a single elementary step while holding constant the kinetics of all other elementary steps. In this approach the degree of rate control sums to 1 for every elementary step in a serial reaction and the degree of rate control can be linked with reaction orders, apparent activation energies, and coverages. This approach has been successfully implemented to identify kinetically relevant important elementary steps and used to design new catalysts<sup>188</sup>.

Lastly, dominant reaction pathways are identified over both catalysts surfaces by employing a graph-based algorithm that selects reaction steps based on their reaction rates. The nodes of the graph represent different surface intermediates and edges represent the direction and rates of the corresponding reaction step. The graph includes all forward/backward reactions represented in Figure 4. 1. We then employ an algorithm that uses this representation to input reaction rates and further identifies the pathway that contributes the most towards product formation, i.e. highest methane formation rate ( $\text{mole}_{\text{CH}_4} \cdot \text{g}_{\text{cat}}^{-1} \cdot \text{h}^{-1}$ ). Since the overall reaction rate of a pathway is as good as its rate-limiting step, the algorithm compares reaction rates of every possible pathway and selects the one with the highest limiting rate i.e.  $\max(\min(\text{reaction rate of reaction steps starting from reactants and ending at products}) \text{ over different pathways})$ . Since the CO<sub>2</sub> methanation reaction is exothermic in nature, a reaction temperature of 550 K was selected for the microkinetic modeling and sensitivity analysis. Further details of the reaction conditions are given in section 4.2.2.

### 4.3. Results and Discussions

#### 4.3.1 DFT study of CO<sub>2</sub> methanation on Ni (111) and Ru (001)

The reaction network in the current study consists of CO<sub>2</sub>\*, CO\* and C\* hydrogenation routes, CO<sub>2</sub>\* and CO\* direct dissociation routes, other side reactions, and product desorption (*cf* Figure 4. 1 and Table 4. 1). Altogether we considered 46 elementary

reactions and all these reactions are studied on both Ni (111) and Ru (001) surfaces and are described in the following sub-sections. Also, note that the reaction energy and reaction barriers of all these reactions are calculated and reported as Gibbs free energy change. The reaction free energies and free energy barriers of all elementary reactions are listed in Table 4. 1 and comparison of electronic energies with previous works are reported in the appendix to chapter 4.

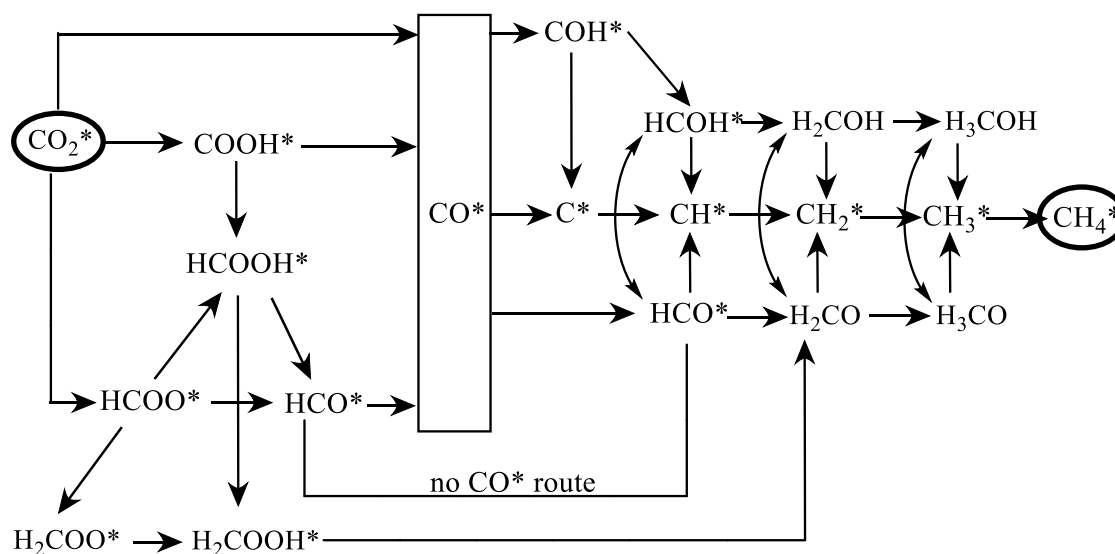


**Figure 4. 1** CO<sub>2</sub> direct dissociation and hydrogenation with/without CO\* intermediate routes. Though not shown as reversible reactions here, the microkinetic model takes into account all of these reactions as reversible.

**Table 4. 1** Calculated free energy barriers and reaction free energies (550K and 10 atm pressure) of all elementary reactions for CO<sub>2</sub> methanation on Ni (111) and Ru (001) surfaces. The reactions include CO<sub>2</sub> and CO direct dissociation routes, CO<sub>2</sub>, CO and C hydrogenation routes, other side reactions (H<sub>2</sub>O formation, Boudouard reaction), and desorption of products. Note that the microkinetic model takes into account all of these reactions as reversible.

Reaction	Activation barrier		Reaction free energy	
	(kJ/mol)		(kJ/mol)	
	Ni (111)	Ru (001)	Ni (111)	Ru (001)



R1	$\text{CH}_3^* + \text{H}^* \rightarrow \text{CH}_4^*$	81	103	-63	-34
R2	$\text{CH}_2^* + \text{H}^* \rightarrow \text{CH}_3^*$	57	71	-5	22
R3	$\text{CH}^* + \text{H}^* \rightarrow \text{CH}_2^*$	64	77	30	67
R4	$\text{C}^* + \text{H}^* \rightarrow \text{CH}^*$	88	101	-40	-1
R5	$\text{CO}_2^* \rightarrow \text{CO}^* + \text{O}^*$	60	51	-106	-170
R6	$\text{CO}_2^* + \text{H}^* \rightarrow \text{COOH}^*$	112	121	25	20
R7	$\text{CO}_2^* + \text{H}^* \rightarrow \text{HCOO}^*$	69	70	-25	-28
R8	$\text{COOH}^* \rightarrow \text{CO}^* + \text{OH}^*$	17	38	-116	-110
R9	$\text{HCOO}^* \rightarrow \text{HCO}^* + \text{O}^*$	146	104	43	-17
R10	$\text{HCO}^* \rightarrow \text{CO}^* + \text{H}^*$	19	5	-123	-125
R11	$\text{COOH}^* + \text{H}^* \rightarrow \text{HCOOH}^*$	83	114	16	53
R12	$\text{HCOO}^* + \text{H}^* \rightarrow \text{HCOOH}^*$	113	125	67	101
R13	$\text{HCOOH}^* \rightarrow \text{HCO}^* + \text{OH}^*$	64	44	-9	-39
R14	$\text{CH}_2\text{OH}^* + \text{H}^* \rightarrow \text{CH}_3\text{OH}^*$	84	104	-46	-7
R15	$\text{CHOH}^* + \text{H}^* \rightarrow \text{CH}_2\text{OH}^*$	89	64	19	26
R16	$\text{COH}^* + \text{H}^* \rightarrow \text{CHOH}^*$	89	96	68	103
R17	$\text{CO}^* + \text{H}^* \rightarrow \text{COH}^*$	209	198	112	100
R18	$\text{CH}_3\text{OH}^* \rightarrow \text{CH}_3^* + \text{OH}^*$	160	113	-29	-63
R19	$\text{CH}_2\text{OH}^* \rightarrow \text{CH}_2^* + \text{OH}^*$	64	43	-70	-92
R20	$\text{CHOH}^* \rightarrow \text{CH}^* + \text{OH}^*$	62	30	-81	-133
R21	$\text{COH}^* \rightarrow \text{C}^* + \text{OH}^*$	166	105	27	-29
R22	$\text{CH}_2\text{O}^* + \text{H}^* \rightarrow \text{CH}_3\text{O}^*$	60	82	-42	-10
R23	$\text{CHO}^* + \text{H}^* \rightarrow \text{CH}_2\text{O}^*$	73	66	35	49
R24	$\text{CH}_3\text{O}^* \rightarrow \text{CH}_3^* + \text{O}^*$	127	117	-6	-84
R25	$\text{CH}_2^* + \text{O}^* \rightarrow \text{CH}_2\text{O}^*$	133	188	44	117
R26	$\text{CHO}^* \rightarrow \text{CH}^* + \text{O}^*$	104	105	-40	-135
R27	$\text{CO}^* \rightarrow \text{C}^* + \text{O}^*$	282	217	124	-9
R28	$\text{CH}_3\text{OH}^* + ^* \rightarrow \text{CH}_3\text{O}^* + \text{H}^*$	94	78	-38	-58
R29	$\text{CH}_2\text{OH}^* + ^* \rightarrow \text{CH}_2\text{O}^* + \text{H}^*$	67	86	-41	-55
R30	$\text{CHOH}^* + ^* \rightarrow \text{HCO}^* + \text{H}^*$	61	68	-56	-79

R31	$O^* + H^* \rightarrow OH^*$	118	166	15	80
R32	$OH^* + H^* \rightarrow H_2O^*$	133	125	29	38
R33	$H_2 \rightarrow H^* + H^*$	64	51	-6	-32
R34	$OH^* + OH^* \rightarrow H_2O^* + O^*$	87	64	13	-42
R35	$CO_2^* + C^* \rightarrow 2CO^*$	153	142	-229	-161
R36	$HCOO^* + H^* \rightarrow H_2COO^*$	192	168	104	93
R37	$HCOOH^* + H^* \rightarrow H_2COOH^*$	118	121	47	42
R38	$H_2COO^* + H^* \rightarrow H_2COOH^*$	90	156	10	51
R39	$H_2COO^* \rightarrow H_2CO^* + O^*$	32	36	-26	-60
R40	$H_2COOH^* \rightarrow H_2CO^* + OH^*$	34	18	-21	-32
R41	$CO_2 \rightarrow CO_2^*$	-	-	53	29
R42	$CO^* \rightarrow CO$	-	-	73	96
R43	$H_2O^* \rightarrow H_2O + ^*$	-	-	-33	-19
R44	$CH_4^* \rightarrow CH_4$	-	-	-23	-11
R45	$HCOOH^* \rightarrow HCOOH$	-	-	-30	-13
R46	$CH_3OH^* \rightarrow CH_3OH$	-	-	-31	-25

#### 4.3.1.1 CO<sub>2</sub> direct dissociation route vs CO<sub>2</sub> hydrogenation routes to form CO\* intermediate

CO<sub>2</sub> can either undergo direct dissociation to CO\* and O\* or it can react with H\* adatom to form COOH\*/HCOO\* intermediate that dissociates to form CO\* intermediate. We investigated both these routes on Ni and Ru and the corresponding free energies are reported in Figure 4. 2.

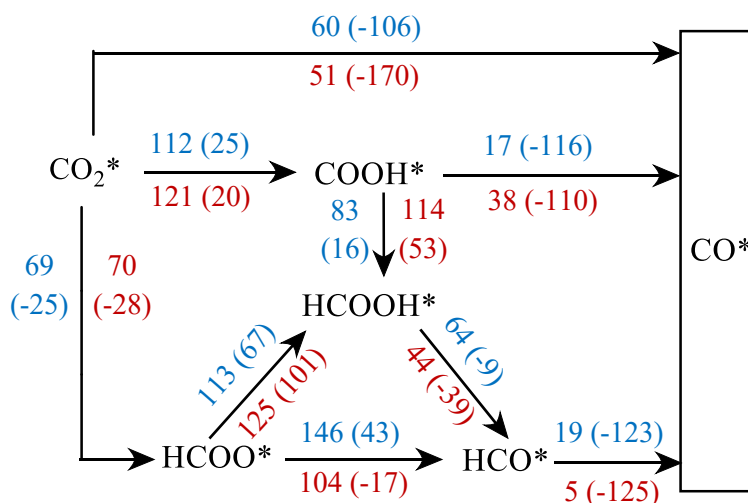


**Figure 4. 2** CO<sub>2</sub> activation and dissociation on Ni (111) and Ru. Free energy barriers and reaction free energies (inside brackets) on Ni (111) and Ru (001) are shown in blue and red color respectively.

CO<sub>2</sub> binds weakly on Ni (111) surface with binding energy (electronic energy) of -17 kJ/mol. The direct dissociation of CO<sub>2</sub> to CO\* and O\* is kinetically feasible with a free energy barrier of 60 kJ/mol and has a reaction free energy of -106 kJ/mol. H\* adatom is formed via H<sub>2</sub> dissociation (R33) and this reaction has a barrier and reaction energy of 64 kJ/mol and -6 kJ/mol respectively. In comparison to CO<sub>2</sub>\* direct dissociation, CO<sub>2</sub> hydrogenation to HCOO\* is less exergonic with a reaction free energy of -25 kJ/mol and has a free energy barrier of 69 kJ/mol. However, HCOO\* dissociation to form HCO\* (R9) is endergonic (43 kJ/mol) and has a very high barrier of 146 kJ/mol. Interestingly, HCO\* dissociation to form CO\* (R10) is highly exergonic (-123 kJ/mol) and has a very low barrier (19 kJ/mol). In comparison, CO<sub>2</sub> hydrogenation to COOH\* is endergonic (25 kJ/mol) and has a significantly high barrier of 112 kJ/mol. However, the dehydroxylation of COOH\* to form CO\* (R8) is highly exergonic (-116 kJ/mol) and has a low barrier (17 kJ/mol). Nevertheless, the high barrier for COOH\* formation makes it a less favorable route. The hydrogenation of COOH\*/HCOO\* leads to HCOOH\* formation (R11 and R12). HCOO\* and COOH\* hydrogenation reactions are endergonic (67 kJ/mol and 16 kJ/mol for HCOO\* and COOH\* hydrogenation respectively) and has barriers of 113

kJ/mol and 83 kJ/mol respectively. Interestingly, HCOO\* hydrogenation to HCOOH\* is kinetically favored over HCOO\* dissociation to HCO\*. In addition, the dehydroxylation of HCOOH\* to HCO\* is slightly exergonic (9 kJ/mol) and has a low barrier of 64 kJ/mol.

Compared to Ni (111), CO<sub>2</sub> adsorbs strongly on Ru (001) surface with a binding energy of (electronic energy) of -45 kJ/mol. Similar to Ni (111), CO<sub>2</sub> direct dissociation is highly exergonic (-170 kJ/mol) and has a very low barrier (51 kJ/mol) on Ru (001). H<sub>2</sub> dissociation (R33) is more exergonic (-32 kJ/mol) and has a low barrier (51 kJ/mol) on Ru compared to Ni. CO<sub>2</sub> hydrogenation to COOH\*/HCOO\* has reaction free energy (20 kJ/mol and 28 kJ/mol for COOH\* and HCOO\* formation respectively) and barrier (121 kJ/mol and 70 kJ/mol for COOH\* and HCOO\* formation respectively) similar to that on Ni (111). The high barrier for COOH\* formation makes it a less favorable route. Interestingly, HCOO\* dissociation is exergonic (-17 kJ/mol) and has a lower barrier (104 kJ/mol) compared to Ni (111). However, the hydrogenation of COOH\*/HCOO\* to HCOOH\* (R11 and R12) has a slightly high barrier (114 kJ/mol and 125 kJ/mol for COOH\* and HCOO\* hydrogenation respectively) compared to Ni. Therefore, in contrast to Ni, HCOO\* dissociation to HCO\* is more favored compared to HCOO\* hydrogenation.

In short, the direct dissociation route of CO<sub>2</sub> is kinetically and thermodynamically feasible compared to the hydrogenation routes on both Ni (111) and Ru (001) surfaces. This is in excellent agreement with previously reported works mentioned in the introduction<sup>167,170</sup>. Interestingly, the direct dissociation of CO<sub>2</sub> is more exergonic (difference of 64 kJ/mol) and has slightly lower (lower by 9 kJ/mol) free energy barrier on Ru (001) compared to Ni (111). In addition, it is worthy to mention that the CO<sub>2</sub> hydrogenation to form HCOO\* intermediate is exergonic and has very low free energy barriers on both Ni and Ru. However, these routes are not considered in many studies<sup>167,169</sup>. Our DFT calculations show that it is essential to include HCOO\* intermediate routes to ascertain the dominant reaction pathway. HCOO\* direct dissociation to HCO\* is favored on Ru (001) while HCOO\* hydrogenation to HCOOH\* followed by dissociation to form HCO\* is favored on Ni (111).

4.3.1.2 CO direct dissociation route vs CO hydrogenation routes to form CH<sub>x</sub>\* (x = 0 - 3)

CO can either undergo direct dissociation to C\* and O\* or it can react with H\* adatom to form COH\*/HCO\* intermediate. These intermediates may dissociate to form C\*/CH\* intermediate or undergoes further hydrogenation to form CH<sub>x</sub>OH/CH<sub>x</sub>O (x = 1 - 3) intermediates followed by its dissociation to CH<sub>x</sub> (x = 1 - 3). These routes are investigated on both Ni (111) and Ru (001) and free energies are shown in Figure 4. 3.

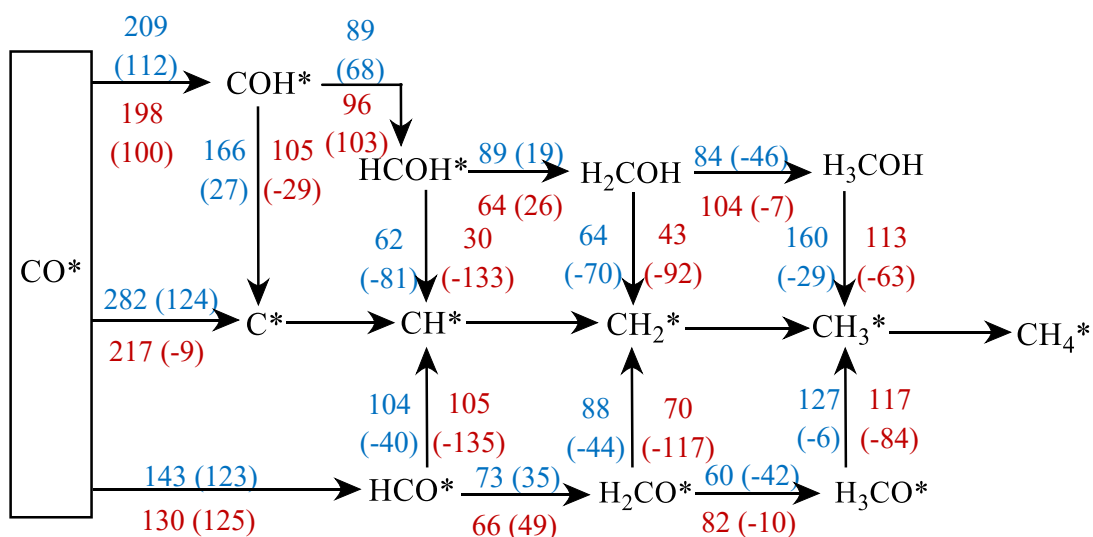


**Figure 4. 3** Free energy barriers and reaction free energies (inside brackets) for CO\* dissociation routes. Reaction free energies and barriers on Ni (111) and Ru (001) are presented in blue and red color, respectively.

On Ni (111), the direct dissociation of CO\* to C\* and O\* (R27) must overcome a huge barrier of 282 kJ/mol and this reaction is highly endergonic with a reaction free energy of 124 kJ/mol. In comparison, the hydrogenation of CO\* to COH\* (R17) and HCO\* (backward reaction of R10) are also highly endergonic with a reaction free energy of 112 kJ/mol and 123 kJ/mol respectively and must overcome a barrier of 209 kJ/mol and 143 kJ/mol respectively. This high barrier for CO\* activation could result in CO\* poisoning on the Ni surface. The COH\* can undergo dissociation to form C\* and OH\* (R21) and this reaction is endergonic (27 kJ/mol) and must overcome a high barrier of 166 kJ/mol. Thus, C\* formation (via CO\* direct dissociation or COH\* dissociation) reactions are

thermodynamically and kinetically not favored. This finding explains the experimental observation that C\* formation was not likely on Ni surface under methanation reaction conditions<sup>172,173</sup>. The COH\*/HCO\* formed (via CO\* hydrogenation) can undergo sequential hydrogenation to form CH<sub>x</sub>OH\* (x = 1 - 3)/CH<sub>x</sub>O\* (x = 2 - 3) intermediates as shown in Figure 4. 3. Interestingly COH\*/HCO\* sequential hydrogenation reactions (R14, R15, R16, R22 and R23) have lower barrier and these reactions are endergonic except CH<sub>2</sub>O\* (R22) and CH<sub>2</sub>OH\* (R14) hydrogenation steps. Notably, the barriers for HCO\* hydrogenation to CH<sub>x</sub>O\* (x = 2 - 3) is slightly lower than COH\* hydrogenation to CH<sub>x</sub>OH\* (x = 1 - 3). Besides the sequential hydrogenation routes, the CH<sub>x</sub>OH\*/CH<sub>x</sub>O\* (x = 1 - 3) intermediates can undergo dissociation to form CH<sub>x</sub> (x = 1 - 3) species (R18, R19, R20, R24, R25 and R26). Interestingly, the CH<sub>x</sub>OH\*/CH<sub>x</sub>O\* (x = 1 - 3) dissociation steps are exergonic and have lower barriers except for CH<sub>3</sub>O\* (127 kJ/mol) and CH<sub>3</sub>OH\* (160 kJ/mol) dissociation. However, the CH<sub>x</sub>OH (x = 1 - 3) routes (both hydrogenation and dissociation) are limited by the high barrier of COH\* formation from CO\* (R17). Therefore, CH\* and CH<sub>2</sub>\* formation via HCO\* and CH<sub>2</sub>O\* dissociation (with barriers of 104 kJ/mol and 88 kJ/mol respectively) are the feasible reactions.

In contrast to Ni (111), the CO\* direct dissociation to C\* and O\* (R27) is slightly exergonic (-9 kJ/mol) on Ru (001). However, this reaction has a huge barrier of 217 kJ/mol making it kinetically challenging. In comparison, CO\* hydrogenation to COH\* (R17) and HCO\* (backward reaction of R10) are endergonic with reaction free energies of 100 kJ/mol and 125 kJ/mol respectively. In addition, CO\* hydrogenation to COH\* must overcome a huge barrier of 198 kJ/mol. The dehydroxylation of COH\* dissociation to form C\* (R21) is exergonic (-29 kJ/mol) and has a barrier of 105 kJ/mol. Similar to Ni (111), the sequential hydrogenation ((R14, R15, and R16) barriers for COH\* to form CH<sub>x</sub>OH (x = 1 - 3) are lower on Ru (001). Nevertheless, the COH\* hydrogenation routes are limited by the high barrier (similar to Ni) of COH\* formation from CO\* (R17). Interestingly, HCO\* formation (backward reaction of R10) via CO\* hydrogenation has a significantly low barrier (123 kJ/mol) compared to CO\* direct dissociation (217 kJ/mol) and CO\* hydrogenation to COH\* (198 kJ/mol). Notably, the barrier for CO\* hydrogenation to HCO\* is 20 kJ/mol lower on Ru (001) compared to that on Ni (111). The further hydrogenation of HCO\* to

CH<sub>2</sub>O\* (R23) and CH<sub>3</sub>O\* (R22) has a low barrier of 66 kJ/mol and 82 kJ/mol respectively. In addition, the CH<sub>x</sub>O (x = 1 - 2) dissociation (backward reaction of R25 and R26) to CH<sub>x</sub> (x = 1 - 2) has lower barriers compared to CH<sub>3</sub>O\* dissociation (R24). Therefore, similar to Ni (111), CH\* and CH<sub>2</sub>\* formation via HCO\* and CH<sub>2</sub>O\* dissociation are feasible reactions on Ru (001).

In short, CO\* activation barriers are comparatively higher than CO<sub>2</sub> activation barriers. Notably, CO\* activation via hydrogenation to form HCO\* is the kinetically favored route on both Ni and Ru surfaces. It must be noted though that this reaction is highly endergonic on both Ni and Ru (123 kJ/mol and 125 kJ/mol respectively) and Ru has 13 kJ/mol less barrier compared to Ni. On both Ni and Ru, HCO\* prefers hydrogenation to form CH<sub>2</sub>O\* followed by its dissociation to form CH<sub>2</sub>\*. Notably, the sequential hydrogenation of COH\*/HCO\* to form CH<sub>x</sub>OH\* (x= 1 - 3)/CH<sub>x</sub>O\* (x = 2 - 3) intermediates are not considered in majority of the studies mentioned in introduction. However, we established that these routes are relevant as the barriers are comparatively lower and these reactions must be included in the study to ascertain the reaction pathway.

#### 4.3.1.3 CO<sub>2</sub> activation routes without CO\* intermediate

From the above discussion, it is clear that the CO\* activation is thermodynamically and kinetically challenging on both Ni and Ru. Hence, we investigated CO<sub>2</sub> activation routes without forming CO\* as an intermediate. These routes involve CO<sub>2</sub> hydrogenation via HCOO\* intermediate and the free energies are shown in Figure 4. 4.

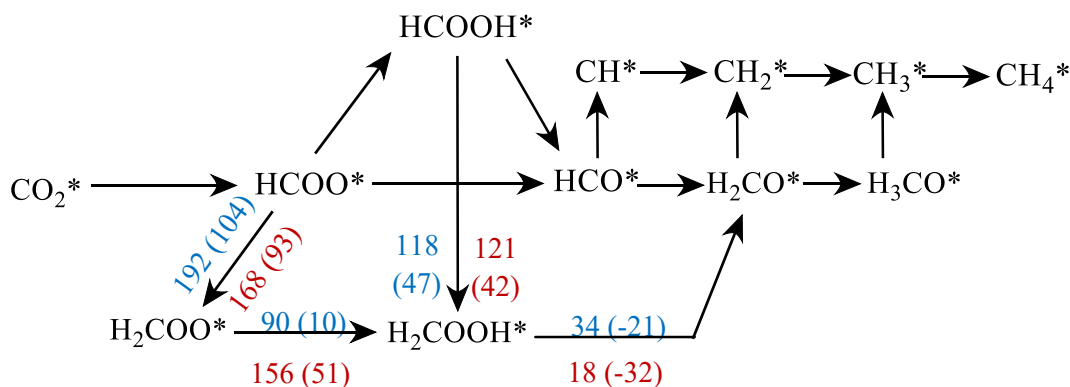


**Figure 4. 4** Free energy barriers and reaction free energies (inside brackets) for CO<sub>2</sub>\* dissociation routes without forming CO\* as an intermediate. Reaction free energies and barriers on Ni (111) and Ru (001) are presented in blue and red color, respectively.

HCOO\*, formed via CO<sub>2</sub> hydrogenation, undergoes further hydrogenation to form H<sub>2</sub>COO\* (R36) and this reaction must overcome a huge barrier of 192 kJ/mol. In addition, this reaction is highly endergonic with reaction free energy of 104 kJ/mol making it thermodynamically and kinetically challenging. In comparison HCOOH\* (formed by HCOO\* hydrogenation (R12)) hydrogenation to form H<sub>2</sub>COOH\* (R37) has a barrier and reaction free energy of 118 kJ/mol and 47 kJ/mol. However, the dehydroxylation of HCOOH\* to form HCO\* (R13) is exergonic (-9 kJ/mol) and has a low barrier of 64 kJ/mol. Therefore, HCO\* formation route (CO<sub>2</sub>\* → HCOO\* → HCOOH\* → HCO\*) is kinetically preferred over further hydrogenation routes of HCOO\*/HCOOH\* (R36 and R37). Importantly, HCO\* formation via CO<sub>2</sub> hydrogenation (CO<sub>2</sub>\* → HCOO\* → HCOOH\* → HCO\*) has 30 kJ/mol lower barrier and less endergonic by 56 kJ/mol compared to HCO\* formation via CO\* hydrogenation (CO<sub>2</sub>\* → CO\* → HCO\*). The HCO\* thus formed favors to undergo further hydrogenation to form CH<sub>2</sub>O\* followed by its dissociation to form CH<sub>2</sub>\* as discussed in the previous section.

On Ru, the barriers for hydrogenation of HCOO\* to H<sub>2</sub>COO\* (R36) and HCOOH\* hydrogenation to H<sub>2</sub>COOH\* (R37) are 168 kJ/mol and 121 kJ/mol. In comparison, the dehydroxylation of HCOOH\* is exergonic (-38 kJ/mol) and has a low barrier of 44 kJ/mol



making it thermodynamically and kinetically favorable reaction. Interestingly, HCO\* formation via HCOO\* intermediate ( $\text{CO}_2^* \rightarrow \text{HCOO}^* \rightarrow \text{HCOOH}^* \rightarrow \text{HCO}^*$ ) and CO\* intermediate ( $\text{CO}_2^* \rightarrow \text{CO}^* \rightarrow \text{HCO}^*$ ) has similar barriers (125 kJ/mol and 123 kJ/mol respectively). Therefore, both these routes are kinetically feasible on Ru.

In short, CO<sub>2</sub> hydrogenation without CO\* intermediate route is favored on Ni (111) whereas both routes (with/without CO\* intermediates) are feasible on Ru (001) surface.

#### 4.3.1.4 CH<sub>x</sub>\* (x = 0 - 3) hydrogenation

C\*/CH\* formed from COH\*/HCO\* undergoes sequential hydrogenation to form CH<sub>4</sub>. C\* hydrogenation to CH\* (R4) is exergonic (-40 kJ/mol) and has a barrier of 88 kJ/mol making it thermodynamically and kinetically favorable reaction on Ni (111) surface (*cf* Figure 4. 5). However, this reaction is limited by the high barrier of C\* formation from COH\* or CO\* dissociation. CH\* hydrogenation to CH<sub>2</sub>\* (R3) is endergonic (30 kJ/mol) but has a low barrier of 64 kJ/mol. CH<sub>2</sub>\* hydrogenation to CH<sub>3</sub>\* (R2) and CH<sub>4</sub> (R1) has to overcome barriers of 57 kJ/mol and 81 kJ/mol respectively and these reactions are exergonic making it thermodynamically and kinetically feasible reactions.

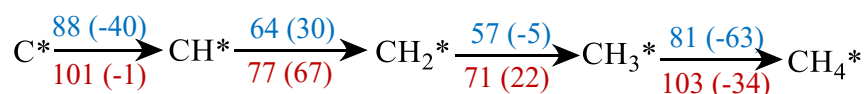


**Figure 4. 5** Free energy barriers and reaction free energies (inside brackets) for sequential hydrogenation of C\*. Reaction free energies and barriers on Ni (111) and Ru (001) are presented in blue and red color, respectively.

The CH<sub>x</sub> hydrogenation barriers are slightly higher on Ru (001) surface. The barrier for C\* (R4), CH\* (R3), CH<sub>2</sub>\* (R2), and CH<sub>3</sub>\* (R1) hydrogenation reactions are 101 kJ/mol, 77 kJ/mol, 71 kJ/mol and 103 kJ/mol respectively. CH\* and CH<sub>2</sub>\* hydrogenation reactions are endergonic while CH<sub>3</sub>\* hydrogenation is exergonic on Ru (001).

In short, the hydrogenation reactions are kinetically favorable. Notably, these reactions are thermodynamically and kinetically more favored on Ni (111) compared to Ru (001) surface.

#### 4.3.1.5 Side reactions (water formation) and desorption of products

O\* adatom formed from CO<sub>2</sub> dissociation undergoes hydrogenation to form OH\* (R31). This reaction is endergonic (15 kJ/mol) and has to overcome a barrier of 118 kJ/mol on Ni (111). H<sub>2</sub>O\*, one of the products, is formed from OH\* and we considered two H<sub>2</sub>O\* formation routes (R32 and R34). Both these reactions are endergonic (29 kJ/mol for R32 and 13 kJ/mol for R34). The free energy barrier for R34 (87 kJ/mol) is 46 kJ/mol lower than that of R32 making it kinetically favored route. However, this reaction (R34) is not considered in the majority of the studies reported.

In comparison, O\* hydrogenation (R31) is more endergonic (80 kJ/mol) and has a high barrier of 166 kJ/mol on Ru compared to Ni. Similar to Ni the OH\* hydrogenation (R32) is endergonic (38 kJ/mol) and must overcome a barrier of 125 kJ/mol on Ru. However, H<sub>2</sub>O\* formation via R34 is exergonic (-42 kJ/mol) and has a low barrier of 64 kJ/mol making it thermodynamically and kinetically favored route.

The desorption energy (electronic energy) of CH<sub>4</sub> (R44) and H<sub>2</sub>O (R43) are 12 kJ/mol and 31 kJ/mol on Ni (111) and 19 kJ/mol and 45 kJ/mol on Ru (001) surfaces respectively.

### 4.3.2 Microkinetic Analysis

In this section, we discuss and compare the results from the microkinetic model analysis of CO<sub>2</sub> methanation reaction over Ni (111) and Ru (001). The rate expressions and species balance equations of the microkinetic model were developed using equations 4.1 – 4.4 and solved. Rate constants of reactions over Ni (111) and Ru (001) at 550 K and 10 bar pressure are tabulated in the appendix to chapter 4. The microkinetic model was validated against experimental data<sup>189</sup>.

## 4.3.2.1 Surface Coverage

The surface coverages of reaction intermediates over Ni (111) and Ru (001) were obtained after solving the microkinetic model. The fractional coverages of the most abundant intermediates ( $\theta_i > 1 \times 10^{-3}$ ) are given in Table 4. 2.

**Table 4. 2** Fractional surface coverages of most abundant surface species ( $\theta_i > 1 \times 10^{-3}$ ) and fractional conversion of CO<sub>2</sub> ( $x_{\text{CO}_2}$ ) and H<sub>2</sub> ( $x_{\text{H}_2}$ ) computed by the model at a reaction temperature of 550 K, 10 bar pressure, and an inlet feed composition of 20% volume fraction CO<sub>2</sub> and 80% volume fraction of H<sub>2</sub>.

Species	Ni (111)	Ru (001)
CO*	$1.45 \times 10^{-2}$	$9.79 \times 10^{-3}$
HCOO*	$3.74 \times 10^{-5}$	$7.20 \times 10^{-3}$
O*	$1.25 \times 10^{-2}$	$9.79 \times 10^{-3}$
H*	$8.18 \times 10^{-1}$	$9.61 \times 10^{-1}$
OH*	$1.88 \times 10^{-3}$	$1.13 \times 10^{-6}$
Free Site (*)	$1.54 \times 10^{-1}$	$1.19 \times 10^{-2}$
$x_{\text{CO}_2}$	$7.24 \times 10^{-2}$	$8.50 \times 10^{-2}$
$x_{\text{H}_2}$	$5.12 \times 10^{-1}$	$6.05 \times 10^{-1}$

H\* is identified as the most abundant surface intermediate on both surfaces with 96% and 82% coverage on Ru (001) and Ni (111) respectively. Notably, H<sub>2</sub> dissociation has very low Gibbs free energy barriers on both Ni (111) and Ru (001) surfaces (64 kJ/mol and 51 kJ/mol respectively). The H\* coverage is followed by the free site (\*), CO\* and O\* coverages. These surface species (H\*, CO\*, and O\*) are relevant intermediates regardless of the catalyst surface therefore, their corresponding binding energies are reasonable reaction descriptors for the CO<sub>2</sub> methanation reaction. A catalyst can be optimized by optimizing binding energies of the above species so that the formation of these intermediates is favored but they do not poison the catalyst surface.

However, it should be noted that HCOO\* coverage on Ru (001) is almost the same as CO\* and O\* coverages suggesting that HCOO\* is also a relevant intermediate on Ru (001). Another key observation from Table 4. 2 is that the HCOO\* coverage is significantly high on Ru (001) ( $7.20 \times 10^{-3}$ ) compared to that on Ni (111) ( $3.74 \times 10^{-5}$ ). This implies that some of the CO<sub>2</sub> get hydrogenated to HCOO\* and stays on the surface since the HCOO\* activation barrier is high (*cf* Table 4. 1). This observation outlines one of the major problems with descriptor-based catalyst optimization approaches, i.e. pre-defined reaction descriptors. The reaction descriptors are different when considering Ru (001) as initial catalyst than Ni (111) for further catalyst optimization. Although scaling relations could help generalize the reaction descriptors to atomic C, H and O binding energies.

Moreover, it is also important to include all relevant elementary reaction steps in the above analysis. For example, most of the reported studies <sup>167,168</sup> on CO<sub>2</sub> methanation over Ru (001) do not include HCOO\* dissociation and hydrogenation reactions as a possible pathway for CH<sub>4</sub> production, despite it being among the most abundant surface species on this catalyst surface. This might severely impact the overall optimization.

#### 4.3.2.2 Sensitivity analysis (SA)

The following analysis was conducted to identify the relevant reaction steps. The partial pressure of CH<sub>4</sub> ( $p_{\text{CH}_4}$ ) was taken as the model response and the reaction conditions are adapted from section 4.2.2. Since it is important to understand the relative contribution of each reaction step, a relative sensitivity coefficient ( $S_{k,j}^r$ ) of each elementary step was generated using equation (7) and plotted against the reaction number. The reaction numbers are the same as in Table 4. 1.

$$S_{k,j}^r = \frac{S_{k,j}}{|S_k^{\max}|} \quad (7)$$

where,  $S_k^{\max}$  is the sensitivity coefficient with the highest absolute value for a given model response so that  $|S_{k,j}^r| \leq 1$ .

Furthermore, the reactions in quasi-equilibrium were identified using partial equilibrium analysis (PEA). The results of the partial equilibrium analysis and sensitivity analysis for the model response  $p_{\text{CH}_4}$  and reaction steps for which  $|S_{k,\text{CH}_4}^r| \geq 0.2$  over Ni (111) and Ru (001) are reported in Figure 4. 6 and Figure 4. 7, respectively. The relative sensitivity coefficient and partial equilibrium coefficients for all of the reaction steps are reported in the Supporting Information. The forward and backward reaction rates of all the reaction steps over Ni (111) and Ru (001) are also reported in the appendix to chapter 4.

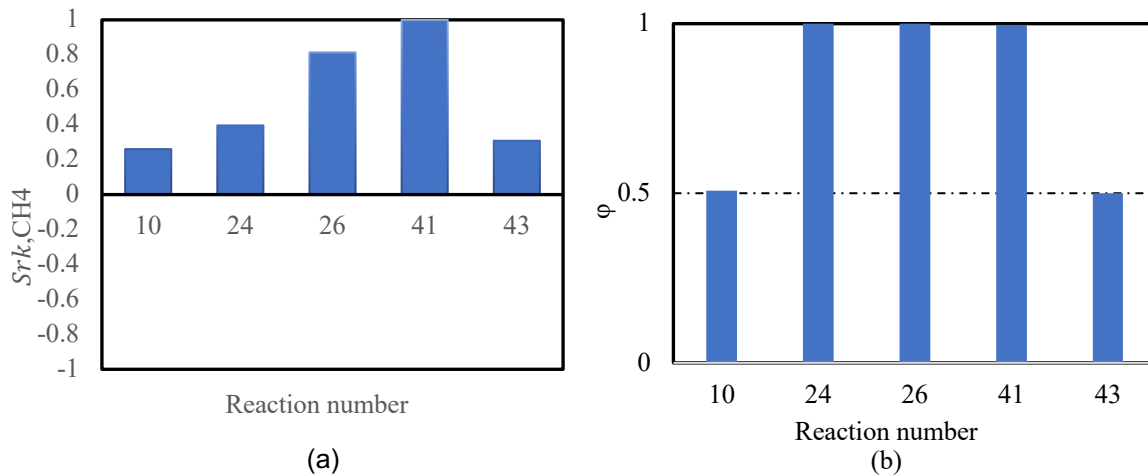


**Figure 4. 6** (a) Relative sensitivity coefficients ( $S_{k,\text{CH}_4}^r$ ) (b) Partial equilibrium coefficient  $\phi$  analysis of CO<sub>2</sub> methanation reaction steps ( $k$ ) for which  $|S_{k,\text{CH}_4}^r| \geq 0.2$  reported over Ni (111) at space-time value of 0.01 gcat·h·mol<sup>-1</sup> at reaction temperature 550 K and 10 atm pressure. R10:  $\text{HCO}^* \rightarrow \text{CO}^* + \text{H}^*$ , R24:  $\text{CH}_3\text{O}^* \rightarrow \text{CH}_3^* + \text{O}^*$ , R26:  $\text{CHO}^* \rightarrow \text{CH}^* + \text{O}^*$ , R41:  $\text{CO}_2 \rightarrow \text{CO}_2^*$  and R43:  $\text{H}_2\text{O}^* \rightarrow \text{H}_2\text{O} + *$ .

Figure 4. 6 shows that of the 46 elementary reactions, five of them satisfy the criteria  $|S_{k,\text{CH}_4}^r| \geq 0.2$  with R41 (CO<sub>2</sub> adsorption) being the most sensitive reaction on Ni (111) followed by CH<sub>x</sub>O\*<sup>(a)</sup> reduction reaction steps R26 (CHO\* reduction) and R24 (CH<sub>3</sub>O\* reduction), H<sub>2</sub>O\* desorption step R43 and lastly CO\* hydrogenation step R10. This analysis suggests that these five reaction steps are kinetically relevant, given the model response  $p_{\text{CH}_4}$  and of these five reactions, two are in quasi-equilibrium. Based on the SA and PEA criteria it was concluded that the remaining three reaction steps i.e. R41, R26, and R24 are candidates for RDS.

A similar analysis was performed to identify dominant reaction pathway for methanation on Ru (001). Figure 4. 7 reports 11 reaction steps that satisfy the criteria  $|S_{k,CH_4}^r| \geq 0.2$  with R1 (CH<sub>3</sub>\* hydrogenation) being the most sensitive reaction on Ru (001).

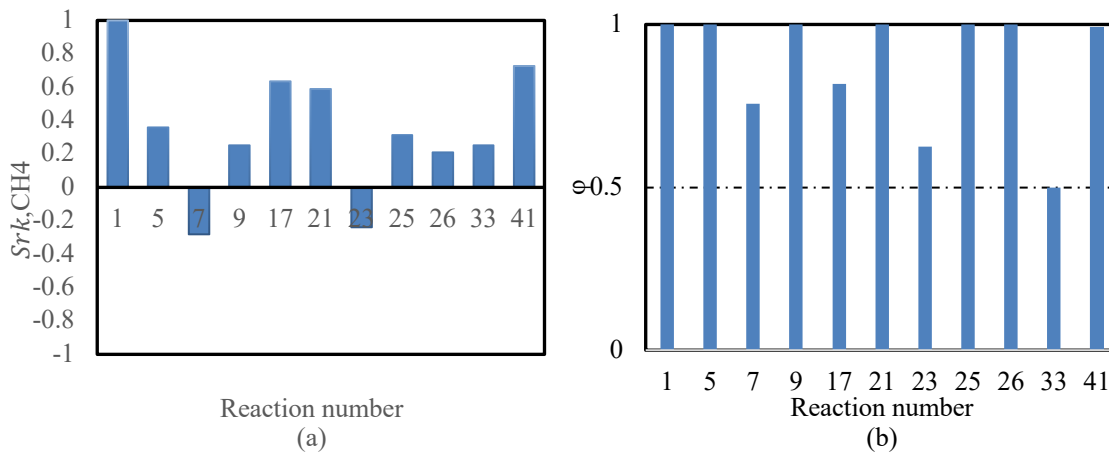


**Figure 4. 7** (a) Relative sensitivity coefficients ( $S_{k,CH_4}^r$ ) and (b) Partial equilibrium coefficient  $\phi$  analysis of CO<sub>2</sub> methanation reaction steps ( $k$ ) for which  $|S_{k,CH_4}^r| \geq 0.2$  reported over Ru (001) at space-time value of 0.01 gcat·h·mol<sup>-1</sup> at reaction temperature 550 K and 10 atm pressure. R1: CH<sub>3</sub>\*+H\*→CH<sub>4</sub>\*, R5: CO<sub>2</sub>\*→CO\*+O\*, R7: CO<sub>2</sub>\*+H\*→HCOO\*, R9: HCOO\*→HCO\*+O\*, R17: CO\*+H\*→COH\*, R21: COH\*→C\*+OH\*, R23: CHO\*+H\*→CH<sub>2</sub>O\*, R25: CH<sub>2</sub>\*+O\*→CH<sub>2</sub>O, R26: CHO\*→CH\*+O\*, R33: H<sub>2</sub>→H\*+H\* and R41: CO<sub>2</sub>→CO<sub>2</sub>\*.

All of these reaction steps, except for R33, follow the partial equilibrium analysis and sensitivity analysis criteria and can be considered a RDS candidate. However, it is difficult to establish the RDS given only SA and PEA coefficients especially when there are more than one highly sensitive reaction step. Hence, to further identify the RDS and dominant pathway of CO<sub>2</sub> methanation over Ni (111) and Ru (001) surfaces, a graph-based algorithm was employed. The following section discusses the results from this analysis.

4.3.2.3 Reaction mechanism analysis of CO<sub>2</sub> methanation

The widest path algorithm was employed for identifying dominant pathways. This algorithm uses a graphical representation of the reaction steps to identify pathways and compare their respective limiting rates. Further details about the graphical representation are presented in section 4.2.3, details regarding the code availability are mentioned in the supporting information. Figure 4. 8 displays the dominant reaction pathway and RDS of CO<sub>2</sub> methanation reaction over Ni (111) and Ru (001) as identified by the algorithm.

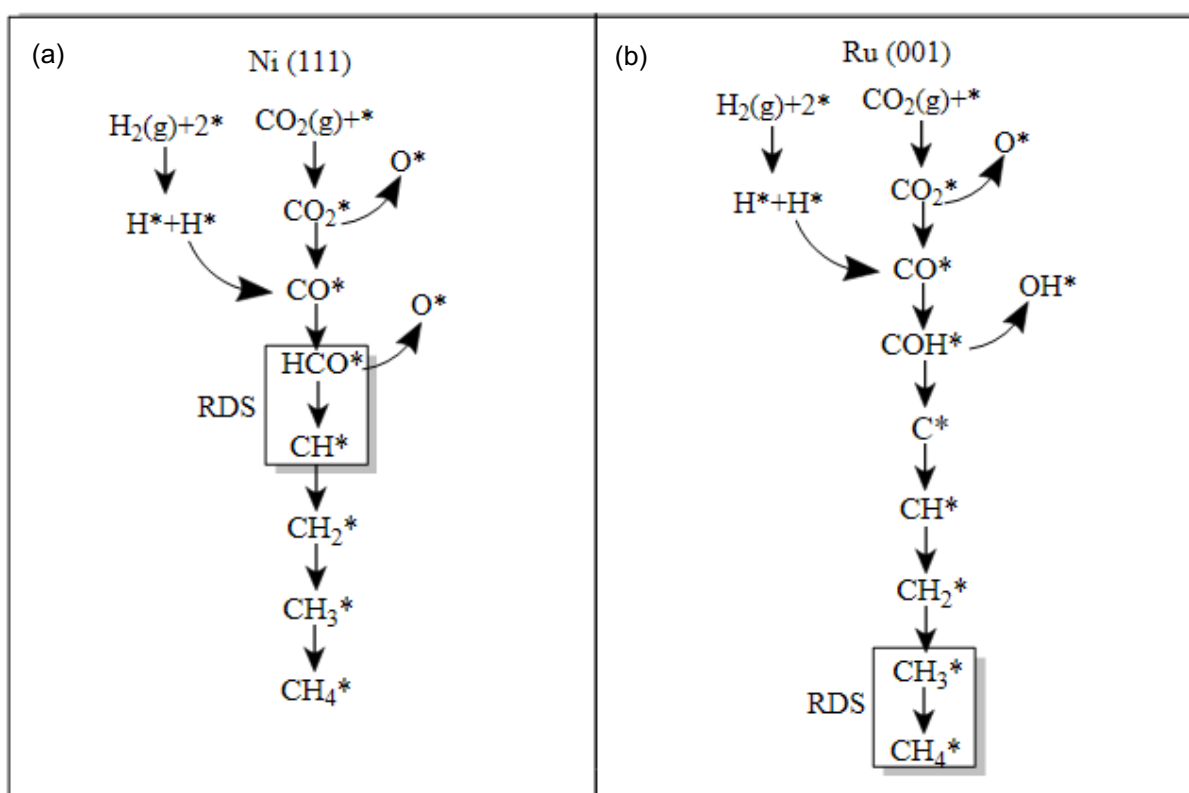


**Figure 4. 8** Dominant reaction pathway and rate-determining steps for CO<sub>2</sub> methanation reaction on (a) Ni (111) and (b) Ru (001) as identified from the algorithm.

The RDS is identified to be R26 (CHO\* reduction to CH\* and O\*) on Ni (111) and R1 (CH<sub>3</sub>\* hydrogenation to form CH<sub>4</sub>) on Ru (001). It should be noted that our algorithm identified multiple pathways with the same RDS, however, only the fastest reaction route from reactant to RDS's reactants and RDS's product to final product is considered in the

dominant pathway. Other pathways with the same RDS are reported in the appendix to chapter 4.

From Figure 4. 8 it is observed that direct dissociation of CO<sub>2</sub>\* to CO\* is favored on both Ni (111) and Ru (001). Our DFT calculations also showed that the direct dissociation of CO<sub>2</sub> is favored compared to hydrogenation on both Ni (111) and Ru (001) surfaces. This is followed by CO\* hydrogenation leading to HCO\* and COH\* formation on Ni (111) and Ru (001) respectively. Interestingly, the CO\* hydrogenation to HCO\* (reversible reaction of R10) was predicted to be the favored CO\* activation route on both Ni (111) and Ru (001) surfaces. However, the microkinetic study reveals that CO\* hydrogenation to COH\* is the favored route on Ru (001). Further reduction of CHO\* leads to CH\* formation on Ni (111) whereas COH\* reduces to C\* on Ru (001) leading to relatively higher C\* formation on Ru (001) as observed in Table 4. 2. Lastly, sequential hydrogenation of CH\* and C\* leads to CH<sub>4</sub> formation on Ni (111) and Ru (001) respectively. Side reaction steps of WGS reactions are not considered in the methanation reaction analysis.

Having known the RDS for methanation on both surfaces, their respective rates were compared to further evaluate the catalytic performance of Ni (111) and Ru (001). It was observed that the rate of RDS for methanation (CHO\* reduction) on Ni (111), i.e.  $5.07 \times 10^{-10}$  mol/g<sub>cat</sub>·h, is higher than the rate of RDS for methanation (CH<sub>3</sub>\* hydrogenation) on Ru (111), i.e.  $1.02 \times 10^{-13}$  mol/g<sub>cat</sub>·h, further suggesting that methane formation is more favored on Ni (111). This observation is the same as that previously seen in literature<sup>190,191</sup>.

In short, the above analysis quantifies and compares catalytic performance that further lays the foundation and provides a pathway for developing better performing catalysts.

#### 4.4. Summary and Conclusions

In summary, we presented the CO<sub>2</sub> methanation reaction mechanism over Ni (111) and Ru (001) surfaces. We employed a benchmarked DFT functional and considered a comprehensive reaction network of 46 elementary reactions. The contradictions in the



reaction pathways (via CO<sub>2</sub>\* direct dissociation vs CO<sub>2</sub>\* hydrogenation, CO\* direct dissociation vs CO\* hydrogenation and with/without CO\* intermediate routes) are addressed. Our DFT calculations predicted that the CO<sub>2</sub> direct dissociation is favored compared to CO<sub>2</sub> hydrogenation on both Ni (111) and Ru (001). Additionally, CO\* hydrogenation to form HCO\* is favored on both the surfaces. Notably, the CH\* stepwise hydrogenation is kinetically and thermodynamically less favored on Ru (001) compared to Ni (111). Based on the DFT calculated energies we developed a MKM, and our microkinetic calculations predicted that Ru (001) has higher activity compared to Ni (111). It is also relatively less likely to deactivate due to CO\* deposition. However, Ni (111) is more selective than Ru (001) due to higher activation barrier for CH<sub>x</sub> hydrogenation on Ru (001). Notably, we also identified the relevant reaction steps and the dominant pathway for CO<sub>2</sub> methanation on Ni (111) and Ru (001). The dominant pathway for methanation on Ni (111) is CO<sub>2</sub>\*→CO\*→HCH\*→CH\*→CH<sub>2</sub>\*→CH<sub>3</sub>\*→CH<sub>4</sub>\* with the RDS being CHO\*→CH\*+O\*. Whereas on Ru (001), the dominant pathway is CO<sub>2</sub>\*→CO\*→COH\*→C\*→CH\*→CH<sub>2</sub>\*→CH<sub>3</sub>\*→CH<sub>4</sub>\* and the RDS is CH<sub>3</sub>\*+H\*→CH<sub>4</sub>\*. It is observed that the rate of RDS for methanation is higher on Ni (111), i.e. 5.07x10<sup>-10</sup> mol/g<sub>cat</sub>·h, compared to Ru (001), i.e. 1.02x10<sup>-13</sup> mol/g<sub>cat</sub>·h, further suggesting methanation more favored over Ni (111). We believe that the current work lays the foundation and provides a pathway for developing active and stable CO<sub>2</sub> methanation catalysts.

## Chapter 5 Investigating methane dry reforming on Ni and B promoted Ni surfaces: DFT assisted microkinetic analysis and addressing the coking problem

*Ni-based catalysts have shown good activity for DRM reaction. However, deactivation due to carbon formation is a serious concern. Several strategies are proposed, including doping by other metals and metalloids, to improve the stability of Ni, and hence we investigated boron-doped Ni (NiB) as a potential catalyst for DRM. Combined DFT and microkinetic modeling are performed to identify the dominant reaction pathways and kinetically relevant steps of the DRM reaction system on Ni and NiB surfaces. A detailed reaction network involving multiple  $\text{CO}_2$  and  $\text{CH}_4$  dissociation routes, side reactions ( $\text{H}_2\text{O}$  formation, Boudouard reaction) and desorption of products is considered on both surfaces. The DFT calculations suggest that both Ni and NiB share similar  $\text{CO}_2$  (direct dissociation to  $\text{CO}^*$ ) and  $\text{CH}_4$  (sequential dehydrogenation to  $\text{C}^*$ ) activation routes. Compared to Ni, the  $\text{CO}_2$  activation barrier on NiB is higher by 44 kJ/mol but the barriers in  $\text{CH}_4$  activation routes are significantly lower. Subsequently, the DFT-calculated energies were used to develop a microkinetic model of the DRM process over Ni (111) and NiB catalysts. It was observed that the dominant pathway on Ni causes carbon formation on the catalyst surface. Whereas the dominant reaction pathway on NiB includes  $\text{CH}_2^*$  oxidation, which prevents carbon formation, making it a more stable catalyst. Furthermore, the forward rate constant of Boudouard reaction ( $\text{CO}_2^* + \text{C}^* \rightarrow 2\text{CO}^*$ ) was significantly higher on NiB and hence the carbon formed is consumed at a faster rate. Thus, NiB is a potential catalyst that can resist deactivation during the DRM process.*

## 5.1 Introduction

### 5.1.1 Dry reforming of methane and potential catalysts

As mentioned in the introduction of this thesis, dry reforming of methane (DRM) converts two greenhouse gases, CH<sub>4</sub> and CO<sub>2</sub>, to syngas (H<sub>2</sub>/CO ratio of 1:1) that can further be used in Fischer-Tropsch synthesis to produce long-chain hydrocarbons. Transition metals such as Pt, Pd, Ru, Rh, Ir, and Ni have shown good catalytic activity for this reaction<sup>66,70</sup>. Wei and Iglesia<sup>71</sup> compared DRM turnover rates on Pt, Ru, Rh, Ir and Ni catalysts. They found that these rates are higher on noble metals compared to Ni catalyst<sup>71</sup>. Even though noble metals are more active and selective, Ni-based catalysts are viable, considering their low cost and availability<sup>62,66,72</sup>.

### 5.1.2 Effect of promoters on Ni catalyst performance for DRM

A serious concern for the Ni-based catalysts is deactivation due to carbon deposition<sup>73,74,192</sup>. For improving the stability of Ni catalysts, several strategies were proposed, including doping by other metals and metalloids<sup>75–79,193</sup>. The addition of promoters, however, often leads to a trade-off between catalyst activity and stability. Recently, Chen et al.<sup>194</sup> proposed that an ideal catalyst for DRM must have lower CO<sub>2</sub> and CH<sub>4</sub> dissociation barriers. Bengaard et al.<sup>77</sup> studied the effect of K doping on Ni (111) and Ni (100) surfaces. DFT calculations showed that the CH<sub>4</sub> dissociation barrier increased by ~20 kJ/mol on K doped Ni surfaces<sup>77</sup>. Hardly any breakthrough has come in improving the stability of Ni-based catalysts because it was done more or less arbitrarily without comprehensive understanding at molecular and process levels. Through several computational and experimental studies, Xu et al.<sup>80–82</sup> showed that boron doping improves the stability of Ni catalysts without downgrading activity. Based on scanning electron microscopy (SEM) and temperature-programmed oxidation (TPO), it was shown that the amount of deposited carbon reduced by 80%<sup>81</sup>. Moreover, DFT studies show that the CH<sub>4</sub> activation barrier is lower by 27 kJ/mol on NiB surface compared to Ni (111) surface

<sup>82</sup>. Thus, NiB can be a potential catalyst for DRM. However, for employing NiB to study DRM necessitates the fundamental understanding of the elementary reaction steps and reaction energetics in the conversion of CO<sub>2</sub> and CH<sub>4</sub> to syngas on Ni and on NiB. To the best of our knowledge, there are no computational studies reported in the literature that investigate NiB as a potential catalyst for the DRM reaction. To evaluate the effects of B doping, it is essential to comprehensively study DRM reaction on clean Ni first and then compare the changes in the reaction pathways and energetics due to B doping.

### 5.1.3 DRM reaction mechanism

DRM reaction network is complex as it involves a large number of elementary reactions that can be grouped under three reaction categories: i) CH<sub>4</sub> stepwise dehydrogenation, ii) formation of surface oxidants (O\*/OH\*, where \* represents metal surface), and iii) CH<sub>x</sub> oxidation <sup>83</sup>. Typically, on Ni (111), the computed activation barriers for the dissociation of CH<sub>4</sub> to CH<sub>3</sub>\* and CH\* to C\* were substantially higher compared to other steps and CH\* dehydrogenation had a larger barrier than CH<sub>4</sub> dissociation <sup>84–86</sup>. However, Wei et al. <sup>71</sup> performed isotopic tracing and exchange measurements and proposed that CH<sub>4</sub> dissociation was the rate-determining step (RDS) in DRM. In addition, Li et al. <sup>85</sup> confirmed that sequential dehydrogenation was favored (both thermodynamically and kinetically) over bimolecular reactions, and that production of gas-phase C<sub>2</sub> hydrocarbon species was highly unlikely. The sequential dehydrogenation of CH<sub>4</sub> leads to the formation of surface carbon that deactivates nickel catalysts by blocking reactive sites and also diffusing into Ni, forming nickel carbide <sup>73,74</sup>.

Very little is known about the subsequent oxidation of CH<sub>x</sub> by surface O\*/OH\*. The oxidants can also be the key decoking media via reactions with surface carbon. In DRM, these oxidants are generated from the dissociation of CO<sub>2</sub>. Various CO<sub>2</sub> dissociation routes (direct dissociation and H-assisted transformation via COOH\*/HCOO\* intermediate) are studied and the direct decomposition of CO<sub>2</sub>\* to CO\* and O\* is proposed to be the dominant CO<sub>2</sub> conversion route on Ni (111) <sup>87,88</sup>.

Hence,  $O^*$  is suggested to be the major oxidizing agent generated from  $CO_2$ . However, Zhu et al.<sup>87</sup> reported a barrier of 129 kJ/mol for forming  $OH^*$  from  $O^*$ , and hence both  $OH^*$  and  $O^*$  can be present during the DRM reaction.

Among the different oxidation routes by  $O^*$  and  $OH^*$ ,  $CH_3^*$  and  $CH_2^*$  oxidation reactions are suggested to be kinetically and thermodynamically impeded and only  $CH^*$  and  $C^*$  oxidation steps are kinetically feasible reactions<sup>64,84,86,87</sup>. It is interesting to note that often the  $CH^*/C^*$  oxidation step is described as the rate-determining step. Interestingly, Fan et al.<sup>64</sup> considered three possible dominant reaction pathways ( $C^*$  oxidation by  $O^*$  and  $OH^*$  and  $CH^*$  oxidation by  $O^*$ ) and the contribution of each path was calculated to be 73.1%, 8.4% and 18.5% respectively, indicating that  $C^*$  oxidation by  $O^*$  is the dominant reaction path.

#### 5.1.4 Challenges in DRM

The methane reforming pathway involves decomposition of  $CH_4$  to form  $CH^*$  or  $C^*$  followed by  $O^*/OH^*$  oxidation and, finally, formation of  $CO^*$ . However, the RDS in DRM is still debated. Some authors describe  $CH_4$  dissociation as the RDS<sup>71</sup> whereas other studies have shown the reactions of  $C^*/CH^*$  oxidation by  $O^*/OH^*$  as the RDS<sup>64</sup>. This inconsistency in the RDS reported in various studies appears to result from the intricacy of the DRM reaction network, making the experimental/computational predictions extremely challenging. In addition, the barriers for  $C^*/CH^*$  oxidation by  $O^*/OH^*$  are closer and hence the differences in theory level employed in different DFT studies may have resulted in different predictions for the RDS by different groups. It was observed that a small deviation in the DFT-predicted barriers and reaction energies affected the results of the microkinetic model significantly<sup>106</sup>. Thus, accuracy of DFT prediction is vital and it predominantly depends on the approximated exchange-correlation functional<sup>146</sup>. Selection of accurate functional is ignored in the majority of the to date DFT studies on DRM and popular functionals such as PBE and PW-91 are employed<sup>87,140</sup>. Additionally, insights about the reaction pathways that control catalyst performance at any given reaction operating conditions can only be obtained by combining DFT

with microkinetic modelling. However, only a few DFT studies reported in the literature are extended to develop a microkinetic model. Another key observation is that the number of reactions included in various studies are different and Boudouard reaction, identified as a potential carbon source, and other side reactions had not been considered in the majority of DFT studies reported to date. Thus, we conclude that the existing DFT studies on DRM are inaccurate, based on incomplete reaction networks, and must have corrections applied before using results of DFT simulations in microkinetic modeling.

In this study, we performed a combined DFT and microkinetic modeling to identify the dominant reaction pathways and kinetically relevant steps of the DRM reaction system on Ni (111) and NiB surfaces. We considered a comprehensive reaction network of 38 elementary reactions (including possible side reactions) and combined DFT and microkinetic model with different operating conditions to explain the effect of operating conditions on RDS. The (111) facet of Ni was selected as it is the lowest energy facet and usually dominates the surface<sup>179</sup>. Based on the benchmarking studies<sup>178</sup> presented in *chapter 3* of the thesis, rPBE-vdW functional with a correction of 28 kJ/mol for gas-phase CO<sub>2</sub> energy is employed for studying this reaction. rPBE-vdW functional was identified as the only functional that predicts both CO<sub>2</sub> and CO adsorption correctly<sup>178</sup>. The dominant reaction pathways were identified on Ni (111) and NiB surfaces.

In Section 5.2, details of computational methods and the simulation system are discussed. Multiple pathways for activation of CO<sub>2</sub> and CH<sub>4</sub> are presented on Ni (111) and NiB surfaces. The DFT calculated activation barriers along with free energy values are reported in Section 5.3, along with the results from the microkinetic study. The key findings from this study are summarized in Section 5.4.

## 5.2. Computational details

### 5.2.1 DFT calculations

Vienna *ab initio* Simulation Package (VASP) was used to perform all DFT calculations. The interaction between valence electron and ions was described using projector augmented wave (PAW) method. Periodic spin-polarized calculations were performed with a plane wave cut-off energy of 450 eV and a k-points sampling of 3x3x1 with Monkhorst-pack scheme. Energy convergence criteria of  $10^{-6}$  eV/Å per unit cell and a force tolerance of 0.05 eV/Å were employed to ensure high level of accuracy.

Generalized gradient approximation (GGA) based exchange-correlation functional is employed in the formulation of rPBE-vdW functional based on the previous benchmarking studies presented in *Chapter 3* <sup>178</sup>. Based on the activation barrier and DFT-simulated XPS shift calculations rPBE-vdW functional was identified as the best available choice of functional for studying CO<sub>2</sub> conversion reactions <sup>178</sup>. Ni and B-doped Ni surfaces were modeled by considering the most stable (111) facet using 4- or 5- layer, p (4x4) unit cell. On NiB surface, boron occupies the subsurface octahedral sites present in Ni and the strong interaction between neighboring boron atoms leads to the surface reconstruction of Ni atoms and it begins to resemble a stepped surface as shown in Figure 5. 1. Details about the structure (location of boron promotion) and stability of NiB surface is given in appendix to chapter 5. To avoid interaction with the adjacent cell in the z-direction, an inter-slab distance of 12 Å was added. The bottom two layers were fixed in all our calculations.

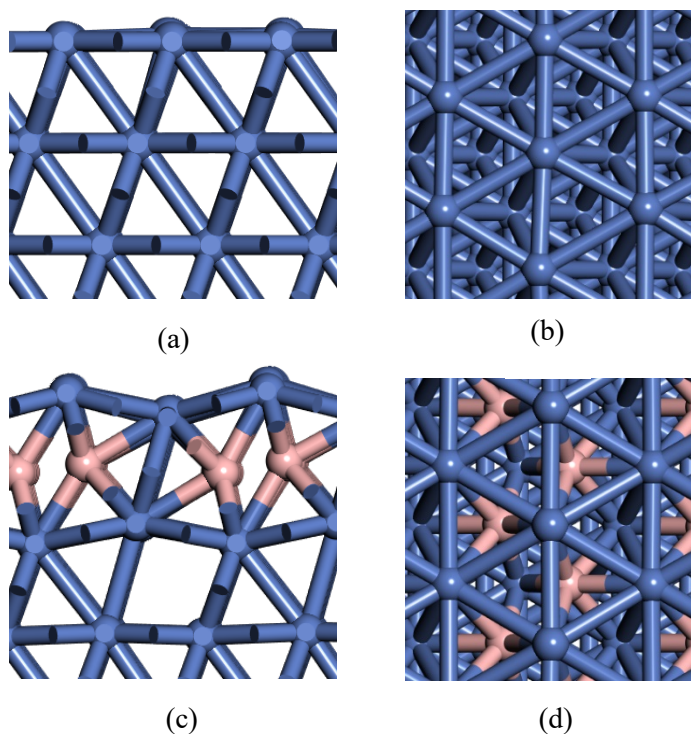


**Figure 5. 1** Structure of Ni (111) (side (a) and top (b) view) and Ni with subsurface B after reconstruction (side (a) and top (b) view). Ni atoms are represented as blue balls and B in salmon.

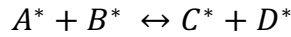
The transition state (TS) for all reactions were calculated using the Nudged Elastic Band (NEB) method. 8-12 images were used in NEB and the NEB image closest to TS was optimized using the quasi-Newton algorithm. Besides, vibrational frequency analysis was performed to confirm TS. We calculated zero-point energy and thermodynamic corrections at pertinent experimental conditions. The enthalpy corrections for gas-phase molecules are taken from thermodynamic tables while we employed statistical thermodynamics using vibrational partition function for the adsorbed system. All the reaction energies and activation barriers are reported as Gibbs free energy change. We considered reactants/products in separate unit cell and reaction free energy,  $G_r$ , is calculated as  $G_r = G_{\text{tot}}(\text{FS}) - G_{\text{tot}}(\text{IS})$ , with FS and IS referring to final and initial state structures. The corresponding activation barrier,  $G_a$ , is calculated as  $G_a = G_{\text{tot}}(\text{TS}) - G_{\text{tot}}(\text{IS})$ , with TS referring to transition state structure.



### 5.2.2 Microkinetic model

The simulations are based on a previously proposed model of the dry reforming process over Ni surface <sup>64</sup>. The model reported a list of 33 relevant elementary reaction steps whose kinetic rate constants are evaluated based on the DFT data using the transition state theory <sup>64,87</sup>. We employed the same methodology to generate values of rate constants for each elementary reaction step. Once the rate constants are known the elementary rate equations are written.

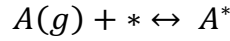
Consider the surface reaction



The forward rates are computed for a given reaction condition using the following equation

$$r_f = (k_{f,r_i} \theta_A \theta_B) \times N_{\text{site,total}} \quad (5.1)$$

where,  $r_f$  is the forward reaction rate in mol/g<sub>cat</sub>·s,  $k_{f,r_i}$  is the forward reaction rate constant in s<sup>-1</sup>,  $\theta_A$  and  $\theta_B$  are the fractional coverages of species A and B,  $N_{\text{site,total}}$  is the total number of active sites in mol/g<sub>cat</sub>. If the reacting species is in gas phase



then the forward rates are given as

$$r_f = k_{f,r_i} \times \frac{P_A}{P_{\text{std}}} \times \theta^* \times N_{\text{site,total}} \quad (5.2)$$

where,  $\theta^*$  is the fractional surface coverage of the free site,  $P_A$  is the partial pressure of A and  $P_{\text{std}}$  1 bar. The backward reaction rates are also written in a similar fashion as equation (5.1) for surface reactants and equation (5.2) for gas phase reactants. The rate constants in equation (5.1) and (5.2) respectively are computed using transition state theory (equation 5.3).

$$k_f = k_B T/h \exp \left[ \frac{-\Delta G_{\text{act},f}}{RT} \right] \quad (5.3)$$

where,  $k_B$  is the Boltzmann constant,  $h$  is the Planck's constant,  $R$  is the universal gas constant,  $T$  is the reaction temperature and  $\Delta G_{\text{act},f}$  is the Gibbs free energy of activation step computed after adding temperature and entropic corrections to the

DFT generated energies. Further details on evaluating these rate constants and Gibbs energies are mentioned in the appendix.

Once the rate constants are computed, the rate equations are evaluated and are then assembled for each species to generate differential equations of species balance. Considering an ideal PFR reactor as a reasonable simplification for a typical fixed-bed reactor, the reactants conversions are also written from the differential equations of reactant balance.

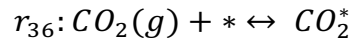
$$\frac{d\theta_j}{d\left(\frac{W}{F_0}\right)} = \sum_i^{\# \text{ of reactions}} \sigma_{i,j} r_i \quad (5.4)$$

where,  $W$  is the weight of catalyst in g,  $F_0$  is the total molar flow rate of gases in  $\text{mol}\cdot\text{h}^{-1}$ ,  $\sigma_{i,j}$  is the stoichiometric coefficient of species  $j$  in reaction  $i$ ,  $r_i$  is the rate of reaction  $i$  and  $\theta_j$  is the surface coverage of species  $j$

$$\frac{dx_{CH_4}}{d\left(\frac{W}{F_{CH_4}}\right)} = r_1 \quad (5.5)$$

$$\frac{dx_{CO_2}}{d\left(\frac{W}{F_{CO_2}}\right)} = r_{36} \quad (5.6)$$

where,  $x_{CH_4}$  and  $x_{CO_2}$  are conversions of gaseous reactants  $CH_4$  and  $CO_2$  and  $r_{CH_4}$  and  $r_{CO_2}$  are their respective rates of adsorption on the catalyst surface:



The surface coverages are obtained as a function of space-time by solving the above system of differential equations; solution was obtained using the MATLAB-implemented ode-solver ode15s. The partial pressure of the gaseous species is evaluated using expressions that were previously reported <sup>64</sup>.

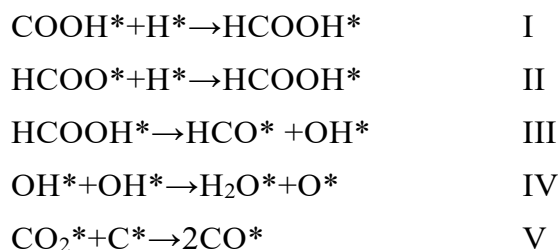
Herein, we re-compute the results of the previous model<sup>64</sup> since it is the most extensive DFT based microkinetic study of DRM available in the open literature. We then propose an extension of the model, which includes further elementary reactions and DFT corrections, to demonstrate the effects of the choice of DFT functional and inclusion of side reactions. Table 5. 1 enlists the specifications of the microkinetic model developed in this study. It should be noted that our model is

constructed and refined based on a study of a series of models that differ in the number of elementary reaction steps and DFT corrections used, and validated against experimental data <sup>195</sup>.

**Table 5. 1** Different model specifications based on the values of DFT functionals, corrections, elementary reactions, and standard pressure.

Specification	Literature model <sup>64</sup>	This work
DFT functional	PBE <sup>124</sup>	rPBE-vdW <sup>128</sup>
Dispersion correction <sup>196</sup>	No	Yes
Number of elementary steps	33	38
P <sub>std</sub>	1 Pa	10 <sup>5</sup> Pa

The following five extra reactions are included in this study in addition to the 33 reactions in the literature model <sup>64</sup>: reactions I-III are second hydrogenation of CO<sub>2</sub>, IV is a possible side reaction and reaction V is the Boudouard reaction.



Following assumptions were made while constructing the microkinetic models

1. Each site can be occupied by at most one adsorbate. This is referred to as the "exclusion principle".
2. All catalytic sites are equivalent, and any surface species has the same "stability" (quantified by the binding energy) at any site on the surface. Consequently, the probability of finding any site occupied by a species is equal to its fractional surface coverage.
3. No spatial correlations are observed between adsorbates.
4. Kinetic constants are independent of coverage

5. The gradient of temperature and pressure along the catalyst bed is negligible.

### 5.2.3 Rate determining step

After developing the microkinetic model for the methane dry reforming process, further analysis is performed using this model to identify the rate determining step (RDS). The previously reported studies<sup>95,181,183</sup> have employed the sensitivity analysis and partial equilibrium analysis criteria<sup>183,197</sup> on their respective microkinetic models to identify the RDS and the kinetically relevant steps for the WGS reaction on Pt<sup>95</sup> and Ni<sup>181</sup>, and for the WGS, steam and dry reforming reactions over Rh<sup>183</sup>. Here, a similar strategy was applied to identify the kinetically relevant steps from the list of all considered elementary reactions over Ni (111) and B-doped Ni. The sensitivity analysis identifies the most sensitive reaction steps towards product formation. These reaction steps are candidates for RDS. The partial equilibrium analysis then eliminates the candidate reaction steps that are in equilibrium. Knowing that the overall reaction is in not equilibrium at the given reaction condition, its RDS cannot be in equilibrium.

The sensitivity analysis (SA) and partial equilibrium analysis were performed on the microkinetic model and the rate-determining steps for different reaction conditions were predicted. The partial equilibrium (PE) coefficient ( $\varphi_j$ ) of each reaction  $j$  is evaluated using the following expression (5.7)

$$\varphi_j = \frac{r_j^f}{r_j^f + r_j^b} \quad (5.7)$$

where,  $r_j^f$ ,  $r_j^b$  are the forward and backward rates of the  $j^{\text{th}}$  elementary reaction. Whereas the sensitivity coefficients of each reaction steps were computed by applying a small perturbation ( $\frac{\Delta k_j}{k_j} = 5\%$ ) to the rate constant ( $k_j$ ) of each step  $j$  separately, and a series of simulations were carried out to observe the influence on a selected model response ( $M_k$ ), e.g. the reactant fractional conversion. Given that rate constants of different elementary steps are over several orders of magnitude

higher than the model responses, a sensitivity coefficient is defined for each reaction  $j$  using the following expression (5.8),

$$S_{k,j} = \frac{\partial \ln M_k}{\partial \ln k_j} \approx \frac{\Delta M_k k_j}{M_k \Delta k_j} \quad (5.8)$$

where  $S_{k,j}$  is the sensitivity coefficient and  $M_k$  is the model response for the  $k^{\text{th}}$  variable. This analysis is carried out to identify the kinetically relevant steps of the reaction on Ni (111) and B-doped Ni catalyst surfaces.

Since RDS of the DRM reaction process is debatable and depends on reaction conditions and the choice of a catalyst, we also performed simulations over a wide range of reaction conditions on Ni (111) surface in order to identify the different kinetically relevant steps for each reaction conditions. As the DRM reaction is highly endothermic, high reaction temperatures were selected for the sensitivity analysis i.e. 873 K, 973 K, and 1073 K. Moreover, the sensitivity coefficients were computed for different reaction pressures and inlet feed ratios (reactants vs inert gas) taken from experimental studies. Details of these reaction conditions (or cases) and their results are given in the appendix to chapter 5.

## 5.3 Results and Discussion

### 5.3.1 DFT study of DRM on Ni (111) and NiB

DRM reaction network in the current study includes  $\text{CH}_4$  sequential dehydrogenation routes,  $\text{CO}_2$  dissociation routes,  $\text{CH}_x$  ( $x = 0$  to 3) oxidation by  $\text{OH}^*$  and  $\text{O}^*$  routes, other side reactions ( $\text{H}_2\text{O}$  formation, Boudouard reaction) and desorption of products (*cf* Figure 5. 2 and Table 5. 2). All these reactions are studied on Ni and NiB surfaces and are presented in the following sub-sections. We report the reaction energy and reaction barriers as Gibbs free energy change (unless otherwise stated). Since majority of the published articles only report electronic energies, we compared the electronic energy barrier for different reactions with previous works (to validate) and reported in appendix to chapter 5. The reaction

energies and activation barriers (free energy) of all the elementary reactions on Ni (111) and NiB are listed in Table 5. 2.

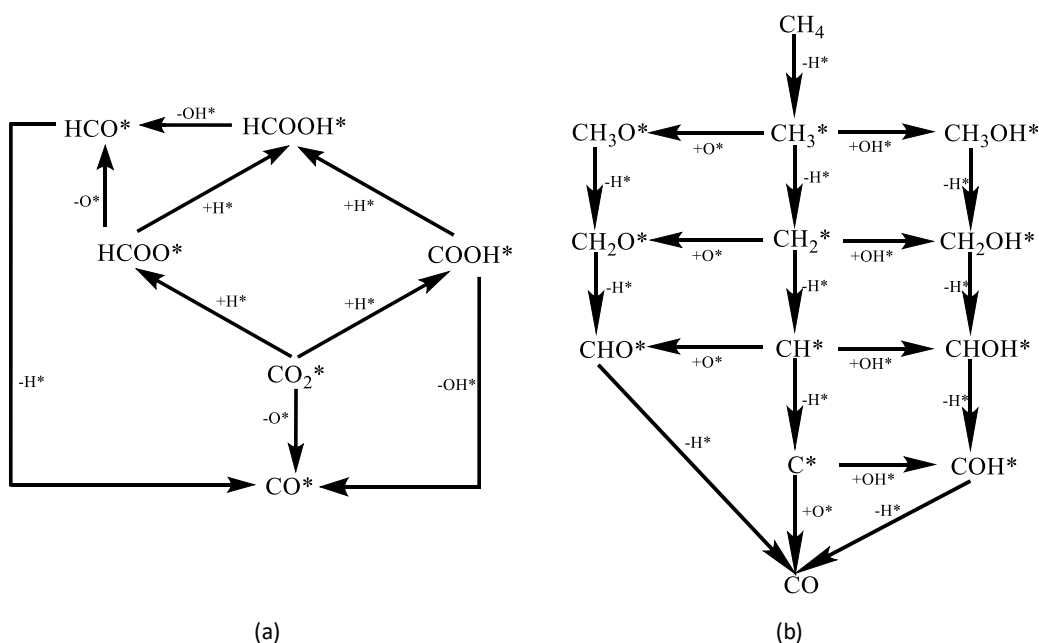


**Figure 5. 2** (a) CO<sub>2</sub> dissociation routes and (b) CH<sub>4</sub> sequential dehydrogenation routes and CH<sub>x</sub> (x = 0 to 3) oxidation by OH\* and O\* routes. Also, note that the microkinetic model takes into account all of these reactions as reversible

**Table 5. 2** Calculated free energy barriers and reaction free energies (973K and 10 bar pressure) of all elementary reactions for DRM on Ni (111) and NiB surfaces. The reactions include CH<sub>4</sub> sequential dehydrogenation routes, CO<sub>2</sub> dissociation routes, CH<sub>x</sub> (x = 0 to 3) oxidation by OH\* and O\* routes, other side reactions (H<sub>2</sub>O formation, Boudouard reaction) and desorption of products. Though not shown as reversible reactions here, the microkinetic model takes into account all of these reactions as reversible.

Reaction		Activation barrier (kJ/mol)		Reaction free energy (kJ/mol)	
		Ni (111)	NiB	Ni (111)	NiB
R1	CH <sub>4</sub> →CH <sub>3</sub> *+H*	164	107	83	55
R2	CH <sub>3</sub> *→CH <sub>2</sub> *+H*	58	87	5	62
R3	CH <sub>2</sub> *→CH*+H*	35	56	-25	13

R4	$\text{CH}^* \rightarrow \text{C}^* + \text{H}^*$	126	96	41	55
R5	$\text{CO}_2^* \rightarrow \text{CO}^* + \text{O}^*$	63	107	-101	-48
R6	$\text{CO}_2^* + \text{H}^* \rightarrow \text{COOH}^*$	112	143	30	26
R7	$\text{CO}_2^* + \text{H}^* \rightarrow \text{HCOO}^*$	69	61	-18	-54
R8	$\text{COOH}^* \rightarrow \text{CO}^* + \text{OH}^*$	7	59	-120	-120
R9	$\text{HCOO}^* \rightarrow \text{HCO}^* + \text{O}^*$	148	226	45	113
R10	$\text{HCO}^* \rightarrow \text{CO}^* + \text{H}^*$	14	13	-126	-107
R11	$\text{COOH}^* + \text{H}^* \rightarrow \text{HCOOH}^*$	82	89	11	27
R12	$\text{HCOO}^* + \text{H}^* \rightarrow \text{HCOOH}^*$	104	132	60	107
R13	$\text{HCOOH}^* \rightarrow \text{HCO}^* + \text{OH}^*$	63	72	-5	-39
R14	$\text{CH}_3\text{OH}^* \rightarrow \text{CH}_2\text{OH}^* + \text{H}^*$	143	113	60	45
R15	$\text{CH}_2\text{OH}^* \rightarrow \text{CHOH}^* + \text{H}^*$	72	72	-19	11
R16	$\text{CHOH}^* \rightarrow \text{COH}^* + \text{H}^*$	20	65	-69	18
R17	$\text{COH}^* \rightarrow \text{CO}^* + \text{H}^*$	100	72	-112	-176
R18	$\text{CH}_3^* + \text{OH}^* \rightarrow \text{CH}_3\text{OH}^*$	182	218	18	63
R19	$\text{CH}_2^* + \text{OH}^* \rightarrow \text{CH}_2\text{OH}^*$	133	94	73	45
R20	$\text{CH}^* + \text{OH}^* \rightarrow \text{CHOH}^*$	137	146	79	44
R21	$\text{C}^* + \text{OH}^* \rightarrow \text{COH}^*$	133	139	-30	7
R22	$\text{CH}_3\text{O}^* \rightarrow \text{CH}_2\text{O}^* + \text{H}^*$	102	89	46	42
R23	$\text{CH}_2\text{O}^* \rightarrow \text{CHO}^* + \text{H}^*$	34	43	-37	-14
R24	$\text{CH}_3^* + \text{O}^* \rightarrow \text{CH}_3\text{O}^*$	130	151	6	-5
R25	$\text{CH}_2^* + \text{O}^* \rightarrow \text{CH}_2\text{O}^*$	132	102	47	-26
R26	$\text{CH}^* + \text{O}^* \rightarrow \text{CHO}^*$	142	158	35	-53
R27	$\text{C}^* + \text{O}^* \rightarrow \text{CO}^*$	156	159	-131	-215
R28	$\text{CH}_3\text{OH}^* + ^* \rightarrow \text{CH}_3\text{O}^* + \text{H}^*$	97	87	-23	-23
R29	$\text{CH}_2\text{OH}^* + ^* \rightarrow \text{CH}_2\text{O}^* + \text{H}^*$	70	96	-37	-26
R30	$\text{CHOH}^* + ^* \rightarrow \text{HCO}^* + \text{H}^*$	57	72	-54	-51
R31	$\text{O}^* + \text{H}^* \rightarrow \text{OH}^*$	114	117	10	-45
R32	$\text{OH}^* + \text{H}^* \rightarrow \text{H}_2\text{O}^*$	125	121	18	14
R33	$\text{H}^* + \text{H}^* \rightarrow \text{H}_2$	57	58	-39	-54
R34	$\text{OH}^* + \text{OH}^* \rightarrow \text{H}_2\text{O}^* + \text{O}^*$	89	113	8	59

R35	$\text{CO}_2^* + \text{C}^* \rightarrow 2\text{CO}^*$	154	132	-232	-263
R36	$\text{CO}_2 \rightarrow \text{CO}_2^*$	-	-	99	58
R37	$\text{CO}^* \rightarrow \text{CO}$	-	-	25	33
R38	$\text{H}_2\text{O}^* \rightarrow \text{H}_2\text{O} + *$	-	-	-59	-32

#### 5.3.1.1 CH<sub>4</sub> stepwise dehydrogenation (R1 - R4)

Methane activation is anticipated to occur irrespective of the presence of CO<sub>2</sub><sup>71</sup>. CH<sub>4</sub> adsorbs very weakly on Ni (111) surface with binding energy (electronic energy) of -12 kJ/mol which is in close agreement with the computed value (-20 kJ/mol) predicted by Han et al.<sup>84</sup>. The stepwise dehydrogenation of CH<sub>4</sub> to surface methyl (CH<sub>3</sub>\*), methyldene (CH<sub>2</sub>\*), methyne (CH\*) and carbon/coke (C\*) is studied and the free energy diagram is shown in Figure 5. 3. CH<sub>4</sub> dehydrogenation to CH<sub>3</sub>\* and H\* has the highest free energy barrier (164 kJ/mol) and this reaction is endergonic with reaction free energy of 83 kJ/mol. The dehydrogenation of CH<sub>2</sub>\* to CH\* is the only exergonic reaction (reaction free energy of -25 kJ/mol) and has the lowest free energy barrier (35 kJ/mol), making it thermodynamically and kinetically favorable reaction. C\* formation on Ni (111) must overcome a barrier of 126 kJ/mol and this reaction is also endergonic with reaction free energy of 41 kJ/mol.

On NiB surface, CH<sub>4</sub> adsorbs with similar binding energy (electronic energy) of -12 kJ/mol. However, the activation barrier for CH<sub>4</sub> dehydrogenation to CH<sub>3</sub>\* and H\* is only 107 kJ/mol which is 57 kJ/mol lower than that on Ni (111) surface. This difference in the activation barrier is consistent with the calculated barrier by Xu et al.<sup>82</sup>. Interestingly, this reaction is less endergonic on NiB (55 kJ/mol) compared to Ni (111), which is attributed to the stronger binding of CH<sub>3</sub>\* and H\* on NiB surface compared to Ni (111) surface (*cf* Table 5. 2). On NiB surface all the dehydrogenation steps are endergonic. The subsequent dehydrogenation of CH<sub>3</sub>\* to CH<sub>2</sub>\* is more endergonic (62 kJ/mol) with a slight increase in the barrier (87 kJ/mol) on NiB surface compared to Ni (111) surface. CH<sub>2</sub>\* dehydrogenation to CH\* has the lowest free energy barrier (56 kJ/mol) and is slightly endergonic. For CH\* dehydrogenation to C\*, the reaction free energy is slightly higher on NiB (55 kJ/mol). However, the



CH\* dissociation barrier is much lower (96 kJ/mol) than that on Ni (111). In addition, because of the comparatively higher barrier for CH\* dehydrogenation on both Ni (111) and NiB, CH\* coverage is expected to be relatively higher than CH<sub>2</sub>\* and CH<sub>3</sub>\* coverages. Interestingly, the overall reaction energy on NiB is 186 kJ/mol which is 82 kJ/mol more than that on Ni (111) surface. This high overall reaction energy may change the CH<sub>4</sub> activation route via the sequential dehydrogenation (to form C\*) on NiB surface and subsequently can have an effect on the carbon coverages.

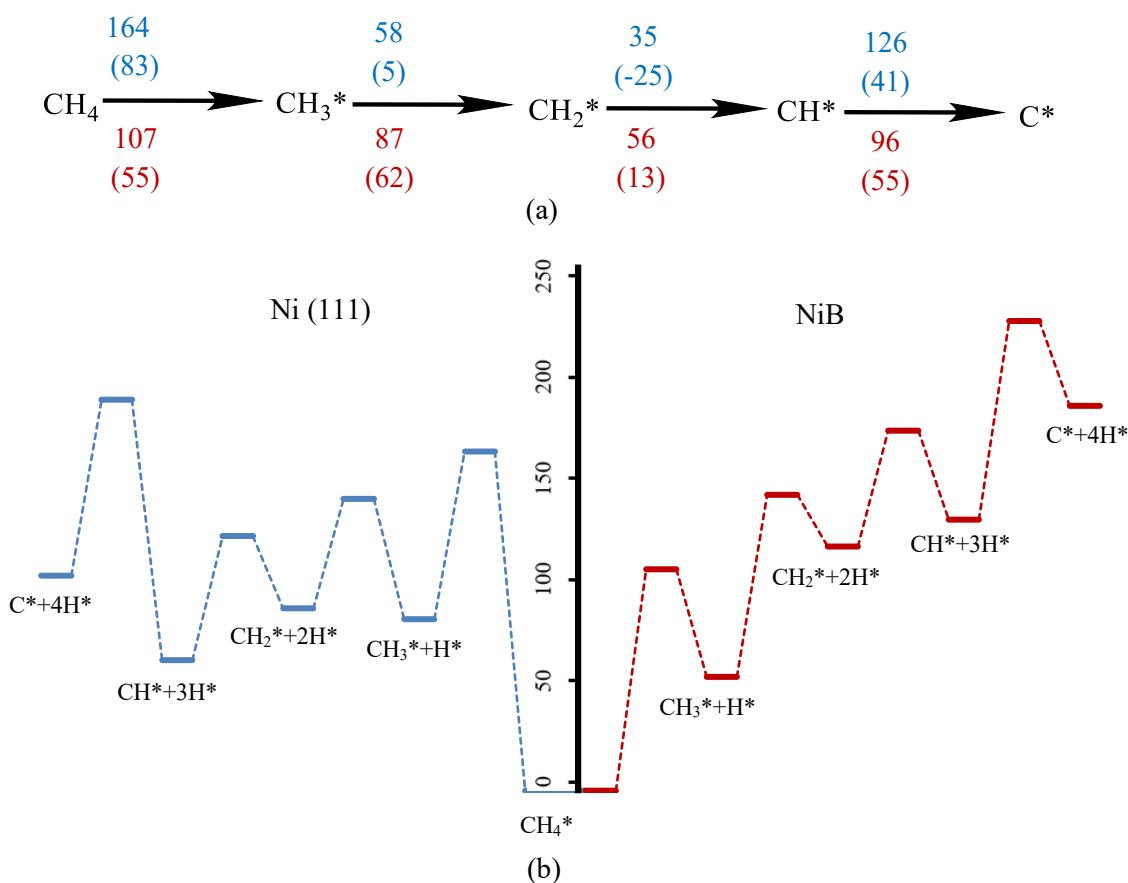


**Figure 5. 3** Methane dissociation on Ni (111) and NiB. (a) Free energy barriers and reaction free energies (inside brackets) and (b) free energy profile for sequential dehydrogenation of CH<sub>4</sub> to C\*. Free energies on Ni (111) and NiB are presented in blue and red color respectively.

To summarize, the  $\text{CH}_4$  and  $\text{CH}^*$  dissociation barriers are substantially higher on both Ni (111) and NiB surfaces compared to other steps. In addition, on NiB surface the  $\text{CH}_4$  and  $\text{CH}^*$  dissociation barriers are lower by 57 kJ/mol and 30 kJ/mol respectively compared to Ni (111).

#### 5.3.1.2 $\text{CO}_2$ activation mechanism

Two key routes are possible for the conversion of  $\text{CO}_2$  to  $\text{CO}^*$  and  $\text{O}^*$ : i) direct dissociation of  $\text{CO}_2$  and ii)  $\text{H}^*$ -mediated formate route. We analyze both these routes on Ni (111) and NiB surfaces and the corresponding free energy profiles are shown in Figure 5. 4.

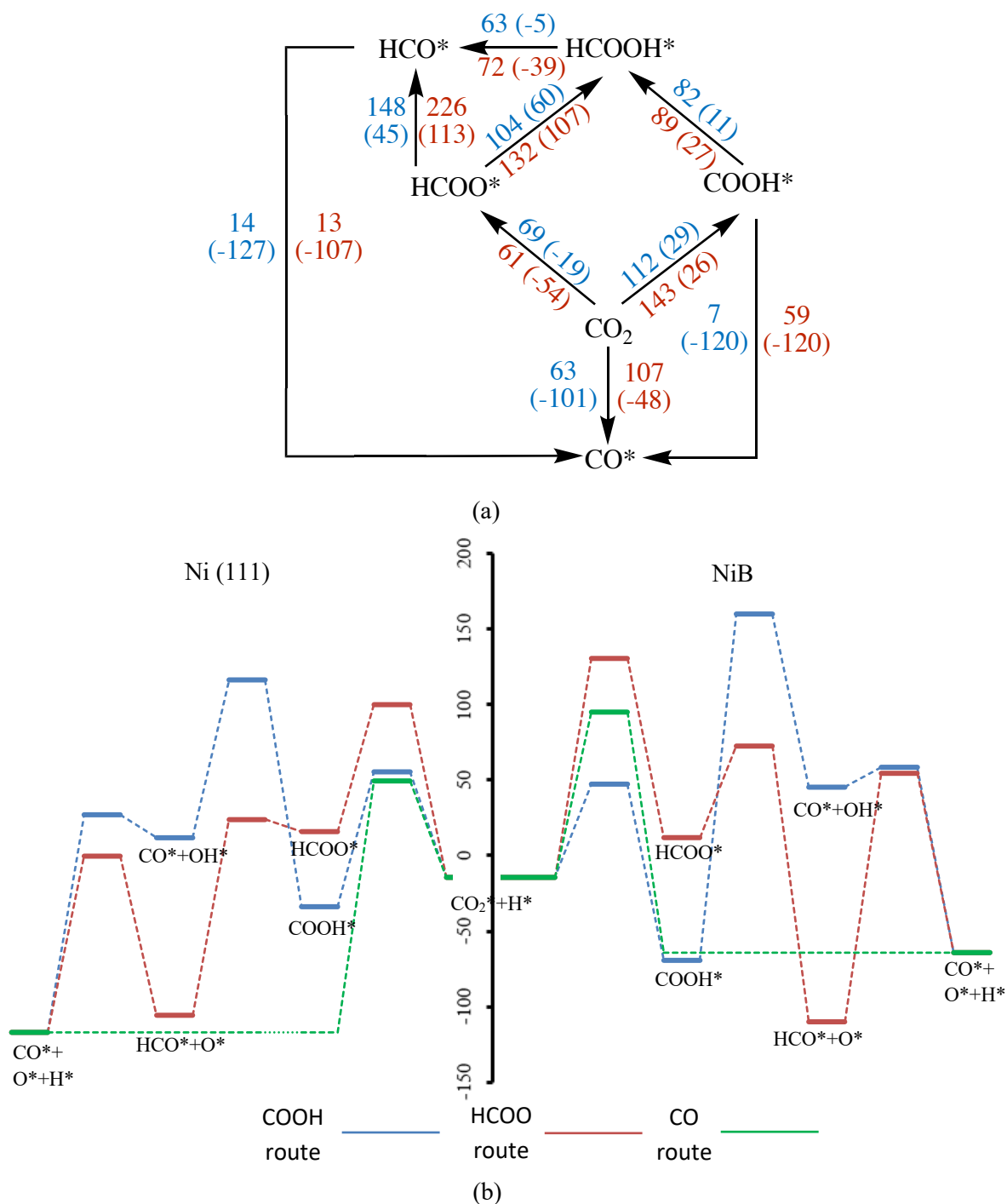


**Figure 5. 4**  $\text{CO}_2$  activation and dissociation on Ni (111) and NiB. (a) Free energy barriers and reaction free energies (inside brackets), (b) free energy profile for different  $\text{CO}_2$  activation routes. In (a), barriers and energies on Ni (111) and NiB are shown in blue and red color respectively. The green, blue and orange lines in (b) indicate direct dissociation,  $\text{COOH}^*$  route and  $\text{HCOO}^*$  route, respectively.

CO<sub>2</sub> adsorption and direct dissociation (R36, R5)

The most stable configuration of chemisorbed CO<sub>2</sub> on Ni (111) is shown in Figure 5. 5 a. CO<sub>2</sub> binding energy (electronic energy) on Ni (111) surface is -17 kJ/mol and it is 36 kJ/mol higher than the reported binding energy by Wang et al.<sup>88</sup>. This difference in binding energy is attributed to the choice of the functional employed. Wang et al.<sup>88</sup> employed PBE functional while we used rPBE-vdW functional with a correction of 28 kJ/mol for gas phase CO<sub>2</sub> energy. Base on the previous study (*chapter 3*) we found that rPBE-vdW functional, with a correction of 28 kJ/mol for gas phase CO<sub>2</sub> energy, is the accurate functional choice for studying CO<sub>2</sub> conversion reactions<sup>178</sup>. Moreover, several studies (including our previous study) have shown that rPBE-vdW functional is the accurate functional choice for predicting CO interactions with metal<sup>156,178</sup>.

On NiB, CO<sub>2</sub> binds with two Ni atoms present in the top layer forming two Ni-O and C prefers the bridge site between two Ni atoms (*cf* Figure 5. 5 b). Compared to Ni (111), CO<sub>2</sub> adsorbs strongly on NiB with binding energy (electronic energy) of -61 kJ/mol. This strong adsorption is due to two reasons: i) boron binds strongest at the sub-surface octahedral position of Ni transforming the flat geometry of Ni (111) to stepped geometry making it more active, ii) boron is an electron-donating species and it can transfer charge to Ni which can be further transferred to the adsorbed CO<sub>2</sub> making its adsorption stronger<sup>82</sup>.

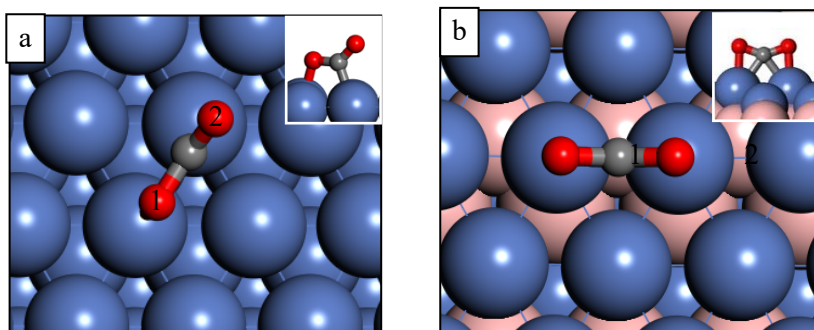


**Figure 5. 5** Most stable chemisorption configuration of CO<sub>2</sub> on a) Ni (111) and b) NiB. Blue balls represent Ni atoms, salmon balls represent B atoms, red balls represent oxygen atoms, and grey balls represents carbon atoms.

The direct dissociation of  $\text{CO}_2^*$  to  $\text{CO}^*$  on Ni (111) has a barrier of 63 kJ/mol. This reaction is highly exergonic with reaction free energy of -101 kJ/mol making it kinetically and thermodynamically feasible reaction. On NiB the direct activation barrier of  $\text{CO}_2^*$  has a moderate barrier of 107 kJ/mol. This increase in the barrier is attributed to strong binding of  $\text{CO}_2^*$  on NiB compared to Ni (111). Even though this reaction is exergonic, the reaction free energy (-48 kJ/mol) is substantially lower than that on Ni (111) surface.

#### $\text{CO}_2$ hydrogenation route (R6 – R13)

The  $\text{H}^*$  adatom generated from  $\text{CH}_4$  sequential dehydrogenation subsequently can activate  $\text{CO}_2^*$  by binding to either one of the oxygen atoms ( $\text{O}_2$  in Figure 5. 5) to form  $\text{COOH}^*$ , or to carbon atom to form  $\text{HCOO}^*$  intermediate (*cf* Figure 5. 4). On Ni (111) surface, the activation barrier and reaction free energy are calculated to be 112 kJ/mol and 30 kJ/mol respectively for forming  $\text{COOH}^*$  and 69 kJ/mol and -18 kJ/mol respectively for  $\text{HCOO}^*$  formation. The  $\text{COOH}^*$  formation barrier is much higher than the  $\text{CO}_2^*$  direct dissociation barrier. Interestingly, splitting this activated C-O bond in  $\text{COOH}^*$  (dehydroxylation of  $\text{COOH}^*$  to form  $\text{CO}^*$  (R8)) is facile with a barrier and reaction free energy of 7 kJ/mol and -120 kJ/mol, respectively. Even though this barrier is much lower, the high barrier for forming  $\text{COOH}^*$  from  $\text{CO}_2$  (compared to direct dissociation barrier) makes it a less favorable route. Formation of  $\text{HCOO}^*$  is kinetically and thermodynamically feasible. Nevertheless, dissociation of  $\text{HCOO}^*$  to  $\text{HCO}^*$  and  $\text{O}^*$  (R10) must overcome a much higher barrier of 148 kJ/mol. Interestingly,  $\text{CO}^*$  formation from  $\text{HCO}^*$  (R11) is highly exergonic with reaction free energy of -126 kJ/mol. This reaction has a lower barrier of 14 kJ/mol making it both thermodynamically and kinetically feasible reaction. However,  $\text{CO}^*$  formation via  $\text{HCOO}^*$  route is limited by the higher barrier of reaction R10. We also considered hydrogenation of  $\text{COOH}^*$  and  $\text{HCOO}^*$  to form  $\text{HCOOH}^*$  (R11, R12). The barriers for forming  $\text{HCOOH}^*$  from  $\text{COOH}^*$  and  $\text{HCOO}^*$  on Ni (111) are 82 kJ/mol and 104 kJ/mol, respectively. For the subsequent dehydroxylation of  $\text{HCOOH}^*$  to  $\text{HCO}^*$  (R13), the activation barrier is 63 kJ/mol. All these routes have a barrier higher than that for direct dissociation of  $\text{CO}_2^*$ .

On NiB surface, the activation barrier for forming COOH\* from CO<sub>2</sub>\* (R6) and subsequent dehydroxylation (R8) of COOH\* to CO\* is 143 kJ/mol and 59 kJ/mol respectively. Thus, the CO<sub>2</sub> hydrogenation barrier is higher than the CO<sub>2</sub>\* direct dissociation barrier by 36 kJ/mol. The activation barrier for forming HCOO\* from CO<sub>2</sub>\* (R7) on NiB is calculated to be 61 kJ/mol which is 46 kJ/mol lower than the barrier for direct dissociation of CO<sub>2</sub>. In addition, this reaction is exergonic with reaction free energy of -54 kJ/mol making it both kinetically and thermodynamically more feasible reaction. However, the barrier for forming HCO\* from HCOO\* (R9) has to overcome a huge barrier of 226 kJ/mol with reaction free energy of 113 kJ/mol making it both kinetically and thermodynamically challenging. This huge barrier is attributed to strong binding of HCOO\* on NiB surface. Dehydrogenation of HCO\* to form CO\* (R10) has a lower barrier of 13 kJ/mol and this reaction is highly exergonic with reaction free energy of -107 kJ/mol. However, the huge barrier and endergonicity for reaction R10 kinetically hinder the formation of HCO\*. The barriers for subsequent hydrogenation of COOH\* (R11) and HCOO\* (R12) to HCOOH\* are 89 kJ/mol and 132 kJ/mol respectively and dehydroxylation of HCOOH\* to HCO\* (R13) has to overcome a barrier of 72 kJ/mol. As mentioned before, since the barrier for forming COOH\* is high, reaction R11 may not be a preferred pathway on NiB. However, the formation of HCOO\* is both kinetically and thermodynamically feasible and, hence, HCOO\* is likely to form on NiB. Nevertheless, the barrier for hydrogenation of HCOO\* to HCOOH\* is much higher and hence CO\* formation via this route (R12 followed by R13) is also not expected. In short, comparing the activation barriers and reaction free energies for CO<sub>2</sub> direct dissociation and H-assisted route, the direct dissociation of CO<sub>2</sub>\* to CO\* is favored on both Ni (111) and NiB surface. However, the direct dissociation of CO<sub>2</sub> is less exergonic (lower by 53 kJ/mol) and the activation barrier is 44 kJ/mol higher on NiB compared to Ni (111).

### 5.3.1.3 CH<sub>x</sub> (x = 0 - 3) Oxidation (O\*/OH\*) (R18 – R21, R24 – R27)

As discussed before, direct dissociation of CO<sub>2</sub>\* to CO\* and O\* is the dominant reaction pathway for the CO<sub>2</sub> activation route. The O\* adatom thus formed can

undergo subsequent reaction with  $\text{CH}_x$  ( $x = 0 - 3$ ) species forming  $\text{CH}_x\text{O}$  ( $x = 0 - 3$ ) on the surface. In addition,  $\text{OH}^*$  formation from the hydrogenation of  $\text{O}^*$  is thermodynamically possible on Ni (111) and NiB with reaction free energy of 10 kJ/mol and -45 kJ/mol, respectively. Therefore, the  $\text{CH}_x^*$  species can undergo subsequent oxidation by  $\text{OH}^*$  adatom forming  $\text{CH}_x\text{OH}^*$ . The  $\text{CH}_x$  oxidation by  $\text{O}^*$  and  $\text{OH}^*$  on Ni and NiB surfaces are investigated, and free energies are shown in Figure 5. 6.

The barrier for the oxidation of  $\text{CH}_3^*$ ,  $\text{CH}_2$  and  $\text{CH}^*$  by  $\text{OH}^*$  (R18, R19, and R20) on Ni (111) are 182 kJ/mol, 133 kJ/mol and 137 kJ/mol respectively and for  $\text{O}^*$  oxidation (R24, R25, and R26) the barriers are 130 kJ/mol, 132 kJ/mol and 142 kJ/mol respectively. Both  $\text{O}^*$  and  $\text{OH}^*$  oxidation barriers are higher than the corresponding dehydrogenation barriers (R2, R3, and R4), and hence the formation of  $\text{C}^*$  from  $\text{CH}_4$  via dehydrogenation is kinetically favored compared to the  $\text{CH}_x^*$  ( $x = 1 - 3$ ) oxidation by  $\text{OH}^*/\text{O}^*$ . The adsorbed carbon thus formed can undergo  $\text{O}^*/\text{OH}^*$  oxidation. The barrier for  $\text{C}^*$  oxidation by  $\text{OH}^*$  (R21) and  $\text{O}^*$  (R27) is calculated to be 133 kJ/mol and 156 kJ/mol respectively. Thus, the  $\text{OH}^*$  oxidation barrier is 23 kJ/mol less than  $\text{O}^*$  oxidation barrier making it the kinetically favorable oxidation route. This finding is in excellent agreement with the previous work by Zhu et. al. <sup>87</sup>, who predicted  $\text{OH}^*$  oxidation route has a lower barrier than the  $\text{O}^*$  oxidation barrier. The  $\text{COH}^*$  thus formed undergoes dehydrogenation (R17) to form  $\text{CO}^*$  and this reaction is highly exergonic with reaction free energy of -112 kJ/mol and has to overcome a barrier of 100 kJ/mol.

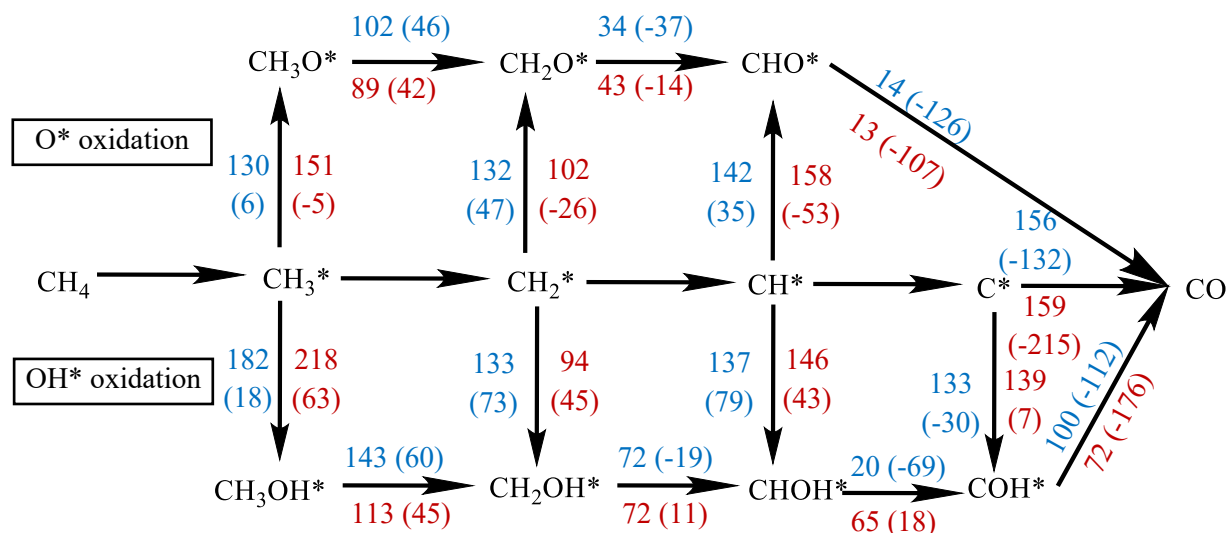


**Figure 5. 6** Free energy barriers and reaction free energies (inside brackets) for  $\text{CH}_x$  oxidation by  $\text{O}^*/\text{OH}^*$  routes. Reaction free energies and barriers on Ni (111) and NiB are presented in blue and red color, respectively.

The calculated barriers show similar trends on NiB surface also. The  $\text{CH}_3^*$ ,  $\text{CH}_2^*$  and  $\text{CH}^*$  oxidation (both  $\text{O}^*$  and  $\text{OH}^*$ ) barriers are higher than the corresponding dehydrogenation barriers (*cf* Table 5. 2 and Figure 5. 6). Interestingly, the  $\text{CH}_x^*$  oxidation barriers are higher on NiB compared to Ni (111) except for  $\text{CH}_2^*$  oxidation (both  $\text{O}^*$  and  $\text{OH}^*$ ). On NiB surface, the  $\text{C}^*$  oxidation by  $\text{O}^*$  (R27) is highly exergonic (-215 kJ/mol) with an activation barrier of 159 kJ/mol. The barrier for  $\text{C}^*$  oxidation by  $\text{OH}^*$  (R21) is calculated to be 139 kJ/mol. This reaction is slightly endergonic with reaction free energy of 7 kJ/mol. This barrier is 20 kJ/mol lower than  $\text{O}^*$  oxidation barrier on NiB and hence  $\text{OH}^*$  oxidation of  $\text{C}^*$  is kinetically favored over  $\text{O}^*$  oxidation. Interestingly, the  $\text{OH}^*$  oxidation barrier of  $\text{C}^*$  is slightly higher than the corresponding barriers on Ni (111) surface by 6 kJ/mol. The barrier (72 kJ/mol) for the subsequent dehydrogenation of  $\text{COH}^*$  (R17) on NiB is 28 kJ/mol less than that on Ni (111) surface. The reaction is even more exergonic with a reaction heat of -176 kJ/mol making this reaction kinetically and thermodynamically more feasible.



In brief, both OH\* and O\* oxidations of CH<sub>x</sub> (x = 1 – 3) have higher barriers compared to that of the dehydrogenation reaction and hence sequential dehydrogenation of CH<sub>x</sub> (x = 1 - 4) is the kinetically favored route on both Ni (111) and NiB forming C\*. Interestingly, C\* oxidation by OH\* is kinetically favored compared to O\* oxidation on both surfaces.

#### 5.3.1.4 CH<sub>x</sub>OH and CH<sub>x</sub>O (x = 1 - 3) dehydrogenation (R14 – R16, R22, R23)

The reaction free energies and activation barriers for successive dehydrogenation of CH<sub>x</sub>OH and CH<sub>x</sub>O (x = 1 - 3) on Ni (111) and NiB are discussed here, and free energies are shown in Figure 5. 6. Note that the dehydrogenation of CHO\* (R10) has been discussed in Section 3.1.2. The barriers for reactions R14, R15, R16, R22, and R23 are 143, 72, 20, 102 and 34 kJ/mol respectively on Ni (111) and 113, 72, 65, 89 and 43 kJ/mol respectively on NiB. Since the sequential dehydrogenation of CH<sub>4</sub> to C\* has a lower barrier than CH<sub>x</sub> (x = 1-3) oxidation on both Ni (111) and NiB surfaces, the CH<sub>x</sub>OH and CH<sub>x</sub>O (x = 1-3) dehydrogenation steps are not favored kinetically.

#### 5.3.1.5 Side reactions (R31, R32, R33)

Surface hydrogenation of O\* leads to the formation of OH\* (R31). The barrier and reaction free energy for this reaction on Ni (111) are 114 kJ/mol and 10 kJ/mol respectively. We considered two routes for H<sub>2</sub>O formation (R32 and R34). Both reactions are endergonic on Ni (111) surface with reaction free energies of 18 (R32) and 8 kJ/mol (R34). The activation barriers for these reactions are calculated to be 125 and 89 kJ/mol respectively. Thus, H<sub>2</sub>O\* formation via reaction R34 is favored kinetically compared to reaction R32. Notably, this reaction is not included in the majority of studies mentioned in the introduction.

Reaction R31 is exergonic on NiB surface with reaction free energy of -45 kJ/mol. Despite this, the activation barrier for OH\* formation (117 kJ/mol) is only 3 kJ/mol lower compared to Ni (111) surface. Reactions R32 and R34 must overcome barriers

of 121 and 113 kJ/mol respectively on NiB surface. Even though the barrier for reaction R34 is lower, this reaction is more endergonic with reaction free energy of 59 kJ/mol whereas reaction R32 has a lower reaction free energy of 14 kJ/mol. It is worth mentioning that H<sub>2</sub>O formation has a higher barrier on NiB than Ni (111).



The surface C\* formed from sequential dehydrogenation of CH<sub>4</sub> can react with CO<sub>2</sub> (co-reactant) to form CO\*. To the best of our knowledge, this reaction is ignored in majority of DRM studies on Ni (111) surface reported to date. We found that this reaction is highly exergonic (-232 kJ/mol) and has to overcome an activation barrier of 154 kJ/mol on Ni (111) surface. However, this barrier is much higher than the direct dissociation (R5) barrier (54 kJ/mol) and hence kinetically not favored.

Interestingly on NiB surface, the activation barrier (132 kJ/mol) for this reaction is 24 kJ/mol lower than that on Ni (111) surface. Like Ni (111), this reaction is also highly exergonic with reaction free energy of -263 kJ/mol. Since C\* oxidation by OH\* (R21) has a slightly higher barrier (139 kJ/mol) on NiB surface, Boudouard reaction provides an additional path for C\* conversion to CO\*. Hence, surface C\* is expected to be consumed at a faster rate on NiB surface. In short, on NiB surface, the Boudouard reaction provides an alternate low barrier route for C\* conversion to form CO\*, leading to faster consumption of surface carbon.

#### 5.3.1.6 Desorption of products (R33, R37)

CO\* desorption energy (electronic energy) on Ni (111) is calculated to be 148 kJ/mol. This value is much lower than the desorption energy reported by Wang et al.<sup>88</sup> (183 kJ/mol) and Zhu et al.<sup>87</sup> (184 kJ/mol). This difference in binding energy is due to the difference in the functional employed. Wang et al.<sup>88</sup> and Zhu et al.<sup>87</sup> employed PBE functional which is known to over-estimate CO binding energy. However, the calculated desorption energy (electronic energy) in this work is closer to the experimental value (122 kJ/mol)<sup>141</sup>. The combinative desorption of H<sub>2</sub> has to

overcome a barrier of 57 kJ/mol and this reaction is exergonic with reaction free energy of -39 kJ/mol.

CO\* desorption energy on NiB is 144 kJ/mol, which is similar to the corresponding desorption energy on Ni (111) surface. However, the combinative desorption of H<sub>2</sub> has a similar barrier (58 kJ/mol) and is more exergonic (-54 kJ/mol) compared to that on Ni (111).

### 5.3.2 Microkinetic Analysis

In this section, we discuss and compare results of the microkinetic model analysis of the DRM reaction over Ni (111) and B-doped Ni catalysts. Using the DFT-computed free energies for reactants, products, intermediates, and transition states of each reaction step, the reaction rate constants for a given reaction condition were determined. Subsequently, the rate expressions and species balance equations of the microkinetic model were developed and solved. Rate constants of reactions over Ni (111) and B-doped Ni at 973 K and 10 bar pressure are tabulated in the appendix to chapter 5.

In this study, we re-computed the results of the previously reported model<sup>64</sup> for validation purpose, and then developed a series of models that varied based on the number of elementary reaction steps and the DFT corrections used to demonstrate their effect. The most comprehensive model implemented in this paper is using 38 elementary reaction steps and the appropriate DFT functional, including corrections (Table 5. 1). We validated this model against experimental data<sup>195</sup> and the details are given in the appendix to chapter 5.

#### 5.3.2.1 Surface Coverage

Herein, we present the surface coverage of species computed over Ni (111) and NiB surfaces and compare them. Details of the model can be found in Figure 5. 1. The simulations were carried out as per the reported experimental conditions<sup>64</sup>: the

reaction temperature and pressure were set as 973.15 K and 10 bar respectively. The BET area of Ni catalyst was taken to be  $7.2 \text{ m}^2 \cdot \text{g}^{-1}$  and the initial volume fractions of  $\text{CH}_4$  and  $\text{CO}_2$  were 0.5 and 0.5, respectively. The value of  $W/F_0$  was set as  $0.01 \text{ g}_{\text{cat}} \cdot \text{h}^{-1} \cdot \text{mol}^{-1}$ , to ensure low conversions of  $\text{CH}_4$  and  $\text{CO}_2$  which in turn ensures minor gradients in concentration and temperature down the catalyst bed. The surface coverages of reaction intermediates obtained after solving the microkinetic model are given in Table 5. 3.

**Table 5. 3** Fractional surface coverages of surface species computed by the model at a reaction temperature of 973.15 K, 10 bar pressure, and an inlet feed composition of 50% volume fraction  $\text{CH}_4$  and 50% volume fraction of  $\text{CO}_2$ .

Species	Ni (111)	B-doped Ni
$\text{CH}_3^*$	$9.71 \times 10^{-8}$	$5.22 \times 10^{-5}$
$\text{CH}_2^*$	$7.58 \times 10^{-7}$	$1.21 \times 10^{-6}$
$\text{CH}^*$	$2.46 \times 10^{-4}$	$1.32 \times 10^{-5}$
$\text{C}^*$	$2.17 \times 10^{-5}$	$8.12 \times 10^{-7}$
$\text{CO}_2^*$	$1.02 \times 10^{-6}$	$1.57 \times 10^{-4}$
$\text{CO}^*$	$9.25 \times 10^{-1}$	$9.32 \times 10^{-1}$
$\text{COOH}^*$	$1.84 \times 10^{-9}$	$1.08 \times 10^{-7}$
$\text{HCOO}^*$	$7.43 \times 10^{-7}$	$2.47 \times 10^{-3}$
$\text{HCO}^*$	$9.78 \times 10^{-9}$	$2.8 \times 10^{-8}$
$\text{HCOOH}^*$	$3.16 \times 10^{-11}$	$7.11 \times 10^{-11}$
$\text{CH}_3\text{OH}^*$	$4.21 \times 10^{-12}$	$2.59 \times 10^{-10}$
$\text{CH}_2\text{OH}$	$3.14 \times 10^{-13}$	$1.4 \times 10^{-9}$
$\text{CHOH}^*$	$1.76 \times 10^{-12}$	$6.41 \times 10^{-10}$
$\text{COH}^*$	$7.66 \times 10^{-8}$	$1.09 \times 10^{-9}$
$\text{CH}_3\text{O}^*$	$9.52 \times 10^{-10}$	$2.49 \times 10^{-9}$
$\text{CH}_2\text{O}^*$	$8.61 \times 10^{-12}$	$1.56 \times 10^{-10}$
$\text{H}_2\text{O}^*$	$2.08 \times 10^{-6}$	$4.37 \times 10^{-5}$

O*	$1.605 \times 10^{-2}$	$3.17 \times 10^{-3}$
H*	$3.84 \times 10^{-3}$	$8.19 \times 10^{-4}$
OH*	$3.09 \times 10^{-4}$	$1.54 \times 10^{-2}$
Free Site (*)	$5.41 \times 10^{-2}$	$4.59 \times 10^{-2}$
$x_{CH_4}$	$7.67 \times 10^{-2}$	$3.10 \times 10^{-2}$
$x_{CO_2}$	$8.84 \times 10^{-2}$	$4.30 \times 10^{-2}$

Our DFT calculations (Table 5. 2) show that the barrier for CH<sub>4</sub> dehydrogenation to CH<sub>3</sub>\* is 57 kJ/mol lower on NiB compared to Ni (111) surface. Interestingly, the fractional surface coverage predictions from the microkinetic model (Table 5. 3) indicate that CH<sub>3</sub>\* surface coverage on NiB ( $5.22 \times 10^{-5}$ ) is significantly higher than that on Ni (111) surface ( $9.71 \times 10^{-8}$ ). This clearly implies that NiB is better in activating CH<sub>4</sub>. In addition, the surface coverage of CO<sub>2</sub>\* is much higher on NiB ( $1.57 \times 10^{-4}$ ) than that on Ni (111) ( $1.02 \times 10^{-6}$ ). The DFT-calculated activation barrier for direct CO<sub>2</sub> dissociation on NiB is 43 kJ/mol higher than that on Ni (111) surface. Thus, the trend in surface coverage of CO<sub>2</sub>\* is in accordance with the DFT calculations. Remarkably, the fractional coverage of carbon is significantly reduced over NiB ( $8.12 \times 10^{-7}$ ) as compared to the Ni (111) ( $2.17 \times 10^{-5}$ ) surface. As the forward rate constant of Boudouard reaction (R35) is considerably higher on NiB, the carbon formed is consumed at a faster rate. Based on this observation we can conclude that NiB is less susceptible to deactivation by carbon deposition. However, this resistance from deactivation is achieved at the cost of reduced reactant conversion, as shown in Table 5. 3.

### 5.3.2.2 Reverse water gas shift reaction on Ni and B-doped Ni (111)

Knowing that DRM reaction is accompanied by RWGS reaction<sup>198</sup>, we investigated the kinetics of the two reactions as a function of space-time on both Ni (111) and B-doped Ni catalyst surfaces at 973.15 K and 10 bar pressure. The reaction conditions are adapted from Section 5.3.2.1. We compared the fractional surface coverages of

$\text{H}_2\text{O}^*$ ,  $\text{H}^*$ ,  $\text{CO}_2^*$  and  $\text{CO}^*$  vs space-time for the two catalysts (Figure 5. 7 and Figure 5. 8).

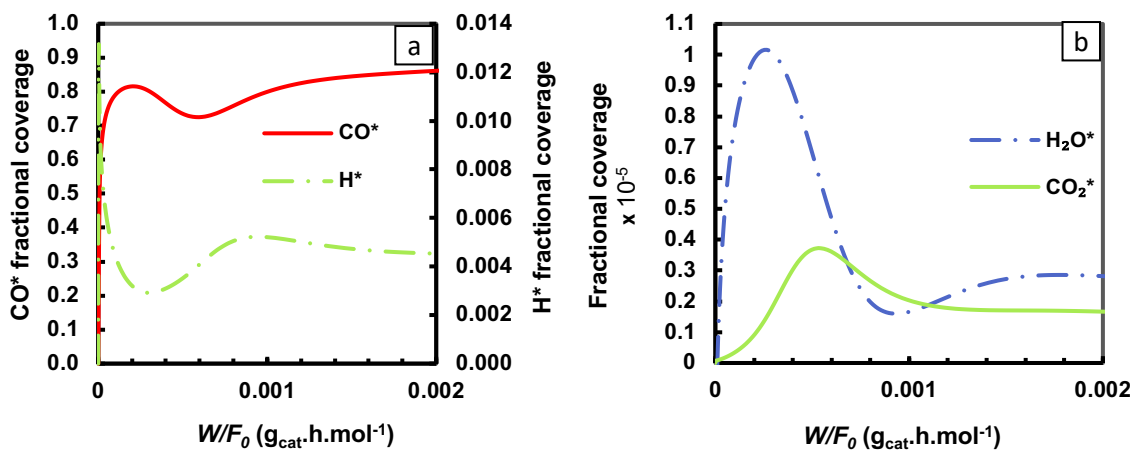


**Figure 5. 7** Fractional surface coverages of  $\text{CO}^*$ ,  $\text{H}^*$  (a) and  $\text{H}_2\text{O}^*$ ,  $\text{CO}_2^*$  (b) vs space-time over Ni (111) at reaction temperature 973.15 K and 10 bar pressure.

In Figure 5. 7 we can see that for the space-time  $W/F_0 \ll 2 \times 10^{-4} \text{ g}_{\text{cat}} \cdot \text{h} \cdot \text{mol}^{-1}$ ,  $\text{H}^*$  coverage is significantly higher. However, as space-time reaches  $2 \times 10^{-4} \text{ g}_{\text{cat}} \cdot \text{h} \cdot \text{mol}^{-1}$ ,  $\text{H}^*$  coverage decreases drastically as  $\text{CO}^*$  coverage and  $\text{H}_2\text{O}$  coverage increase. This is due to the fact that as space-time increases, the reaction proceeds from dissociation of  $\text{CH}_4$  to RWGS, which leads to formation of  $\text{H}_2\text{O}$  and  $\text{CO}$ . Soon  $\text{CO}^*$  and  $\text{H}_2\text{O}^*$  coverages reach a local maxima ( $W/F_0 = 4 \times 10^{-4} \text{ g}_{\text{cat}} \cdot \text{h} \cdot \text{mol}^{-1}$ ) after which DRM reaction competes with RWGS and RWGS finally approaches thermodynamic equilibrium at  $W/F_0 = 2 \times 10^{-3} \text{ g}_{\text{cat}} \cdot \text{h} \cdot \text{mol}^{-1}$ .

Similar surface coverage trends are observed in the B-doped Ni system, Figure 5. 8, but at lower space-time values, suggesting that kinetics of the RWGS is more favored over the B-doped Ni catalyst than on Ni. A partial equilibrium analysis of the reaction steps in RWGS at space-time value of  $1 \times 10^{-3} \text{ g}_{\text{cat}} \cdot \text{h} \cdot \text{mol}^{-1}$ , further supports our observation. The results shown in Figure 5. 9 suggest that given the space-time, the reaction steps over B-doped Ni are almost at the equilibrium but those on Ni are far from equilibrium.

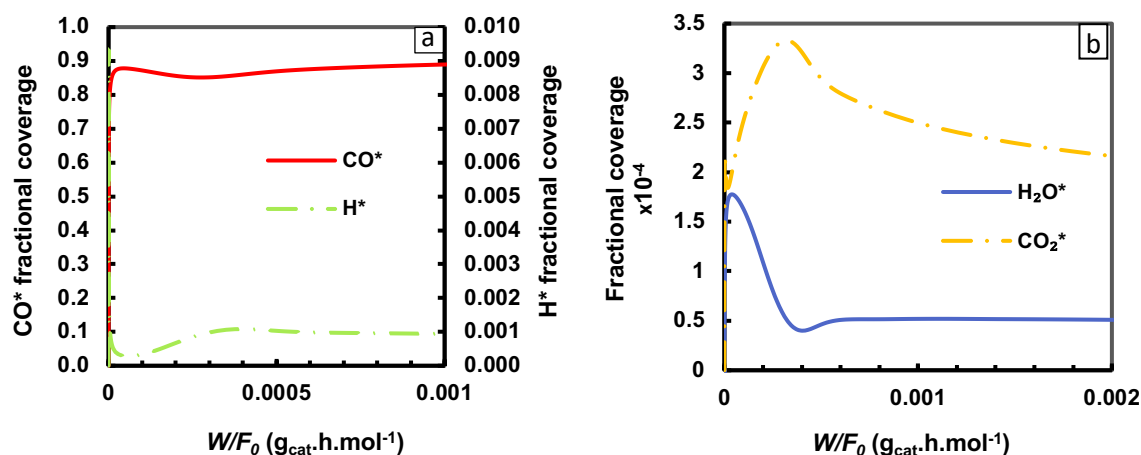


**Figure 5. 8** Fractional surface coverages of  $\text{CO}^*$ ,  $\text{H}^*$ (a) and  $\text{H}_2\text{O}^*$ ,  $\text{CO}_2^*$ (b) vs space-time over B-doped Ni at reaction temperature 973.15 K and 10 bar pressure.

Figure 5. 7 and Figure 5. 8 show that fractional coverages approach a constant value as the space-time increases, which indicates that RWGS reaches a thermodynamic equilibrium as space-time increases. However, it reaches equilibrium at a lower space-time for the boron-doped Ni as compared to Ni (111). This is due to the energetics favoring  $\text{CO}_2$  adsorption over B-doped Ni; as a result, the  $\text{CO}_2$  adsorption rate and the  $\text{CO}_2^*$  fractional coverage are high for the boron-doped Ni surface. This improved  $\text{CO}_2$  adsorption favors the side reaction RWGS rather than the main reaction DRM on B-doped Ni causing it to reach equilibrium at a lower space-time than Ni.

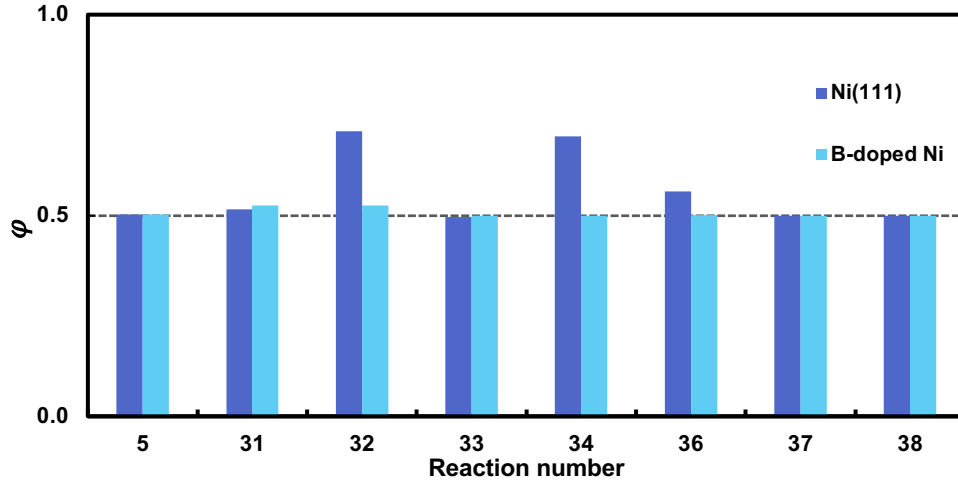


**Figure 5.9** Partial equilibrium coefficient  $\phi$  analysis of RWGS reaction steps over Ni (111) and NiB surfaces at space-time value of  $1 \times 10^{-3} \text{ g}_{\text{cat}} \cdot \text{h} \cdot \text{mol}^{-1}$  at reaction temperature 973.15 K and 10 bar pressure (R32 and R34 represents  $\text{OH}^* + \text{H}^* \rightarrow \text{H}_2\text{O}^*$  and  $\text{OH}^* + \text{OH}^* \rightarrow \text{H}_2\text{O}^* + \text{O}^*$  respectively).

### 5.3.3 Sensitivity analysis

In order to understand the reaction pathway and kinetically relevant steps over the catalyst surface, sensitivity analysis of each reaction step was performed for the model responses that include methane fractional conversion ( $x_{\text{CH}_4}$ ),  $\text{CO}_2$  fractional conversion ( $x_{\text{CO}_2}$ ) and partial pressure of CO ( $P_{\text{CO}}$ ) and  $\text{H}_2$  ( $P_{\text{H}_2}$ ) at the reactor exit. Sensitivity analysis was performed for DRM on Ni (111) and NiB, which identified the kinetically relevant steps for each case.  $\text{CH}_4$  dissociation (R1) and  $\text{CH}_2^*$  oxidation (R25) are found to be the rate-determining steps of DRM reaction on both, Ni (111) and NiB. Then sensitivity analysis for DRM on Ni (111) was performed to identify the different kinetically relevant steps at different reaction conditions.

#### 5.3.3.1 Reactants conversion on Ni (111) and B-doped Ni

Since we are interested in the relative contribution of each reaction step, a relative sensitivity coefficient ( $S_{k,j}^r$ ) of each elementary step was generated for both cases



using equation (5.9) and plotted against the reaction number. The reaction numbers are the same as in Table 5. 2.

$$S_{k,j}^r = \frac{S_{k,j}}{|S_k^{max}|} \quad (5.8)$$

where,  $S_k^{max}$  is the sensitivity coefficient with the highest absolute value for a given model response so that  $|S_{k,j}^r| \leq 1$ .

Furthermore, the reactions in quasi-equilibrium were identified using partial equilibrium analysis. The relative sensitivity coefficients over different model responses (i.e.  $x_{CH_4}$ ,  $x_{CO_2}$ ,  $P_{H_2}$ ,  $P_{CO}$ ) were found to be exactly same up to two decimal places. The results of partial equilibrium analysis and sensitivity analysis are shown in and Figure 5. 11, respectively.

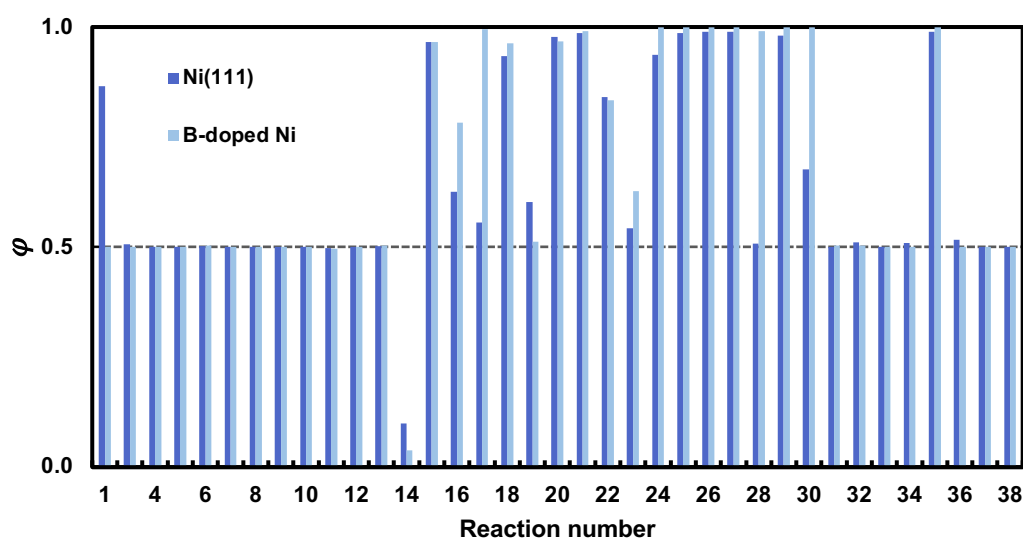


**Figure 5. 10** Partial equilibrium coefficient  $\phi$  analysis of DRM reaction steps over Ni (111) and NiB surfaces at space-time value of 0.01 gcat·h·mol<sup>-1</sup> at reaction temperature 973.15 K and 10 bar pressure.

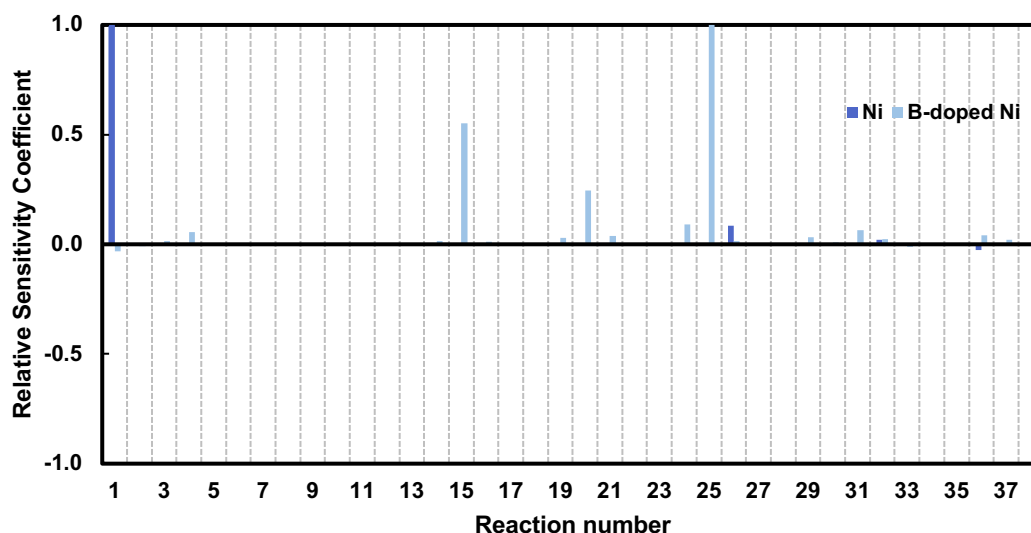


**Figure 5. 11** Sensitivity analysis of DRM reaction steps over Ni (111) and NiB surfaces at space-time value of  $0.01 \text{ g}_{\text{cat}} \cdot \text{h} \cdot \text{mol}^{-1}$  at reaction temperature 973.15 K and 10 bar pressure.

Figure 5. 11 shows that of the 38 elementary reactions, R1 ( $\text{CH}_4$  dissociation) and R25 ( $\text{CH}_2^*$  oxidation) are the most sensitive reactions on Ni (111) and B-doped Ni respectively. Moreover, the partial equilibrium analysis () suggest that the elementary reaction R1 over Ni(111) and R25 over B-doped Ni are not in equilibrium and thus, as per the partial equilibrium analysis and sensitivity analysis criteria <sup>183,197</sup>, R1 and R25 are the rate-determining steps (RDS) of DRM over Ni (111) and NiB respectively.

Now, given the complete list of elementary reaction steps, the dominant pathway was formulated for CO and  $\text{H}_2$  formation over Ni (111) and NiB surface using the strategy explained in section 5.2.4.

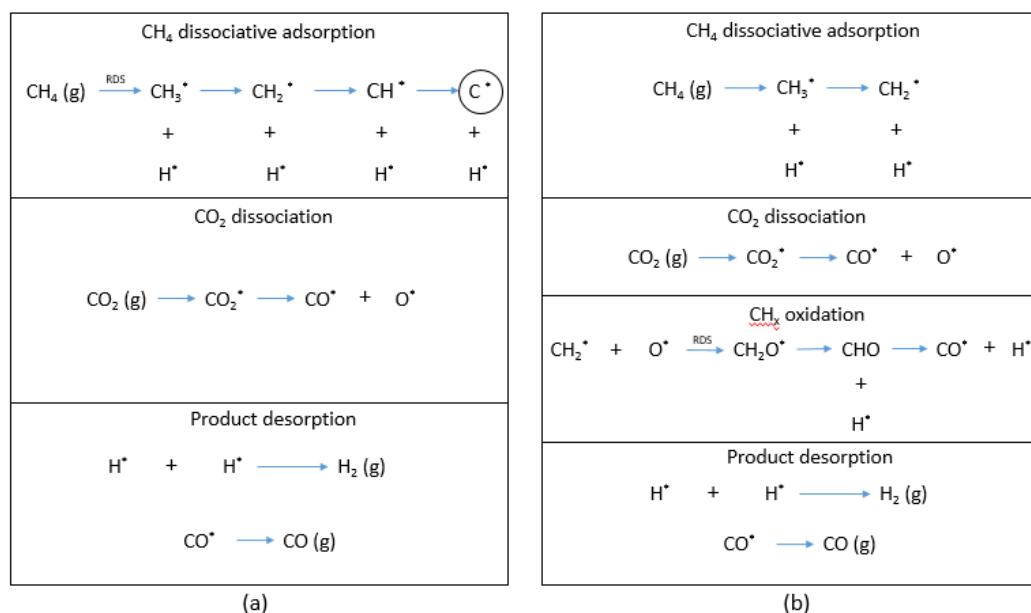


**Figure 5. 12** Dominant reaction pathway on Ni (111) (a) and NiB (b) based on sensitivity analysis and reaction rates at reaction conditions adapted from Section 5.2.2.

Figure 5. 12 shows the dominant reaction pathways on both the catalyst surfaces. Our analysis suggests that on Ni (111) surface, direct dissociation of CO<sub>2</sub> to CO\* and O\* is favored compared to the H-assisted route. The CH<sub>4</sub> activation route involves sequential dehydrogenation and oxidation of CH<sub>x</sub> (x = 0-3). We found that both O\* and OH\* oxidation of CH<sub>3</sub>, CH<sub>2</sub>, and CH are not preferred and sequential dehydrogenation of CH<sub>4</sub> is favored leading to the formation of C\*. The rate-limiting step is CH<sub>4</sub> dehydrogenation to CH<sub>3</sub> (R1) (*cf* Figure 5. 11) which is in agreement with the experimental findings of Wei et al.<sup>71</sup> in which they performed isotopic tracing and exchange measurements. Interestingly, our DFT calculations also predict that the CH<sub>4</sub> activation barrier is higher than that of other reactions.

It should be noted that the dominant pathway for product formation on Ni (111) does not include oxidation of CH<sub>x</sub>\* species even though its reaction rate (i.e. 1.28 mol·h<sup>-1</sup>·g<sub>cat</sub><sup>-1</sup>) is comparable to RDS (1.60 mol·h<sup>-1</sup>·g<sub>cat</sub><sup>-1</sup>). This is because the rate-limiting step of the dominant pathway must be the RDS of the overall reaction. Thus, reaction steps with rates lower than RDS are not included in this pathway. However, CH\* oxidation contributes towards product formation via alternative pathways.

Although, by definition, contribution from these alternative pathways will always be less compared to that from the dominant pathway.

It is also noted that the dominant pathway for product formation on Ni (111) leads to a net carbon formation. Whereas the dominant pathway on B-doped Ni doesn't include C formation. Instead  $\text{CH}_2^*$  oxidizes preventing further  $\text{CH}_2^*$  dehydrogenation that leads to carbon formation. Our calculations suggest that both Ni and NiB share similar  $\text{CO}_2$  activation route (direct dissociation to  $\text{CO}^*$ ). The  $\text{CH}_4$  activation route involves sequential dehydrogenation of  $\text{CH}_4$  to  $\text{CH}_2^*$ , followed by its  $\text{O}^*$  oxidation to form  $\text{CH}_2\text{O}^*$ , which sequentially dehydrogenates to give  $\text{CO}^*$ .  $\text{CH}_2^*$  oxidation (R25) (*cf* Figure 5. 11) is found to be the rate-limiting step. It is worthy to mention that this pathway is different from that predicted by DFT alone. The  $\text{CH}_2^*$  dehydrogenation was favored kinetically compared to its oxidation.

Further analysis was performed on the forward reaction rates of RDS on Ni (111), i.e. R1 and RDS on B-doped Ni, i.e. R25. Figure 5. 11 shows the forward rates R1 and R25 on their respective catalysts as a function of space-time.

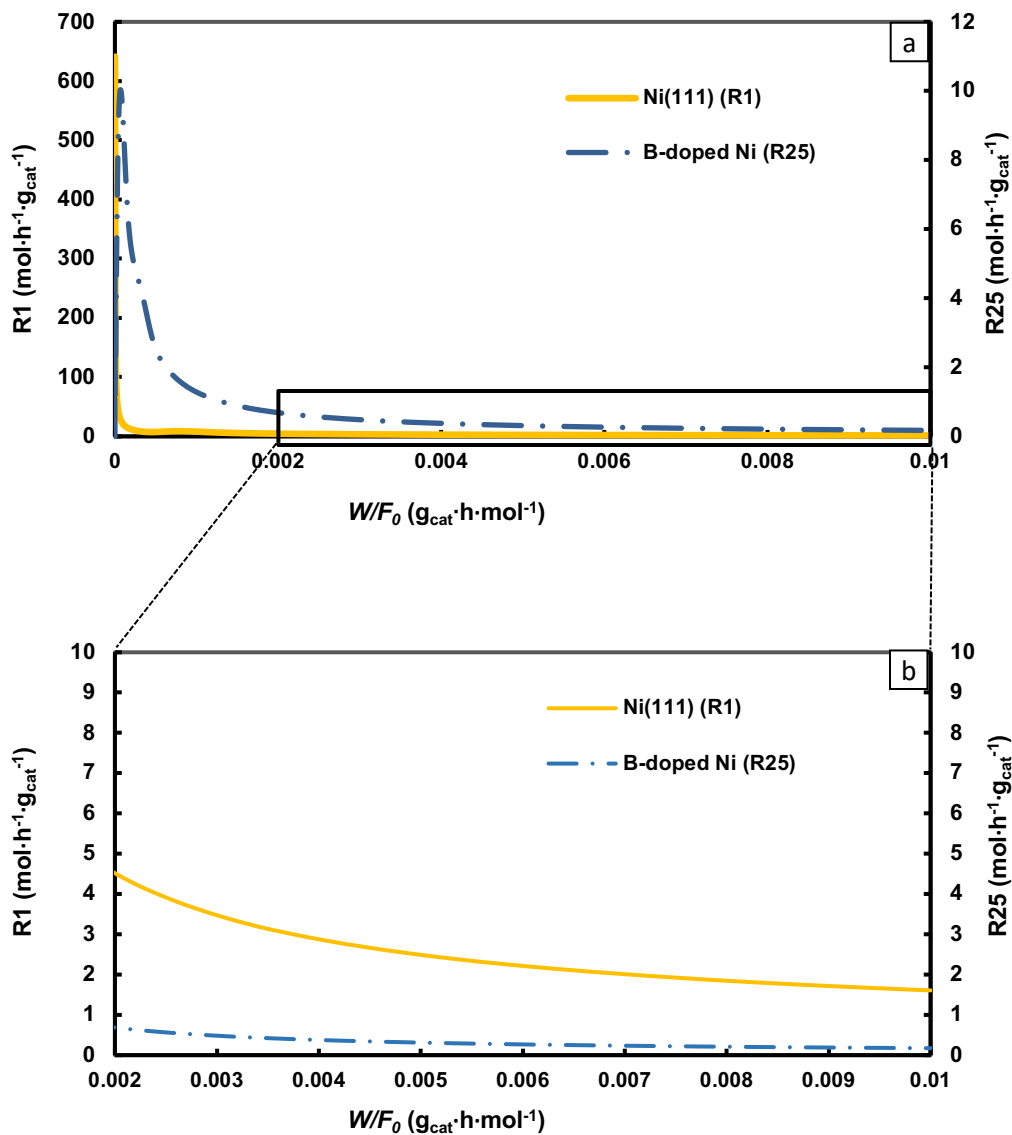


**Figure 5. 13** Forward reaction rates of R1 and R25 vs space-time at a reaction temperature of 973.15 K and 10 bar pressure (a) and zoomed-in image (b).

Figure 5. 13 shows that reaction rates for  $\text{CH}_4$  dissociation on Ni are always greater than the  $\text{CH}_2^*$  oxidation reaction on B-doped Ni, which further supports the lower conversion value of methane on NiB, previously observed in Section 5.3.2.2. As mentioned in Section 5.3.1.2,  $\text{O}^*$  is the primary oxidizing agent and it is generated from  $\text{CO}_2$ . Since the barrier for  $\text{CO}_2$  dissociation is higher (*cf* Figure 5. 4) on NiB compared to Ni (111), the  $\text{O}^*$  coverage (*cf* Table 5. 3) on NiB is lower compared to that on Ni (111). This could be the reason for the decrease in  $\text{CH}_2^*$  oxidation rate

on NiB. Figure 5. 13 also indicates that the DRM reaction will reach thermodynamic equilibrium at higher values of space-time on NiB when compared to Ni.

### 5.3.3.2 Sensitivity analysis for DRM on Ni (111) at varying reaction conditions

As mentioned previously in Section 5.2.3, the RDS of the DRM reaction process is debatable and depends on reaction conditions and the choice of catalysts. In this study, we settle this debate by identifying the kinetically relevant reaction steps for the DRM reaction over Ni (111) surface via sensitivity and partial equilibrium analyses of all the elementary steps at three temperatures (873 K, 973 K, and 1073 K) and different reaction conditions. Results pertaining to partial equilibrium analysis and sensitivity analysis are presented case wise in the appendix to chapter 5.

Our findings suggest that different elementary steps become kinetically relevant at different reaction conditions. At low  $\text{CH}_4$  and  $\text{CO}_2$  partial pressures ( $< 10$  kPa) and at low total reaction pressure (1 bar), both  $\text{CH}_4$  dissociative adsorption and  $\text{CO}_2$  adsorption dominate the overall reaction rate. However, at high total reaction pressure (10 bar) and low reaction temperatures (873 and 973 K), only  $\text{CH}_4$  dissociation dominates the overall rate, but as we increase temperature (1073 K),  $\text{CH}^*$  oxidation becomes the dominant reaction step.

## 5.4 Summary and Conclusions

In summary, considering a comprehensive reaction network of 38 elementary reactions, we investigate DRM reaction network on Ni (111) and on boron-doped Ni (NiB) surfaces. We employed the benchmarked rPBE-vdW functional with a correction of 28 kJ/mol for gas-phase  $\text{CO}_2$  to accurately compute the energetics of DRM reactions, using DFT. Based on DFT calculations, we predicted that direct dissociation of  $\text{CO}_2$  to  $\text{CO}^*$  and  $\text{CH}_4$  sequential dehydrogenation to  $\text{C}^*$  were the favored routes on both, Ni and NiB surfaces. However, in comparison with Ni (111), the  $\text{CO}_2$  activation barrier was higher and  $\text{CH}_4$  activation barrier was significantly

lower on the NiB surface. Besides this, CO formation by Boudouard reaction ( $\text{CO}_2^* + \text{C}^* \rightarrow 2\text{CO}^*$ ) also has a lower barrier on NiB compared to Ni. Employing the DFT calculated energies a microkinetic model (MKM) was developed and we identified the dominant reaction pathway and RDS on Ni (111) and NiB surfaces. The dominant reaction pathway was  $\text{CO}_2^* \rightarrow \text{CO}^* + \text{O}^*$ ;  $\text{CH}_4 \rightarrow \text{CH}_3^* \rightarrow \text{CH}_2^* \rightarrow \text{C}^* \rightarrow \text{CO}^*$  and  $\text{CO}_2^* \rightarrow \text{CO}^* + \text{O}^*$ ;  $\text{CH}_4 \rightarrow \text{CH}_3^* \rightarrow \text{CH}_2^* \rightarrow \text{CH}_2\text{O}^* \rightarrow \text{CHO}^* \rightarrow \text{CO}^*$  on Ni (111) and NiB surfaces, respectively. The dominant reaction pathway on NiB surface includes  $\text{CH}_2^*$  oxidation, that prevents carbon formation. Subsequently, it was also observed that carbon coverage over NiB surface was lower than that on the Ni (111) surface by almost two orders of magnitude. However, the resistance from deactivation was achieved at the cost of reduced reactant conversion. Further, sensitivity analysis of kinetic constants on the two surfaces showed that  $\text{CH}_4$  dissociation to  $\text{CH}_3^*$  and  $\text{CH}_2^*$  oxidation to  $\text{CH}_2\text{O}^*$  were the rate-determining steps (RDS) of the DRM reaction on Ni and NiB, respectively. However, these RDSs differ with reaction conditions, resulting in discrepancies of RDSs reported in previous literature. This study addresses this discrepancy by analyzing sensitivity of reaction steps at different reaction conditions. It is observed that at high temperatures (around 1073 K) and pressure (10 bars),  $\text{CH}^*$  oxidation becomes kinetically relevant on Ni (111) and dominates the overall reaction rate, whereas at lower temperatures and pressure,  $\text{CO}_2$  adsorption and  $\text{CH}_4$  dissociative adsorption steps dominate. It is further observed that the forward rate of the RDS at 973 K and 10 bar on Ni ( $\text{CH}_4$  dissociation) is higher than the forward rate of RDS ( $\text{CH}_2^*$  oxidation reaction) on NiB, which again confirms the lower reactant conversion on NiB. We believe that the combined DFT and microkinetic modeling approach adopted in this investigation and the insights into the DRM reaction pathways on Ni and NiB would instigate further theoretical and experimental works, for developing novel Ni or NiB based alloy catalysts that can prevent carbon deposition without compromising the catalytic activity.

## **Chapter 6 Prediction of NiB based single atom alloy as a novel catalyst for CO<sub>2</sub> conversion reactions: computational screening and reaction mechanism analysis**

*In this work, a computational screening is performed to predict thermodynamically stable NiB based single atom alloy (SAA) catalyst for CO<sub>2</sub> conversion reactions. The strategy is to modify NiB to improve the activity (reduce CO<sub>2</sub> activation barrier) without affecting the stability. Based on the ability to break the C-O bond, we considered 15 SAAs based on NiB (Ru, Pt, Pd, Rh, Co, Fe, Os, Ir, Re, W, Mo, Cu, Mn, Zn, and K). Only 5 of them are found to be thermodynamically stable (Pt, Pd, Rh, Cu, and Mn) and further calculated the CO<sub>2</sub> activation barrier on these 5 SAA's. Mn-NiB SAA was found to be the only candidate on which there is a significant reduction of the CO<sub>2</sub> activation barrier (barrier of 68 kJ/mol). Considering a comprehensive reaction network, CO<sub>2</sub> methanation (46 elementary reactions) and DRM (38 elementary reactions) reactions were studied on Mn-NiB SAA. High CO<sub>2</sub> adsorption energy and low CO<sub>2</sub> (direct dissociation) and CO\* (hydrogenation via HCO\*) activation barriers make Mn-NiB SAA a suitable catalyst for CO<sub>2</sub> methanation reaction. Correspondingly, the low CO<sub>2</sub> and CH<sub>4</sub> activation barriers make Mn-NiB SAA a perfect candidate for DRM reaction. Most importantly, the high endergonicity for CH<sub>4</sub> stepwise dehydrogenation combined with low free energy barrier (122 kJ/mol) for Boudouard reaction reduces the on-surface coke formation and thereby prevents the deactivation of the catalyst. Thus, the Mn SAA of NiB can be a potential catalyst for CO<sub>2</sub> methanation and DRM reactions.*



## 6.1 Introduction

Ni-based catalysts can catalyze both CO<sub>2</sub> methanation and DRM reactions to produce methane and syngas respectively. However, Ni-based catalysts are less active and are prone to deactivation under aggressive operating conditions <sup>73,74</sup>. Promising approaches (doping by metals/ metalloids) are being investigated to reduce these shortcomings without affecting the good selectivity of Ni-based catalysts <sup>75–79</sup>.

### 6.1.1 CO<sub>2</sub> methanation: effect of promoters and reaction mechanism

To improve the activity of Ni-based catalysts, microstructure modifications including doping by noble metals <sup>89,199–201</sup> or other transition metals <sup>90,91,202–209</sup> are studied. These studies are summarized in Table 6. 1. Even though many studies were performed, hardly any breakthrough has come in improving the activity of Ni-based catalysts. Majority of these studies were done more or less arbitrarily and the fundamental reason behind their role is not explained. Additionally, some metal doping helps in better dispersion of Ni and has little effect in the methanation reaction <sup>89,91,199,204</sup>. Moreover, these studies were performed on different supports. So, if we must design a novel catalyst using a bottom-up approach, these studies don't help much, and a detailed understanding of the underlying reaction mechanism is essential.

**Table 6. 1.** Summary of key results for CO<sub>2</sub> methanation on modified Ni catalysts

Catalyst	Highlights of the work	Ref.
Rh-Ni/LaAlO <sub>3</sub>	<ul style="list-style-type: none"> <li>52% increase in methanation TOF</li> <li>Increased surface adsorbed oxygen sites and basic sites result in stronger adsorption of CO<sub>2</sub> resulting in better CO<sub>2</sub> activation</li> </ul>	199
Mo-Ni/Al <sub>2</sub> O <sub>3</sub>	<ul style="list-style-type: none"> <li>Mo helps in better dispersion of Ni loading resulting in an increase in catalyst activity</li> </ul>	204

Fe-Ni/CeO <sub>2</sub>	<ul style="list-style-type: none"> <li>• Fe improved activity, but the selectivity shifted towards CO</li> </ul>	205
Ru-Ni/Al <sub>2</sub> O <sub>3</sub>	<ul style="list-style-type: none"> <li>• High CO<sub>2</sub> conversion (82%)</li> <li>• Surface segregation of Ru resulted in higher activity</li> </ul>	89
Co-Ni/Al <sub>2</sub> O <sub>3</sub>	<ul style="list-style-type: none"> <li>• 78% CO<sub>2</sub> conversion and 99% methane selectivity</li> <li>• Co helps in increased H<sub>2</sub> uptake resulting in higher activity</li> </ul>	90
M- Ni/Al <sub>2</sub> O <sub>3</sub> (M = Fe, Co, Zr, La, and Cu)	<ul style="list-style-type: none"> <li>• Activity increased except Cu alloy</li> <li>• 70% conversion for 30wt%Ni 5wt%Fe/Al<sub>2</sub>O<sub>3</sub></li> <li>• Higher activity is due to increased surface area and pore volume</li> </ul>	91
Re-Ni (111) SAA	<ul style="list-style-type: none"> <li>• Combined DFT (employing PBE functional) and MKM study (18 elementary reactions)</li> <li>• Re helps in breaking C-O bond resulting in better CO<sub>2</sub> activation</li> </ul>	201
Pt-Ni (111) SAA	<ul style="list-style-type: none"> <li>• DFT study (employing PBE functional)</li> <li>• CO<sub>2</sub> hydrogenation via COOH* is the dominant pathway</li> <li>• Pt lowers the CO<sub>2</sub> hydrogenation barrier and also helps in the reduction of C deposition</li> </ul>	200
M- NiAlO <sub>x</sub> (M = Mn, Fe)	<ul style="list-style-type: none"> <li>• Mn adsorbs CO<sub>2</sub> strongly resulting in better CO<sub>2</sub> activation</li> <li>• Fe improves the stability of the catalyst</li> </ul>	209

Evaluating the dominant reaction pathway and rate-determining step (RDS) abets in efficient catalyst design and modifications<sup>93,134,210</sup>. The reaction pathway could be altered, or the barriers of crucial reaction steps (including RDS) could be reduced by adding suitable dopants. Consequently, evaluation and comparison of reaction pathways are essential to assess the effect of dopants<sup>93,134,210</sup>. Hence, elucidation of the complex reaction mechanism on the catalyst (both clean and modified) is of vital importance. However, the methanation reaction mechanism is debated on Ni surface<sup>37,38</sup>. The reaction mechanism

reported in various studies is summarized in Table 6. 2. The most argued steps are the activation routes of CO<sub>2</sub> and CO\* (\* represents adsorbed species). These can undergo direct dissociation or reacts with H adatom (H can attach to carbon or oxygen) and undergoes hydrogenation. Additionally, methanation reaction can proceed with or without forming CO\* intermediate (*cf* Table 6. 2). Furthermore, Ni suffers from CO\* poisoning and typically CO\* activation step is regarded as the RDS. Hence, elucidating the exact reaction pathway and understand if the reaction follows CO\* intermediate route is crucial in modifying Ni-based catalysts.

**Table 6. 2** Comparison of CO<sub>2</sub> methanation reaction mechanism on Ni and modified Ni catalysts

Catalyst	Reaction mechanism	RDS and activation barrier	Ref.
Ni (111)	CO <sub>2</sub> → CO* → C* → CH* → CH <sub>2</sub> * → CH <sub>3</sub> * → CH <sub>4</sub>	CO* → C* + O* 237.4 kJ/mol	166
Ni (111)	CO <sub>2</sub> → HCOO* → HCOOH* → HCO* → HCOH* → CH* → CH <sub>2</sub> * → CH <sub>3</sub> * → CH <sub>4</sub>	HCO* + H* → HCOH* 93.1 kJ/mol	167
Ni (111)	CO <sub>2</sub> → CO* → HCO* → HCOH* → CH <sub>2</sub> OH* → CH <sub>2</sub> * → CH <sub>3</sub> * → CH <sub>4</sub>	CO* + H* → HCO* 123 kJ/mol	169
Re-Ni (111)	CO <sub>2</sub> → CO* → HCO* → CH* → CH <sub>2</sub> * → CH <sub>3</sub> * → CH <sub>4</sub>	CO* + H* → HCO* 138.2 kJ/mol	201
Pt-Ni (111)	CO <sub>2</sub> → COOH* → CO* → HCO* → HCOH* → CH <sub>2</sub> OH* → CH <sub>2</sub> * → CH <sub>3</sub> * → CH <sub>4</sub>	COOH* → CO* + OH* 198.7 kJ/mol	200

In our previous work (*chapter 4*), we studied and compared the CO<sub>2</sub> methanation reaction mechanism on Ni (111) and Ru (001) (most active catalyst for CO<sub>2</sub> methanation) surfaces. We combined DFT and microkinetic model (MKM) and employed a comprehensive reaction network of 46 elementary reactions and predicted the activity, selectivity, and the dominant reaction pathways on both Ni (111) and Ru (001) surfaces. High CO<sub>2</sub> conversion was predicted on Ru, because of high CO<sub>2</sub> adsorption energy and low CO<sub>2</sub> activation barriers.

Even though the CO<sub>2</sub> activation barrier is low (electronic energy of 54 kJ/mol) on Ni, the CO<sub>2</sub> absorbs very weakly (-12 kJ/mol) resulting in low CO<sub>2</sub> conversion. On Ru, CO<sub>2</sub> direct dissociation route (via CO\* intermediate route) is favored over its hydrogenation route. Whereas on Ni, the CO<sub>2</sub> hydrogenation reaction (without forming CO\* intermediate) is also feasible, and hence the reaction can bypass CO\* intermediate route. This results in high CO\* coverage (formed via CO<sub>2</sub> direct dissociation) and could lead to CO poisoning on Ni. On both Ni and Ru, the CO\* activation barriers (CO\* hydrogenation to form HCO\*) were significantly high (141 kJ/mol and 126 kJ/mol on Ni (111) and Ru (001) respectively), and this reaction was highly endergonic making it the most challenging step in CO<sub>2</sub> methanation.

Based on the above discussion, novel catalysts based on Ni should have following abilities in order to catalyze the methanation reaction i) high CO<sub>2</sub> binding energy ii) low CO<sub>2</sub> activation barriers iii) follows the CO intermediate route (to reduce CO poisoning) and iv) low CO\* hydrogenation barriers.

### 6.1.2 DRM: effect of promoters and reaction mechanism

Ni-based catalysts suffer from deactivation due to carbon deposition under DRM reaction conditions. Two main strategies to decrease the carbon deposition<sup>211</sup> are i) to improve the surface oxidation of carbon and ii) to alter the reaction pathway by promoting the CH<sub>x</sub> (x = 1 - 3) oxidation reactions, so that no carbon intermediate is formed. In this regard, many dopants (metals and metalloids) are tried on Ni surface<sup>75,76,216–219,77,79,92,194,212–215</sup>. A summary of these studies is given in Table 6. 3. In many cases, there is a compromise between stability and activity owing to the addition of promoters to Ni and hardly any breakthrough has come (*cf* Table 6. 3). Additionally, methane activation barriers have increased as a result of doping metals such as K, Au, Sn, etc. For instance, the CH<sub>4</sub> dissociation barrier increased by 16 kJ/mol for Ni with one Au atom and 38 kJ/mol with two Au atoms<sup>78</sup>. This increase in the barrier is attributed to the lowering in the local density of *d* state at the Ni atom present near Au atom. Consequently, the increased methane activation barrier could result in lowering methane conversion. Conversely, Xu et al.<sup>80–82</sup>

showed that the methane activation barrier reduced by 27 kJ/mol on boron promoted Ni (NiB) compared to Ni (111) surface. Thus, NiB could be a potential DRM catalyst. It is essential to simulate the DRM reaction mechanism on NiB and compare it with that on Ni (111) to evaluate the effects of boron doping.

**Table 6. 3** Summary of key results for DRM on modified Ni catalysts

Catalyst	Highlights of the work	Ref.
Sn-Ni/Al <sub>2</sub> O <sub>3</sub>	<ul style="list-style-type: none"> <li>• Coke resistance achieved with the loss of reforming activity</li> <li>• The reducibility of Ni is improved by the surface enrichment of Sn</li> </ul>	92
Rh-Ni/SBA-15	<ul style="list-style-type: none"> <li>• Rh helps in activating CO<sub>2</sub> and releases oxygen adatom that can react with the carbon</li> </ul>	213
Co-Ni/Al <sub>2</sub> O <sub>3</sub>	<ul style="list-style-type: none"> <li>• The surface carbon undergoes faster oxidation on Co-Ni surface</li> <li>• Oxygen atom migrates from Co to Ni through oxygen spillover</li> </ul>	212
La <sub>2</sub> O <sub>3</sub> -Ni	<ul style="list-style-type: none"> <li>• DFT study (employing PBE functional)</li> <li>• A complex intermediate CO<sub>2</sub>(La<sub>2</sub>O<sub>2</sub>-O) is formed by the strong interaction of CO<sub>2</sub> with La<sub>2</sub>O<sub>3</sub>. The C/CH intermediate is oxidized by the partially dissociated O atom in this complex intermediate</li> </ul>	219
Pt- Ni SAA	<ul style="list-style-type: none"> <li>• The barrier for CH dissociation increased on Pt-Ni (163 kJ/mol) resulting in less carbon formation</li> <li>• However, there is a decrease in the activation of methane</li> </ul>	218
K- Ni/Al <sub>2</sub> O <sub>3</sub>	<ul style="list-style-type: none"> <li>• Coke deposition reduced on K doped catalyst</li> <li>• K migrates to the surface of the catalyst and blocks the active site and thus reduces carbon formation on the surface</li> <li>• However, there is a reduction in catalytic activity</li> </ul>	75

Mn@Ni (111) (Mn adsorbed on Ni)	<ul style="list-style-type: none"> <li>• Mn alters the reaction pathway.</li> <li>• CH<sub>2</sub> prefers oxidation compared to dehydrogenation preventing carbon formation</li> </ul>	214
---------------------------------------	---	-----

In our previous work (*chapter 5*), we combined DFT and MKM to simulate the DRM reaction mechanism on both Ni and NiB surfaces. Considering a comprehensive reaction network of 38 elementary reactions, we predicted the fractional surface coverages of surface species and the dominating reaction pathways on both the surfaces. Interestingly the carbon coverage on NiB was predicted to be almost two orders of magnitude lower than that on Ni surface. Notably, the methane activation route is altered due to boron doping. On Ni (111), the dehydrogenation of methane ( $\text{CH}_4 \rightarrow \text{C}^* + 4\text{H}^*$ ) is favored that leads to the formation of carbon intermediate. On the contrary,  $\text{CH}_2^*$  oxidation is preferred over its dehydrogenation on the NiB surface, which prevents carbon formation. Additionally, the overall reaction energy of methane dehydrogenation to carbon is 82 kJ/mol more on NiB than that on Ni making the dehydrogenation route to form  $\text{C}^*$  thermodynamically unfavorable on NiB. Moreover, the barrier for Boudouard reaction ( $\text{C}^* + \text{CO}_2 \rightarrow 2\text{CO}^*$ ) is significantly lower on NiB compared to that on Ni. Thus, the Boudouard reaction poses a supplementary route for carbon conversion. Even though, methane activation routes are different on Ni and NiB the  $\text{CO}_2$  activation route remains the same. Direct dissociation of  $\text{CO}_2$  is favored on both the surfaces. Importantly, the  $\text{CO}_2$  binding energy is significantly high on NiB (-61 kJ/mol) compared to Ni (111) (-12 kJ/mol). However, the  $\text{CO}_2$  activation barrier is significantly high on NiB (124 kJ/mol) compared to that on Ni (111) (54 kJ/mol). Since the  $\text{CO}_2$  supplies the primary oxidizing agent ( $\text{O}^*/\text{OH}^*$ ), the high barrier affects the  $\text{CH}_2^*$  oxidation rates on NiB. Therefore, the resistance from deactivation is achieved at the cost of reduced reactant conversion. Hence, NiB should be modified to reduce  $\text{CO}_2$  activation barriers so that the catalyst activity is not compromised.

### 6.1.3 NiB based single atom alloy (SAA)

As mentioned before, the catalyst for  $\text{CO}_2$  methanation/DRM reaction would require high  $\text{CO}_2$  binding energy and low  $\text{CO}_2$  activation barriers. Even though the  $\text{CO}_2$  activation

barrier is low on Ni, CO<sub>2</sub> binds very weakly. From our previous study (*chapter 5*), NiB has high CO<sub>2</sub> binding energy and it could be a potential catalyst for methanation and DRM reactions. Most importantly NiB is good in resisting the deactivation due to carbon deposition. NiB was selected in the current study as the microstructure details of NiB are better understood and fundamentals of reaction mechanisms are known<sup>80–82</sup>. However, the CO<sub>2</sub> activation barrier on NiB is significantly high compared to that on Ni. Hence NiB should be modified to reduce CO<sub>2</sub> activation barriers without affecting the energetics of other crucial reactions. Investigations into SAA (one of the surface atoms from the slab is replaced by a host atom) for selective catalysis are now gaining traction to develop catalysts with high stability and activity<sup>220,221,230–233,222–229</sup>. For instance, Marcinkowski et al.<sup>233</sup> studied the C-H activation ability of Pt-Cu SAA (Pt doped on Cu) under ultra-high vacuum conditions. They found that the methane dehydrogenation barriers were significantly reduced on Pt-Cu SAA compared to that on the clean Cu surface. The results from temperature-programmed reaction (TPR) and scanning tunneling microscope (STM) results revealed that Pt-Cu SAA activates the C-H bond in the methyl group at 350K, which is 100K lower than that on Cu<sup>233</sup>. Hence, SAA catalysts are very promising, and NiB based SAAs are never explored before. In the current work, the strategy is to develop NiB-based SAA for methanation and DRM reactions.

In this regard, the screening search for NiB-based SAA catalysts that can reduce CO<sub>2</sub> activation barriers is required. Computational techniques involving DFT can be used for an extensive search of potential NiB-based SAA catalysts. Even though the screening of catalysts is based on its thermodynamic stability and its CO<sub>2</sub> activation ability, the barriers of other reactions should not be affected undesirably. To ensure this, the entire reaction mechanism of CO<sub>2</sub> methanation and DRM reactions must be simulated on NiB SAA (that reduces CO<sub>2</sub> activation barrier) and compare with that on Ni and NiB. Additionally, the thermodynamic stability of SAA must be assessed to ensure the possibility of the existence of such an alloy catalyst. In the majority of DFT studies mentioned in Table 6. 1 and Table 6. 3, the thermodynamic stability of the alloy catalysts was not tested.

From the above discussion, it is clear that a screening of different NiB based SAA has to be performed to identify a suitable dopant that reduces the CO<sub>2</sub> activation barrier without adversely affecting other reactions in CO<sub>2</sub> conversion reactions. In the current study, a screening search of thermodynamically stable NiB-based SAA is performed. The SAA surface on which there is a significant reduction of the CO<sub>2</sub> activation barrier is identified. Subsequently, CO<sub>2</sub> methanation (46 elementary reactions) and DRM (38 elementary reactions) reactions are simulated on the SAA and compared to that on Ni and NiB surfaces. Computational and thermodynamic stability calculation details are discussed in Section 6.2. Screening search of NiB SAA catalyst along with thermodynamic stability calculations is presented in Section 6.3.1. In Section 6.3.2 and 6.3.3, the DFT calculated free energy barriers and reaction free energies are reported for CO<sub>2</sub> methanation and DRM reactions respectively. The key findings from the study are summarized in Section 6.4.

## 6.2 Computational details

The DFT simulations were performed using the Vienna *ab initio* Simulation Package (VASP) <sup>131,132</sup>. All calculations were done using the projector augmented wave (PAW) method <sup>142</sup> employing a plane with cut-off energy of 450 eV and a Monkhorst-pack scheme k-point sampling of 3x3x1. Spin-polarized calculations were performed, and a high level of accuracy is ensured with force convergence criteria of 10<sup>-6</sup> eV/Å per unit cell and force tolerance of 0.05 eV/Å. Generalized gradient approximation (GGA) based rPBE-vdW exchange-correlation functional is employed for studying both CO<sub>2</sub> methanation and DRM reactions. This functional, with a correction of 28 kJ/mol for gas-phase CO<sub>2</sub> energy was identified as the best functional choice for studying CO<sub>2</sub> conversion reactions irrespective of the catalyst employed <sup>178</sup>. The catalyst was modeled using 5-layer, p(4x4) unit cell with an inter-slab distance of 12 Å. The transition state (TS) for all reactions was identified using the Nudged Elastic Band (NEB) method (with 8 to 12 images) <sup>146</sup>. Using the quasi-Newton algorithm, the image closest to TS is optimized and TS was confirmed by performing vibrational frequency analysis <sup>143</sup>. The reaction energies and activation barriers of all elementary reactions in this study are reported as Gibbs free energy change. The zero-point energy and thermodynamic corrections (enthalpy and entropy) were calculated at



CO<sub>2</sub> methanation and DRM reaction conditions. For the given final state (FS), initial state (IS) and TS structures, the reaction free energy ( $G_r$ ) is calculated as  $G_r = G_{\text{tot}}(\text{FS}) - G_{\text{tot}}(\text{IS})$  and the corresponding activation barrier ( $G_a$ ) is calculated as  $G_a = G_{\text{tot}}(\text{TS}) - G_{\text{tot}}(\text{IS})$ .

The stability of SAA towards aggregation (dimer/trimer structures) is evaluated by computing the energy of aggregation ( $\Delta E_{\text{agg}}$ ). It is defined as <sup>224</sup>,

$$\Delta E_{\text{agg}}(m) = E_{\text{tot}}(m) + (m - 1) \cdot E_{\text{tot}}(\text{NiB}) - m \cdot E_{\text{tot}}(\text{SAA}) \quad (6.1)$$

where  $m$  is the cluster size ( $m = 2, 3$  for dimer and trimer respectively) and  $E_{\text{tot}}(m)$  is the total energy of  $m$  in a bulk crystal structure,  $E_{\text{tot}}(\text{NiB})$ , and  $E_{\text{tot}}(\text{SAA})$  are the DFT total energy of the surface of NiB and SAA respectively. It is to be noted that equation 6.1 corresponds to solid state reaction. A positive value of  $\Delta E_{\text{agg}}$  indicates the preference for the dispersion of dopant atom (favoring SAA structure) and a negative value indicates the preference for clustering of atoms (to form dimer/trimer) on the surface. Also, note that the entropic contributions are not accounted for calculating  $\Delta E_{\text{agg}}$  since the greater disorder of having several single atoms over a cluster (dimer/trimer) would anyways result in loss of entropy and the SAA structure will be favored. The likelihood of the dopant atom to form a single atom (by replacing one of the Ni atoms from NiB) or to form an adsorbed atom (dopant binding to surface Ni atoms) is evaluated by calculating the formation energy and adsorption energy of the dopant. The formation energy is defined as,

$$\Delta E_{\text{form}} = E_{\text{SAA}} + E_{\text{Ni-bulk}} - E_{\text{NiB}} - E_{\text{M-bulk}} \quad (6.2)$$

where  $M$  represents dopant,  $E_{\text{SAA}}$  and  $E_{\text{NiB}}$  represent DFT total energies of SAA and NiB slab respectively and  $E_{\text{bulk}}$  represents the energy of the bulk atom. The adsorption energy is defined as,

$$\Delta E_{\text{ads}} = E_{\text{M}^*} - E_{\text{NiB}} - E_{\text{M-bulk}} \quad (6.3)$$

where  $E_{\text{M}^*}$  represents DFT total energy of the adsorbed system ( $M$  adsorbed on NiB).

## 6.3 Results and Discussions

### 6.3.1 Screening of NiB-based SAA

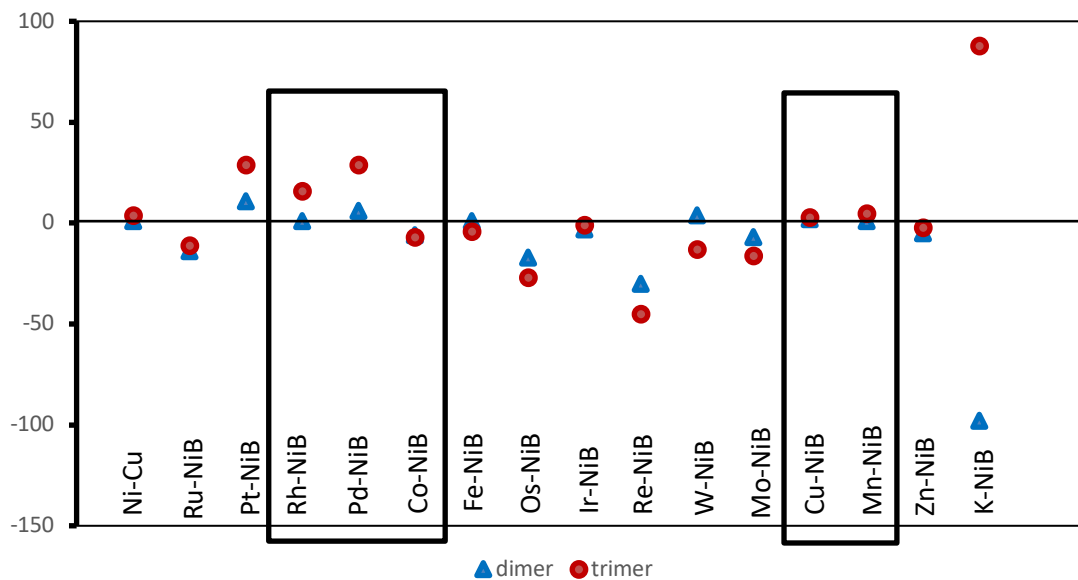


**Figure 6. 1** The energy of aggregation relative to the SAA for the clustering of dopant atoms into dimers (blue triangle) and trimers (red circle). The metal combinations that prefer dispersion are shown inside the box.

We explored NiB based SAAs that can reduce CO<sub>2</sub> activation barriers compared to clean NiB surface. Based on the ability to break C-O bond<sup>91,194,207,234–237</sup>, we considered 15 SAAs: Ru, Pt, Pd, Rh, Co, Fe, Os, Ir, Re, W, Mo, Cu, Mn, Zn, and K based NiB. The dopant atom replaces one of the surface atoms on NiB. However, NiB has two types of surface Ni atoms (with the same coordination number). As a result of surface reconstruction due to boron doping, one row of Ni atom moves up (represented as Ni (I)) while the adjacent row moves down (represented as Ni (II)) (resembling a stepped site) (*cf* Figure 5. 1 b). We identified the most stable dopant site on NiB. All the dopant atoms except Re and W prefer to replace Ni (I) from the NiB surface. In addition, the dopant atom must prefer dispersion (favor SAA configuration) on the NiB surface compared to clustering (dimer or trimer structure). A thorough computational screening is performed to

identify SAAs that are thermodynamically stable and prefer to stay as a single atom (dispersed) on NiB. To assess the thermodynamic stability of SAA, we computed the energy of aggregation for dimer and trimer structures for all metal combinations. As mentioned before, a positive value of the energy of aggregation indicates the preference for favoring the SAA structure. A similar analysis was performed by Darby et al. to assess the stability SAA catalysts<sup>223,224,226</sup>. We compared the energy of aggregation for Ni-Cu alloy and found to be exactly matching with the previously reported values<sup>223,224,226</sup>. The energy of aggregation for all metal combinations (15 dopants on NiB) is calculated and the results are shown in Figure 6. 1. It is clear that for the majority of dopants, the clustering is favored (negative energy of aggregation for dimer/trimer structures) over dispersion. Among the different dopants considered in the current study, majority of the dopants were transition state metals that can exhibit multiple oxidation states whereas K is an alkali metal with valency 1 which explains the huge difference in energy between dimer and trimer structures of K. Notably, we identified that only five of the metal (Pt, Pd, Rh, Cu and Mn on NiB) combinations are stable (favours dispersion). Consequently, CO<sub>2</sub> activation barriers are calculated only for these stable metal combinations.

#### 6.3.1.1 CO<sub>2</sub> activation barrier on NiB SAA

As mentioned before, our goal is to reduce CO<sub>2</sub> activation barriers on NiB surface and hence we evaluated the CO<sub>2</sub> direct dissociation (to form CO\* and O\*) barrier on Pt, Pd, Rh, Cu, and Mn-based NiB SAAs and compared them with that on Ni (111) and NiB surfaces. The calculated CO<sub>2</sub> activation barriers along with CO<sub>2</sub>\*, CO\*, and O\* adsorption energies (electronic energies) on all surfaces are given in Table 6. 4. The CO<sub>2</sub> direct dissociation barrier on clean NiB (124 kJ/mol) is significantly high compared to that on Ni (111) surface (54 kJ/mol). Surprisingly, there isn't a substantial reduction of CO<sub>2</sub> dissociation barriers on Pt, Pd, Rh, and Cu based NiB SAA surfaces (108 kJ/mol, 131 kJ/mol, 133 kJ/mol and 89 kJ/mol respectively) compared to clean NiB surface. However, the CO<sub>2</sub> dissociation barrier reduced significantly on Mn-NiB SAA (68 kJ/mol). Additionally, the CO<sub>2</sub> (binding energy of -94 kJ/mol) and O\* adatom (binding energy of -262 kJ/mol) binds much strongly on Mn-NiB SAA surface compared to all other surfaces

considered. Dietz et al.<sup>237</sup> predicted that metals with high oxygen affinity aids in CO<sub>2</sub> dissociation. Clearly, the low CO<sub>2</sub> activation barrier on Mn-NiB SAA is substantiated by its high oxygen affinity. The ability to bind CO<sub>2</sub> strongly and a low CO<sub>2</sub> activation barrier make Mn-NiB SAA a potential catalyst for both CO<sub>2</sub> methanation and DRM reactions. The most stable configuration of CO<sub>2</sub> adsorption on Mn-NiB SAA is shown in Figure 6. 2. However, to provide evidence for the existence of the Mn-NiB SAA catalyst, more thermodynamic stability calculations must be performed.

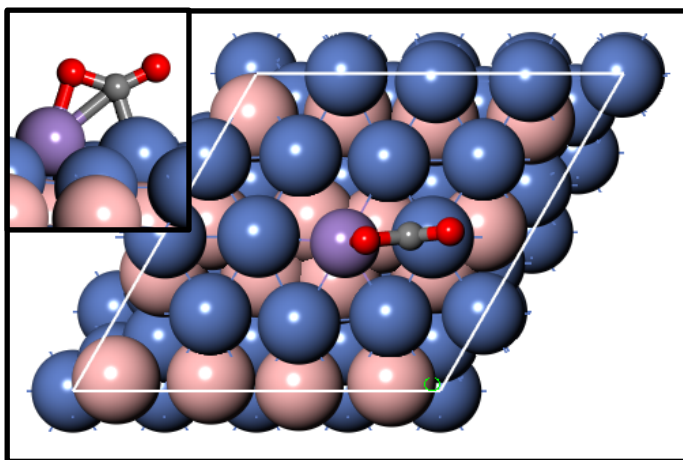


**Figure 6. 2** The most stable chemisorption configuration of CO<sub>2</sub> on Mn-NiB SAA. Blue balls represent Ni atoms, salmon balls represent B atoms, violet balls represent Mn atom, red balls represent oxygen atoms, and grey balls represents carbon atom.

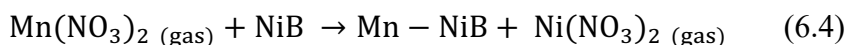
**Table 6. 4** CO<sub>2</sub>\*, CO\* and O\* adsorption energies (electronic energies) and CO<sub>2</sub> activation barriers (electronic energies) on Ni (111), NiB and Pt, Pd, Rh, Cu, and Mn-based NiB SAA surfaces

Catalyst	CO <sub>2</sub> * binding energy (kJ/mol)	CO* binding energy (kJ/mol)	O* binding energy (kJ/mol)	CO <sub>2</sub> dissociation barrier (kJ/mol)
Ni (111)	-12	-148	-230	54
NiB	-61	-144	-209	124
Pt-NiB SAA	-37	-144	-194	108

Pd-NiB SAA	-39	-140	-215	131
Rh-NiB SAA	-57	-141	-194	133
Cu-NiB SAA	-43	-145	-223	89
Mn-NiB SAA	-94	-144	-262	68

### 6.3.1.2 Stability of Mn-NiB SAA

We have comprehended that Mn prefers to exist as a single atom (by replacing one of the surface Ni atoms) on NiB compared to dimer/trimer structures. Additionally, we calculated the formation energy (Eq. 6.1) of Mn single atom on NiB. We found that the Mn formation energy is -12kJ/mol, indicating that the SAA structure is favorable. The Mn single atom could adsorb (without replacing any Ni atoms) on top of NiB slab or it can also diffuse to the bulk. The possibility of these configurations is evaluated by computing the adsorption energy of Mn on NiB (Eq. 6.2) and the diffusion barrier. A positive value of Mn adsorption energy (+15 kJ/mol) and diffusion energy (+25 kJ/mol) indicates that these structures are not favored. Furthermore, to test the stability of Mn-NiB SAA under reaction conditions, we evaluated the Gibbs free energy change of the synthesis reaction



under methanation (573 K, 10 bar) and DRM (973 K, 1 bar) conditions. This method is widely employed to assess the stabilities of boron promoted transition metals (Cu-B<sup>102</sup>, Ni-B<sup>82</sup>, Pd-B<sup>238</sup>). Mn (NO<sub>3</sub>)<sub>2</sub> is used as the source of Mn as it is the precursor used for doping Mn on Ni surfaces<sup>239–243</sup>. We found that the Gibbs free energy change for the reaction (6.4) under methanation and DRM conditions are -274 kJ/mol and -248 kJ/mol respectively. Clearly, the Mn single atom doping is favorable under these conditions. Consequently, we studied CO<sub>2</sub> methanation and DRM reactions on the Mn-NiB SAA surface.

### 6.3.2 CO<sub>2</sub> methanation on Mn-NiB SAA

For CO<sub>2</sub> methanation, we considered 46 elementary reactions consisting of CO<sub>2</sub> direct dissociation and its hydrogenation routes, CO\* direct dissociation and its hydrogenation routes, C\* hydrogenation routes, and other side reactions (*cf* Figure 6. 3 and Table 6. 5).

These reactions are studied on Mn-NiB SAA and compared with previous results on Ni (111) and Ru (001) and are described in the following sub-sections. The reaction energy and reaction barriers of all these elementary reactions are calculated and reported as Gibbs free energy change and are listed in Table 6. 5.

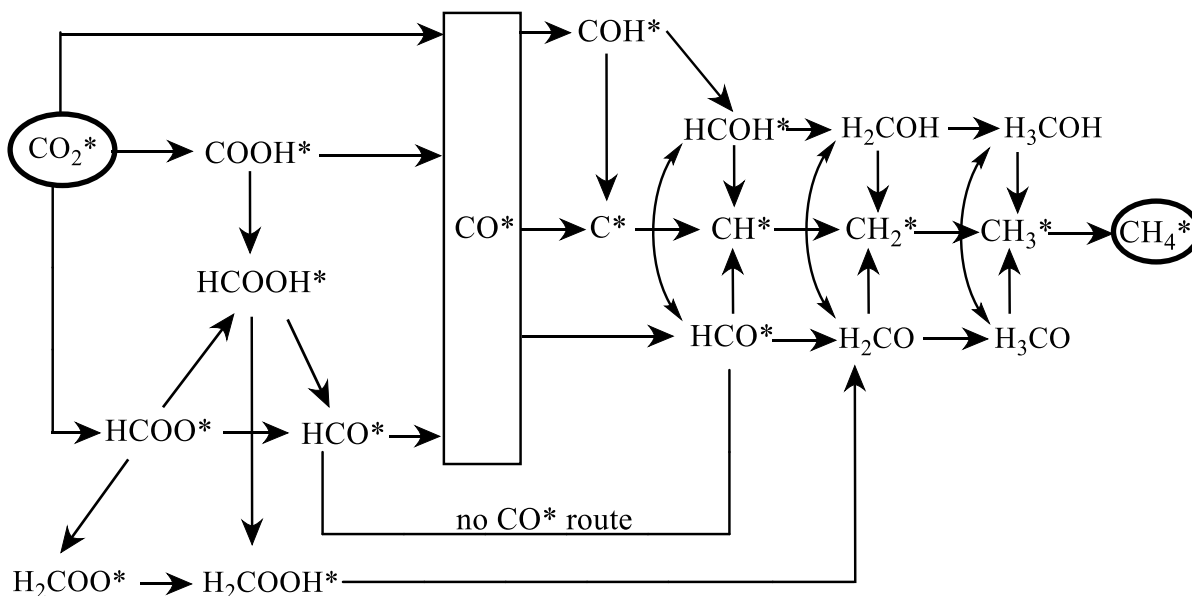


**Figure 6. 3** CO<sub>2</sub> direct dissociation and hydrogenation with/without CO\* intermediate routes.

**Table 6. 5** Calculated free energy barriers and reaction free energies (550K and 10 atm pressure) of all elementary reactions for CO<sub>2</sub> methanation on Ni (111), Ru (001), and Mn-NiB SAA surfaces. The reactions include CO<sub>2</sub> and CO direct dissociation routes, CO<sub>2</sub>, CO\* and C\* hydrogenation routes, other side reactions (H<sub>2</sub>O formation, Boudouard reaction), and desorption of products.

Reaction		Activation barrier (kJ/mol)			Reaction free energy (kJ/mol)		
		Ni (111)	Ru (001)	Mn-NiB	Ni (111)	Ru (001)	Mn-NiB
R1	CH <sub>3</sub> *+H*→CH <sub>4</sub> *	81	103	81	-63	-34	-20
R2	CH <sub>2</sub> *+H*→CH <sub>3</sub> *	57	71	43	-5	22	-46

R3	$\text{CH}^* + \text{H}^* \rightarrow \text{CH}_2^*$	64	77	46	30	67	-11
R4	$\text{C}^* + \text{H}^* \rightarrow \text{CH}^*$	88	101	54	-40	-1	-54
R5	$\text{CO}_2^* \rightarrow \text{CO}^* + \text{O}^*$	60	51	69	-106	-170	-61
R6	$\text{CO}_2^* + \text{H}^* \rightarrow \text{COOH}^*$	112	121	152	25	20	31
R7	$\text{CO}_2^* + \text{H}^* \rightarrow \text{HCOO}^*$	69	70	62	-25	-28	-47
R8	$\text{COOH}^* \rightarrow \text{CO}^* + \text{OH}^*$	17	38	13	-116	-110	-129
R9	$\text{HCOO}^* \rightarrow \text{HCO}^* + \text{O}^*$	146	104	201	43	-17	56
R10	$\text{HCO}^* \rightarrow \text{CO}^* + \text{H}^*$	19	5	35	-123	-125	-69
R11	$\text{COOH}^* + \text{H}^* \rightarrow \text{HCOOH}^*$	83	114	103	16	53	37
R12	$\text{HCOO}^* + \text{H}^* \rightarrow \text{HCOOH}^*$	113	125	147	67	101	117
R13	$\text{HCOOH}^* \rightarrow \text{HCO}^* + \text{OH}^*$	64	44	69	-9	-39	-97
R14	$\text{CH}_2\text{OH}^* + \text{H}^* \rightarrow \text{CH}_3\text{OH}^*$	84	104	90	-46	-7	-19
R15	$\text{CHOH}^* + \text{H}^* \rightarrow \text{CH}_2\text{OH}^*$	89	64	91	19	26	-29
R16	$\text{COH}^* + \text{H}^* \rightarrow \text{CHOH}^*$	89	96	49	68	103	11
R17	$\text{CO}^* + \text{H}^* \rightarrow \text{COH}^*$	209	198	249	112	100	152
R18	$\text{CH}_3\text{OH}^* \rightarrow \text{CH}_3^* + \text{OH}^*$	160	113	115	-29	-63	-130
R19	$\text{CH}_2\text{OH}^* \rightarrow \text{CH}_2^* + \text{OH}^*$	64	43	19	-70	-92	-102
R20	$\text{CHOH}^* \rightarrow \text{CH}^* + \text{OH}^*$	62	30	39	-81	-133	-121
R21	$\text{COH}^* \rightarrow \text{C}^* + \text{OH}^*$	166	105	109	27	-29	-56
R22	$\text{CH}_2\text{O}^* + \text{H}^* \rightarrow \text{CH}_3\text{O}^*$	60	82	57	-42	-10	-32
R23	$\text{CHO}^* + \text{H}^* \rightarrow \text{CH}_2\text{O}^*$	73	66	61	35	49	4
R24	$\text{CH}_3\text{O}^* \rightarrow \text{CH}_3^* + \text{O}^*$	127	117	160	-6	-84	-20
R25	$\text{CH}_2^* + \text{O}^* \rightarrow \text{CH}_2\text{O}^*$	133	188	131	44	117	6
R26	$\text{CHO}^* \rightarrow \text{CH}^* + \text{O}^*$	104	105	160	-40	-135	8
R27	$\text{CO}^* \rightarrow \text{C}^* + \text{O}^*$	282	217	294	124	-9	132
R28	$\text{CH}_3\text{OH}^* + ^* \rightarrow \text{CH}_3\text{O}^* + \text{H}^*$	94	78	64	-38	-58	-73
R29	$\text{CH}_2\text{OH}^* + ^* \rightarrow \text{CH}_2\text{O}^* + \text{H}^*$	67	86	70	-41	-55	-60
R30	$\text{CHOH}^* + ^* \rightarrow \text{HCO}^* + \text{H}^*$	61	68	92	-56	-79	-94
R31	$\text{O}^* + \text{H}^* \rightarrow \text{OH}^*$	118	166	129	15	80	-37
R32	$\text{OH}^* + \text{H}^* \rightarrow \text{H}_2\text{O}^*$	133	125	177	29	38	71

R33	$\text{H}_2 \rightarrow \text{H}^* + \text{H}^*$	111	77	107	43	18	43
R34	$\text{OH}^* + \text{OH}^* \rightarrow \text{H}_2\text{O}^* + \text{O}^*$	87	64	186	13	-42	108
R35	$\text{CO}_2^* + \text{C}^* \rightarrow 2\text{CO}^*$	153	142	116	-229	-161	-194
R36	$\text{HCOO}^* + \text{H}^* \rightarrow \text{H}_2\text{COO}^*$	192	168	204	104	93	138
R37	$\text{HCOOH}^* + \text{H}^* \rightarrow \text{H}_2\text{COOH}^*$	118	121	112	47	42	3
R38	$\text{H}_2\text{COO}^* + \text{H}^* \rightarrow \text{H}_2\text{COOH}^*$	90	156	112	10	51	-18
R39	$\text{H}_2\text{COO}^* \rightarrow \text{H}_2\text{CO}^* + \text{O}^*$	32	36	46	-26	-60	-79
R40	$\text{H}_2\text{COOH}^* \rightarrow \text{H}_2\text{CO}^* + \text{OH}^*$	34	18	20	-21	-32	-96
R41	$\text{CO}_2 \rightarrow \text{CO}_2^*$	-	-		81	58	-2
R42	$\text{CO}^* \rightarrow \text{CO}$	-	-		49	72	52
R43	$\text{H}_2\text{O}^* \rightarrow \text{H}_2\text{O} + ^*$	-	-		-49	-34	-4
R44	$\text{CH}_4^* \rightarrow \text{CH}_4$	-	-		-49	-37	-33
R45	$\text{HCOOH}^* \rightarrow \text{HCOOH}$	-	-		-17	-1	-25
R46	$\text{CH}_3\text{OH}^* \rightarrow \text{CH}_3\text{OH}$	-	-		-14	-1	1

#### 6.3.2.1 CO<sub>2</sub> direct dissociation route vs CO<sub>2</sub> hydrogenation routes to form CO\* intermediate (R5 – R13)

As mentioned in the previous section, CO<sub>2</sub> direct dissociation (R5) is exergonic (-61 kJ/mol) and has a low barrier of 69 kJ/mol. Additionally, CO<sub>2</sub> can undergo hydrogenation by reacting with H\* adatom (*cf* Figure 6. 3). We investigated these routes and the corresponding free energies are reported in Figure 6. 4.



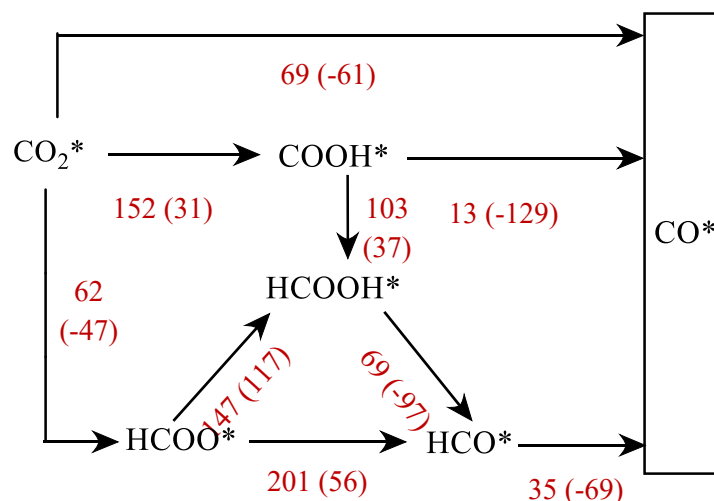


**Figure 6. 4** CO<sub>2</sub> activation and dissociation on Mn-NiB SAA. Free energy barriers and reaction free energies (inside brackets) on Mn-NiB SAA are shown in red color.

The H\* adatom formed via H<sub>2</sub> dissociation (R33) can react with CO<sub>2</sub> to form COOH\*/HCOO\* intermediates. Interestingly the COOH\* formation (R6) is endergonic (31 kJ/mol) and must overcome a high barrier of 152 kJ/mol. On the contrary, HCOO\* formation (R7) is exergonic (-47 kJ/mol) and has a low barrier of 62 kJ/mol. Therefore, this reaction is kinetically and thermodynamically feasible. However, the activation of HCOO\* has significantly high barriers. HCOO\* can either undergo further hydrogenation to form HCOOH\* (R12) or dissociates to form HCO\* (R9). Both these reactions must overcome very high barriers (147 kJ/mol for R12 and 201 kJ/mol for R9). Hence, CO\* formation via CO<sub>2</sub> hydrogenation is not thermodynamically and kinetically favored and CO<sub>2</sub> direct dissociation to form CO\* is the preferred CO<sub>2</sub> activation route on Mn-NiB SAA.

#### 6.3.2.2 CO direct dissociation route vs CO hydrogenation routes to form CH<sub>x</sub>\* (x = 0 - 3) (R14 – R30)

CO can either dissociate to form C\* intermediate or undergoes hydrogenation to form COH\*/HCO\* intermediates. These can undergo further hydrogenation (forming CH<sub>x</sub>OH\*/CH<sub>x</sub>O\* (x = 1 - 3)) followed by dissociation to form CH<sub>x</sub> (x = 1 - 3) intermediates. These routes are investigated, and the free energies are shown in Figure 6. 5.

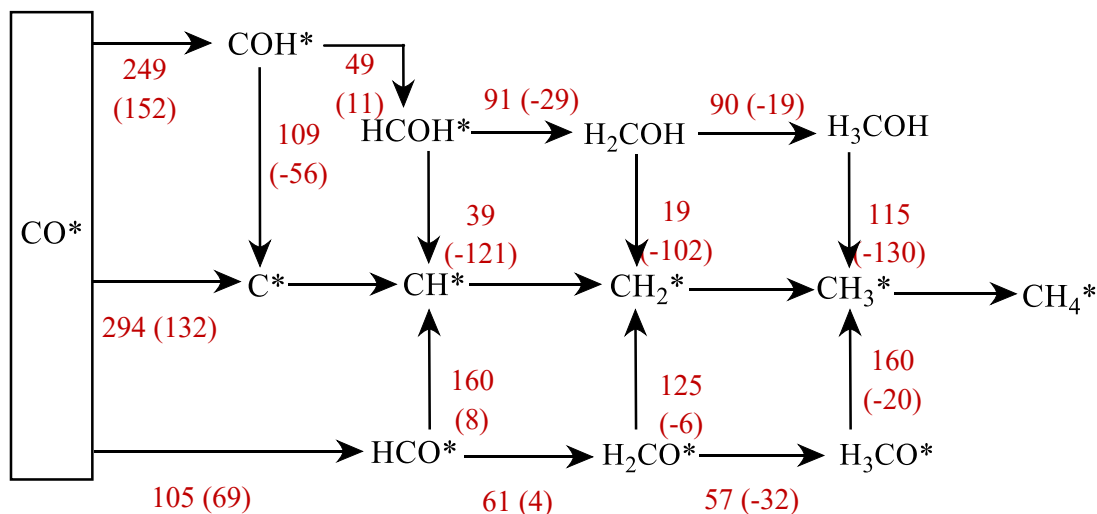


**Figure 6. 5** Free energy barriers and reaction free energies (inside brackets) for CO\* dissociation routes.

The dissociation of CO\* to form C\* and O\* (R27) must overcome a huge barrier of 294 kJ/mol. Similarly, CO\* hydrogenation to form COH\* (R17) also has a very high barrier (249 kJ/mol). Notably, both these reactions are highly endergonic, making them thermodynamically not favorable. On the contrary, CO\* hydrogenation to HCO\* (reversible reaction of R10) has a significantly low barrier (105 kJ/mol) making it the kinetically favored CO\* activation route. Both COH\* and HCO\* can undergo sequential hydrogenation to form CH<sub>x</sub>OH/CH<sub>x</sub>O (x = 1 - 3) intermediates. The CH<sub>x</sub>OH\*/CH<sub>x</sub>O\* (x = 1 - 3) intermediates may dissociate to form CH<sub>x</sub> (x = 1 - 3). Notably, the CH<sub>x</sub>OH\* (x = 1 - 3) dissociation is highly exergonic and has significantly lower barriers than CH<sub>x</sub>O (x = 1 - 3) dissociation (*cf* Figure 6. 5). However, the high barrier of COH\* formation from CO\* makes the CH<sub>x</sub>OH (x = 1 - 3) routes (COH\* hydrogenation and CH<sub>x</sub>OH dissociation) less favorable. The sequential hydrogenation of HCO\* leads to the formation of CH<sub>2</sub>O\* (R23) and CH<sub>3</sub>O\* (R22) and these reactions have barriers of 61 kJ/mol and 57 kJ/mol respectively. Particularly, the CH<sub>2</sub>O\* dissociation to form CH<sub>2</sub>\* (reversible reaction of R25) has a lower barrier (125 kJ/mol) compared to HCO\* (R26) and CH<sub>3</sub>O\* (R24) dissociation (160 kJ/mol for both R24 and R26). In short, the CO\* hydrogenation via HCO\* intermediate is the most

avored  $\text{CO}^*$  activation route. The  $\text{HCO}^*$  formed undergoes hydrogenation forming  $\text{CH}_2\text{O}^*$  followed by its dissociation to form  $\text{CH}_2^*$ .

### 6.3.2.3 $\text{CO}_2$ activation routes without $\text{CO}^*$ intermediate (R36 – R40)

In the previous section,  $\text{CO}_2$  activation via  $\text{CO}^*$  intermediate was discussed. Here we investigate  $\text{CO}_2$  activation routes without forming  $\text{CO}^*$  as an intermediate (via  $\text{HCOO}^*$  intermediate) and the free energies are shown in Figure 6. 6.

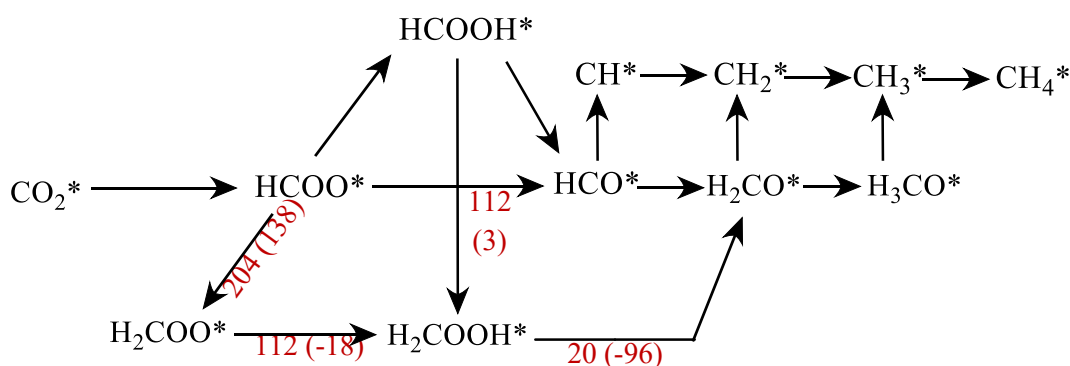


**Figure 6. 6** Free energy barriers and reaction free energies (inside brackets) for  $\text{CO}_2^*$  dissociation routes without forming  $\text{CO}^*$  as an intermediate.

The  $\text{HCOO}^*$  and  $\text{HCOOH}^*$  formed (via  $\text{CO}_2$  hydrogenation) can undergo further hydrogenation to form  $\text{H}_2\text{COO}^*$  (R36) and  $\text{H}_2\text{COOH}^*$  (R38) respectively. However, the barriers for these reactions are much higher (204 kJ/mol and 112 kJ/mol respectively) than  $\text{CO}_2$  direct dissociation (69 kJ/mol) barriers are hence these routes are not favored. Hence,  $\text{CO}_2$  methanation without forming  $\text{CO}^*$  intermediate is not favored on Mn-NiB SAA.

### 6.3.2.4 $\text{CH}_x^*$ ( $x = 0 - 3$ ) hydrogenation (R1 – R4)

The  $\text{CH}_x$  ( $x = 0 - 3$ ) formed from the dissociation of  $\text{CH}_x\text{OH}/\text{CH}_x\text{O}$  ( $x = 0 - 3$ ) can undergo sequential hydrogenation to form  $\text{CH}_4$ . The sequential hydrogenation of  $\text{C}^*$  is exergonic and has low barriers as shown in Figure 6. 7. The highest barrier (81 kJ/mol) is for the  $\text{CH}_3^*$  hydrogenation (R1) step. It must be noted though that  $\text{C}^*$  hydrogenation to  $\text{CH}^*$  (R4)

is limited by the very high barriers for C\* formation (via COH\* (R21) or CO\* (R27) dissociation). Additionally, CH<sub>2</sub>\* formation (via CH<sub>2</sub>O\* dissociation) was identified as the favored route for CO\* hydrogenation (*cf* Figure 6. 5). Subsequently, the CH<sub>2</sub>\* thus formed favors sequential hydrogenation to form CH<sub>4</sub>.

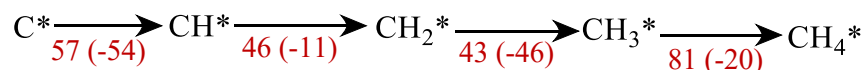


**Figure 6. 7** Free energy barriers and reaction free energies (inside brackets) for sequential hydrogenation of C\*.

#### 6.3.2.5 Side reactions (water formation) and desorption of products (R31 – R35, R43, and R44)

Hydrogenation of O\* adatom (formed from CO<sub>2</sub> dissociation) leads to OH\* formation (R31). This reaction is exergonic (-37 kJ/mol) and must overcome a barrier of 129 kJ/mol. The OH\* can react with H\* (R32) or OH\* (R34) to form H<sub>2</sub>O, one of the products. Both these reactions (R32 and R34) are endergonic and have to overcome a barrier of 177 kJ/mol and 186 kJ/mol respectively.

The desorption energy (electronic energy) of the products, CH<sub>4</sub> (R44) and H<sub>2</sub>O (R43) are 28 kJ/mol and 80 kJ/mol respectively.

#### 6.3.2.6 Comparison of reactions on Ni (111), Ru (001) and Mn-NiB SAA

The energetics for the important reactions in CO<sub>2</sub> methanation on Mn-NiB SAA is compared to that on Ni (111) and Ru (001) (*cf* Table 6. 5) and are presented here.

CO<sub>2</sub> activation route: CO<sub>2</sub> adsorbs much strongly on Mn-NiB SAA (electronic energy of -94 kJ/mol) than on Ni (111) (-12 kJ/mol) and Ru (001) (-44 kJ/mol). The free energy diagram of CO<sub>2</sub> activation routes (direct dissociation and hydrogenation via HCOO\*) are shown in Figure 6. 8. Direct dissociation CO<sub>2</sub> to form CO\* and O\* (R5) is exergonic on all three surfaces and has low free energy barriers (60 kJ/mol, 51 kJ/mol and 69 kJ/mol on

Ni (111), Ru (001) and Mn-NiB SAA respectively). Interestingly, CO<sub>2</sub> hydrogenation to form HCOO\* (R7) also has low barriers on all the surfaces (69 kJ/mol, 70 kJ/mol, and 62 kJ/mol on Ni (111), Ru (001) and Mn-NiB SAA respectively). However, the activation of HCOO\* (dissociation to form HCO\* (R9) or hydrogenation to form H<sub>2</sub>COO\* (R36)/HCOOH\* (R12)) has very high barriers compared to CO<sub>2</sub> direct dissociation route. Notably, the barriers via the HCOO\* route is significantly higher on Mn-NiB SAA compared to Ni and Ru (*cf* Figure 6. 8). Additionally, CO<sub>2</sub> hydrogenation via COOH\* (R6) intermediate (not shown in Figure 6. 8) is also higher on Mn-NiB SAA compared to Ni and Ru (*cf* Table 6. 5). Therefore, CO<sub>2</sub> direct dissociation is the most preferred CO<sub>2</sub> activation route on Mn-NiB SAA and the activation barrier is similar to that on Ni and Ru surfaces. Due to high CO<sub>2</sub> adsorption energy and a low CO<sub>2</sub> activation barrier, we expect high CO<sub>2</sub> conversion on Mn-NiB SAA.

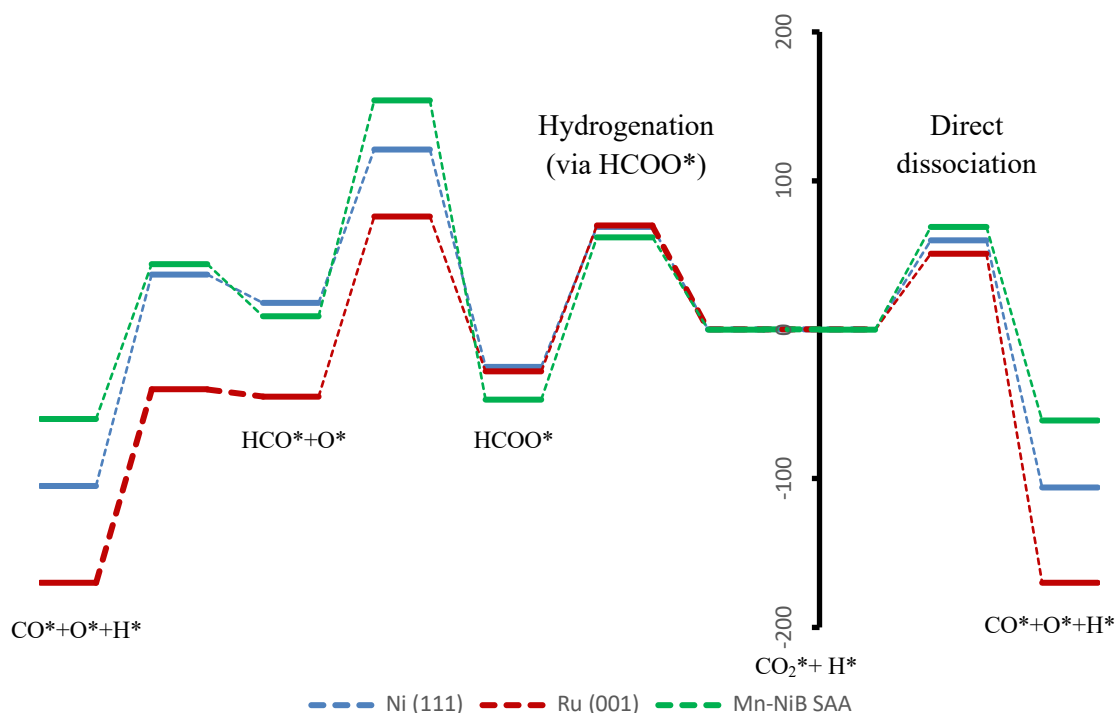


**Figure 6. 8** The free energy diagram of the CO<sub>2</sub> activation route on Ni (111) (blue), Ru (001) (red), and Mn-NiB SAA (green). The diagram on the right side shows the direct dissociation path and the one on the left side shows hydrogenation via the HCOO\* route.

CO\* activation route: The CO\* (formed via CO<sub>2</sub> direct dissociation) dissociation to form C\* (R27) has significantly higher barriers (282 kJ/mol, 217 kJ/mol and 294 kJ/mol on Ni

(111), Ru (001) and Mn-NiB SAA respectively) compared to CO\* hydrogenation on all three surfaces. CO\* hydrogenation (to form COH\* (R17) or HCO\* (reversible reaction of R10)) is endergonic on all the surfaces and the free energy diagram is shown in Figure 6.9. Notably, on Mn-NiB SAA, the CO\* hydrogenation to form COH\* is more endergonic than on Ni and Ru (more by 40 kJ/mol and 52 kJ/mol respectively). Whereas HCO\* formation on Mn-NiB SAA is less endergonic compared to Ni and Ru surfaces (lower by 54 kJ/mol and 56 kJ/mol respectively). Importantly, the free energy barrier for COH\* formation (209 kJ/mol, 198 kJ/mol and 249 kJ/mol on Ni (111), Ru (001) and Mn-NiB SAA respectively) is much higher than that of HCO\* formation (143 kJ/mol, 130 kJ/mol and 105 kJ/mol on Ni (111), Ru (001) and Mn-NiB SAA respectively) on all the surfaces. Hence, CO\* activation via the HCO\* route is kinetically preferred on these surfaces. Particularly, CO\* hydrogenation to form HCO\* has the lowest barrier on the Mn-NiB SAA surface. Therefore, the most preferred CO\* activation route (via HCO\*) is kinetically and thermodynamically more favored on Mn-NiB SAA compared to Ni and Ru surfaces. Subsequently, CO\* can react at a faster rate and would result in less CO\* poisoning on Mn-NiB SAA.

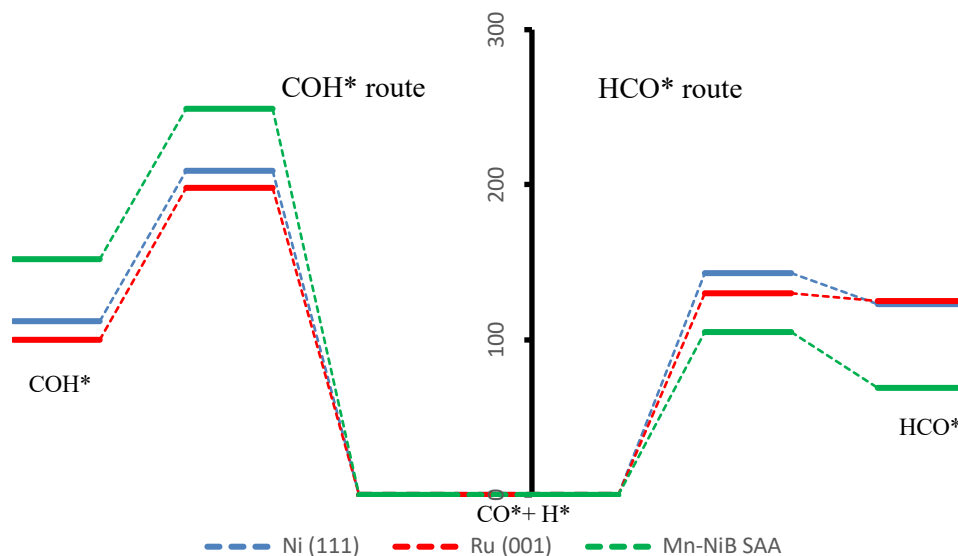


**Figure 6. 9** The free energy diagram of the CO activation route on Ni (111) (blue), Ru (001) (red), and Mn-NiB SAA (green). The diagram on the right side shows CO\*

hydrogenation via  $\text{HCO}^*$  and the one on the left side shows  $\text{CO}^*$  hydrogenation via  $\text{COH}^*$  route.

**$\text{CH}^*$  sequential hydrogenation:** The sequential hydrogenation of  $\text{CH}^*$  leads to  $\text{CH}_4$  (R1 – R3) formation and the free energy diagram is shown in Figure 6. 10. Interestingly, all the  $\text{CH}_x^*$  ( $x = 1 - 3$ ) hydrogenation reactions are exergonic on Mn-NiB SAA whereas only  $\text{CH}_3^*$  hydrogenation (R1) is exergonic on Ru (*cf* Table 6. 4). Both  $\text{CH}_2^*$  (R2) and  $\text{CH}_3^*$  hydrogenation are exergonic on Ni. Consequently, the overall reaction is exergonic on Mn-NiB SAA (-77 kJ/mol) whereas it is endergonic on Ru (001) (55 kJ/mol) and less exergonic on Ni (111) (-38 kJ/mol). Additionally, the barriers are significantly lower on Mn-NiB SAA compared to Ni and Ru. Thus, the sequential hydrogenation reactions (to form  $\text{CH}_4$ ) are thermodynamically and kinetically favorable on Mn-NiB SAA.

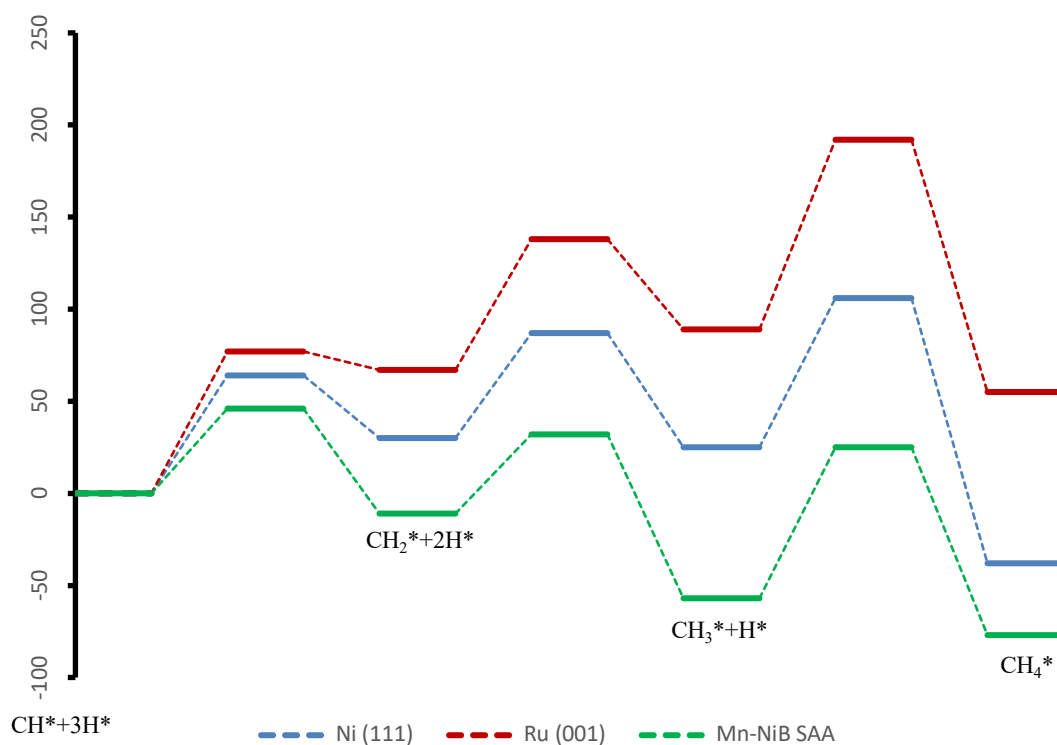


**Figure 6. 10** The free energy diagram of  $\text{CH}^*$  stepwise hydrogenation on Ni (111) (blue), Ru (001) (red), and Mn-NiB SAA (green).

In short,  $\text{CO}_2$  adsorbs much strongly on Mn-NiB SAA. The  $\text{CO}_2$  activation barrier (direct dissociation) is also low and comparable to that on Ni and Ru. Additionally,  $\text{CO}^*$  activation

(hydrogenation via  $\text{HCO}^*$ ) is thermodynamically and kinetically more favored on Mn-NiB SAA compared to Ni and Ru. Thus, we expect high  $\text{CO}_2$  conversion and low  $\text{CO}^*$  poisoning on Mn-NiB SAA. Moreover, the  $\text{CH}^*$  sequential hydrogenation reactions are exergonic and have low barriers on Mn-NiB SAA. Thus, Mn-NiB SAA is a potential catalyst for  $\text{CO}_2$  methanation.

### 6.3.3 DRM on Mn-NiB SAA

In the current study, we considered 38 elementary reactions for DRM. The reaction network includes multiple  $\text{CO}_2$  activation routes (direct dissociation and hydrogenation),  $\text{CH}_4$  activation routes (sequential dehydrogenation,  $\text{CH}_x$  ( $x = 0 - 3$ ) oxidation by  $\text{OH}^*$  and  $\text{O}^*$ , other side reactions ( $\text{H}_2\text{O}$  formation, Boudouard reaction) and desorption of products (*cf* Figure 6. 11 and Table 6. 6). We studied all these reactions on the Mn-NiB SAA surface and are presented in the following sub-sections. The reaction energies and reaction barriers of all the elementary reactions are reported as Gibbs free energy change (unless otherwise stated) and are listed in Table 6. 6.

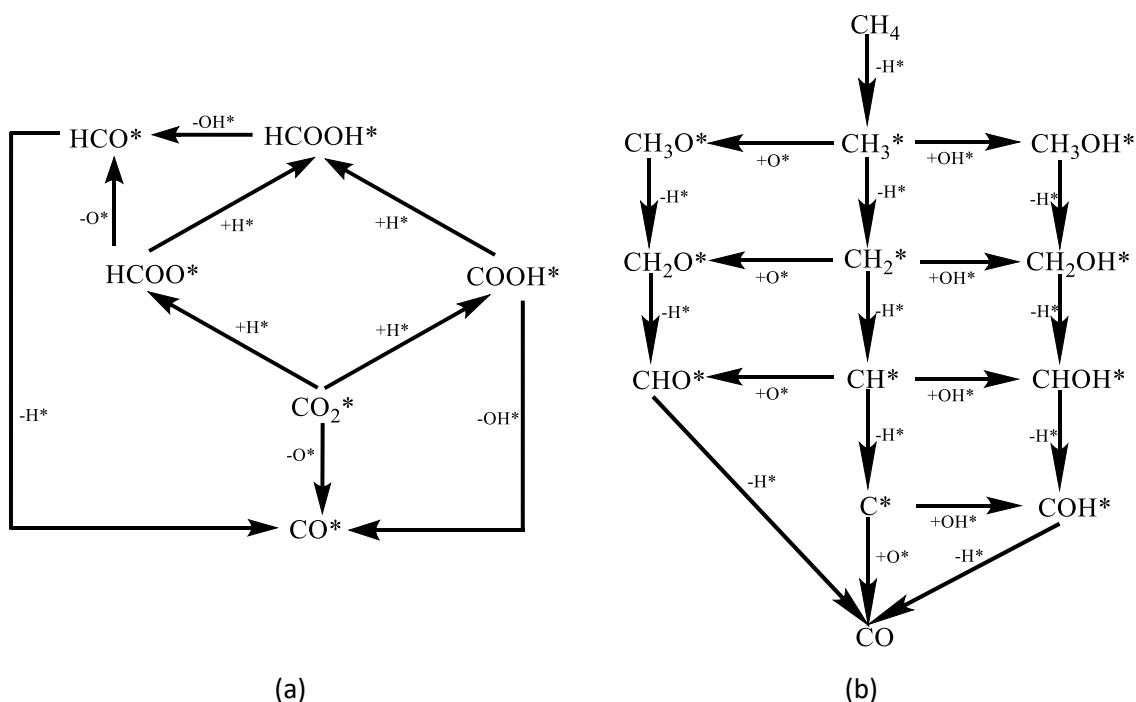


**Figure 6. 11** (a)  $\text{CO}_2$  dissociation routes and (b)  $\text{CH}_4$  sequential dehydrogenation routes and  $\text{CH}_x$  ( $x = 0$  to 3) oxidation by  $\text{OH}^*$  and  $\text{O}^*$  routes.



**Table 6. 6** Calculated free energy barriers and reaction free energies of all elementary reactions for DRM on Ni (111), NiB, and Mn-NiB SAA surfaces. The reactions include CH<sub>4</sub> sequential dehydrogenation routes, CO<sub>2</sub> dissociation routes, CH<sub>x</sub> (x = 0 - 3) oxidation by OH\* and O\* routes, other side reactions (H<sub>2</sub>O formation, Boudouard reaction) and desorption of products.

Reaction		Activation barrier (kJ/mol)			Reaction free energy (kJ/mol)		
		Ni (111)	NiB	Mn-NiB	Ni (111)	NiB	Mn-NiB
R1	CH <sub>4</sub> * → CH <sub>3</sub> * + H*	164	107	113	83	55	36
R2	CH <sub>3</sub> * → CH <sub>2</sub> * + H*	58	87	93	5	62	46
R3	CH <sub>2</sub> * → CH* + H*	35	56	59	-25	13	15
R4	CH* → C* + H*	126	96	104	41	55	52
R5	CO <sub>2</sub> * → CO* + O*	63	107	70	-101	-48	-62
R6	CO <sub>2</sub> * + H* → COOH*	112	143	156	30	26	37
R7	CO <sub>2</sub> * + H* → HCOO*	69	61	64	-18	-54	-39
R8	COOH* → CO* + OH*	7	59	5	-120	-120	-139
R9	HCOO* → HCO* + O*	148	226	196	45	113	52
R10	HCO* → CO* + H*	14	13	34	-126	-107	-75
R11	COOH* + H* → HCOOH*	82	89	103	11	27	34
R12	HCOO* + H* → HCOOH*	104	132	140	60	107	110
R13	HCOOH* → HCO* + OH*	63	72	68	-5	-39	-97
R14	CH <sub>3</sub> OH* → CH <sub>2</sub> OH* + H*	143	113	116	60	45	24
R15	CH <sub>2</sub> OH* → CHOH* + H*	72	72	117	-19	11	21
R16	CHOH* → COH* + H*	20	65	38	-69	18	-7
R17	COH* → CO* + H*	100	72	97	-112	-176	-159
R18	CH <sub>3</sub> * + OH* → CH <sub>3</sub> OH*	182	218	238	18	63	130
R19	CH <sub>2</sub> * + OH* → CH <sub>2</sub> OH*	133	94	119	73	45	108
R20	CH* + OH* → CHOH*	137	146	159	79	44	115
R21	C* + OH* → COH*	133	139	166	-30	7	55

R22	$\text{CH}_3\text{O}^* \rightarrow \text{CH}_2\text{O}^* + \text{H}^*$	102	89	88	46	42	32
R23	$\text{CH}_2\text{O}^* \rightarrow \text{CHO}^* + \text{H}^*$	34	43	55	-37	-14	-6
R24	$\text{CH}_3^* + \text{O}^* \rightarrow \text{CH}_3\text{O}^*$	130	151	177	6	-5	20
R25	$\text{CH}_2^* + \text{O}^* \rightarrow \text{CH}_2\text{O}^*$	132	102	130	47	-26	6
R26	$\text{CH}^* + \text{O}^* \rightarrow \text{CHO}^*$	142	158	145	35	-53	-14
R27	$\text{C}^* + \text{O}^* \rightarrow \text{CO}^*$	156	159	159	-131	-215	-143
R28	$\text{CH}_3\text{OH}^{**} \rightarrow \text{CH}_3\text{O}^* + \text{H}^*$	97	87	61	-23	-23	-70
R29	$\text{CH}_2\text{OH}^{**} \rightarrow \text{CH}_2\text{O}^* + \text{H}^*$	70	96	71	-37	-26	-62
R30	$\text{CHOH}^{**} \rightarrow \text{HCO}^* + \text{H}^*$	57	72	94	-54	-51	-91
R31	$\text{O}^* + \text{H}^* \rightarrow \text{OH}^*$	114	117	125	10	-45	-39
R32	$\text{OH}^* + \text{H}^* \rightarrow \text{H}_2\text{O}^*$	125	121	173	18	14	65
R33	$\text{H}^* + \text{H}^* \rightarrow \text{H}_2$	57	58	59	-69	-84	-66
R34	$\text{OH}^* + \text{OH}^* \rightarrow \text{H}_2\text{O}^* + \text{O}^*$	89	113	191	8	59	104
R35	$\text{CO}_2^* + \text{C}^* \rightarrow 2\text{CO}^*$	154	132	122	-232	-263	-205
R36	$\text{CO}_2 \rightarrow \text{CO}_2^*$	-	-	-	107	67	24
R37	$\text{CO}^* \rightarrow \text{CO}$	-	-	-	19	26	28
R38	$\text{H}_2\text{O}^* \rightarrow \text{H}_2\text{O} + ^*$	-	-	-	-65	-39	-23

### 6.3.3.1 CH<sub>4</sub> stepwise dehydrogenation (R1 - R4)

Methane weakly adsorbs on Mn-NiB SAA with binding energy (electronic energy) of -29 kJ/mol. The stepwise dissociation of methane produces methyl ( $\text{CH}_3^*$ ), methyldene ( $\text{CH}_2^*$ ), methyne ( $\text{CH}^*$ ), and carbon/coke ( $\text{C}^*$ ) and the free energies are shown in Figure 6. 12. Interestingly, the dehydrogenation steps are endergonic and  $\text{CH}_4$  dissociation (R1) has the highest barrier (113 kJ/mol), forming  $\text{CH}_3^*$  (R2).  $\text{CH}_3^*$  dissociation must overcome a barrier of 93 kJ/mol to form  $\text{CH}_2^*$ .  $\text{CH}_2^*$  (R3) dissociation has the lowest barrier (59 kJ/mol) and has a reaction free energy of 15 kJ/mol. Coke formation via  $\text{CH}^*$  dissociation (R4) has high endergonicity (52 kJ/mol) and must overcome a barrier of 104 kJ/mol.

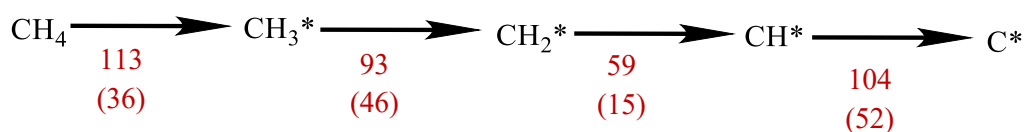


**Figure 6. 12** Free energy barriers and reaction free energies (inside brackets) form methane dissociation on Mn-NiB SAA.

### 6.3.3.2 CO<sub>2</sub> activation mechanism (R5, R6 – R13)

We have considered direct dissociation and hydrogenation (H\* adatom is generated from CH<sub>4</sub> sequential dehydrogenation) routes for CO<sub>2</sub> conversion to form CO\*. These pathways are already discussed in section 6.3.2.1 for the methanation reaction. The trends in reaction energetics and the most preferred pathway remains the same for DRM reaction. However, there is a slight difference in energetics as a result of the change in reaction conditions. These free energies are shown in Figure 6. 13. Direct dissociation of CO<sub>2</sub> (reaction free energy of -62 kJ/mol and free energy barrier of 70 kJ/mol) is the most preferred CO<sub>2</sub> activation route.

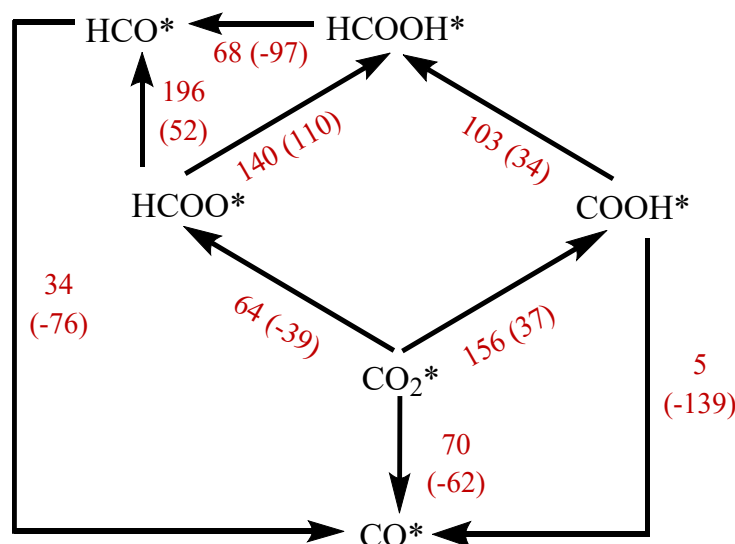


**Figure 6. 13** Free energy barriers and reaction free energies (inside brackets) for CO<sub>2</sub> activation and dissociation on Mn-NiB SAA.

6.3.3.3  $\text{CH}_x$  ( $x = 0 - 3$ ) Oxidation ( $\text{O}^*/\text{OH}^*$ ) (R18 – R21, R24 – R27)

The  $\text{O}^*$  adatom formed from  $\text{CO}_2$  dissociation can react with  $\text{H}^*$  adatom (from  $\text{CH}_4$  dissociation) to form  $\text{OH}^*$ . This reaction is thermodynamically feasible with a reaction free energy of -39 kJ/mol. Subsequently,  $\text{O}^*/\text{OH}^*$  can react with  $\text{CH}_x$  ( $x = 0 - 3$ ) species forming  $\text{CH}_x\text{O}$  ( $x = 0 - 3$ )/  $\text{CH}_x\text{OH}^*$  ( $x = 0 - 3$ ) on the surface. These oxidation reactions are discussed here, and the free energies are shown in Figure 6. 14.

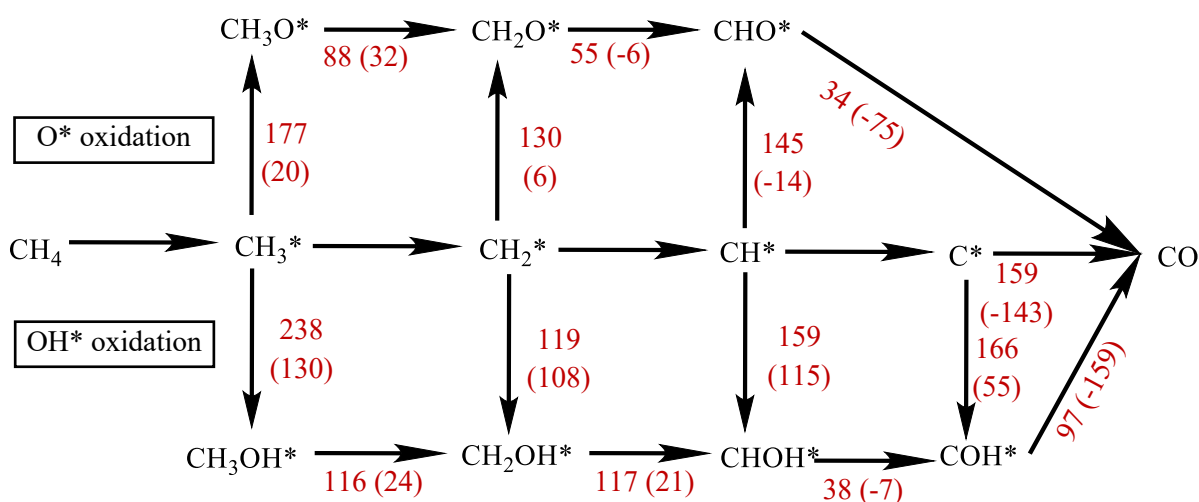


**Figure 6. 14** Free energy barriers and reaction free energies (inside brackets) for  $\text{CH}_x$  oxidation by  $\text{O}^*/\text{OH}^*$  routes.

Notably,  $\text{CH}_x$  ( $x = 0 - 3$ ) oxidation by  $\text{OH}^*$  to form  $\text{CH}_x\text{OH}^*$  ( $x = 0 - 3$ ) is highly endergonic compared to  $\text{CH}_x\text{O}$  ( $x = 0 - 3$ ) formation (via  $\text{CH}_x$  ( $x = 0 - 3$ ) oxidation by  $\text{O}^*$ ). Interestingly,  $\text{CH}_3^*$  oxidation (both  $\text{O}^*$  (R24) and  $\text{OH}^*$  (R18)) has the highest barriers (238 kJ/mol and 177 kJ/mol respectively). The barrier for  $\text{CH}_2^*$  oxidation by  $\text{O}^*$  (R25) is 11 kJ/mol higher than the corresponding  $\text{OH}^*$  (R19) oxidation barrier (119 kJ/mol). However, the  $\text{O}^*$  oxidation of  $\text{CH}_2^*$  has less endergonicity (6 kJ/mol) compared to  $\text{OH}^*$  oxidation (108 kJ/mol). The  $\text{CH}^*$  oxidation by  $\text{O}^*$  (R26) is exergonic (-14 kJ/mol) and has a low barrier (145 kJ/mol) compared to corresponding  $\text{OH}^*$  oxidation (R20) (barrier of 159 kJ/mol) step. Lastly,  $\text{C}^*$  oxidation by  $\text{OH}^*$  (R21) is also endergonic (55 kJ/mol) and must overcome a high barrier of 166 kJ/mol whereas  $\text{C}^*$  oxidation by  $\text{O}^*$  (R27) is highly exergonic (-143 kJ/mol) and has to overcome a barrier of 159 kJ/mol. Clearly, the barriers for sequential

dehydrogenation of  $\text{CH}_x$  ( $x = 1 - 3$ ) are significantly lower than corresponding oxidation by both  $\text{O}^*$  and  $\text{OH}^*$ . Hence, sequential dehydrogenation of  $\text{CH}_x$  ( $x = 1 - 4$ ) is the kinetically favored  $\text{CH}_4$  activation route. Interestingly,  $\text{C}^*$  oxidation by  $\text{O}^*$  is kinetically and thermodynamically favored compared to  $\text{OH}^*$  oxidation.

#### 6.3.3.4 $\text{CH}_x\text{OH}$ and $\text{CH}_x\text{O}$ ( $x = 1 - 3$ ) dehydrogenation (R14 – R16, R22, R23)

The free energies for successive dehydrogenation of  $\text{CH}_x\text{OH}$  and  $\text{CH}_x\text{O}$  ( $x = 1 - 3$ ) are discussed here. Notably, the reaction free energies and free energy barriers for  $\text{CH}_x\text{OH}$  ( $x = 1 - 3$ ) dehydrogenation is lower than that for  $\text{CH}_x\text{O}$  ( $x = 1 - 3$ ) dehydrogenation. The free energies are shown in Figure 6. 14. It must be noted though that the sequential dehydrogenation of  $\text{CH}_4$  to  $\text{C}^*$  has a lower barrier than  $\text{CH}_x$  ( $x = 1-3$ ) oxidation (both  $\text{O}^*$  and  $\text{OH}^*$ ), the  $\text{CH}_x\text{OH}$  and  $\text{CH}_x\text{O}$  ( $x = 1-3$ ) dehydrogenation steps are not favored kinetically.

#### 6.3.3.5 Side reactions (water formation and Boudouard reaction) (R31, R32, R34 and R35) and Desorption of products (R33 and R37)

The  $\text{H}_2\text{O}$  formation reactions are already discussed in section 3.2.5 and the free energies are given in Table 6. 6. Interestingly Boudouard reaction (R35) is highly exothermic (-205 kJ/mol) and the activation barrier (122 kJ/mol) is 34 kJ/mol lower than  $\text{C}^*$  oxidation by  $\text{O}^*$ . Thus, the Boudouard reaction offers a supplementary route for  $\text{C}^*$  conversion to form  $\text{CO}^*$  and hence we expect high  $\text{C}^*$  conversion on Mn-NiB SAA.

The desorption energy (electronic energy) of  $\text{CO}^*$  (R37) was calculated to be 144 kJ/mol. The combinative desorption of hydrogen (R33) is exergonic (-66 kJ/mol) and has a barrier of 59 kJ/mol.

## 6.3.3.6 Comparison of reactions on Ni (111), NiB and Mn-NiB SAA

The comparison of energetics for the important reactions in DRM on Ni (111), NiB, and Mn-NiB SAA and are presented here (*cf* Table 6. 6).

CO<sub>2</sub> activation route: The direct dissociation of CO<sub>2</sub> (R5) is favored on Ni (111), NiB, and Mn-NiB SAA surfaces. The free energy diagram of CO<sub>2</sub> direct dissociation to form CO\* and O\* is shown in Figure 6. 15. Notably, CO<sub>2</sub> dissociation is highly exergonic (-101 kJ/mol, -48 kJ/mol, -62 kJ/mol on Ni (111), NiB, and Mn-NiB respectively) on all three surfaces. Ni (111) has the lowest CO<sub>2</sub> activation barrier (63 kJ/mol) followed by Mn-NiB SAA (70 kJ/mol) and NiB (107 kJ/mol). Particularly, the CO<sub>2</sub> activation barrier on Mn-NiB SAA is 37 kJ/mol lower than that on the NiB surface. Since CO<sub>2</sub> specifies the oxidizing agent (O\*/OH\*) for possible CH<sub>x</sub> (x = 0 - 3) oxidation reactions (including carbon conversion) and for Boudouard reaction, the reduced CO<sub>2</sub> activation barrier plays a crucial role in favoring the reaction rates of oxidation steps on Mn-NiB SAA.

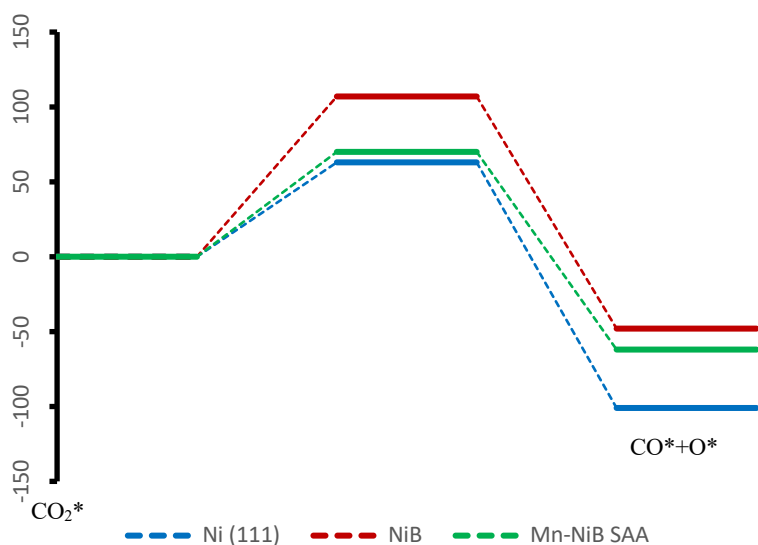


**Figure 6. 15** The free energy diagram of CO<sub>2</sub> direct dissociation on Ni (111) (blue), NiB (red), and Mn-NiB SAA (green).

CH<sub>4</sub> activation: The free energy diagram of CH<sub>4</sub> stepwise dehydrogenation (R1 – R4) on Ni (111), NiB, and Mn-NiB SAA is shown in Figure 6. 16. Noticeably, CH<sub>x</sub> (x = 1 - 4)

dehydrogenation steps are endergonic on all three surfaces except  $\text{CH}_2^*$  dehydrogenation on Ni (111) (-25 kJ/mol). Among the  $\text{CH}_x$  ( $x = 1 - 4$ ) dehydrogenation steps, the  $\text{CH}_4$  dissociation barrier to form  $\text{CH}_3^*$  and  $\text{H}^*$  has the highest barrier on all three surfaces. Notably, the  $\text{CH}_4$  dissociation barrier is significantly lower on Mn-NiB SAA (114 kJ/mol) and NiB (107 kJ/mol) compared to Ni (111) (164 kJ/mol). Additionally, Mn-NiB SAA has the lowest endergonicity (36 kJ/mol) for this step. Comparatively,  $\text{CH}_3^*$  dehydrogenation barrier is lowest on Ni (111) (58 kJ/mol) surface compared to NiB (87 kJ/mol) and Mn-NiB SAA (94 kJ/mol).  $\text{CH}_2^*$  dehydrogenation has the lowest barrier among  $\text{CH}_x$  ( $x = 1 - 4$ ) dehydrogenation steps on all three surfaces (35 kJ/mol, 56 kJ/mol and 60 kJ/mol on Ni (111), NiB and Mn-NiB SAA respectively). The subsequent dehydrogenation of  $\text{CH}^*$  to form  $\text{C}^*$  and  $\text{H}^*$  has the highest barrier on Ni (111) (126 kJ/mol) compared to NiB (96 kJ/mol) and Mn-NiB SAA (105 kJ/mol). Interestingly, NiB has the highest endergonicity (185 kJ/mol) for the overall reaction whereas Ni (111) has the lowest (104 kJ/mol). Notably, the overall reaction is 45 kJ/mol more endergonic on Mn-NiB SAA than on Ni (111). Similar to NiB, the high endergonicity on Mn-NiB SAA is presumed to alter the reaction pathway by favoring  $\text{CH}_x$  ( $x = 1 - 3$ ) oxidation in lieu of  $\text{CH}_x$  ( $x = 1 - 3$ ) dehydrogenation. This would indeed result in low coke formation on Mn-NiB SAA.

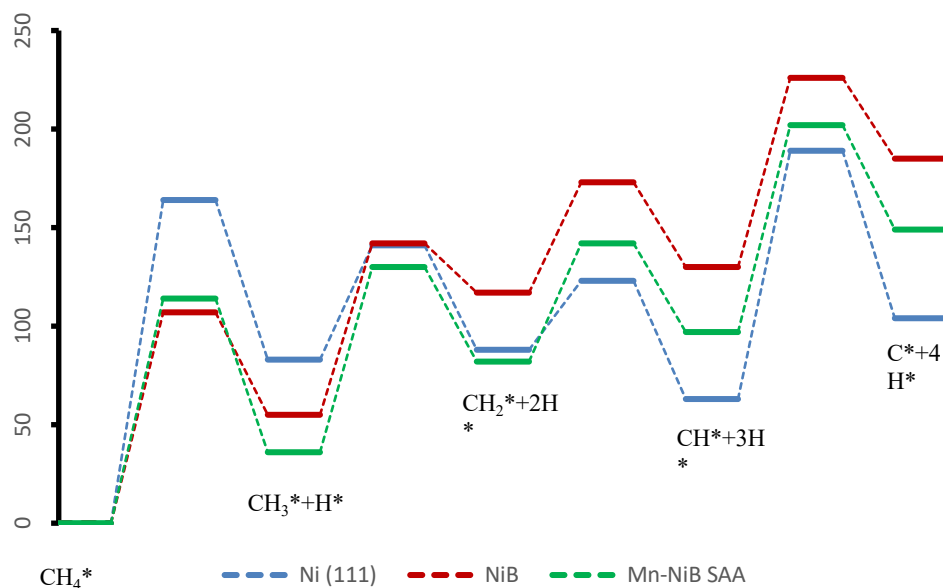


**Figure 6. 16** The free energy profile for sequential dehydrogenation of  $\text{CH}_4$  to  $\text{C}^*$  on Ni (111) (blue), NiB (red) and Mn-NiB SAA (green)

Boudouard reaction: The free energy diagram of the Boudouard reaction (R35) on Ni (111), NiB, and Mn-NiB SAA is shown in Figure 6. 17. Notably, Boudouard reaction is highly exergonic (-232 kJ/mol, -263 kJ/mol, -205 kJ/mol on Ni (111), NiB, and Mn-NiB respectively) on all three surfaces. The barrier for the Boudouard reaction is 154 kJ/mol on Ni (111) surface. However, the Boudouard reaction is kinetically not favored on Ni (111) as the barrier for C\* oxidation (by OH\* (R21)) is lower (133 kJ/mol) than the barrier for Boudouard reaction. Remarkably, the barrier for Boudouard reaction is significantly lower on NiB (132 kJ/mol) and Mn-NiB SAA (122 kJ/mol) compared to that on Ni (111). Hence, the Boudouard reaction provides an additional path for the conversion of coke on NiB and Mn-NiB SAA surface. Hence, we expect less coke formation on the Mn-NiB SAA surface.

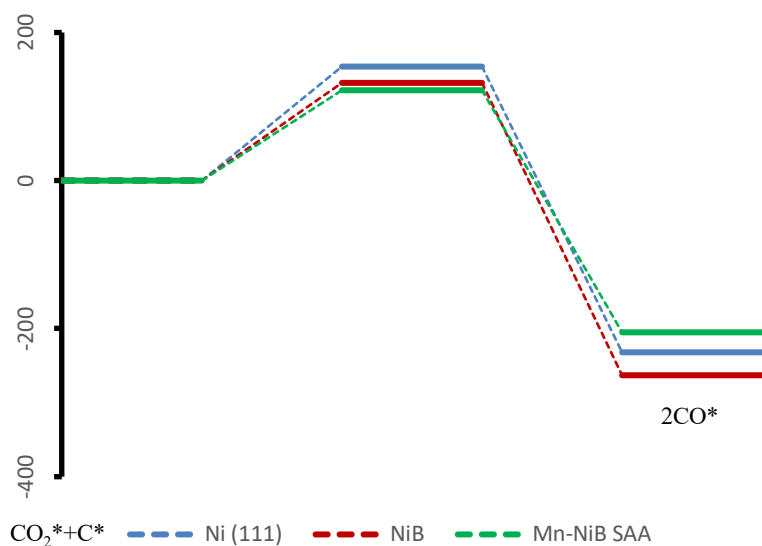


**Figure 6. 17** The free energy profile for Boudouard reaction on Ni (111) (blue), NiB (red) and Mn-NiB SAA (green).

In short, the Mn-NiB SAA has low  $\text{CO}_2$  activation barrier (comparable to that on Ni (111)) and  $\text{CH}_4$  activation barrier (comparable to that on NiB). Additionally, the high endergonicity of  $\text{CH}_4$  stepwise dehydrogenation combined with the low barrier for Boudouard reaction would result in low carbon formation on Mn-NiB SAA. Thus, Mn-NiB SAA is a potential catalyst for the DRM reaction that can resist deactivation due to coke formation without affecting the activity.



## 6.4 Conclusions

In summary, we investigated NiB-based SAAs that are thermodynamically stable and can reduce CO<sub>2</sub> activation barriers. Mn-NiB SAA was identified as a potential SAA catalyst that is thermodynamically stable. Subsequently, employing a benchmarked DFT functional and considering a comprehensive reaction network, we investigated CO<sub>2</sub> methanation and DRM reactions on Mn-NiB SAA. Our DFT calculations predict low CO<sub>2</sub> (direct dissociation) and CO\* (hydrogenation via HCO\* intermediate) activation barriers on Mn-NiB SAA compared to Ni (111) and Ru (001) surfaces. Additionally, we found that the reaction proceeds via CO\* intermediate and thereby reducing CO poisoning on Mn-NiB SAA. Moreover, the CH\* stepwise hydrogenation barriers were thermodynamically and kinetically more favored on Mn-NiB SAA compared to that on Ni and Ru surfaces making it a suitable catalyst for CO<sub>2</sub> methanation reaction. For the DRM reaction, Mn-NiB SAA has a significantly lower barrier for CH<sub>4</sub> activation compared to that on Ni (111) surface. Additionally, the low CO<sub>2</sub> activation (to form CO\* and O\*) barriers could supply O\* adatom at a faster rate than on Ni (111) and clean NiB surfaces. Thus, the oxidation of CH<sub>x</sub> intermediate is more favored on Mn-NiB SAA. Moreover, the CH<sub>x</sub> (x = 0 - 4) stepwise dehydrogenation is more endergonic on Mn-NiB SAA compared to Ni (111). Thus, coke formation via CH<sub>4</sub> dehydrogenation is thermodynamically less favored on Mn-NiB SAA. Additionally, the low barrier for the Boudouard reaction also favors carbon destruction at a faster rate. Thus, we expect Mn-NiB SAA to reduce coke formation without affecting the reaction rate. The computational screening of SAA in this investigation and the gained insights from SAA would instigate further theoretical and experimental works, for the development of better catalysts (active and stable) for CO<sub>2</sub> methanation and DRM reactions.

## Chapter 7 Conclusions and perspectives

This thesis identifies a Density Functional Theory (DFT) functional that should be used for studying CO<sub>2</sub> conversion reactions, establish the reaction mechanism of CO<sub>2</sub> methanation (on Ni and Ru) and dry reforming of methane (DRM) (on Ni and boron-doped Ni (NiB)) reactions and proposes more active and coke resistant NiB based single atom alloy (SAA) catalyst for these reactions. Even though CO<sub>2</sub> conversion reactions are widely studied, the underlying reaction mechanisms are debated. This is partly because of employing an inappropriate functional choice for studying such systems using DFT resulting in an erroneous prediction of reaction energetics. Hence, a benchmarking study must be conducted to select an accurate functional. This is addressed primarily by considering Ni (110) as a model catalyst surface. Based on CO<sub>2</sub> and CO binding energy calculations, we found that the functional that correctly predicts CO<sub>2</sub> binding energy (optPBE-vdW) fails to predict CO binding energy (rPBE-vdW correctly predicted CO binding energy). By using an alternate reaction system (that replaces gas-phase CO<sub>2</sub>), density of states, and DFT-XPS calculations we found that rPBE-vdW functional correctly predicts metal-CO<sub>2</sub> interactions and the error in predicting CO<sub>2</sub> binding energy by rPBE-vdW functional is due to the wrong treatment of C=O double bonds in gas phase CO<sub>2</sub>. Subsequently, we identified rPBE-vdW functional, with a correction of 28 kJ/mol for gas-phase CO<sub>2</sub> energy, as the best functional choice and this functional must be employed for studying CO<sub>2</sub> conversion reaction. We established that the proposed functional and the correction factor applies to other metals since the source of error lies in predicting the energy of gas-phase CO<sub>2</sub>. This study emphasizes the importance of functional benchmarking and identified the best functional choice that must be employed for studying CO<sub>2</sub> conversion reactions on any metal surface.

Employing the benchmarked functional, CO<sub>2</sub> methanation reaction is studied on both Ni and Ru surfaces. The existing studies on CO<sub>2</sub> methanation reaction mechanisms are inconsistent which may have resulted from the use of an inaccurate functional and studying only selected elementary reactions. The most debated steps are CO<sub>2</sub> and CO activation routes (direct dissociation and multiple hydrogenation pathways). Also, whether the

reaction proceeds with/without forming a CO\* intermediate is also debated. We addressed these discrepancies in the CO<sub>2</sub> methanation reaction mechanism on both Ni and Ru surfaces by considering a comprehensive reaction network of 46 elementary reactions involving multiple CO<sub>2</sub>, CO and C activation routes (including dissociation and hydrogenation), side reactions (H<sub>2</sub>O formation, Boudouard reaction) and desorption of products. To predict the conversion and coverages under reaction conditions, a microkinetic model (MKM) was developed using the DFT predicted energetics. The dominant pathway for methanation on Ni (111) is CO<sub>2</sub>\*→CO\*→HCO\*→CH\*→CH<sub>2</sub>\*→CH<sub>3</sub>\*→CH<sub>4</sub>\* with the RDS being CHO\*→CH\*+O\*. Whereas on Ru (001), the dominant pathway is CO<sub>2</sub>\*→CO\*→COH\*→C\*→CH\*→CH<sub>2</sub>\*→CH<sub>3</sub>\*→CH<sub>4</sub>\* and the RDS is CH<sub>3</sub>\*+H\*→CH<sub>4</sub>\*. It was observed that the rate of RDS for methanation was higher on Ni (111), i.e. 5.07x10<sup>-10</sup> mol/g<sub>cat</sub>·h, compared to Ru (001), i.e. 1.02x10<sup>-13</sup> mol/g<sub>cat</sub>·h, further suggesting methanation more favored over Ni (111). This study resolves the discrepancies in CO<sub>2</sub> methanation reaction mechanisms on Ni and Ru surfaces. This study also lays the foundation for developing more active and stable Ni-based methanation catalysts by altering the reaction pathways or reducing the barriers of key reaction steps in the dominant pathways.

The widely studied DRM catalyst, Ni, suffers from deactivation due to carbon formation, and the challenge to successfully modify Ni-based catalysts to make them stable under DRM conditions remains to be solved. Boron doping prevents the diffusion of carbon to the bulk of Ni and hence would be a potential DRM catalyst that improves the coke resistance of Ni. We combined DFT calculations (with an accurate and benchmarked functional choice), together with MKM to provide mechanistic insights into the DRM reaction network (38 elementary reactions) on Ni and NiB catalyst surfaces. We reveal that boron doping reduces CH<sub>4</sub> activation barriers and alters the dominant reaction pathway to kinetically hinder carbon formation and favor carbon consumption. Based on combined DFT and microkinetic study, the dominant reaction pathways were identified on Ni and NiB surfaces. The dominant reaction pathway is CO<sub>2</sub>\*→CO\*+O\*; CH<sub>4</sub>→CH<sub>3</sub>\*→CH<sub>2</sub>\*→C\*→CO\* and CO<sub>2</sub>\*→CO\*+O\*; CH<sub>4</sub>→CH<sub>3</sub>\*→CH<sub>2</sub>\*→CH<sub>2</sub>O\*→CHO\*→CO\* on Ni (111) and NiB surfaces respectively. The dominant reaction pathway

on Ni involves  $C^*$  intermediate that would lead to coke formation whereas the pathway on NiB surface includes  $CH_2^*$  oxidation, which prevents carbon formation and thus making it a more stable catalyst. However, it was observed that the forward rate of the RDS at 973 K and 10 bar on Ni ( $CH_4$  dissociation) was higher than the forward rate of RDS ( $CH_2^*$  oxidation reaction) on NiB, implying lower reactant conversion on NiB. The lower rate for  $CH_2^*$  oxidation is attributed to the increased  $CO_2$  activation barrier as  $CO_2$  supplies the primary oxidizing agent ( $O^*$ ). This study unravels the DRM reaction mechanisms on Ni and NiB surfaces. The mechanistic insights presented in this study would instigate the development of Ni-based alloy catalysts that reduces  $CO_2$  activation barriers and hence prevents deactivation without compromising the catalytic activity.

Even though the  $CH_4$  activation barrier was low on NiB, the  $CO_2$  activation barrier increased significantly resulting in reduced reactant conversion. We performed a computational screening for identifying a NiB based SAA catalyst that can reduce  $CO_2$  activation barriers. We evaluated the thermodynamic stability of 15 SAAs based on NiB (Ru, Pt, Pd, Rh, Co, Fe, Os, Ir, Re, W, Mo, Cu, Mn, Zn, and K) and further calculated  $CO_2$  activation barrier on stable SAA surfaces. The thermodynamic stability of the catalyst structure against clustering was evaluated. We reveal that Mn-NiB SAA was the only surface that was thermodynamically stable and significantly reduces the  $CO_2$  activation barrier (reduction of 56 kJ/mol) compared to the clean NiB surface. Lower  $CO_2$  activation barrier is favorable for both  $CO_2$  methanation and DRM reactions and hence we simulated these reactions on Mn-NiB SAA. High  $CO_2$  binding energy (-94 kJ/mol), low  $CO_2$  (direct dissociation to form  $CO^*$  - free energy barrier of 69 kJ/mol) and  $CO^*$  (hydrogenation to form  $HCO^*$  - free energy barrier of 105 kJ/mol) activation barriers and low  $CH^*$  sequential hydrogenation barriers (to form  $CH_4$ ) makes Mn-NiB SAA a perfect candidate for  $CO_2$  methanation reaction. Moreover, the low  $CO_2$  and  $CH_4$  activation barriers make Mn-NiB SAA a promising catalyst for DRM reaction. Most importantly, the high endergonicity for  $CH_4$  stepwise dehydrogenation (to form  $C^*$ ) combined with low free energy barrier (122 kJ/mol) for Boudouard reaction reduces the on-surface coke formation and thereby prevents the deactivation of the catalyst. Based on the computational screening presented in this work, the stable microstructure of Mn-NiB SAA is predicted theoretically, and this

would further prompt the development/synthesis of the catalyst. Moreover, mechanistic insights gained from CO<sub>2</sub> methanation and DRM reactions on Mn-NiB SAA would persuade further theoretical and experimental works, for the development of similar alloy catalysts for other CO<sub>2</sub> conversion reactions.

In summary, this thesis identifies the best available functional for studying CO<sub>2</sub> conversion reactions and presents the reaction mechanisms of CO<sub>2</sub> methanation (on Ni and Ru) and DRM (on Ni and NiB) reactions. The coking issue on Ni is addressed by boron doping. Based on a systematic computational screening, Mn-NiB SAA was identified as a novel catalyst for CO<sub>2</sub> methanation and DRM reactions that can prevent coking without compromising the catalytic activity. The CO<sub>2</sub> methanation and DRM reaction mechanisms on Mn-NiB SAA have been detailed.

The combined microkinetic and DFT approach employed in this thesis is more appropriate for low adsorbent coverages since the lateral interactions among adsorbing molecules were neglected. However, the DFT data presented in this study would be useful for future studies considering lateral interactions. Several schemes were proposed to include the coverage effect. Often the binding energies change significantly with the increase in adsorbate coverages. Cluster expansion (CE) is one of the widely used schemes to estimate coverage effects<sup>244</sup>. In this approach a Mathematical relationship is described between adsorbate coverage and surface binding energy. Notably, many empirical functional forms have been proposed to describe the coverage dependent binding energy<sup>245</sup>. The CE's once parametrised, can be used to compute reaction rates under realistic reaction conditions using either kinetic or grand canonical Monte Carlo simulations. However, the use of several parameters introduces uncertainties in the computed rates<sup>246</sup>. Even then, successful advances in predicting the reaction chemistry at high coverages have been made. Interestingly, in the CE method, the different parameters are obtained using regression analysis from a training dataset (set of configurations and energies). With the advancement of computational power and recourses, novel schemes employing Machine learning tools have been developed<sup>247,248</sup>. For low symmetry surfaces (eg. Steps, multielement alloys) the challenge is to identify unique adsorbate configuration on different sites present on the

catalyst surface. Recently, Python-based algorithms were developed to generate graphical representation of surfaces<sup>249</sup>. These are used to detect unique adsorbate configurations and adsorption sites on the surface of the catalyst. Other future research directions from this thesis include i) performing microkinetic analysis for CO<sub>2</sub> methanation and DRM reactions on Mn-NiB SAA for predicting the reaction mechanism, coverage, and conversions under reaction conditions ii) further investigations to understand the effect of support on the reaction mechanism of CO<sub>2</sub> methanation and DRM reactions iii) synthesize and experimentally test the novel Mn-NiB SAA catalyst for CO<sub>2</sub> methanation and DRM reactions.



## APPENDIX

### 8.1 Appendix to chapter 3

#### 8.1.1. Lattice constant optimization

Nickel has only one parameter of lattice constant since it has fcc crystal structure. The total energy of the primitive cell of bulk structure fcc Ni is plotted against different lattice constant values as shown in Figure. 8.1.1. The optimum lattice constant is the one that corresponds to the minimum energy of the fcc Ni. The optimized lattice constant calculated from Figure. 8.1.1 is tabulated in Table 8.1.1. Percentage error is calculated based on experimental lattice constant (formula 8.1.1)

$$\% \text{ Error} = \frac{|A_{\text{func}} - A_{\text{exp}}|}{A_{\text{exp}}} \quad (8.1.1)$$

where  $A_{\text{func}}$  is the optimized lattice parameter calculated using functional and  $A_{\text{exp}}$  is the experimental value of the lattice parameter. All functionals are predicting the lattice parameter within 3% error which is acceptable.

**Table 8.1.1** Optimized lattice constant for Ni with different functionals

<b>Functional</b>	<b>Lattice parameter (Å)</b>	<b>Percentage error (%)</b>
<b>PBE</b>	3.513	0.31
<b>rPBE</b>	3.544	0.56
<b>PW91</b>	3.516	0.22
<b>vdW-DF2</b>	3.606	2.32
<b>PBE D2</b>	3.516	0.23
<b>opt86b-vdW</b>	3.497	0.76
<b>rPBE-vdW</b>	3.571	1.33
<b>optPBE-vdW</b>	3.529	0.14
<b>Experiment</b>	3.524	-



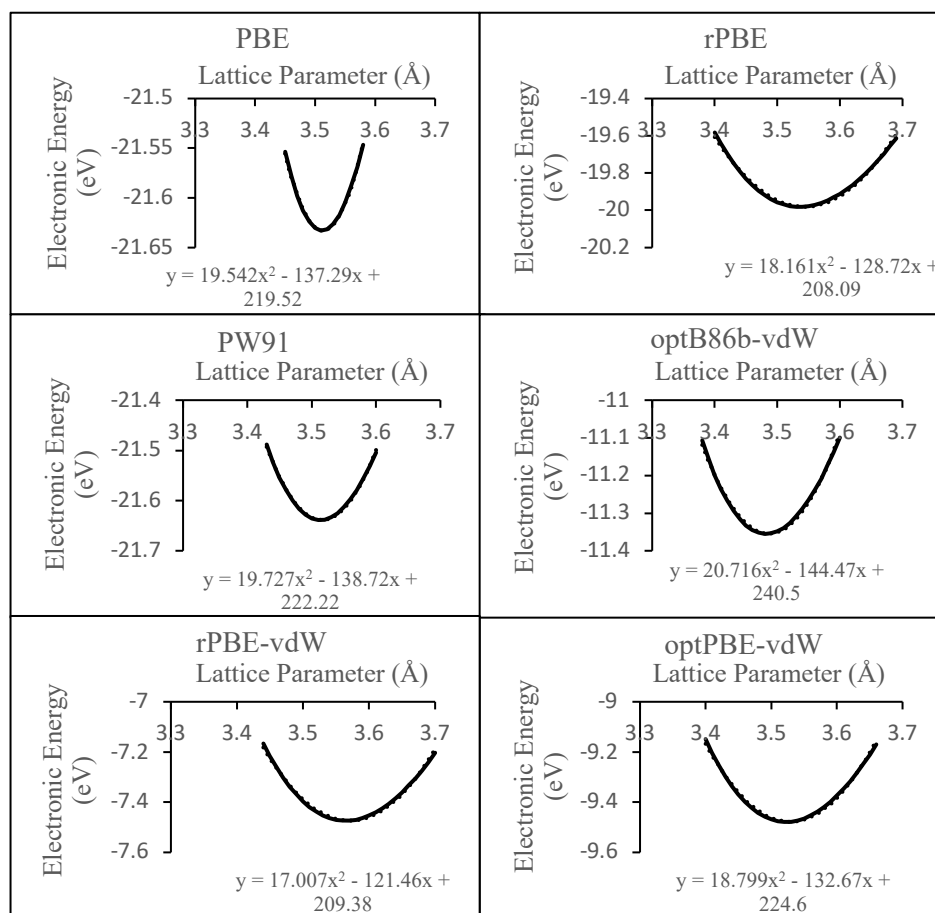


**Figure. 8.1.1** Calculation of optimized lattice constant for Ni using different functionals. From lattice parameter-energy plot, lattice parameter corresponding to minimum energy is calculated

### 8.1.2. Computational Parameter optimization

The number of slab layers, vacuum and the density of K point grids were chosen to ensure the adsorption energies were well converged within 5 kJ/mol with respect to the computational setup discussed in this study and are tabulated from Table 8.1.2 a - c.

**Table 8.1.2 a.** Number of slab layers optimization

<b>Number of layers</b>	<b>Binding energy of CO<sub>2</sub> (kJ/mol)</b>
4	-46.16
5	-33.25
6	-41.35
7	-41.26

**Table 8.1.2 b.** K-points optimization

<b>K-points</b>	<b>Binding energy of CO<sub>2</sub> (kJ/mol)</b>
3x3x1	-41.35
4x4x1	-40.8
5x5x1	-40.35
6x6x1	-41.02

**Table 8.1.2.** Vacuum Thickness optimization

<b>Vacuum Thickness (Å)</b>	<b>Binding energy of CO<sub>2</sub> (kJ/mol)</b>
12	-41.35
15	-39.12
20	-39.6

### 8.1.3. Adsorption configuration of CO<sub>2</sub> and CO on Ni (110)

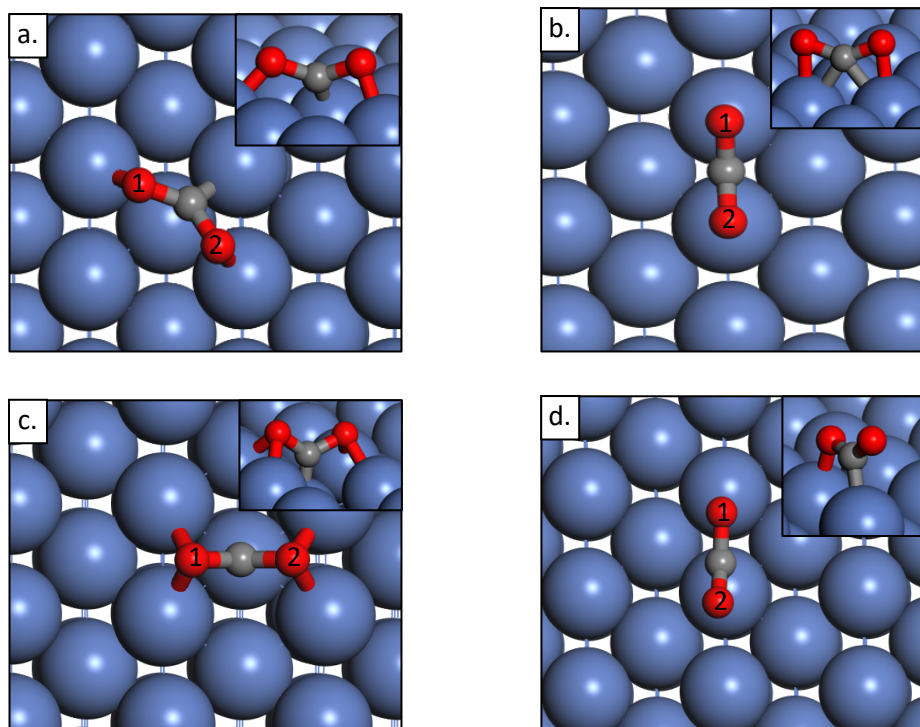


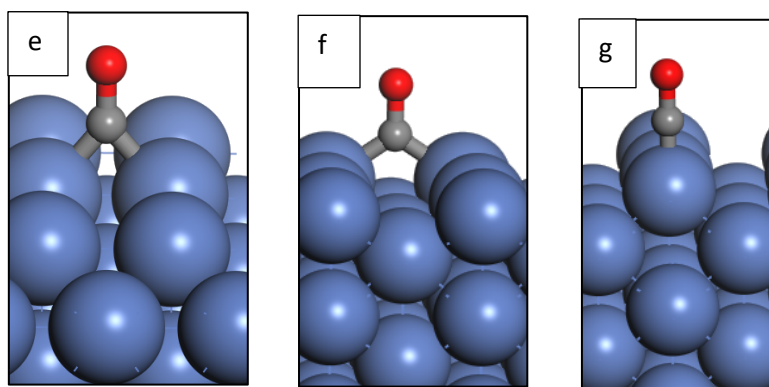
**Figure. 8.1.3** a-d shows different adsorption configuration of CO<sub>2</sub> on Ni (110). Blue balls represent Ni atoms, red balls represent oxygen atoms, and the grey ball represents carbon atom.

Four different configurations are identified for CO<sub>2</sub> adsorption on Ni (110) surface. The different adsorption configurations are shown in Figure. 8.1.3 a-d and adsorption energies and geometric parameters are tabulated in Table 8.1.3. All the calculations are performed using PBE functional and configuration (a) corresponds to the most stable configuration.

**Table 8.1.3 a** Geometric parameters and calculated adsorption energy of CO<sub>2</sub> on Ni (110)

Parameter	Configuration			
	a	b	c	d
<b>d<sub>C-O1</sub> (Å)</b>	1.279	1.243	1.308	1.261
<b>d<sub>C-O2</sub> (Å)</b>	1.278	1.244	1.306	1.223
<b>O1-C-O2 (deg)</b>	126.704	139.036	121.323	139.200
<b>E<sub>ads</sub> (kJ/mol)</b>	-41.35	-32.22	-31.57	-29.44

We found that CO prefers to sit on Ni with carbon bonded vertical configuration on all sites. The different adsorption configurations are shown in Figure. 8.1.3 e-g and adsorption energies and geometric parameters are tabulated in Table 8.1.3 b.

**Fig. 8.1.3 e-g** shows different adsorption configuration of CO on Ni (110).**Table 8.1.3 b** Geometric parameters and calculated adsorption energy of CO on Ni (110)

Parameter	Configuration		
	a	b	c
<b>d<sub>C-O</sub> (Å)</b>	1.128	1.196	1.165
<b>E<sub>ads</sub> (kJ/mol)</b>	-173.92	-134.15	-159.52

The most stable adsorption configuration was the one in which CO sits vertically in the bridge site between two-nickel atoms. The bond angle and bond length of CO<sub>2</sub>\* calculated by different functionals are given in Table 8.1.3 c.

**Table 8.1.3 c.** Bond angle and bond length of CO<sub>2</sub>\* calculated by different functionals

Parameter	Functional						
	PBE	rPBE	PW91	vdWDF2	opt86b-vdW	rPBE-vdW	optPBE-vdW
dC-O1 (Å)	1.279	1.281	1.276	1.280	1.283	1.279	1.282
dC-O2 (Å)	1.278	1.283	1.278	1.279	1.278	1.281	1.278
O1-C-O2 (deg)	126.704	126.416	127.713	127.782	125.896	126.913	126.239

#### 8.1.4. Zero-point energy and enthalpy corrections using different functionals

The zero-point energies calculated using different functionals for CO<sub>2</sub> are given in following Table 8.1.4

**Table 8.1.4.** ZPE and  $\Delta H$  calculated using different functionals for CO<sub>2</sub>

Functional	ZPE (kJ/mol)	Enthalpy correction, $\Delta H$ (kJ/mol)
PBE	27.733	5.197
rPBE	27.398	5.308
PW91	27.735	5.172
vdW-DF2	26.787	5.318
opt86b-vdW	27.734	5.113
PBE D2	27.566	5.159
rPBE-vdW	26.959	5.389
optPBE-vdW	27.342	5.277

### 8.1.5. Adsorption configuration of CO<sub>2</sub> and CO on different metals

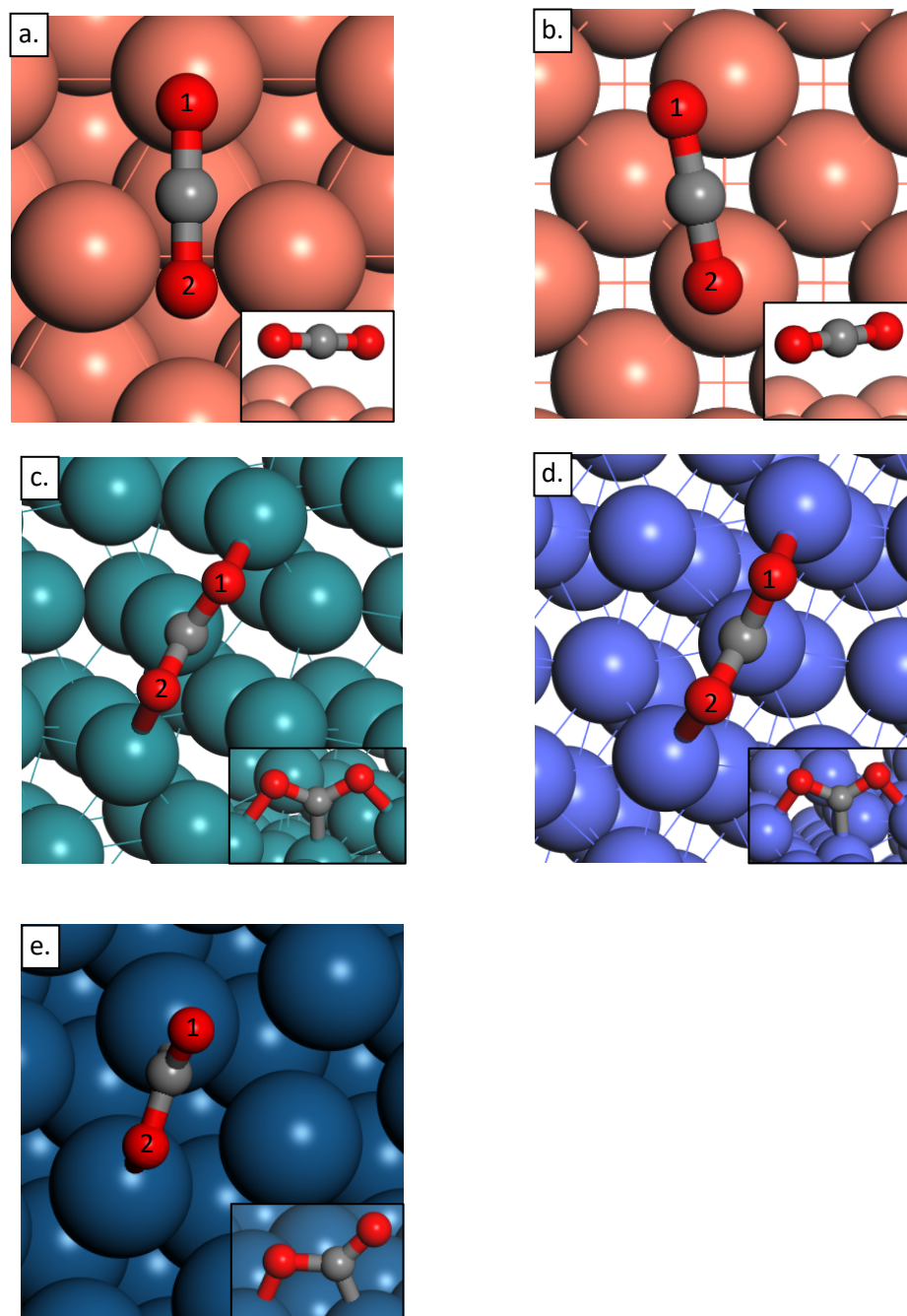


**Figure. 8.1.5** the adsorption configuration of CO<sub>2</sub> on **a.** Cu (111), **b.** Cu (100), **c.** Ru (111), **d.** Co (111), **e.** Pt (111). Salmon balls represent Cu atoms, green balls represent Ru atoms, blue balls represent Co atoms, dark blue balls represent Pt atoms, red balls represent oxygen atoms, and the grey ball represents carbon atom.

**Table 8.1.5** Geometric parameters CO<sub>2</sub> on Cu, Ru, Co, and Pt surfaces

Parameter	Configuration				
	Cu		Ru	Co	Pt (111)
	(111)	(100)	(111)	(111)	
<b>d<sub>C-O1</sub> (Å)</b>	1.18	1.180	1.296	1.289	1.214
<b>d<sub>C-O2</sub> (Å)</b>	1.181	1.182	1.300	1.290	1.295
<b>O1-C-O2 (deg)</b>	179.43	179.29	122.62	123.21	132.32

## 8.2 Appendix to chapter 4

### 8.2.1 Comparison of electronic energy with reported values from literature

**Table 8.2.1.** Activation barriers computed for reaction steps on Ni (111) compared with values reported in literature.

Reaction	Activation barrier (kJ/mol)	
	Ni (111)	
	This work	Reported
R1: $\text{CH}_4^* \rightarrow \text{CH}_3^* + \text{H}^*$	115	112 <sup>88</sup> , 118 <sup>250</sup> , 112 <sup>251</sup> , 129 <sup>252,253</sup>
R2: $\text{CH}_3^* \rightarrow \text{CH}_2^* + \text{H}^*$	75	78 <sup>88</sup> , 81 <sup>250</sup> , 79 <sup>251</sup> , 66 <sup>9</sup>
R3: $\text{CH}_2^* \rightarrow \text{CH}^* + \text{H}^*$	35	35 <sup>88</sup> , 28 <sup>250</sup> , 36 <sup>251</sup> , 26 <sup>9</sup>
R4: $\text{CH}^* \rightarrow \text{C}^* + \text{H}^*$	137	138 <sup>254</sup> , 132 <sup>251</sup> , 135 <sup>9</sup>
R5: $\text{CO}_2^* \rightarrow \text{CO}^* + \text{O}^*$	54	64 <sup>87</sup> , 43 <sup>167</sup> , 39 <sup>98</sup> , 53 <sup>251</sup>
R6: $\text{CO}_2^* + \text{H}^* \rightarrow \text{COOH}^*$	109	108 <sup>87</sup> , 99 <sup>167</sup>
R7: $\text{CO}_2^* + \text{H}^* \rightarrow \text{HCOO}^*$	67	52 <sup>167</sup> , 56 <sup>98</sup>
R8: $\text{COOH}^* \rightarrow \text{CO}^* + \text{OH}^*$	37	54 <sup>87</sup> , 36 <sup>98</sup>
R9: $\text{HCOO}^* \rightarrow \text{HCO}^* + \text{O}^*$	148	134 <sup>98</sup>
R10: $\text{HCO}^* \rightarrow \text{CO}^* + \text{H}^*$	30	19 <sup>87</sup> , 28 <sup>251</sup> , 20 <sup>9</sup>
R11: $\text{COOH}^* + \text{H}^* \rightarrow \text{HCOOH}^*$	83	-
R12: $\text{HCOO}^* + \text{H}^* \rightarrow \text{HCOOH}^*$	127	77 <sup>167</sup>
R13: $\text{HCOOH}^* \rightarrow \text{HCO}^* + \text{OH}^*$	100	86 <sup>167</sup>
R14: $\text{CH}_3\text{OH}^* \rightarrow \text{CH}_2\text{OH}^* + \text{H}^*$	119	84 <sup>87</sup>
R15: $\text{CH}_2\text{OH}^* \rightarrow \text{CHOH}^* + \text{H}^*$	74	51 <sup>87</sup>
R16: $\text{CHOH}^* \rightarrow \text{COH}^* + \text{H}^*$	27	14 <sup>87</sup>
R17: $\text{COH}^* \rightarrow \text{CO}^* + \text{H}^*$	101	94 <sup>87</sup> , 86 <sup>9</sup>
R18: $\text{CH}_3^* + \text{OH}^* \rightarrow \text{CH}_3\text{OH}^*$	197	211 <sup>87</sup> , 174 <sup>255</sup> , 125 <sup>9</sup>
R19: $\text{CH}_2^* + \text{OH}^* \rightarrow \text{CH}_2\text{OH}^*$	132	126 <sup>87</sup> , 85 <sup>9</sup>
R20: $\text{CH}^* + \text{OH}^* \rightarrow \text{CHOH}^*$	154	142 <sup>87</sup> , 138 <sup>255</sup> , 123 <sup>9</sup>
R21: $\text{C}^* + \text{OH}^* \rightarrow \text{COH}^*$	149	140 <sup>87</sup> , 126 <sup>9</sup>



R22: $\text{CH}_3\text{O}^* \rightarrow \text{CH}_2\text{O}^* + \text{H}^*$	113	$89^{87}, 62^{251}$
R23: $\text{CH}_2\text{O}^* \rightarrow \text{CHO}^* + \text{H}^*$	50	$34^{87}, 37^{251}$
R24: $\text{CH}_3^* + \text{O}^* \rightarrow \text{CH}_3\text{O}^*$	133	$152^{87}, 90^{251}, 152^9$
R25: $\text{CH}_2^* + \text{O}^* \rightarrow \text{CH}_2\text{O}^*$	130	$139^{87}, 75^{251}, 131^9$
R26: $\text{CH}^* + \text{O}^* \rightarrow \text{CHO}^*$	145	$146^{87}, 77^{251}, 108^{255}, 151^9$
R27: $\text{C}^* + \text{O}^* \rightarrow \text{CO}^*$	162	$152^{87}, 206^9$
R28: $\text{CH}_3\text{OH}^{*+*} \rightarrow \text{CH}_3\text{O}^* + \text{H}^*$	101	-
R29: $\text{CH}_2\text{OH}^{*+*} \rightarrow \text{CH}_2\text{O}^* + \text{H}^*$	76	-
R30: $\text{CHOH}^{*+*} \rightarrow \text{HCO}^* + \text{H}^*$	83	-
R31: $\text{O}^* + \text{H}^* \rightarrow \text{OH}^*$	125	$129^{87}, 128^{251}$
R32: $\text{OH}^* + \text{H}^* \rightarrow \text{H}_2\text{O}^*$	147	$137^{251}$
R33: $\text{H}^* + \text{H}^* \rightarrow \text{H}_2$	86	$81^{256}$
R34: $\text{OH}^* + \text{OH}^* \rightarrow \text{H}_2\text{O}^* + \text{O}^*$	92	-
R35: $\text{CO}_2^* + \text{C}^* \rightarrow 2\text{CO}^*$	153	-
R36: $\text{CO}_2 \rightarrow \text{CO}_2^*$	-	-
R37: $\text{CO}^* \rightarrow \text{CO}$	-	-
R38: $\text{H}_2\text{O}^* \rightarrow \text{H}_2\text{O} + *$	-	-

**Table 8.2.2.** Free energy barrier and reaction free energy computed for Ru (001) compared with values reported in literature.

Reaction	Free energy barrier <sup>#</sup> (kJ/mol)		Reaction free energy <sup>#</sup> (kJ/mol)	
	This work	Ref <sup>170</sup>	This work	Ref <sup>170</sup>
$\text{CO}_2^* + \text{H}^* = \text{HCOO}^*$	72	81	-27	-9
$\text{HCOO}^* = \text{HCO}^* + \text{O}^*$	103	96	-17	-2
$\text{CO}_2^* = \text{CO}^* + \text{O}^*$	53	24	-168	-144
$\text{CO}^* + \text{H}^* = \text{HCO}^*$	121	121	122	113
$\text{CO}_2^* + \text{H}^* = \text{COOH}^*$	122	126	21	9
$\text{COOH}^* = \text{CO}^* + \text{OH}^*$	40	41	-107	-84

<sup>#</sup>T=500K, P=1 atm

**Table 8.2.3.** Gibbs energy of Activation and kinetic rate constants of all elementary reactions for CO<sub>2</sub> methanation on Ni (111) and Ru (001) surfaces at 550K and 10 atm pressure.

Reaction		Reaction rate constants (s <sup>-1</sup> )			
		Ni (111)		Ru (001)	
		$k_f$	$k_r$	$k_f$	$k_r$
R1	$\text{CH}_3^* + \text{H}^* \rightarrow \text{CH}_4^*$	208919.6	0.524709	1347.305	2.441573
R2	$\text{CH}_2^* + \text{H}^* \rightarrow \text{CH}_3^*$	37745038	13913714	1868717	2.75E+08
R3	$\text{CH}^* + \text{H}^* \rightarrow \text{CH}_2^*$	7652915	7.84E+09	498307.7	1.31E+12
R4	$\text{C}^* + \text{H}^* \rightarrow \text{CH}^*$	44421.15	6.666576	2401.538	2061.15
R5	$\text{CO}_2^* \rightarrow \text{CO}^* + \text{O}^*$	27572191	0.00168	8.82E-09	1.18E+08
R6	$\text{CO}_2^* + \text{H}^* \rightarrow \text{COOH}^*$	252.5203	57057.9	2419.314	26.13819

R7	$\text{CO}_2^* + \text{H}^* \rightarrow \text{HCOO}^*$	3102230	9298.02	3420.3	1612741
R8	$\text{COOH}^* \rightarrow \text{CO}^* + \text{OH}^*$	1.6E+11	1.488235	0.091599	2.17E+09
R9	$\text{HCOO}^* \rightarrow \text{HCO}^* + \text{O}^*$	0.132758	1557.163	34.48702	1523.432
R10	$\text{HCO}^* \rightarrow \text{CO}^* + \text{H}^*$	1.31E+11	0.226697	19.01433	1.22E+13
R11	$\text{COOH}^* + \text{H}^* \rightarrow \text{HCOOH}^*$	107570.4	5478868	11993923	77.85729
R12	$\text{HCOO}^* + \text{H}^* \rightarrow \text{HCOOH}^*$	131.6249	5.05E+08	7.19E+10	10.69954
R13	$\text{HCOOH}^* \rightarrow \text{HCO}^* + \text{OH}^*$	9563720	1006165	150475.4	8.57E+08
R14	$\text{CH}_2\text{OH}^* + \text{H}^* \rightarrow \text{CH}_3\text{OH}^*$	95795.34	7.577101	1345.649	395.825
R15	$\text{CHOH}^* + \text{H}^* \rightarrow \text{CH}_2\text{OH}^*$	43978.07	3196145	8380568	3.31E+09
R16	$\text{COH}^* + \text{H}^* \rightarrow \text{CHOH}^*$	38998.66	1.42E+11	7893.678	4.98E+13
R17	$\text{CO}^* + \text{H}^* \rightarrow \text{COH}^*$	1.44E-07	6923.75	1.44E-06	4378.859
R18	$\text{CH}_3\text{OH}^* \rightarrow \text{CH}_3^* + \text{OH}^*$	0.007913	7.47E-06	137.5723	8.82E-05
R19	$\text{CH}_2\text{OH}^* \rightarrow \text{CH}_2^* + \text{OH}^*$	7751075	1.569935	7.23E+08	0.92526
R20	$\text{CHOH}^* \rightarrow \text{CH}^* + \text{OH}^*$	11653542	0.16737	1.3E+10	0.002508
R21	$\text{COH}^* \rightarrow \text{C}^* + \text{OH}^*$	0.001534	0.534658	1148.915	1.624997
R22	$\text{CH}_2\text{O}^* + \text{H}^* \rightarrow \text{CH}_3\text{O}^*$	18490918	1764.082	143240.4	17112.05
R23	$\text{CHO}^* + \text{H}^* \rightarrow \text{CH}_2\text{O}^*$	1192557	2.55E+09	6087513	2.67E+11
R24	$\text{CH}_3\text{O}^* \rightarrow \text{CH}_3^* + \text{O}^*$	7.823719	1.828083	39.31285	3.2E-07
R25	$\text{CH}_2^* + \text{O}^* \rightarrow \text{CH}_2\text{O}^*$	35944.48	2.173662	1758756	1.16E-05
R26	$\text{CHO}^* \rightarrow \text{CH}^* + \text{O}^*$	1572.132	0.198399	836.0739	9.23E-11

R27	$\text{CO}^* \rightarrow \text{C}^* + \text{O}^*$	1.58E-14	0.00765	2.93E-08	2.42E-09
R28	$\text{CH}_3\text{OH}^* + * \rightarrow \text{CH}_3\text{O}^* + \text{H}^*$	14733.33	1.728199	515067.2	0.77744
R29	$\text{CH}_2\text{OH}^* + * \rightarrow \text{CH}_2\text{O}^* + \text{H}^*$	4810323	467.8057	75883.07	0.282022
R30	$\text{CHOH}^* + * \rightarrow \text{HCO}^* + \text{H}^*$	11932089	39.42917	3199263	0.106941
R31	$\text{O}^* + \text{H}^* \rightarrow \text{OH}^*$	46.2431	1592.633	0.001125	58670.6
R32	$\text{OH}^* + \text{H}^* \rightarrow \text{H}_2\text{O}^*$	1.513508	1414.68	8.739192	59699.95
R33	$\text{H}_2 \rightarrow \text{H}^* + \text{H}^*$	462733.3	110537.4	1.47E+08	142058
R34	$\text{OH}^* + \text{OH}^* \rightarrow \text{H}_2\text{O}^* + \text{O}^*$	58612.36	1590722	10509254	1376.317
R35	$\text{CO}_2^* + \text{C}^* \rightarrow 2\text{CO}^*$	0.029297	3.68E-24	0.29313	2.66E-16
R36	$\text{HCOO}^* + \text{H}^* \rightarrow \text{H}_2\text{COO}^*$	5.81E-06	44714.13	0.001205	1102549
R37	$\text{HCOOH}^* + \text{H}^* \rightarrow \text{H}_2\text{COOH}^*$	63.86364	1601882	47.29992	405971
R38	$\text{H}_2\text{COO}^* + \text{H}^* \rightarrow \text{H}_2\text{COOH}^*$	19929.78	249293.3	0.01637	1032.831
R39	$\text{H}_2\text{COO}^* \rightarrow \text{H}_2\text{CO}^* + \text{O}^*$	7.69E+09	25041370	5.31E+09	5773.071
R40	$\text{H}_2\text{COOH}^* \rightarrow \text{H}_2\text{CO}^* + \text{OH}^*$	3.68E+09	32999721	1.75E+11	1.58E+08
R41	$\text{CO}_2 \rightarrow \text{CO}_2^*$	0.181415	17938.19	33.08832	17860.66
R42	$\text{CO}^* \rightarrow \text{CO}$	0.120096	980621.3	0.005165	0.005165
R43	$\text{H}_2\text{O}^* \rightarrow \text{H}_2\text{O} + *$	8.43E+09	8.43E+08	3.66E+09	63570870
R44	$\text{CH}_4^* \rightarrow \text{CH}_4$	2.96E+10	2.09E+08	1.08E+12	9.7E+10
R45	$\text{HCOOH}^* \rightarrow \text{HCOOH}$	4.12E+09	4.12E+09	68125975	3671009
R46	$\text{CH}_3\text{OH}^* \rightarrow \text{CH}_3\text{OH}$	2.01E+10	2.01E+10	7.51E+08	3400962

### 8.2.2. Model validation

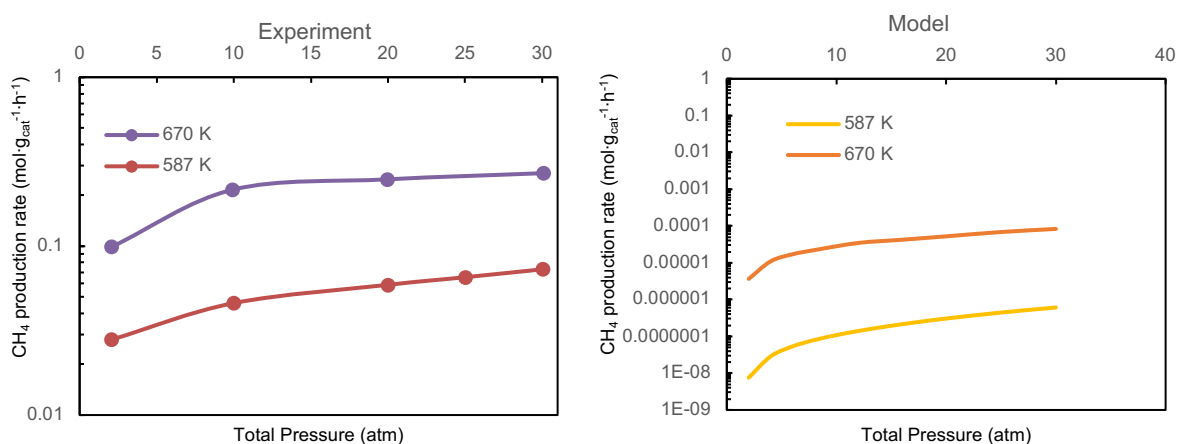


**Figure 8.2.1** Overall  $\text{CH}_4$  production rate ( $\text{mol}\cdot\text{g}_{\text{cat}}^{-1}\cdot\text{h}^{-1}$ ) over Ni surface as observed in experiments<sup>189</sup> vs as predicted by model for varying reaction temperature and pressure. Inlet feed ratio is  $\text{CO}_2:\text{H}_2::0.2:0.8$ .

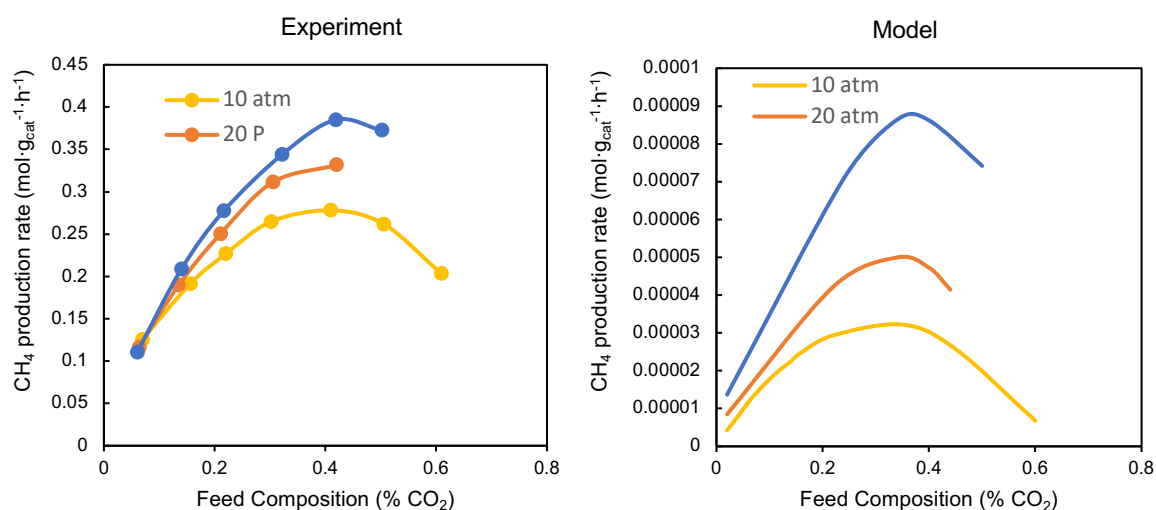


**Figure 8.2.2** Overall  $\text{CH}_4$  production rate over Ni ( $\text{mol}\cdot\text{g}_{\text{cat}}^{-1}\cdot\text{h}^{-1}$ ) as observed in experiments<sup>189</sup> vs as predicted by model for varying feed composition and reaction pressure. Reaction temperature is 670 K.

$\text{CH}_4$  production rate predicted by our model follows the trend observed in experiments as per reaction conditions. However, the huge difference in the order of magnitude of reaction rate is because, at the given range of the reaction temperatures, the reaction is kinetically

controlled. Lateral interaction and coverage depended rate constants significantly affect the model results in this range. Infact, reaction rates predicted to be within 7-8 orders of magnitude of the experimental values are considered reasonable for our model assumptions

### 8.2.3 Reaction mechanism analysis

**Table 8.2.4.** Forward/backward reaction rates, relative sensitivity coefficients and partial equilibrium coefficients of elementary steps on Ni (111) surface

Reaction		$r_f$ ( $\text{mol} \cdot \text{g}_{\text{cat}}^{-1} \cdot \text{h}^{-1}$ )	$r_b$ ( $\text{mol} \cdot \text{g}_{\text{cat}}^{-1} \cdot \text{h}^{-1}$ )	Relative sensitivity coefficient	Partial equilibrium coefficient
R1	$\text{CH}_3^* + \text{H}^* \rightarrow \text{CH}_4^*$	9.49E-10	1.13E-13	0.001522	0.99988
R2	$\text{CH}_2^* + \text{H}^* \rightarrow \text{CH}_3^*$	1.25E-08	1.19E-08	0.000372	0.51236
R3	$\text{CH}^* + \text{H}^* \rightarrow \text{CH}_2^*$	4.87E-07	4.87E-07	-0.002729	0.50029
R4	$\text{C}^* + \text{H}^* \rightarrow \text{CH}^*$	8.69E-14	7.97E-14	0.004528	0.52162
R5	$\text{CO}_2^* \rightarrow \text{CO}^* + \text{O}^*$	1.368674	4.66E-06	-0.090242	1
R6	$\text{CO}_2^* + \text{H}^* \rightarrow \text{COOH}^*$	6.68E-05	4.76E-10	0.120573	0.99999
R7	$\text{CO}_2^* + \text{H}^* \rightarrow \text{HCOO}^*$	0.820233	0.818628	-0.018488	0.50049
R8	$\text{COOH}^* \rightarrow \text{CO}^* + \text{OH}^*$	0.001338	0.000621	0.000682	0.68284
R9	$\text{HCOO}^* \rightarrow \text{HCO}^* + \text{O}^*$	1.17E-05	4.1E-11	0.020437	1
R10	$\text{HCO}^* \rightarrow \text{CO}^* + \text{H}^*$	0.042224	0.041078	0.261848	0.50688
R11	$\text{COOH}^* + \text{H}^* \rightarrow \text{HCOOH}^*$	4.78E-09	0.00065	0.000404	7.4E-06
R12	$\text{HCOO}^* + \text{H}^* \rightarrow \text{HCOOH}^*$	0.061726	0.059942	0.001904	0.50733

R13	$\text{HCOOH}^* \rightarrow \text{HCO}^* + \text{OH}^*$	0.001134	3.99E-09	0.052142	1
R14	$\text{CH}_2\text{OH}^* + \text{H}^* \rightarrow \text{CH}_3\text{OH}^*$	1.07E-13	7.96E-14	0.000923	0.5729
R15	$\text{CHOH}^* + \text{H}^* \rightarrow \text{CH}_2\text{OH}^*$	1.28E-12	6.69E-13	0.00031	0.65736
R16	$\text{COH}^* + \text{H}^* \rightarrow \text{CHOH}^*$	7.79E-07	7.78E-07	0.002408	0.50002
R17	$\text{CO}^* + \text{H}^* \rightarrow \text{COH}^*$	2.62E-08	2.59E-08	0.002015	0.50208
R18	$\text{CH}_3\text{OH}^* \rightarrow \text{CH}_3^* + \text{OH}^*$	8.32E-17	7.82E-23	0.000811	1
R19	$\text{CH}_2\text{OH}^* \rightarrow \text{CH}_2^* + \text{OH}^*$	1.62E-12	1.2E-18	-0.00029	1
R20	$\text{CHOH}^* \rightarrow \text{CH}^* + \text{OH}^*$	6.39E-11	2.46E-17	0.071626	1
R21	$\text{COH}^* \rightarrow \text{C}^* + \text{OH}^*$	5.75E-15	2.41E-21	0.001078	1
R22	$\text{CH}_2\text{O}^* + \text{H}^* \rightarrow \text{CH}_3\text{O}^*$	8.07E-08	7.83E-08	0.017297	0.50765
R23	$\text{CHO}^* + \text{H}^* \rightarrow \text{CH}_2\text{O}^*$	2.05E-06	2.09E-06	-0.028378	0.4951
R24	$\text{CH}_3\text{O}^* \rightarrow \text{CH}_3^* + \text{O}^*$	3.47E-10	1.27E-16	0.395047	1
R25	$\text{CH}_2^* + \text{O}^* \rightarrow \text{CH}_2\text{O}^*$	2.95E-11	1.1E-17	0.030717	1
R26	$\text{CHO}^* \rightarrow \text{CH}^* + \text{O}^*$	5.07E-10	1.93E-16	0.814521	1
R27	$\text{CO}^* \rightarrow \text{C}^* + \text{O}^*$	5.36E-16	2.29E-22	0.001091	1
R28	$\text{CH}_3\text{OH}^* + * \rightarrow \text{CH}_3\text{O}^* + \text{H}^*$	1.55E-10	4.09E-10	0.000749	0.27485
R29	$\text{CH}_2\text{OH}^* + * \rightarrow \text{CH}_2\text{O}^* + \text{H}^*$	1.01E-12	2.04E-12	-0.000892	0.33025
R30	$\text{CHOH}^* + * \rightarrow \text{HCO}^* + \text{H}^*$	6.54E-11	6.78E-11	0.003339	0.49102
R31	$\text{O}^* + \text{H}^* \rightarrow \text{OH}^*$	7.25811	7.064825	0.002411	0.50675
R32	$\text{OH}^* + \text{H}^* \rightarrow \text{H}_2\text{O}^*$	0.035761	0.034758	0.111552	0.50711

R33	$\text{H}_2 \rightarrow \text{H}^* + \text{H}^*$	1133249	1133250	-0.00957	0.5
R34	$\text{OH}^* + \text{OH}^* \rightarrow \text{H}_2\text{O}^* + \text{O}^*$	3.191636	3.187064	0.000765	0.50036
R35	$\text{CO}_2^* + \text{C}^* \rightarrow 2\text{CO}^*$	1.48E-27	1.18E-26	0.005302	0.11145
R36	$\text{HCOO}^* + \text{H}^* \rightarrow \text{H}_2\text{COO}^*$	2.72E-09	2.56E-14	0.002844	0.99999
R37	$\text{HCOOH}^* + \text{H}^* \rightarrow \text{H}_2\text{COO}$ $\text{H}^*$	4.03E-08	1.77E-11	0.01627	0.99956
R38	$\text{H}_2\text{COO}^* + \text{H}^* \rightarrow \text{H}_2\text{COOH}$ $*$	6.08E-14	2.76E-12	0.001513	0.02158
R39	$\text{H}_2\text{COO}^* \rightarrow \text{H}_2\text{CO}^* + \text{O}^*$	4.4E-09	1.67E-09	-0.006275	0.72441
R40	$\text{H}_2\text{COOH}^* \rightarrow \text{H}_2\text{CO}^* + \text{OH}$ $*$	4.07E-08	3.32E-10	0.00293	0.9919
R41	$\text{CO}_2 \rightarrow \text{CO}_2^*$	1.376141	0.005801	1	0.9958
R42	$\text{CO}^* \rightarrow \text{CO}$	0.026616	0.026616	-0.000955	0.5
R43	$\text{H}_2\text{O}^* \rightarrow \text{H}_2\text{O} + *$	1348637	1348640	0.309791	0.5
R44	$\text{CH}_4^* \rightarrow \text{CH}_4$	0.041513	0.041513	0.001274	0.5
R45	$\text{HCOOH}^* \rightarrow \text{HCOOH}$	3.181979	3.181979	0.011501	0.5
R46	$\text{CH}_3\text{OH}^* \rightarrow \text{CH}_3\text{OH}$	0.001376	0.001376	0.00209	0.5



**Table 8.2.5.** Forward/backward reaction rates, relative sensitivity coefficients and partial equilibrium coefficients of elementary steps on Ru (001) surface at reaction conditions adapted from section 3.2.1

Reaction		$r_f$ ( $\text{mol} \cdot \text{g}_{\text{cat}}^{-1} \cdot \text{h}^{-1}$ )	$r_b$ ( $\text{mol} \cdot \text{g}_{\text{cat}}^{-1} \cdot \text{h}^{-1}$ )	Relative sensitivity coefficient	Partial equilibrium coefficient
R1	$\text{CH}_3^* + \text{H}^* \rightarrow \text{CH}_4^*$	1.02232E-13	1.9E-19	1	0.999998
R2	$\text{CH}_2^* + \text{H}^* \rightarrow \text{CH}_3^*$	2.57074E-10	2.58E-10	-0.0055	0.498758
R3	$\text{CH}^* + \text{H}^* \rightarrow \text{CH}_2^*$	2.22467E-06	2.22E-06	0.1649	0.499982
R4	$\text{C}^* + \text{H}^* \rightarrow \text{CH}^*$	9.29913E-10	1.14E-10	0.0791	0.890996
R5	$\text{CO}_2^* \rightarrow \text{CO}^* + \text{O}^*$	0.911927292	9.42E-13	0.3583	1
R6	$\text{CO}_2^* + \text{H}^* \rightarrow \text{COOH}^*$	1.63503E-05	3.33E-11	-0.1244	0.999998
R7	$\text{CO}_2^* + \text{H}^* \rightarrow \text{HCOO}^*$	1.008823143	0.325923	-0.2824	0.755817
R8	$\text{COOH}^* \rightarrow \text{CO}^* + \text{OH}^*$	2.9937E-05	1.13E-09	0.0108	0.999962
R9	$\text{HCOO}^* \rightarrow \text{HCO}^* + \text{O}^*$	0.145168899	8.04E-13	0.2523	1
R10	$\text{HCO}^* \rightarrow \text{CO}^* + \text{H}^*$	0.345450945	0.199302	-0.1515	0.634142
R11	$\text{COOH}^* + \text{H}^* \rightarrow \text{HCOOH}^*$	8.67643E-11	1.36E-05	0.1478	6.39E-06
R12	$\text{HCOO}^* + \text{H}^* \rightarrow \text{HCOOH}^*$	0.082467568	0.081483	0.0252	0.503003
R13	$\text{HCOOH}^* \rightarrow \text{HCO}^* + \text{OH}^*$	0.000970461	4.04E-13	-0.0963	1
R14	$\text{CH}_2\text{OH}^* + \text{H}^* \rightarrow \text{CH}_3\text{OH}^*$	1.80772E-16	4.01E-17	0.0002	0.818345
R15	$\text{CHOH}^* + \text{H}^* \rightarrow \text{CH}_2\text{OH}^*$	6.69007E-12	5.49E-12	-0.0049	0.549044

R16	$\text{COH}^* + \text{H}^* \rightarrow \text{CHOH}^*$	4.91367E-07	4.91E-07	0.0174	0.500066
R17	$\text{CO}^* + \text{H}^* \rightarrow \text{COH}^*$	1.50727E-08	3.37E-09	0.6349	0.817276
R18	$\text{CH}_3\text{OH}^* \rightarrow \text{CH}_3^* + \text{OH}^*$	1.39466E-17	7.86E-27	2E-07	1
R19	$\text{CH}_2\text{OH}^* \rightarrow \text{CH}_2^* + \text{OH}^*$	1.20042E-12	1.49E-22	0.0088	1
R20	$\text{CHOH}^* \rightarrow \text{CH}^* + \text{OH}^*$	1.28573E-10	1.31E-20	0.1052	1
R21	$\text{COH}^* \rightarrow \text{C}^* + \text{OH}^*$	8.84194E-10	7.38E-19	0.5897	1
R22	$\text{CH}_2\text{O}^* + \text{H}^* \rightarrow \text{CH}_3\text{O}^*$	1.00732E-09	6.1E-10	0.0049	0.622807
R23	$\text{CHO}^* + \text{H}^* \rightarrow \text{CH}_2\text{O}^*$	1.39379E-05	2.32E-05	-0.2391	0.374987
R24	$\text{CH}_3\text{O}^* \rightarrow \text{CH}_3^* + \text{O}^*$	1.40155E-12	2.48E-25	0.0072	1
R25	$\text{CH}_2^* + \text{O}^* \rightarrow \text{CH}_2\text{O}^*$	1.52911E-10	1.63E-23	0.3119	1
R26	$\text{CHO}^* \rightarrow \text{CH}^* + \text{O}^*$	2.36666E-11	4.2E-24	0.2103	1
R27	$\text{CO}^* \rightarrow \text{C}^* + \text{O}^*$	3.79447E-12	9.54E-24	0.0048	1
R28	$\text{CH}_3\text{OH}^* + ^* \rightarrow \text{CH}_3\text{O}^* + \text{H}^*$	5.22159E-14	2.24E-12	-2E-05	0.022761
R29	$\text{CH}_2\text{OH}^* + ^* \rightarrow \text{CH}_2\text{O}^* + \text{H}^*$	1.26031E-16	1.98E-15	-0.0036	0.05975
R30	$\text{CHOH}^* + ^* \rightarrow \text{HCO}^* + \text{H}^*$	3.15747E-14	2.45E-13	0.002	0.114225
R31	$\text{O}^* + \text{H}^* \rightarrow \text{OH}^*$	1.17884E-05	0.000876	-0.0077	0.013283
R32	$\text{OH}^* + \text{H}^* \rightarrow \text{H}_2\text{O}^*$	1.05506E-05	1.79E-06	-6E-09	0.854783
R33	$\text{H}_2 \rightarrow \text{H}^* + \text{H}^*$	7306.752069	7307.781	0.2528	0.499965
R34	$\text{OH}^* + \text{OH}^* \rightarrow \text{H}_2\text{O}^* + \text{O}^*$	1.4888E-05	3.4E-08	-1E-05	0.997718
R35	$\text{CO}_2^* + \text{C}^* \rightarrow 2\text{CO}^*$	6.90104E-20	2.84E-20	1E-07	0.708752

R36	$\text{HCOO}^* + \text{H}^* \rightarrow \text{H}_2\text{COO}^*$	9.2913E-06	1.93E-09	0.1366	0.999793
R37	$\text{HCOOH}^* + \text{H}^* \rightarrow \text{H}_2\text{COO}$ $\text{H}^*$	4.33361E-09	1.02E-14	-0.0888	0.999998
R38	$\text{H}_2\text{COO}^* + \text{H}^* \rightarrow \text{H}_2\text{COOH}$ $*$	2.31468E-15	2.61E-17	0.0065	0.988868
R39	$\text{H}_2\text{COO}^* \rightarrow \text{H}_2\text{CO}^* + \text{O}^*$	9.28936E-06	4.14E-13	-0.0573	1
R40	$\text{H}_2\text{COOH}^* \rightarrow \text{H}_2\text{CO}^* + \text{OH}$ $*$	4.42632E-09	1.3E-12	-0.0069	0.999706
R41	$\text{CO}_2 \rightarrow \text{CO}_2^*$	1.60646894	0.011622	0.727	0.992818
R42	$\text{CO}^* \rightarrow \text{CO}$	5.63177E-05	3.74E-10	-0.0013	0.999993
R43	$\text{H}_2\text{O}^* \rightarrow \text{H}_2\text{O} + *$	0.92554226	0.925519	-1E-05	0.500006
R44	$\text{CH}_4^* \rightarrow \text{CH}_4$	5.63855E-08	5.64E-08	0.0001	0.5
R45	$\text{HCOOH}^* \rightarrow \text{HCOOH}$	0.006492805	0.006492	0.0324	0.500021
R46	$\text{CH}_3\text{OH}^* \rightarrow \text{CH}_3\text{OH}$	6.4039E-09	6.4E-09	-1E-05	0.500085

### 8.2.4. Reaction pathway analysis

Code availability: This code is a modified version of the priority queue problem.

Reaction pathways with same rate limiting step as the RDS of the dominant pathway for CO<sub>2</sub> methanation on Ni (111)

CO<sub>2</sub>(g)-- CO<sub>2</sub>\*-- CO\*-- **CHO\***-- **CH\***-- CH<sub>2</sub>\*-- CH<sub>3</sub>\*-- CH<sub>4</sub>\*-- CH<sub>4</sub>(g) (Dominant pathway)

CO<sub>2</sub>(g)-- CO<sub>2</sub>\*-- HCOO\*-- **CHO\***-- **CH\***-- CH<sub>2</sub>\*-- CH<sub>3</sub>\*-- CH<sub>4</sub>\*-- CH<sub>4</sub>(g)

CO<sub>2</sub>(g)-- CO<sub>2</sub>\*-- COOH\*-- CO\*-- **CHO\***-- **CH\***-- CH<sub>2</sub>\*-- CH<sub>3</sub>\*-- CH<sub>4</sub>\*-- CH<sub>4</sub>(g)

CO<sub>2</sub>(g)-- CO<sub>2</sub>\*-- COOH\*-- HCOOH\*-- **CHO\***-- **CH\***-- CH<sub>2</sub>\*-- CH<sub>3</sub>\*-- CH<sub>4</sub>\*-- CH<sub>4</sub>(g)

CO<sub>2</sub>(g)-- CO<sub>2</sub>\*-- HCOO\*-- HCOOH\*-- **CHO\***-- **CH\***-- CH<sub>2</sub>\*-- CH<sub>3</sub>\*-- CH<sub>4</sub>\*-- CH<sub>4</sub>(g)

CO<sub>2</sub>(g)-- CO<sub>2</sub>\*-- CO\*-- COOH\*-- HCOOH\*-- **CHO\***-- **CH\***-- CH<sub>2</sub>\*-- CH<sub>3</sub>\*-- CH<sub>4</sub>\*-- CH<sub>4</sub>(g)

CO<sub>2</sub>(g)-- CO<sub>2</sub>\*-- COOH\*-- HCOOH\*-- HCOO\*-- **CHO\***-- **CH\***-- CH<sub>2</sub>\*-- CH<sub>3</sub>\*-- CH<sub>4</sub>\*-- CH<sub>4</sub>(g)

CO<sub>2</sub>(g)-- CO<sub>2</sub>\*-- HCOO\*-- H<sub>2</sub>COO\*-- CH<sub>2</sub>O\*-- **CHO\***-- **CH\***-- CH<sub>2</sub>\*-- CH<sub>3</sub>\*-- CH<sub>4</sub>\*-- CH<sub>4</sub>(g)

CO<sub>2</sub>(g)-- CO<sub>2</sub>\*-- CO\*-- COOH\*-- HCOOH\*-- HCOO\*-- **CHO\***-- **CH\***-- CH<sub>2</sub>\*-- CH<sub>3</sub>\*-- CH<sub>4</sub>\*-- CH<sub>4</sub>(g)

CO<sub>2</sub>(g)-- CO<sub>2</sub>\*-- COOH\*-- HCOOH\*-- H<sub>2</sub>COOH\*-- CH<sub>2</sub>O\*-- **CHO\***-- **CH\***-- CH<sub>2</sub>\*-- CH<sub>3</sub>\*-- CH<sub>4</sub>\*-- CH<sub>4</sub>(g)

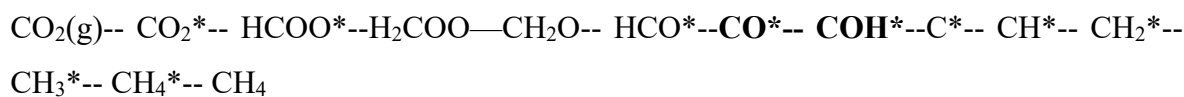
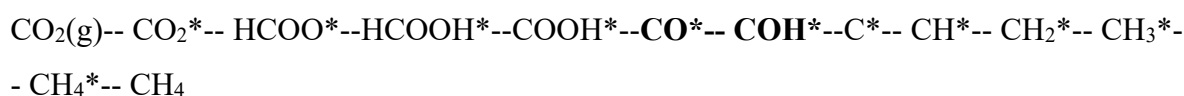
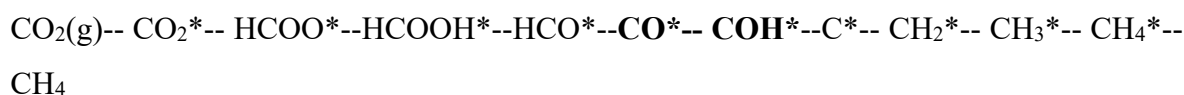
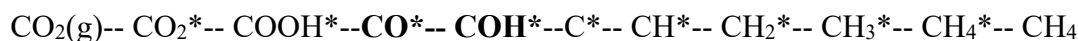
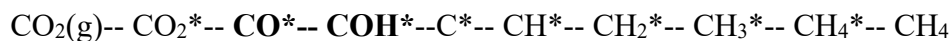
CO<sub>2</sub>(g)-- CO<sub>2</sub>\*-- CO\*-- COOH\*-- HCOOH\*-- H<sub>2</sub>COOH\*-- CH<sub>2</sub>O\*-- **CHO\***-- **CH\***-- CH<sub>2</sub>\*-- CH<sub>3</sub>\*-- CH<sub>4</sub>\*-- CH<sub>4</sub>(g)

CO<sub>2</sub>(g)-- CO<sub>2</sub>\*-- COOH\*-- HCOOH\*-- HCOO\*-- H<sub>2</sub>COO\*-- CH<sub>2</sub>O\*-- **CHO\***-- **CH\***-- CH<sub>2</sub>\*-- CH<sub>3</sub>\*-- CH<sub>4</sub>\*-- CH<sub>4</sub>(g)

CO<sub>2</sub>(g)-- CO<sub>2</sub>\*-- CO\*-- COOH\*-- HCOOH\*-- HCOO\*-- H<sub>2</sub>COO\*-- CH<sub>2</sub>O\*-- **CHO\***-- **CH\***-- CH<sub>2</sub>\*-- CH<sub>3</sub>\*-- CH<sub>4</sub>\*-- CH<sub>4</sub>(g)

Reaction pathways with same rate limiting step as the RDS of the dominant pathway for CO<sub>2</sub> methanation on Ru (001)

There are almost 250 pathways satisfying this criteria. Here we are reporting only 7 of them. These are the fastest routes from reactant ( $\text{CO}_2(\text{g})$ ) to RDS's reactants ( $\text{CH}_3^*$ ). The rate limiting step for these sub-paths ( $\text{CO}_2(\text{g}) \rightarrow \text{CH}_3^*$ ) are the same i.e.  $\text{CO}^* \rightarrow \text{COH}^*$ . The reaction rate of this step is  $2.57 \times 10^{-10} \text{ mol/g}_{\text{cat}} \cdot \text{h}$



### 8.2.5. Estimating rate constants and Gibbs energy for elementary reaction steps

*Ab initio* electronic structure calculations using DFT yields energies at zero kelvin temperatures (electronic energy). Entropic and enthalpic corrections must be applied to the electronic energies to get the Gibbs free energy changes under reaction conditions. Entropy calculations using vibrational frequencies calculated with simple harmonic approximation are widely used.

In some cases, especially for weakly adsorbed system, the simple harmonic approximation underpredicts the entropy<sup>257,258</sup>. Many other schemes were developed recently to accurately predict the vibrational frequency for various systems. In this regard, the semi-empirical Campbell-Sellers equation ( $-\Delta S_{\text{ads}}(T) = 0.3S_{\text{gas}}(T) + 3.3R$ ) was proposed by Sellers et al.<sup>259,260</sup>. Using this approach the entropies of moderate to weak adsorbing molecules (such as  $\text{CH}_3\text{OH}$ ,  $\text{CH}_2\text{O}$ ) under low coverages (0.001 to 100 monolayer/s) were calculated accurately<sup>254</sup>. However, the Campbell-Sellers equation cannot be applied to estimate the

entropy of tightly adsorbing molecules and molecular fragments (they dissociate at temperatures lower than their adsorption temperatures). In the case of molecular fragments, the entropy is evaluated from a combination of harmonic vibrational frequency and 2D diffusion barriers<sup>261</sup>. Additionally, for materials such as zeolites or metal organic frameworks the entropy predicted by Campbell-Sellers equation is not accurate. Here the entropy losses due to confinement (as pore diameter approaches size of adsorbing molecule, confinement dominates molecular motion) must be accounted by expanding the Campbell-Sellers equation. Dauenhauer et al. modified the surface entropy term to a linear combination of entropy lost on flat surface and entropy lost from confinement<sup>262</sup>. They considered nine aluminosilicate zeolite framework and predicted the surface entropy accurately. Researchers are developing more rigorous sampling-based approaches (eg. sampling of the molecular conformational space by means of classical molecular dynamics simulations) to accurately predict the entropy contributions<sup>262</sup>.

The rate constants of each reaction step are determined using the transition state theory<sup>263</sup>

$$k = k_B T/h \exp \left[ \frac{-\Delta G_{act}}{RT} \right] \quad (9)$$

where,  $\Delta G_{act}$  is the Gibbs free energy of activation of the reaction step and R is the universal gas constant.

Once the forward rate constant ( $k_f$ ) is known, the backward rate constant ( $k_r$ ) could be derived using the equilibrium constant ( $K_{eq}$ )

$$\frac{k_f}{k_r} = K_{eq} = \exp \left[ \frac{-\Delta G_{rec}}{RT} \right] \quad (10)$$

where,  $\Delta G_{rec}$  is the Gibbs free energy of the reaction step. Given an elementary reaction step with transition state species  $AB_{\#}$



$\Delta G_{act}$  and  $\Delta G_{rec}$  is defined as

$$\Delta G_{act} = G_{AB_{\#}} - G_A - G_B \quad (11)$$

$$\Delta G_{rec} = G_C + G_D - G_A - G_B \quad (12)$$

The Gibbs energy ( $G_A$ ) for a species is given as

$$G_A = E_{\text{DFT}} + E_{\text{ZPE}} + \Delta H_T(0 \rightarrow T) - T\Delta S \quad (13)$$

where,  $E_{\text{DFT}}$  is the energy obtained from DFT,  $E_{\text{ZPE}}$  is the zero-point energy correction,  $\Delta H_T$  is the temperature correction from 0 K to the reaction temperature T and  $T\Delta S$  is the entropy correction. The zero-point energy correction is calculated as

$$E_{\text{ZPE}} = \sum_{i=1}^{\# \text{ of modes}} \frac{N_A h \vartheta_i}{2} \quad (14)$$

where,  $N_A$  is Avogadro's number,  $h$  is Planck's constant and  $\vartheta_i$  is the frequency of the normal mode. However, temperature and entropy corrections are different for gaseous and surface species<sup>87,263</sup>.

### Gaseous species

These species have all of the translational, rotational and vibrational degrees of freedom active. Hence total enthalpy temperature correction  $\Delta H_T$  at temperature T is given as sum of translational ( $H_{\text{trans}}$ ), rotational ( $H_{\text{rot}}$ ) and vibrational ( $H_{\text{vib}}$ ) enthalpy corrections

$$\Delta H_T = H_{\text{trans}} + H_{\text{rot}} + H_{\text{vib}} \quad (15)$$

where,

$$H_{\text{trans}} = \frac{5}{2} RT \quad (16)$$

$$H_{\text{rot}} = \frac{f}{2} RT \quad (17)$$

$f$  is equal to 2 for linear molecules and 3 for other cases

$$H_{\text{vib}} = \sum_i^{\# \text{ of modes}} \frac{N_A h \nu_i e^{-h\nu_i/k_B T}}{1 - e^{-h\nu_i/k_B T}} \quad (18)$$

$k_B$  is Boltzmann constant.

Similarly, the total entropy correction is given as the sum of translational ( $S_{\text{trans,3D}}$ ), rotational ( $S_{\text{rot}}$ ) and vibrational ( $S_{\text{vib}}$ ) entropy corrections

$$\Delta S = S_{\text{trans,3D}} + S_{\text{rot}} + S_{\text{vib}} \quad (19)$$

The translational entropy correction is given as

$$S_{\text{trans,3D}} = R \left[ \ln \left( \frac{(2\pi m k_B T)^{3/2}}{h^3} \right) + \ln \left[ \frac{V}{N_g} \right] + \frac{5}{2} \right] \quad (20)$$

where  $m$  is the mass of the molecule and  $\frac{V}{N_g}$  is the volume per molecule in the standard state.

The rotational entropy correction for a non-linear molecule is given as

$$S_{\text{rot}} = R \left[ \ln \left( \frac{8\pi^2 \sqrt{8\pi^3 I_{x1} I_{x2} I_{x3}} (k_B T)^{3/2}}{\sigma_r h^3} \right) + \frac{3}{2} \right] \quad (21)$$

where  $I_{x1}$ ,  $I_{x2}$ , and  $I_{x3}$  are the three moments of inertia about the principal axes and  $\sigma_r$  is the rotational symmetry number. For linear molecules however

$$S_{\text{rot,linear}} = R \left[ \ln \left( \frac{8\pi^2 I_{\text{linear}} (k_B T)}{\sigma_r h^2} \right) + 1 \right] \quad (22)$$

where  $I_{\text{linear}}$  is the moment of inertia of a linear molecule. The vibrational entropy correction of a molecule is

$$S_{\text{vib}} = R \sum_i^{\text{\# of modes}} \left( \frac{\frac{h\nu_i}{k_B T}}{e^{h\nu_i/k_B T} - 1} - \ln(1 - e^{-h\nu_i/k_B T}) \right) \quad (23)$$

For the gas phase species at reaction temperature  $T$  and pressure  $P$ , we also include pressure corrections  $\left( S_p = RT \ln \left( \frac{P}{P_0} \right) \right)$  in the right-hand side of equation (5) for computing Gibbs energy.

### Weakly bound species

The weakly bound species such as physisorbed  $\text{CO}_2$  are treated as 2D gases that maintain the full rotational and vibrational modes of their corresponding 3D gaseous species. Therefore, temperature and entropy corrections corresponding to rotation and vibration are the same as for the gaseous species. However, the translational correction terms at temperature  $T$  are given as

$$H_{\text{trans,2D}} = 2RT \quad (24)$$



$$S_{\text{trans},2\text{D}} = R \left[ \ln \left( \frac{2\pi m k_B T}{h^2} \right) + \ln \left( \frac{SA}{N_{\text{sat}}} \right) + 2 \right] \quad (25)$$

where,  $\frac{SA}{N_{\text{sat}}}$  is the area occupied per adsorbed molecule at the standard state conditions which is equal to the reciprocal of the surface concentration for monolayer coverage.

### **Tightly bound species**

All of the intermediate and transition state species are tightly bound species. Since they are bonded to the surface their translational and rotational modes are replaced by vibrational modes corresponding to frustrated translation and rotation on the surface. Their temperature and entropy corrections are given using the same equation (10) and (15).

It should be noted that we do not include these corrections while computing Gibbs energy of the lattice as they anyway get cancelled while computing activation and reaction energies. For computing the rate constants of the adsorption and the desorption reactions, both transition state theory and collision theory can be applied. However, it is known that the expression for the rate of adsorption obtained from collision theory with  $\sigma = 1$  is the same as that obtained from transition state theory for a mobile activated complex with  $E_a(T = 0) = 0$ .<sup>263</sup> Therefore, in this study, the rate constants ( $k_{\text{ads}}$ ) for adsorption reactions are also computed using the transition state theory<sup>88</sup>.

$$k_{\text{ads}} = \sigma k_B T / h \exp \left[ \frac{-\Delta G_{\text{act}}}{RT} \right] \quad (26)$$

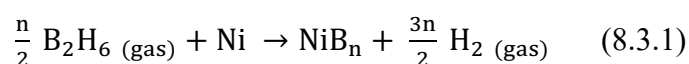
where,  $\sigma$  is the sticking coefficient. The sticking coefficients for Ni (111) and Ru (001) are obtained from literature<sup>3</sup>.

## 8.3 Appendix to chapter 5

### 8.3.1. NiB – Structure and stability

The location of boron promoter on nickel is explored by several computational and experimental studies by Xu et. al.<sup>80–82</sup>. They calculated the binding strength of boron on four on-surface sites present on nickel (top, bridge, fcc hollow, hcp hollow sites) and compared with the binding energy of boron on octahedral site present in first and second subsurface layer. The first subsurface octahedral site was found to be the most stable adsorption site for boron. This site is stable by 28 kJ/mol compared to the most stable on-surface site (hcp hollow site) and 20 kJ/mol more stable compared to the octahedral site in second subsurface layer. The stability of subsurface octahedral site is due to the strong bonding interaction between boron 2p and nickel 3d bands. The bonding orbital shifted to -4.8 eV for octahedral boron compared with -2.8 eV for on-surface boron. To test how boron filling happens, they studied boron binding energy for different configurations of four boron atoms on three adsorption sites (on-surface hollow site and octahedral sites in first and second subsurface layer). They found that a monolayer of boron in the first subsurface was the most stable configuration. In addition, the strong interaction between neighbouring boron atoms leads to the surface reconstruction of nickel atoms and it begins to resemble a stepped surface. Moreover, the surface reconstruction lowers the surface energy by 0.38 J/m<sup>2</sup> as compared to the plane surface. The NiB catalyst was successfully synthesized and characterized with 0.5% to 1% boron loading and also tested under steam reforming reaction conditions (800 °C, 1 atm). From XPS studies, it was observed that Ni:B ratio on surface was 1:0.64 compared to bulk ratio of 1:0.18 which clearly indicates that boron prefers surface sites compared to the bulk. Importantly, the presence of sub-surface B prevents the diffusion of carbon to the bulk and sub-surface sites in Ni. Based on scanning electron microscopy (SEM) and temperature-programmed oxidation (TPO), it was shown that the amount of deposited carbon reduced by 80%<sup>81</sup>.

To test the stability at high pressure (10 atm), we evaluated the Gibbs free energy change of the reaction:



under 1 atm and 10 atm pressures. This method is widely employed to assess the stabilities of boron promoted transition metals (Cu-B (J. Phys. Chem. C 121 (2017) 1099–1112), Ni-B (J. Phys. Chem. C 113 (2009) 4099–4106), Pd-B (ACS Catalysis 5 (2015) 6579)). Diborane ( $B_2H_6$ ) is used as the source of boron as it is more stable than boric acid ( $H_3BO_3$ ) under the reaction conditions. We found that the difference in Gibbs free energy change for the reaction (A) at 1 atm pressure and 10 atm pressure (temperature is kept same at 973 K) is only 1.5 kJ/mol. This clearly indicates that increasing the pressure to 10 atm doesn't affect the stability of NiB.

**Table 8.3.1.** Activation barriers and reaction energies (electronic energy) of all elementary reactions for DRM on Ni (111) and NiB surfaces.

Reaction	Activation barrier (kJ/mol)		
	Ni (111)		NiB
	This work	Reported	
R1: $CH_4^* \rightarrow CH_3^* + H^*$	115	$112^{88}, 118^{250}, 112^{251}, 129^{252,253}$	91
R2: $CH_3^* \rightarrow CH_2^* + H^*$	75	$78^{88}, 81^{250}, 79^{251}, 66^9$	86
R3: $CH_2^* \rightarrow CH^* + H^*$	35	$35^{88}, 28^{250}, 36^{251}, 26^9$	53
R4: $CH^* \rightarrow C^* + H^*$	137	$138^{254}, 132^{251}, 135^9$	106
R5: $CO_2^* \rightarrow CO^* + O^*$	54	$64^{87}, 43^{167}, 39^{98}, 53^{251}$	124
R6: $CO_2^* + H^* \rightarrow COOH^*$	109	$108^{87}, 99^{167}$	140
R7: $CO_2^* + H^* \rightarrow HCOO^*$	67	$52^{167}, 56^{98}$	63
R8: $COOH^* \rightarrow CO^* + OH^*$	37	$54^{87}, 36^{98}$	87
R9: $HCOO^* \rightarrow HCO^* + O^*$	148	$134^{98}$	230
R10: $HCO^* \rightarrow CO^* + H^*$	30	$19^{87}, 28^{251}, 20^9$	38
R11: $COOH^* + H^* \rightarrow HCOOH^*$	83	-	84
R12: $HCOO^* + H^* \rightarrow HCOOH^*$	127	$77^{167}$	154
R13: $HCOOH^* \rightarrow HCO^* + OH^*$	100	$86^{167}$	80
R14: $CH_3OH^* \rightarrow CH_2OH^* + H^*$	119	$84^{87}$	102
R15: $CH_2OH^* \rightarrow CHOH^* + H^*$	74	$51^{87}$	92

R16: $\text{CHOH}^* \rightarrow \text{COH}^* + \text{H}^*$	27	$14^{87}$	67
R17: $\text{COH}^* \rightarrow \text{CO}^* + \text{H}^*$	101	$94^{87}, 86^9$	88
R18: $\text{CH}_3^* + \text{OH}^* \rightarrow \text{CH}_3\text{OH}^*$	197	$211^{87}, 174^{255}, 125^9$	216
R19: $\text{CH}_2^* + \text{OH}^* \rightarrow \text{CH}_2\text{OH}^*$	132	$126^{87}, 85^9$	89
R20: $\text{CH}^* + \text{OH}^* \rightarrow \text{CHOH}^*$	154	$142^{87}, 138^{255}, 123^9$	145
R21: $\text{C}^* + \text{OH}^* \rightarrow \text{COH}^*$	149	$140^{87}, 126^9$	137
R22: $\text{CH}_3\text{O}^* \rightarrow \text{CH}_2\text{O}^* + \text{H}^*$	113	$89^{87}, 62^{251}$	93
R23: $\text{CH}_2\text{O}^* \rightarrow \text{CHO}^* + \text{H}^*$	50	$34^{87}, 37^{251}$	54
R24: $\text{CH}_3^* + \text{O}^* \rightarrow \text{CH}_3\text{O}^*$	133	$152^{87}, 90^{251}, 152^9$	158
R25: $\text{CH}_2^* + \text{O}^* \rightarrow \text{CH}_2\text{O}^*$	130	$139^{87}, 75^{251}, 131^9$	101
R26: $\text{CH}^* + \text{O}^* \rightarrow \text{CHO}^*$	145	$146^{87}, 77^{251}, 108^{255}, 151^9$	168
R27: $\text{C}^* + \text{O}^* \rightarrow \text{CO}^*$	162	$152^{87}, 206^9$	170
R28: $\text{CH}_3\text{OH}^* + ^* \rightarrow \text{CH}_3\text{O}^* + \text{H}^*$	101	-	100
R29: $\text{CH}_2\text{OH}^* + ^* \rightarrow \text{CH}_2\text{O}^* + \text{H}^*$	76	-	110
R30: $\text{CHOH}^* + ^* \rightarrow \text{HCO}^* + \text{H}^*$	83	-	70
R31: $\text{O}^* + \text{H}^* \rightarrow \text{OH}^*$	125	$129^{87}, 128^{251}$	119
R32: $\text{OH}^* + \text{H}^* \rightarrow \text{H}_2\text{O}^*$	147	$137^{251}$	137
R33: $\text{H}^* + \text{H}^* \rightarrow \text{H}_2$	86	$81^{256}$	68
R34: $\text{OH}^* + \text{OH}^* \rightarrow \text{H}_2\text{O}^* + \text{O}^*$	92	-	106
R35: $\text{CO}_2^* + \text{C}^* \rightarrow 2\text{CO}^*$	153	-	123
R36: $\text{CO}_2 \rightarrow \text{CO}_2^*$	-	-	-
R37: $\text{CO}^* \rightarrow \text{CO}$	-	-	-
R38: $\text{H}_2\text{O}^* \rightarrow \text{H}_2\text{O} + ^*$	-	-	-

**Table 8.3.2.** Kinetic rate constants of elementary reactions.

Elementary reactions	Rate Constants (s <sup>-1</sup> )			
	Ni (111)		B-doped Ni	
	k <sub>f</sub>	k <sub>r</sub>	k <sub>f</sub>	k <sub>r</sub>
R1: CH <sub>4</sub> *→CH <sub>3</sub> *+H*	1.65x10 <sup>2</sup>	8.58x10 <sup>8</sup>	1.40x10 <sup>5</sup>	3.23x10 <sup>10</sup>
R2: CH <sub>3</sub> *→CH <sub>2</sub> *+H*	1.4x10 <sup>10</sup>	2.46x10 <sup>10</sup>	3.84x10 <sup>8</sup>	9.25x10 <sup>11</sup>
R3: CH <sub>2</sub> *→CH*+H*	2.49x10 <sup>11</sup>	1.08x10 <sup>10</sup>	1.95x10 <sup>10</sup>	1.01x10 <sup>11</sup>
R4: CH*→C*+H*	3.15x10 <sup>6</sup>	5.01x10 <sup>8</sup>	1.27x10 <sup>8</sup>	1.15x10 <sup>11</sup>
R5: CO <sub>2</sub> *→CO*+O*	7.84x10 <sup>9</sup>	2.90x10 <sup>4</sup>	3.15x10 <sup>7</sup>	7.68x10 <sup>4</sup>
R6: CO <sub>2</sub> *+H*→COOH*	1.66x10 <sup>7</sup>	6.5x10 <sup>8</sup>	3.86x10 <sup>5</sup>	9.87x10 <sup>6</sup>
R7: CO <sub>2</sub> *+H*→HCOO*	3.8x10 <sup>9</sup>	3.71x10 <sup>8</sup>	1.03x10 <sup>10</sup>	1.18x10 <sup>7</sup>
R8: COOH*→CO*+OH*	7.64x10 <sup>12</sup>	2.66x10 <sup>6</sup>	1.21x10 <sup>10</sup>	4.20x10 <sup>3</sup>
R9: HCOO*→HCO*+O*	2.09x10 <sup>5</sup>	5.34x10 <sup>7</sup>	1.26x10 <sup>1</sup>	1.60x10 <sup>7</sup>
R10: HCO*→CO*+H*	3.27x10 <sup>12</sup>	4.86x10 <sup>5</sup>	3.95x10 <sup>12</sup>	6.65x10 <sup>6</sup>
R11: COOH*+H*→HCOOH*	6.94x10 <sup>8</sup>	2.9x10 <sup>9</sup>	3.09x10 <sup>8</sup>	8.5x10 <sup>9</sup>
R12: HCOO*+H*→HCOOH*	4.65x10 <sup>7</sup>	7.77x10 <sup>10</sup>	1.34x10 <sup>6</sup>	8.31x10 <sup>11</sup>
R13: HCOOH*→HCO*+OH*	7.94x10 <sup>9</sup>	4.45x10 <sup>9</sup>	2.73x10 <sup>9</sup>	2.04x10 <sup>7</sup>
R14: CH <sub>3</sub> OH*→CH <sub>2</sub> OH*+H*	3.98x10 <sup>5</sup>	6.86x10 <sup>8</sup>	1.63x10 <sup>7</sup>	4.20x10 <sup>9</sup>
R15: CH <sub>2</sub> OH*→CHOH*+H*	2.77x10 <sup>9</sup>	2.47x10 <sup>8</sup>	2.43x10 <sup>9</sup>	1.03x10 <sup>10</sup>
R16: CHOH*→COH*+H*	1.61x10 <sup>12</sup>	3.13x10 <sup>8</sup>	6.05x10 <sup>9</sup>	5.54x10 <sup>10</sup>
R17: COH*→CO*+H*	8.44x10 <sup>7</sup>	7.85x10 <sup>1</sup>	2.75x10 <sup>9</sup>	8.72x10 <sup>-1</sup>
R18: CH <sub>3</sub> *+OH*→CH <sub>3</sub> OH*	3.13x10 <sup>3</sup>	2.90x10 <sup>4</sup>	3.34x10 <sup>1</sup>	8.60x10 <sup>4</sup>
R19: CH <sub>2</sub> *+OH*→CH <sub>2</sub> OH*	1.31x10 <sup>6</sup>	1.19x10 <sup>10</sup>	1.76x10 <sup>8</sup>	4.86x10 <sup>10</sup>
R20: CH*+OH*→CHOH*	8.41x10 <sup>5</sup>	1.57x10 <sup>10</sup>	2.70x10 <sup>5</sup>	6.12x10 <sup>7</sup>
R21: C*+OH*→COH*	1.34x10 <sup>6</sup>	3.04x10 <sup>4</sup>	6.70x10 <sup>5</sup>	1.53x10 <sup>6</sup>
R22: CH <sub>3</sub> O*→CH <sub>2</sub> O*+H*	6.21x10 <sup>7</sup>	1.84x10 <sup>10</sup>	3.00x10 <sup>8</sup>	5.38x10 <sup>10</sup>
R23: CH <sub>2</sub> O*→CHO*+H*	2.86x10 <sup>11</sup>	2.98x10 <sup>9</sup>	8.96x10 <sup>10</sup>	1.66x10 <sup>10</sup>
R24: CH <sub>3</sub> *+O*→CH <sub>3</sub> O*	1.78x10 <sup>6</sup>	3.70x10 <sup>6</sup>	1.38x10 <sup>5</sup>	73429.8
R25: CH <sub>2</sub> *+O*→CH <sub>2</sub> O*	1.54x10 <sup>6</sup>	5.34x10 <sup>8</sup>	5.78x10 <sup>7</sup>	2.29x10 <sup>6</sup>
R26: CH*+O*→CHO*	4.18x10 <sup>5</sup>	3.49x10 <sup>7</sup>	6.22x10 <sup>4</sup>	8.86x10 <sup>1</sup>

R27: $C^* + O^* \rightarrow CO^*$	$7.44 \times 10^4$	$5.78 \times 10^{-3}$	$5.03 \times 10^4$	$1.33 \times 10^{-7}$
R28: $CH_3OH^* + * \rightarrow CH_3O^* + H^*$	$1.21 \times 10^8$	$7.28 \times 10^6$	$3.94 \times 10^8$	$2.24 \times 10^7$
R29: $CH_2OH^* + * \rightarrow CH_2O^* + H^*$	$3.55 \times 10^9$	$3.67 \times 10^7$	$1.33 \times 10^8$	$5.24 \times 10^6$
R30: $CHOH^* + * \rightarrow HCO^* + H^*$	$1.73 \times 10^{10}$	$2.10 \times 10^7$	$2.54 \times 10^9$	$4.37 \times 10^6$
R31: $O^* + H^* \rightarrow OH^*$	$1.35 \times 10^7$	$4.97 \times 10^7$	$1.03 \times 10^7$	$3.74 \times 10^4$
R32: $OH^* + H^* \rightarrow H_2O^*$	$3.45 \times 10^6$	$3.49 \times 10^7$	$5.76 \times 10^6$	$3.56 \times 10^7$
R33: $H^* + H^* \rightarrow H_2$	$3.45 \times 10^8$	$2.65 \times 10^6$	$7.81 \times 10^8$	$9.62 \times 10^5$
R34: $OH^* + OH^* \rightarrow H_2O^* + O^*$	$3.3 \times 10^8$	$9.11 \times 10^8$	$1.61 \times 10^7$	$2.73 \times 10^{10}$
R35: $CO_2^* + C^* \rightarrow 2CO^*$	$1.00 \times 10^5$	$2.88 \times 10^{-8}$	$1.55 \times 10^6$	$1.00 \times 10^{-8}$
R36: $CO_2 \rightarrow CO_2^*$	$1.18 \times 10^2$	$2.48 \times 10^7$	$1.77 \times 10^3$	$2.39 \times 10^6$
R37: $CO^* \rightarrow CO$	$3.67 \times 10^5$	$8.21 \times 10^6$	$1.40 \times 10^6$	$7.80 \times 10^7$
R38: $H_2O^* \rightarrow H_2O + *$	$2.84 \times 10^{11}$	$2.01 \times 10^8$	$7.45 \times 10^9$	$1.34 \times 10^8$

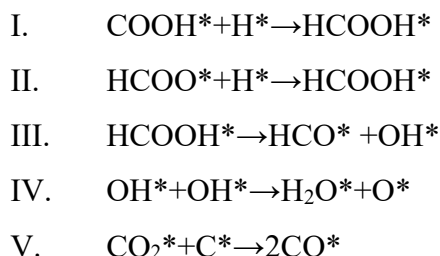
### 8.3.2. Model development and comparison

Herein we re-compute the results of the previously reported model <sup>64</sup> for the DRM reaction over Ni. We then develop a series of models by varying the number of elementary reaction steps and the DFT corrections used (See Table 8.3.3) to finally develop our microkinetic model (Model 4) i.e. the most comprehensive model.

**Table 8.3.3.** Different model specifications

Specification	Reported model	Model 1	Model 2	Model 3	Model 4
DFT functional	PBE <sup>124</sup>	PBE	PBE	rPBE-vdW <sup>128</sup>	rPBE-vdW
Dispersion correction	No	No	No	Yes	Yes
Number of elementary steps	33	33	33	33	38
P <sub>std</sub>	1 Pa	1 Pa	10 <sup>5</sup> Pa	10 <sup>5</sup> Pa	10 <sup>5</sup> Pa

It should be noted that the previously reported kinetic rate constants<sup>64</sup> were directly employed in Models 1 and 2. The following five extra reactions were included in Model 4 apart from the 33 reactions in the reported model<sup>64</sup>



The models were solved for the reaction conditions adapted from section 3.2.1 in the paper. The surface coverages of reaction intermediates obtained after solving these microkinetic models are given in Table 8.3.4.

**Table 8.3.4.** Fractional surface coverages of surface species over Ni computed by different models at a reaction temperature of 973.15 K, 10 bar pressure and an inlet feed composition of 50% volume fraction CH<sub>4</sub> and 50% volume fraction of CO<sub>2</sub>. Model 1 and 2 uses PBE DFT functional and it does not include dispersion corrections. Model 3 and 4 uses rPBE-vdW DFT functional that includes dispersion corrections

Species	Reported <sup>64</sup>	Model 1	Model 2	Model 3	Model 4
CH <sub>3</sub> *	9.98x10 <sup>-7</sup>	9.98x10 <sup>-7</sup>	5.99x10 <sup>-12</sup>	1.02x10 <sup>-7</sup>	9.71x10 <sup>-8</sup>
CH <sub>2</sub> *	3.21x10 <sup>-6</sup>	3.49x10 <sup>-6</sup>	8.81x10 <sup>-14</sup>	7.85x10 <sup>-7</sup>	7.58x10 <sup>-7</sup>
CH*	1.19x10 <sup>-3</sup>	1.41x10 <sup>-3</sup>	2.76x10 <sup>-9</sup>	2.49x10 <sup>-4</sup>	2.46x10 <sup>-4</sup>
C*	1.69x10 <sup>-2</sup>	1.64x10 <sup>-1</sup>	4.34x10 <sup>-4</sup>	2.15x10 <sup>-5</sup>	2.17x10 <sup>-5</sup>
CO <sub>2</sub> *	4.89x10 <sup>-6</sup>	4.61x10 <sup>-6</sup>	3.44x10 <sup>-10</sup>	1.02x10 <sup>-6</sup>	1.02x10 <sup>-6</sup>
CO*	6.60x10 <sup>-1</sup>	5.50x10 <sup>-1</sup>	6.81x10 <sup>-7</sup>	9.24x10 <sup>-1</sup>	9.25x10 <sup>-1</sup>
COOH*	6.47x10 <sup>-10</sup>	4.47x10 <sup>-10</sup>	3.91x10 <sup>-20</sup>	1.88x10 <sup>-9</sup>	1.84x10 <sup>-9</sup>
HCOO*	3.78x10 <sup>-8</sup>	1.18x10 <sup>-10</sup>	2.13x10 <sup>-19</sup>	7.6x10 <sup>-7</sup>	7.43x10 <sup>-7</sup>
HCO*	3.72x10 <sup>-8</sup>	2.85x10 <sup>-8</sup>	2.73x10 <sup>-17</sup>	9.93x10 <sup>-9</sup>	9.78x10 <sup>-9</sup>
HCOOH*	-	-	-	-	3.16x10 <sup>-11</sup>
CH <sub>3</sub> OH*	3.20x10 <sup>-15</sup>	1.94x10 <sup>-15</sup>	2.06x10 <sup>-26</sup>	4.56x10 <sup>-12</sup>	4.21x10 <sup>-12</sup>

CH <sub>2</sub> OH	3.82x10 <sup>-14</sup>	2.67x10 <sup>-14</sup>	6.9x10 <sup>-27</sup>	3.34x10 <sup>-13</sup>	3.14x10 <sup>-13</sup>
CHOH*	4.11x10 <sup>-12</sup>	2.95x10 <sup>-12</sup>	8.34x10 <sup>-24</sup>	1.84x10 <sup>-12</sup>	1.76x10 <sup>-12</sup>
COH*	2.09x10 <sup>-7</sup>	1.62x10 <sup>-7</sup>	4.43x10 <sup>-16</sup>	7.83x10 <sup>-8</sup>	7.66x10 <sup>-8</sup>
CH <sub>3</sub> O*	1.50x10 <sup>-11</sup>	9.84x10 <sup>-12</sup>	1.02x10 <sup>-19</sup>	1.01x10 <sup>-9</sup>	9.52x10 <sup>-10</sup>
CH <sub>2</sub> O*	1.36x10 <sup>-11</sup>	9.62x10 <sup>-12</sup>	6.64x10 <sup>-22</sup>	8.93x10 <sup>-12</sup>	8.61x10 <sup>-12</sup>
H <sub>2</sub> O*	2.66x10 <sup>-6</sup>	2.27x10 <sup>-6</sup>	5.64x10 <sup>-13</sup>	1.22x10 <sup>-6</sup>	2.08x10 <sup>-6</sup>
O*	2.40x10 <sup>-3</sup>	2.43x10 <sup>-3</sup>	9.61x10 <sup>-4</sup>	1.65x10 <sup>-2</sup>	1.605x10 <sup>-2</sup>
H*	5.71x10 <sup>-2</sup>	4.69x10 <sup>-2</sup>	1.48x10 <sup>-4</sup>	4.02x10 <sup>-3</sup>	3.84x10 <sup>-3</sup>
OH*	6.13x10 <sup>-5</sup>	5.69x10 <sup>-5</sup>	1.68x10 <sup>-8</sup>	3.25x10 <sup>-4</sup>	3.09x10 <sup>-4</sup>
Free Site (*)	2.63x10 <sup>-1</sup>	2.35x10 <sup>-1</sup>	9.98x10 <sup>-1</sup>	5.53x10 <sup>-2</sup>	5.41x10 <sup>-2</sup>
$x_{CH_4}$	1.59x10 <sup>-1</sup>	1.44x10 <sup>-1</sup>	2.2x10 <sup>-3</sup>	7.69x10 <sup>-2</sup>	7.67x10 <sup>-2</sup>
$x_{CO_2}$	3.78x10 <sup>-1</sup>	3.51x10 <sup>-1</sup>	3.26x10 <sup>-3</sup>	8.36x10 <sup>-2</sup>	8.84x10 <sup>-2</sup>

From Table 8.3.4 it may be concluded that Model 1 has successfully reproduced the reported values of fractional coverages. However, the correct value of  $P_{std}$ , i.e.  $10^5$  Pa, is not employed in the adsorption rate equations (Equation 2) for this model, instead a value of 1 Pa is assumed. Therefore, in order to correctly employ  $P_{std}$  in the rate equations, Model 2 is constructed and although Model 1 closely resembles the reported study<sup>64</sup>, the surface coverage obtained from Model 2 is considered for further analysis.

Model 3, on the other hand, is constructed from the energy data generated by DFT calculation using appropriate functional and corrections. After incorporating these corrections, we can see that the surface coverages of the adsorbed reactant is significantly improved. The fractional surface coverage of CH<sub>3</sub>\* and CO<sub>2</sub>\* have increased from  $5.99 \times 10^{-12}$  to  $1.02 \times 10^{-7}$  and  $3.44 \times 10^{-10}$  to  $1.02 \times 10^{-6}$  respectively. The fractional coverage of free site (\*) has also decreased notably from  $9.98 \times 10^{-1}$  to  $5.53 \times 10^{-2}$  demonstrating the requirement of accurate DFT functional and corrections in microkinetic modeling.

Furthermore, the surface coverage values obtained by Model 3 indicate that the catalyst surface is mostly covered by CO\* and there is a high possibility of the occurrence of



Boudouard reaction. Hence, to accurately model the whole reaction system, we constructed the most elaborate model, Model 4, by including all relevant elementary reactions from the literature<sup>73,74,84,87,88</sup> in our further analysis.

From the results in Table 8.3.4, we can conclude that including more elementary reaction steps did not affect the fractional surface coverages values on Ni (111) surface significantly. Yet we employ Model 4 to perform microkinetic analysis on Boron-doped Ni as it is a different catalyst surface. A more comprehensive model has better chances of predicting accurate results over a new catalyst surface, moreover, the forward rate constant of Boudouard reaction (R35), is significantly higher on B-doped Ni than on Ni.

### 8.3.3 Model Assessment of the most comprehensive model (Model 4)

The results obtained from the model are compared with the experimental data<sup>195</sup> and data from the previously reported model<sup>64</sup>. We ensured the validity of our Model 4 (see Table S3) by analysing the (i) CH<sub>4</sub> fraction conversion vs space-time ( $W/F_0$ ) curves at different temperatures (Figure 1) and (ii) exit concentration values of reactants (CH<sub>4</sub> and CO<sub>2</sub>) and products (CO and H<sub>2</sub>) vs temperature curves (Figure 2) and comparing our results with previously reported study<sup>64</sup>.

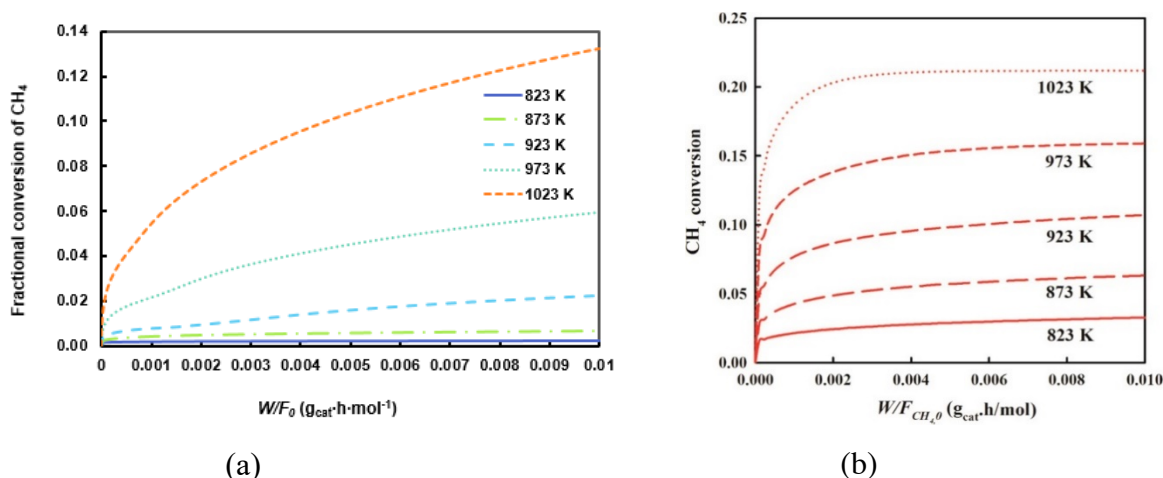


**Figure 8.3.1.** CH<sub>4</sub> fractional conversion vs  $W/F_0$  (g<sub>cat</sub>·h·mol<sup>-1</sup>) (a) predicted by Model 4 and (b) reported<sup>64</sup> at various reaction temperature and a pressure of 10 bar

From Figure 8.3.1, we observe that the reactant conversion increases as the space time increases and higher reactant conversions are achieved at greater reaction temperatures. This observation is in agreement with the previously reported study <sup>64</sup>. The CH<sub>4</sub> conversion increases from ~0.2% at 823 K to ~ 13.2% at 1023 K. This increase is within good quantitative agreement of that observed in the previous model where conversion increases from ~2% at 823 K to 20% at 1023 K. However, the fractional conversion values are quite different from the reported values due to the varying model specification.

We further compared the fractional conversion results, as predicted from the Model 4 with experimental data <sup>195</sup>, in terms of the exit concentration values of reactants (CH<sub>4</sub> and CO<sub>2</sub>) and products (CO and H<sub>2</sub>). The results are shown in Figure 8.3.2.

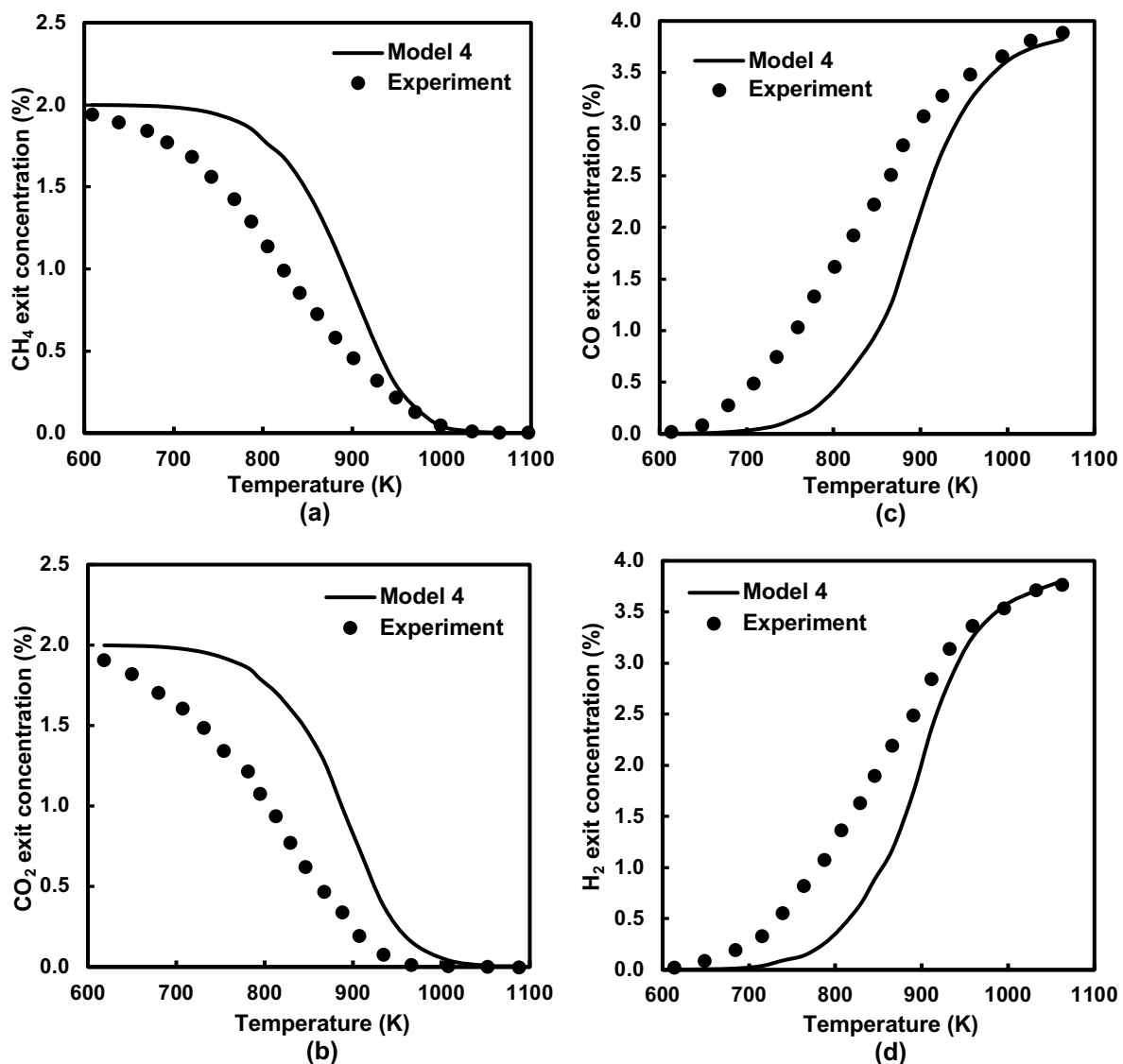


**Figure 8.3.2.** Comparison of the experimentally observed<sup>[195]</sup> (circles) and the numerically predicted (lines) exit concentrations (%) of (a)  $\text{CH}_4$ , (b)  $\text{CO}_2$  (c)  $\text{CO}$  and (d)  $\text{H}_2$  as a function of temperature for dry reforming of methane.

As observed from Figure 8.3.2, the exit concentration of reactants decreases and products increases as temperature increases. This is in accordance with experiments. Moreover, at reaction temperature above 923 K, the value of exit concentrations of both reactants and products are in good agreement with the experimental values. However, as the temperature decreases, the model over predicts the reactant exit concentration (Figure 8.3.2 (a) and (b)) and under predicts the product exit concentration (Figure 8.3.2 (c) and (d)). The reason for

that lies in the simple nature of the model. Considering the assumptions mentioned in Section 5.2.2, not only the kinetic constants are coverage independent but also the catalytic adsorption sites are equivalent and have the same "stability" (quantified by the binding energy). Additionally, our model does not include support interaction.

It is found that the rate of DRM at low CO<sub>2</sub> partial pressure ( $\leq 10$  kPa)<sup>264</sup> is directly depended on the value of the CO<sub>2</sub> partial pressure. This suggests that CO<sub>2</sub> adsorption is among the kinetically relevant reaction steps for the given condition. Moreover, the catalysts that are employed in the experiment have a catalyst support. Typically, these are modified metal oxides like MgO or Al<sub>2</sub>O<sub>3</sub>. These oxides positively affect the basicity of the catalyst and hence improve CO<sub>2</sub> interaction with the catalyst surface. Since our model works within the constraints of the model assumptions (See section 5.2.2) and does not include support interactions, it underestimates the reactant conversion and, hence, overestimates their concentration at the exit for temperatures where the reaction is kinetically controlled.

However, at higher temperatures, the reaction slowly proceeds towards thermodynamic equilibrium and the reactant conversions are more thermodynamically controlled. Therefore, given the exit concentration values at high temperatures, we can explain why this region is in good agreement with experiments.

**Table 8.3.5.** Forward reaction rates of elementary steps on Ni (111) and B-doped Ni surface at reaction conditions adapted from section 3.2.1

Elementary reactions	Forward Reaction Rate (mol·g <sub>cat</sub> <sup>-1</sup> ·h <sup>-1</sup> )	
	Ni (111)	B-doped Ni
R1: CH <sub>4</sub> *→CH <sub>3</sub> *+H*	1.603027027	1074.091219
R2: CH <sub>3</sub> *→CH <sub>2</sub> *+H*	56.80512603	715.7788407
R3: CH <sub>2</sub> *→CH*+H*	7918.634495	845.403961
R4: CH*→C*+H*	32.41876188	59.69663392
R5: CO <sub>2</sub> *→CO*+O*	336.0022487	176.9330479
R6: CO <sub>2</sub> *+H*→COOH*	0.050513086	0.038640049

R7: $\text{CO}_2^* + \text{H}^* \rightarrow \text{HCOO}^*$	11.54853185	1036.222628
R8: $\text{COOH}^* \rightarrow \text{CO}^* + \text{OH}^*$	589.9211959	46.73137006
R9: $\text{HCOO}^* \rightarrow \text{HCO}^* + \text{O}^*$	0.006514089	0.001106794
R10: $\text{HCO}^* \rightarrow \text{CO}^* + \text{H}^*$	1339.217144	3948.375492
R11: $\text{COOH}^* + \text{H}^* \rightarrow \text{HCOOH}^*$	0.003804539	0.021280521
R12: $\text{HCOO}^* + \text{H}^* \rightarrow \text{HCOOH}^*$	0.102806242	2.110301158
R13: $\text{HCOOH}^* \rightarrow \text{HCO}^* + \text{OH}^*$	0.01049494	0.006930301
R14: $\text{CH}_3\text{OH}^* \rightarrow \text{CH}_2\text{OH}^* + \text{H}^*$	7.00431E-08	0.000150214
R15: $\text{CH}_2\text{OH}^* \rightarrow \text{CHOH}^* + \text{H}^*$	3.6391E-05	0.121235684
R16: $\text{CHOH}^* \rightarrow \text{COH}^* + \text{H}^*$	0.119111159	0.13852291
R17: $\text{COH}^* \rightarrow \text{CO}^* + \text{H}^*$	0.270604786	0.107000273
R18: $\text{CH}_3^* + \text{OH}^* \rightarrow \text{CH}_3\text{OH}^*$	7.2561E-08	2.08153E-05
R19: $\text{CH}_2^* + \text{OH}^* \rightarrow \text{CH}_2\text{OH}^*$	0.000237822	2.55077424
R20: $\text{CH}^* + \text{OH}^* \rightarrow \text{CHOH}^*$	0.049621745	0.042415326
R21: $\text{C}^* + \text{OH}^* \rightarrow \text{COH}^*$	0.006960343	0.006492443
R22: $\text{CH}_3\text{O}^* \rightarrow \text{CH}_2\text{O}^* + \text{H}^*$	0.002476634	0.026659696
R23: $\text{CH}_2\text{O}^* \rightarrow \text{CHO}^* + \text{H}^*$	0.103005432	0.497703202
R24: $\text{CH}_3^* + \text{O}^* \rightarrow \text{CH}_3\text{O}^*$	0.002153093	0.01773012
R25: $\text{CH}_2^* + \text{O}^* \rightarrow \text{CH}_2\text{O}^*$	0.014518412	0.173170659
R26: $\text{CH}^* + \text{O}^* \rightarrow \text{CHO}^*$	1.282131382	0.002020685
R27: $\text{C}^* + \text{O}^* \rightarrow \text{CO}^*$	0.020101874	0.000100607
R28: $\text{CH}_3\text{OH}^* + ^* \rightarrow \text{CH}_3\text{O}^* + \text{H}^*$	2.12305E-05	0.003641637
R29: $\text{CH}_2\text{OH}^* + ^* \rightarrow \text{CH}_2\text{O}^* + \text{H}^*$	4.65783E-05	0.006627168
R30: $\text{CHOH}^* + ^* \rightarrow \text{HCO}^* + \text{H}^*$	0.001274997	0.058060651
R31: $\text{O}^* + \text{H}^* \rightarrow \text{OH}^*$	647.2158212	20.71594681
R32: $\text{OH}^* + \text{H}^* \rightarrow \text{H}_2\text{O}^*$	3.172545558	56.29392543
R33: $\text{H}^* + \text{H}^* \rightarrow \text{H}_2$	3944.6944	407.1332247
R34: $\text{OH}^* + \text{OH}^* \rightarrow \text{H}_2\text{O}^* + \text{O}^*$	24.568704	2946.185567
R35: $\text{CO}_2^* + \text{C}^* \rightarrow 2\text{CO}^*$	1.71612E-06	0.000154338
R36: $\text{CO}_2 \rightarrow \text{CO}_2^*$	21.04971811	293.2282616

R37: $\text{CO}^* \rightarrow \text{CO}$	263633.4331	1012873.897
R38: $\text{H}_2\text{O}^* \rightarrow \text{H}_2\text{O} + *$	459062.2087	253156.7925

### 8.3.4. Reaction mechanism analysis

Once the RDS is identified, the dominant reaction pathway is formulated for product formation, i.e. the pathway whose rate limiting step is same as the RDS identified for the overall reaction. The approach is to first compare reaction rates of every elementary reaction steps with the rate of RDS and exclude the steps with rates lower than the RDS. Then compare the rates of selected steps to identify the fastest pathway from gaseous reactants ( $\text{CH}_4(\text{g})$ ,  $\text{CO}_2(\text{g})$ ) to RDS's reactant intermediates and RDS's product intermediates to gaseous products ( $\text{H}_2(\text{g})$ ,  $\text{CO}(\text{g})$ ). Side reaction steps of RWGS, except  $\text{H}_2$  formation/dissociation ( $\text{H}^* + \text{H}^* = \text{H}_2$ ), are not included in the selected reaction steps as they do not lead to desired product formation.

The fastest pathway is identified step by step in the following manner. First the necessary reaction steps, i.e. adsorption of reactants, RDS and desorption of products are listed. Then the reactant dissociation steps are included in this pathway. If there are more than one reaction step for reactant dissociation, only the step with highest rate of dissociation (i.e. fastest dissociation step) is included as it is contributing the most towards reactant dissociation. From the dissociation product, again the fastest reaction step towards RDS's reactant formation is added. Similarly, the fastest step leading to product formation from the RDS's product is incorporated which is followed by the desorption step.

### 8.3.5 Sensitivity analysis for DRM on Ni (111) at varying reaction condition

The results of the simulations performed to identify the different kinetically relevant steps on Ni (111) over a range of reaction conditions are presented here. Table 8.3.6 enlists these different reactions conditions or cases.

**Table 8.3.6.** Different reaction conditions for sensitivity analysis. Pressure and inlet feed composition were varied over four cases and the sensitivity analysis was performed for each case at three reaction temperatures, i.e. 873 K, 973 K, and 1073 K.

	Pressure	Inlet feed composition (Volume fraction)
Case 1	10 bar	CO <sub>2</sub> : 50%, CH <sub>4</sub> : 50%
Case 2	10 bar	CO <sub>2</sub> : 2%, CH <sub>4</sub> : 2%, N <sub>2</sub> : 96%
Case 3	1 bar	CO <sub>2</sub> : 50%, CH <sub>4</sub> : 50%
Case 4	1 bar	CO <sub>2</sub> : 2%, CH <sub>4</sub> : 2%, N <sub>2</sub> : 96%

**Case 1: Pressure 10 bar, CO<sub>2</sub>: 50%, CH<sub>4</sub>: 50%**

Figures 8.3.3 to 8.3.5 report the relative sensitivity coefficients for the above case at temperatures 873 K, 973 K and 1073 K respectively.

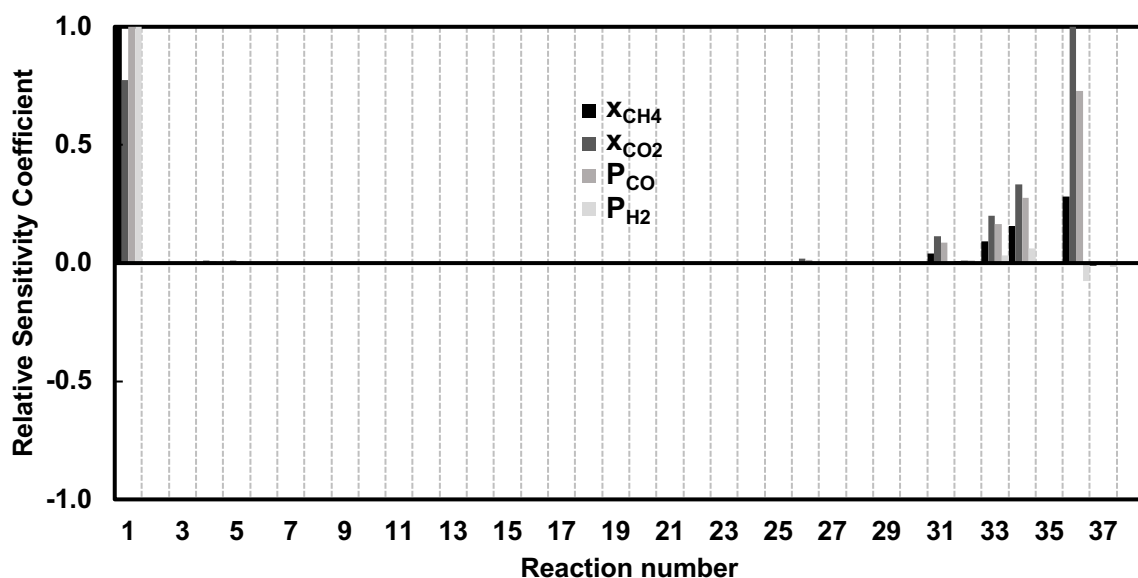


**Figure 8.3.3.** Sensitivity analysis of DRM reaction steps over Ni (111) surfaces at space time value of  $0.01 \text{ g}_{\text{cat}} \cdot \text{h} \cdot \text{mol}^{-1}$  at 873 K for Case 1 (Pressure 10 bar, CO<sub>2</sub>: 50%, CH<sub>4</sub>: 50%) reaction conditions.

At 873 K (see Figure 8.3.3), adsorption of reactants are the most sensitive steps and their conversion is completely dependent on their respective rates of adsorption (R1 and R36). However, the amount of syngas produced is more sensitive towards the elementary step of the dissociative adsorption of  $\text{CH}_4$  (R1).

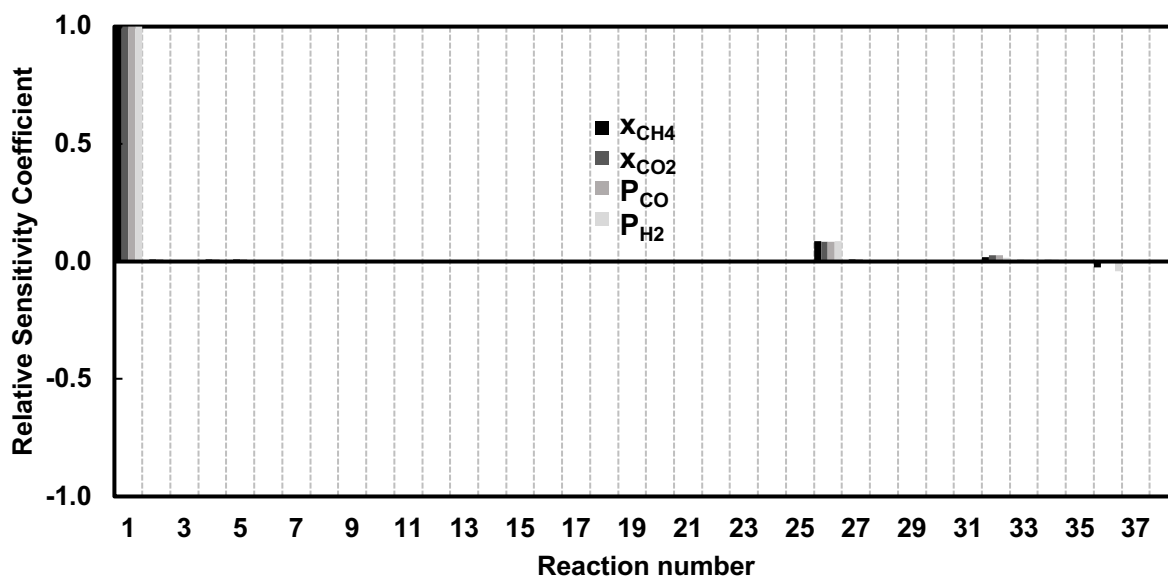


**Figure 8.3.4.** Sensitivity analysis of DRM reaction steps over Ni (111) surfaces at space time value of  $0.01 \text{ g}_{\text{cat}} \cdot \text{h} \cdot \text{mol}^{-1}$  at 973 K for Case 1 (Pressure 10 bar,  $\text{CO}_2$ : 50%,  $\text{CH}_4$ : 50%) reaction conditions.

As the reaction temperature increases to 973 K, the model responses become more sensitive towards R1 but are no longer sensitive to R36. At 1073 K, R1 still remains the most sensitive reaction step, however  $\text{CH}^*$  oxidation (R26) is now among the kinetically relevant steps and is half as sensitive as R1 towards the model responses.



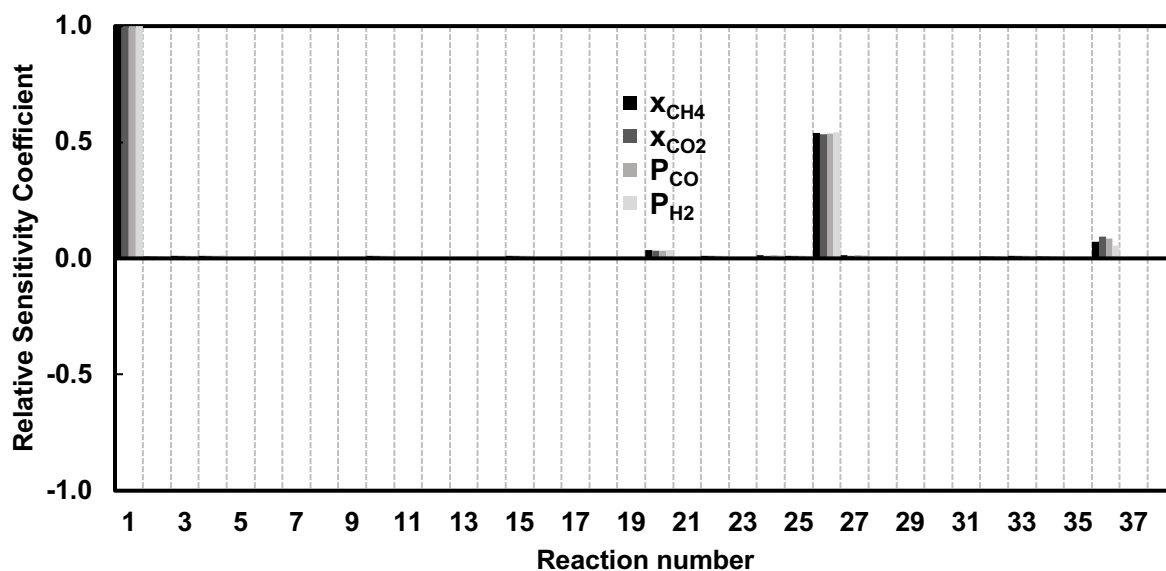


**Figure 8.3.5.** Sensitivity analysis of DRM reaction steps over Ni (111) surfaces at space time value of  $0.01 \text{ g}_{\text{cat}} \cdot \text{h} \cdot \text{mol}^{-1}$  at 1073 K for Case 1 (Pressure 10 bar,  $\text{CO}_2$ : 50%,  $\text{CH}_4$ : 50%) reaction condition

From the sensitivity analysis, we can conclude that  $\text{CH}_4$  dissociation is the most sensitive elementary step throughout the temperature range with the  $\text{CO}_2$  adsorption (R36) and  $\text{CH}^*$  oxidation (R26) being relevant at lower (873 K) and higher (1073 K) temperatures respectively. A partial equilibrium analysis was further performed to identify the RDS for the given the reaction conditions.

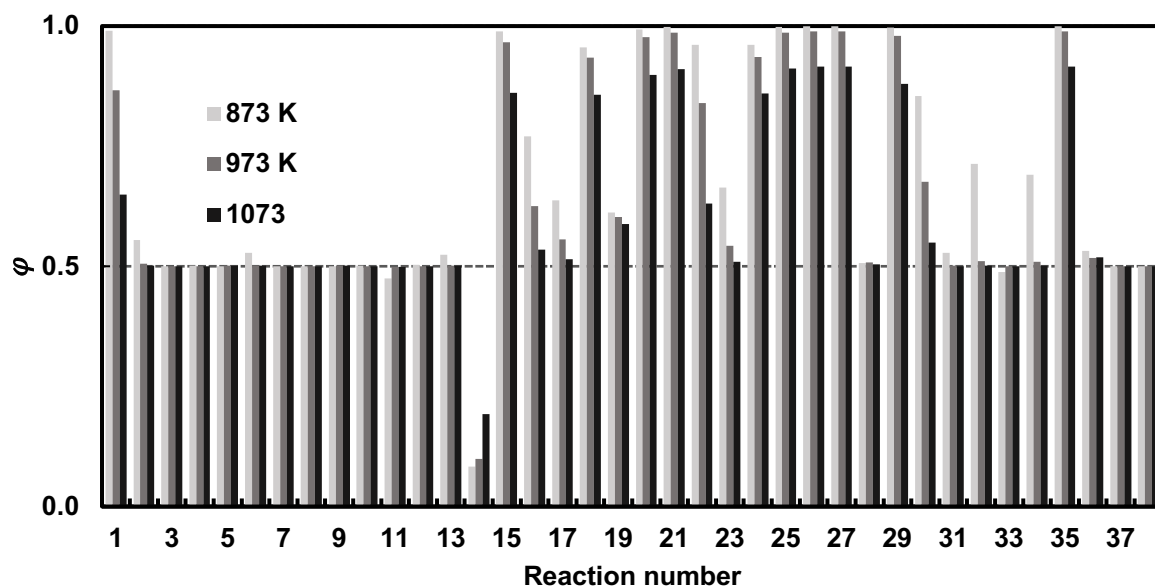


**Figure 8.3.6.** Partial equilibrium coefficient  $\phi$  of DRM reaction steps over Ni (111) surfaces at space time value of  $0.01 \text{ g}_{\text{cat}} \cdot \text{h} \cdot \text{mol}^{-1}$  at varying temperature for Case 1 (Pressure 10 bar,  $\text{CO}_2$ : 50%,  $\text{CH}_4$ : 50%) reaction condition

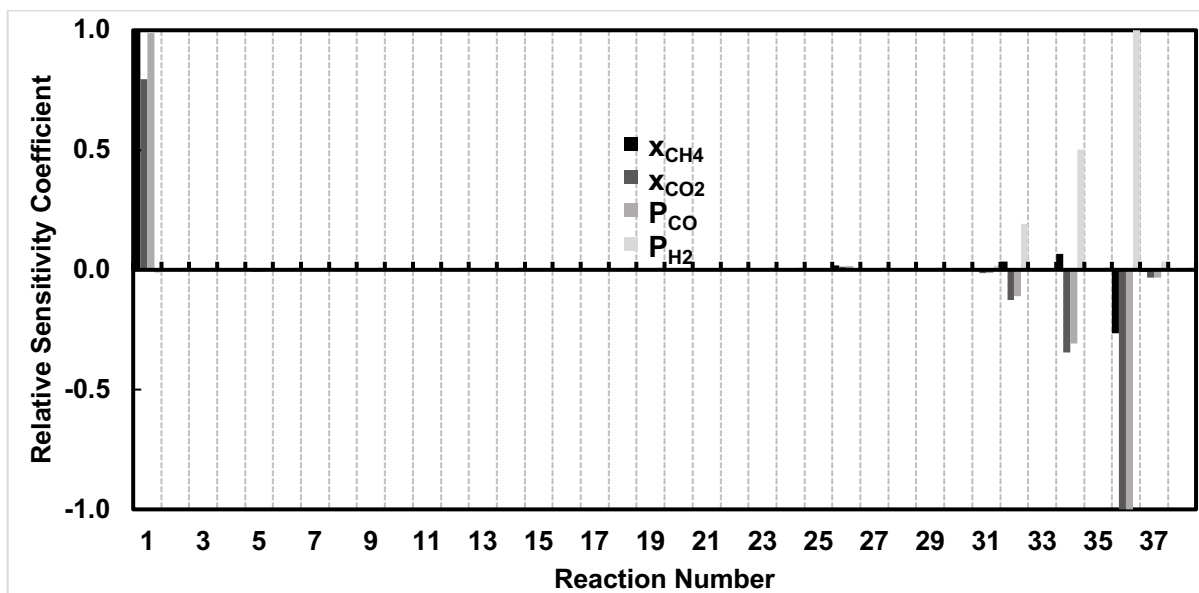
From Figure 8.3.6 we can observe that all three relevant elementary steps obtained from sensitivity analysis (i.e. R1, R26 and R36) are not in quasi equilibrium and are hence candidates for RDS. However, R1 is the most sensitive step given the temperature range and hence contributes the most to the overall reaction rate. Therefore,  $\text{CH}_4$  dissociative adsorption (R1) is the RDS for this case.

#### Case 2: Pressure 10 bar, $\text{CO}_2$ : 2%, $\text{CH}_4$ : 2%, $\text{N}_2$ : 96%

This section reports the relative sensitivity coefficients (at reaction temperatures of 873 K, 973 K and 1073 K) for the case where the inlet feed consists of a major fraction of inert gas.

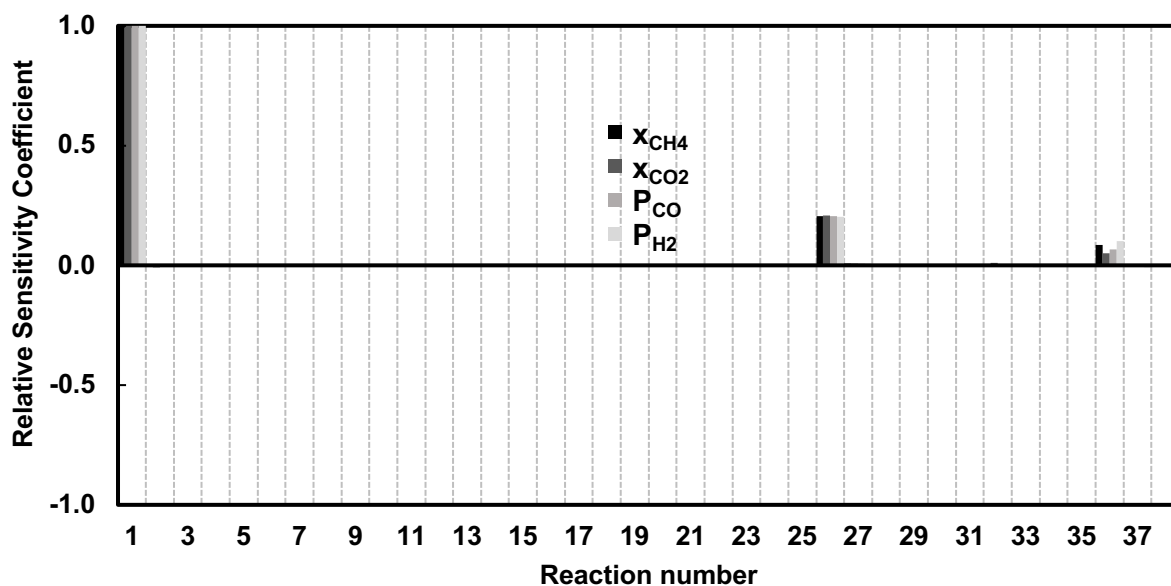
With the inert gas having a volume fraction of 96%, the partial pressure of  $\text{CH}_4$  and  $\text{CO}_2$  reduces to 20 kPa each. The sensitivity analysis at 873 K shows that the dissociative adsorption of  $\text{CH}_4$  (R1) and adsorption of  $\text{CO}_2$  (R2) are the most sensitive steps and the reactant conversions are completely dependent on their respective rates of adsorption (R1

and R36). Although unlike previously observed for Case 1, 873 K, (Figure 8.3.3) the product formation is relatively more sensitive to the CO<sub>2</sub> adsorption step.



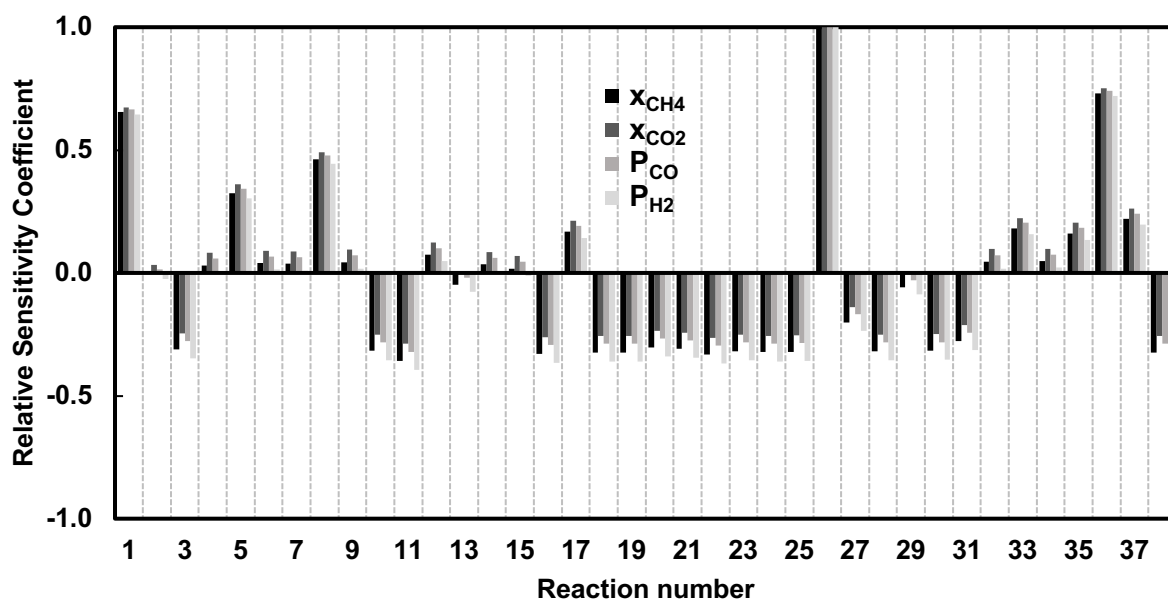
**Figure 8.3.7.** Sensitivity analysis of DRM reaction steps over Ni (111) surfaces at space time value of  $0.01 \text{ g}_{\text{cat}} \cdot \text{h} \cdot \text{mol}^{-1}$  at 873 K for Case 2 (Pressure 10 bar, CO<sub>2</sub>: 2%, CH<sub>4</sub>: 2%, N<sub>2</sub>: 96%) reaction conditions.

This, however, changes as temperature increases to 973 K (see Figure 8.3.8). CH<sub>4</sub> dissociation becomes the most sensitive step and the other relevant steps are similar to those in Case 1 at 1073 K (see Figure 8.3.5).

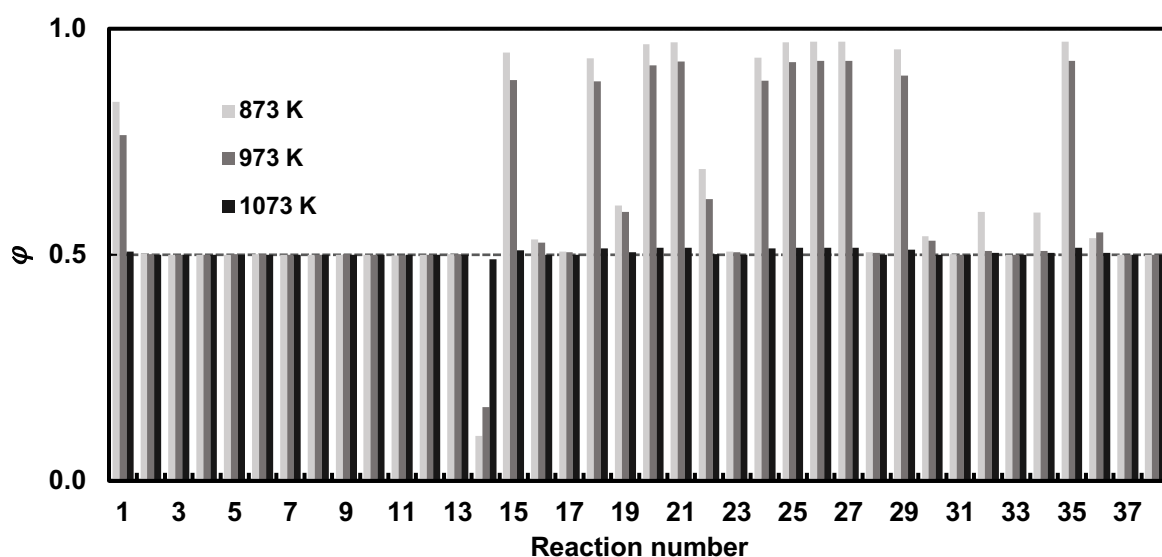


**Figure 8.3.8.** Sensitivity analysis of DRM reaction steps over Ni (111) surfaces at space time value of  $0.01 \text{ g}_{\text{cat}} \cdot \text{h} \cdot \text{mol}^{-1}$  at 973 K for Case 2 (Pressure 10 bar,  $\text{CO}_2$ : 2%,  $\text{CH}_4$ : 2%,  $\text{N}_2$ : 96%) reaction condition

At 1073 K, the overall reaction approaches equilibrium (see Figure 8.3.9) and the model responses are sensitive to more elementary steps, with the most sensitive reaction being  $\text{CH}^*$  oxidation (R26) followed by adsorption of reactants (R1 and R36). A further partial equilibrium analysis was performed to identify the RDS for different reaction temperatures.



**Figure 8.3.9.** Sensitivity analysis of DRM reaction steps over Ni (111) surfaces at space time value of  $0.01 \text{ (g}_{\text{cat}} \cdot \text{h} \cdot \text{mol}^{-1})$  at 1073 K for Case 2 (Pressure 10 bar,  $\text{CO}_2$ : 2%,  $\text{CH}_4$ : 2%,  $\text{N}_2$ : 96%) reaction conditions.



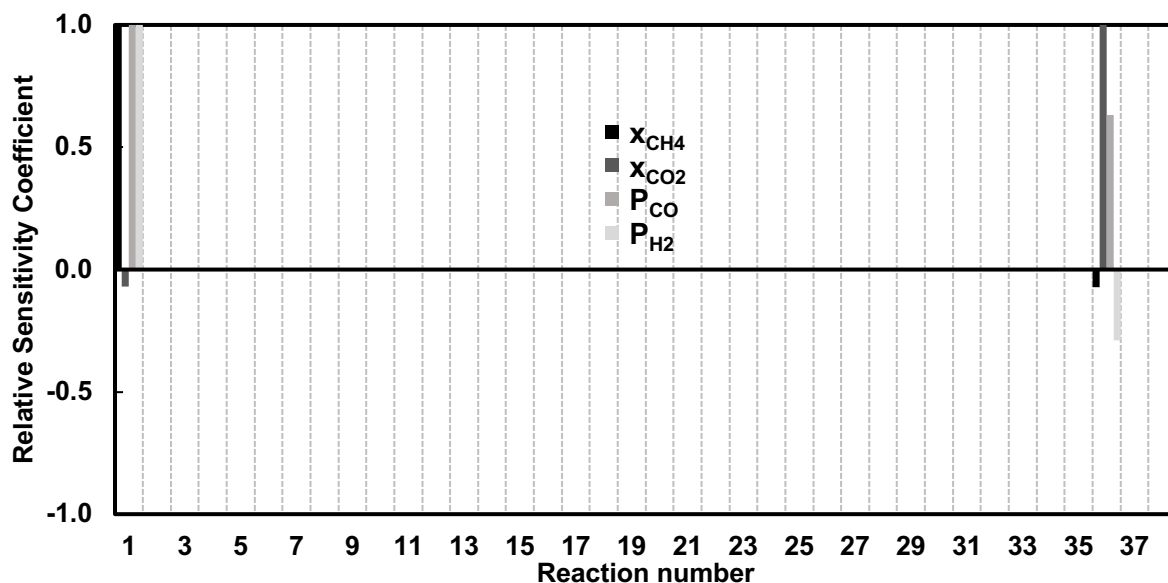
**Figure 8.3.10.** Partial equilibrium coefficient  $\phi$  of DRM reaction steps over Ni (111) surfaces at space time value of  $0.01 \text{ g}_{\text{cat}} \cdot \text{h} \cdot \text{mol}^{-1}$  at varying temperature for Case 2 (Pressure 10 bar,  $\text{CO}_2$ : 2%,  $\text{CH}_4$ : 2%,  $\text{N}_2$ : 96%) reaction conditions.

Figure 8.3.10 shows that all three relevant elementary steps obtained from sensitivity analysis (i.e. R1, R26 and R36) are not in quasi equilibrium except at 1073K. At 873 K,

both reactants conversions are sensitive to their respective adsorption reactions, hence based on the results of sensitivity analysis and partial equilibrium analysis we can conclude that the overall rate for DRM, at 873 K and given reaction conditions, should depend on the rate adsorption of CH<sub>4</sub> and CO<sub>2</sub>. However, if we were to choose a rate determining step, it should be decided directly based on the computed forward rate values. At the given reaction conditions, forward reaction rates of R1 and R36 are 0.017 and 0.116 in mol·h<sup>-1</sup>·g<sub>cat</sub><sup>-1</sup> respectively, hence R1 is the RDS. For reaction temperatures 973 K and 1073 K, the rate determining steps are undoubtedly R1 and R26 respectively.

**Case 3: Pressure 1 bar, CO<sub>2</sub>: 50%, CH<sub>4</sub>: 50% and Case 4: Pressure 1 bar, CO<sub>2</sub>: 2%, CH<sub>4</sub>: 2%, N<sub>2</sub>: 96%**

As observed previously (Figure 8.3.3 and 8.3.7), the reactant adsorption steps (R1 and R36) are found to be the most sensitive steps. However, unlike the previous cases, the reactant adsorption steps remain the most sensitive steps throughout the temperature range (Figure 8.3.11-16). The reactant conversions depend mostly on their respective rates of adsorption (R1 and R36) and the H<sub>2</sub> and CO exit pressures are more sensitive to R1 at lower temperatures (see Figure 8.3.11 and 8.3.14). But, as the temperature increases, the CO exit pressure becomes more sensitive to R36 (see Figure 8.3.13 and 8.3.16).



**Figure 8.3.11.** Sensitivity analysis of DRM reaction steps over Ni (111) surfaces at space time value of  $0.01 \text{ g}_{\text{cat}} \cdot \text{h} \cdot \text{mol}^{-1}$  at 873 K for Case 3 reaction conditions.

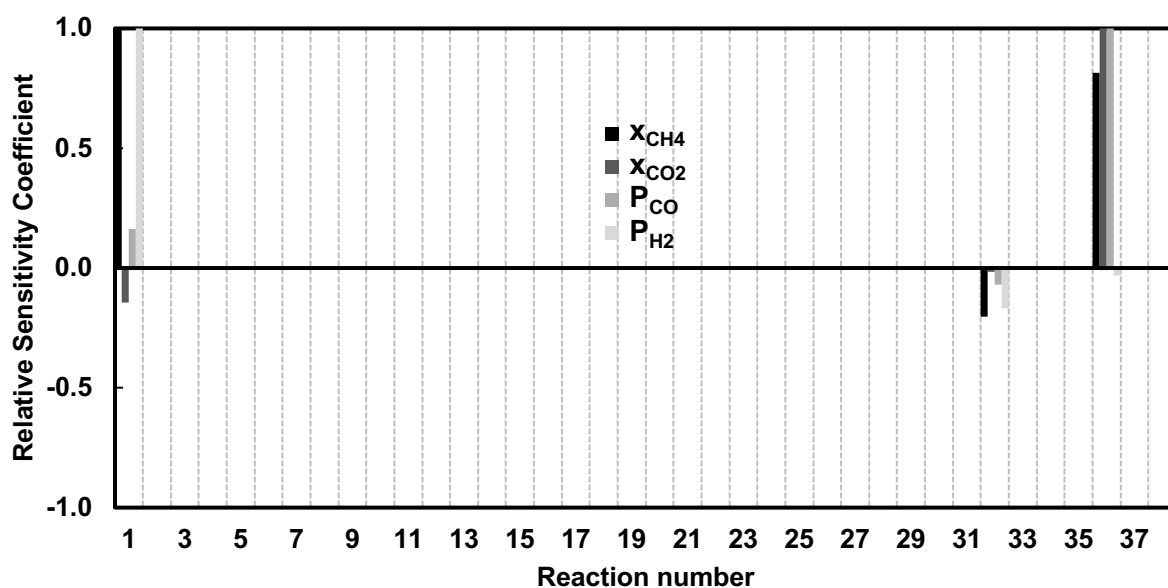


**Figure 8.3.12.** Sensitivity analysis of DRM reaction steps over Ni (111) surfaces at space time value of  $0.01 \text{ g}_{\text{cat}} \cdot \text{h} \cdot \text{mol}^{-1}$  at 973 K for Case 3 reaction conditions.

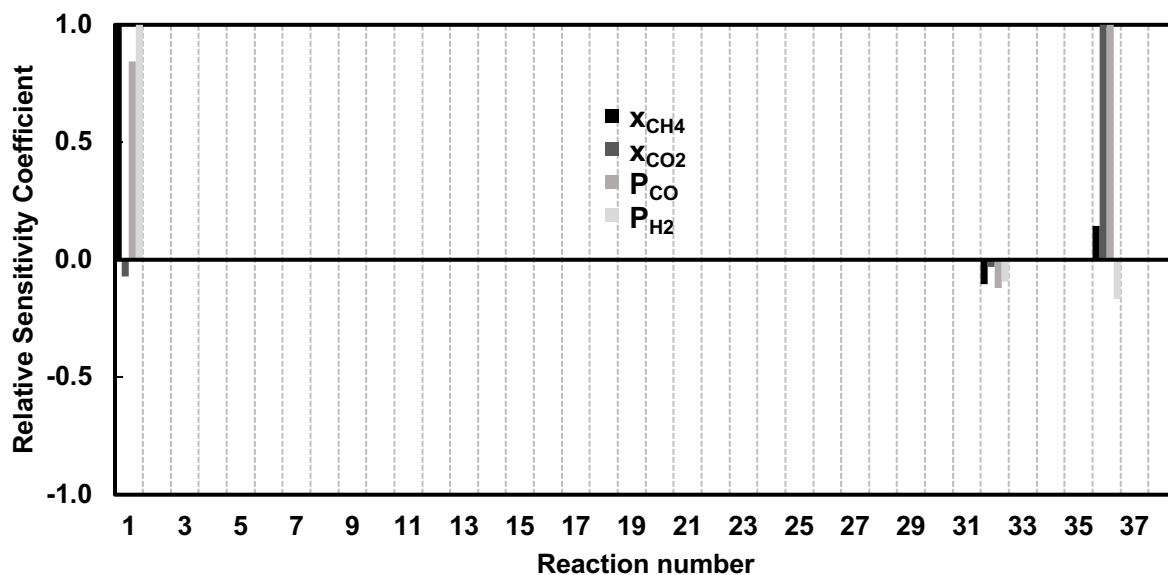


**Figure 8.3.13.** Sensitivity analysis of DRM reaction steps over Ni (111) surfaces at space time value of  $0.01 \text{ g}_{\text{cat}} \cdot \text{h} \cdot \text{mol}^{-1}$  at 1073 K for Case 3 reaction conditions.

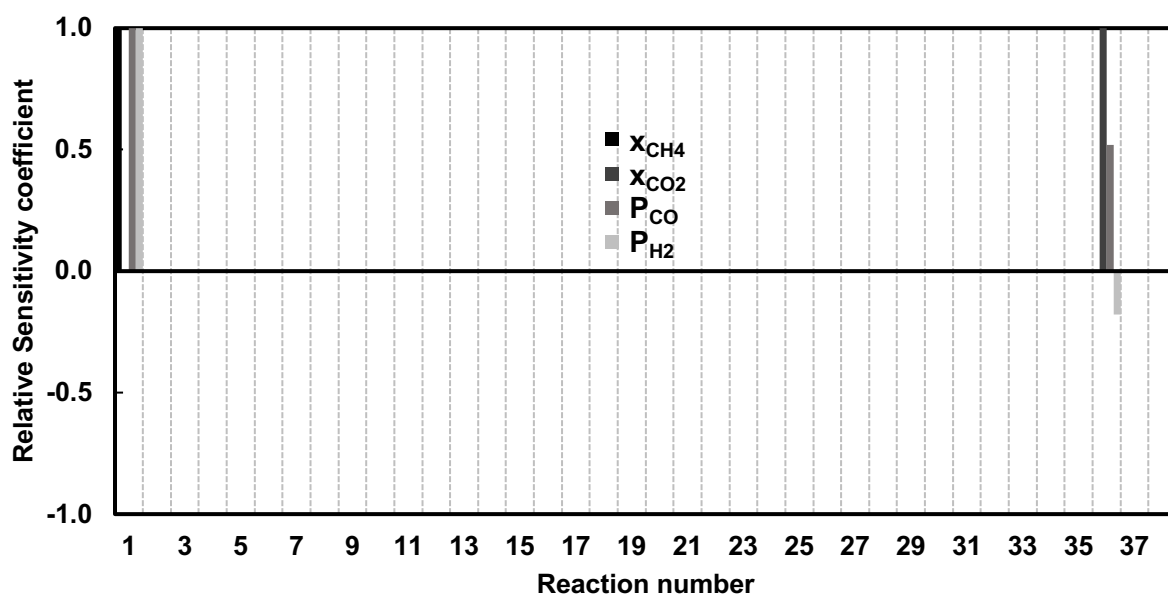


**Figure 8.3.14.** Sensitivity analysis of DRM reaction steps over Ni (111) surfaces at space time value of  $0.01 \text{ g}_{\text{cat}} \cdot \text{h} \cdot \text{mol}^{-1}$  at 873 K for Case 4 reaction conditions.



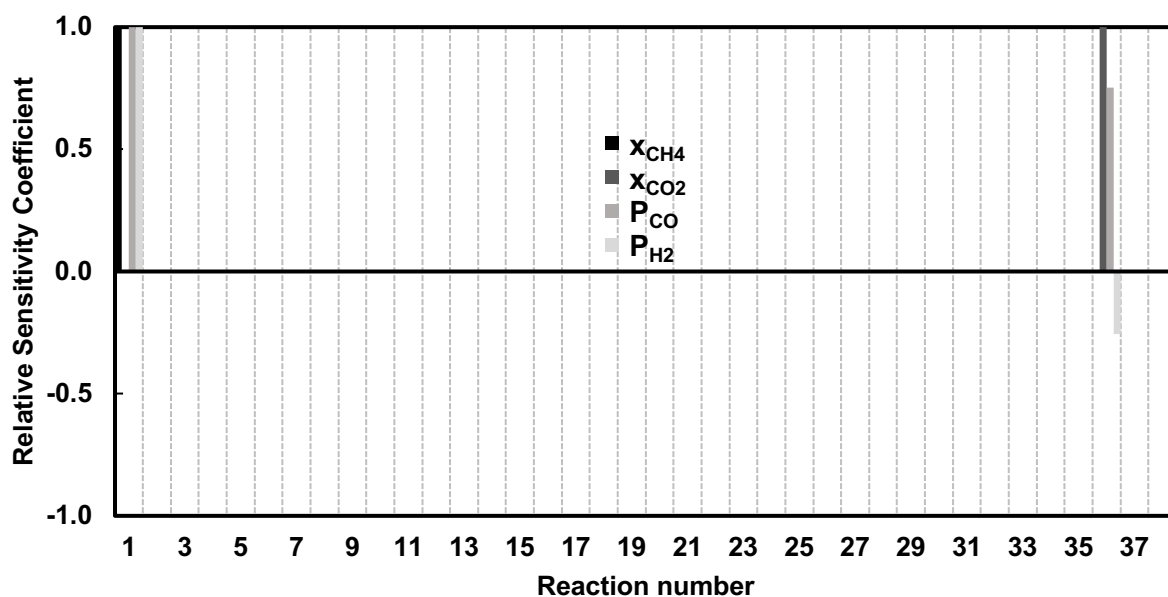


**Figure 8.3.15.** Sensitivity analysis of DRM reaction steps over Ni (111) surfaces at space time value of  $0.01 \text{ g}_{\text{cat}} \cdot \text{h} \cdot \text{mol}^{-1}$  at 973 K for Case 4 reaction conditions.

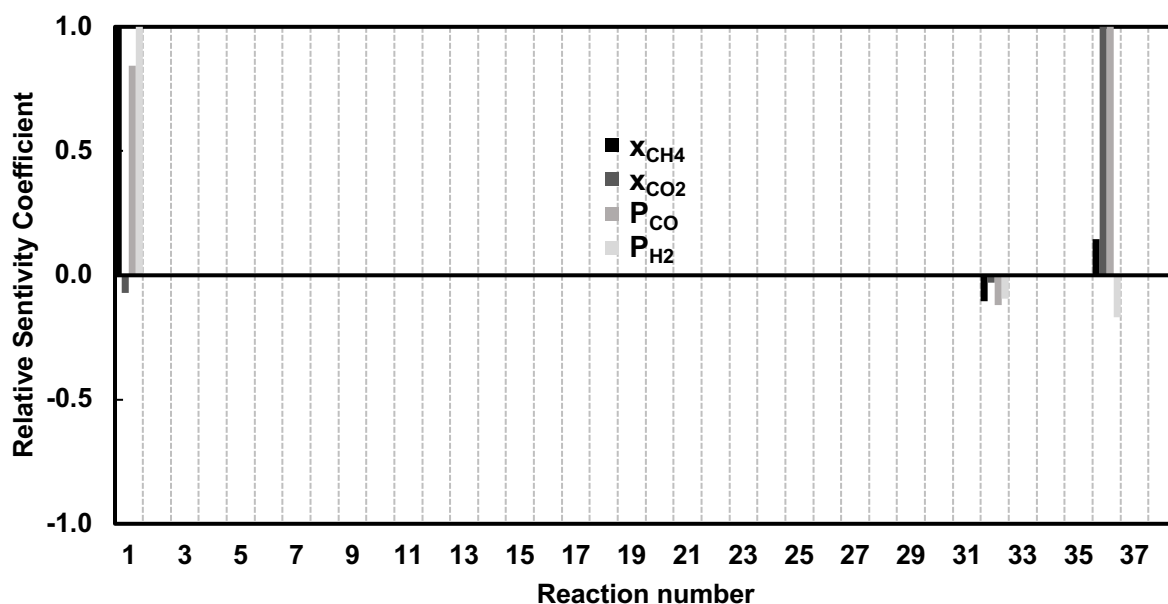


**Figure 8.3.16.** Sensitivity analysis of DRM reaction steps over Ni (111) surfaces at space time value of  $0.01 \text{ (g}_{\text{cat}} \cdot \text{h} \cdot \text{mol}^{-1})$  at 1073 K for Case 4 reaction conditions.

As observed from the sensitivity analysis, the R1 and R36 are the most sensitive steps, and the overall rate of DRM must depend on these adsorption reaction steps. However, it is difficult to identify the RDS solely from the sensitivity analysis. Hence, the RDS for case

3 and 4 were directly decided based on the computed forward reaction rates of R1 and R36. The rates are given in Table 8.3.6.

**Table 8.3.6.** Computed forward reaction rates of R1 and R36 over Ni (111) at space time value of  $0.01 \text{ g}_{\text{cat}} \cdot \text{h} \cdot \text{mol}^{-1}$  for varying temperature for Case 3 and 4 reaction condition.

Temperature	Case 3		Case 4	
	R1 ( $\text{mol} \cdot \text{h}^{-1} \cdot \text{g}_{\text{cat}}^{-1}$ )	R36 ( $\text{mol} \cdot \text{h}^{-1} \cdot \text{g}_{\text{cat}}^{-1}$ )	R1 ( $\text{mol} \cdot \text{h}^{-1} \cdot \text{g}_{\text{cat}}^{-1}$ )	R36 ( $\text{mol} \cdot \text{h}^{-1} \cdot \text{g}_{\text{cat}}^{-1}$ )
873 K	0.612	1.136	0.045	0.046
973 K	3.526	3.605	0.218	0.223
1073 K	10.640	12.016	0.600	0.611

Based on the forward reaction rates reported in Table 8.3.6, we can conclude that R1 is RDS for cases 3 and 4 throughout the temperature range.

However, it should be noted that the difference in the forward rates of R1 and R36 are quite small for case 4. This is because as per the case 4 reaction conditions, the inert gas has a volume fraction of 96% and the partial pressure of  $\text{CO}_2$  reduces to 2 kPa. Experiments have reported that at low  $\text{CO}_2$  partial pressure (i.e.  $\leq 10 \text{ kPa}$ ), varying this partial pressure strongly affects the overall rate of reaction<sup>197,265</sup>, suggesting that the overall rate expression is sensitive to  $\text{CO}_2$  adsorption (R36).

The sensitivity analysis (Figure 8.3.14-16) and the forward reaction rates of R1 and R36 (Table 8.3.6) for case 4 show similar results.  $\text{CO}_2$  adsorption (R36) is among the most sensitive steps of the DRM reaction and although  $\text{CH}_4$  dissociative adsorption (R1) is the RDS, there is only a small difference in the forward rates of R1 and R36.



## References

- 1 Carbon dioxide What is carbon dioxide and how is it discovered ?,  
<https://www.lenntech.com/carbon-dioxide.htm>.
- 2 Carbon Dioxide, [https://www.sciencedaily.com/terms/carbon\\_dioxide.htm](https://www.sciencedaily.com/terms/carbon_dioxide.htm).
- 3 A. Buis, The Atmosphere: Getting a Handle on Carbon Dioxide,  
<https://climate.nasa.gov/news/2915/the-atmosphere-getting-a-handle-on-carbon-dioxide/>.
- 4 R. Lindsey and E. Dlugokencky, Climate Change: Atmospheric Carbon Dioxide.  
NRC, 2009, 22314.
- 6 E. Bryant, Causes of climate change, <http://www.ces.fau.edu/nasa/module-4/causes/sources-carbon-dioxide.php>.
- 7 T. R. Anderson, E. Hawkins and P. D. Jones, *Endeavour*, 2016, **40**, 178–187.
- 8 H. Riebeek, *Retrieved January*, 2010, **11**, 2011.
- 9 IPCC, *Noaa Faq*, 2007, 1–4.
- 10 A. Chapters and F. O. R. Fourth, 2017, 1–29.
- 11 UNFCCC. Conference of the Parties (COP), *Adopt. Paris Agreement. Propos. by Pres.*, 2015, **21932**, 32.
- 12 U. United Nations, in *United Nations Framework Convention on Climate Change*, 2017, pp. 1–4.
- 13 J. B. Horton, D. W. Keith and M. Honegger, *Harvard Proj. Clim. Agreements*, 2016, 1–10.
- 14 Singapore's Efforts in Addressing Climate Change, <https://www.nea.gov.sg/our-services/climate-change-energy-efficiency/climate-change/singapore%27s-efforts-in-addressing-climate-change>.
- 15 G. E. and K. L. James Mulligan, 6 Ways to Remove Carbon Pollution from the Sky,  
<https://www.wri.org/blog/2018/09/6-ways-remove-carbon-pollution-sky>.
- 16 S. Saeidi, N. A. S. Amin and M. R. Rahimpour, *J. CO<sub>2</sub> Util.*, 2014, **5**, 66–81.
- 17 M. A. A. Aziz, A. A. Jalil, S. Triwahyono and A. Ahmad, *Green Chem.*, 2015, **17**, 2647–2663.
- 18 X. Su, J. Xu, B. Liang, H. Duan, B. Hou and Y. Huang, *J. Energy Chem.*, 2016, **25**, 553–565.

- 19 B. C. Sempuga and Y. Yao, *J. CO<sub>2</sub> Util.*, 2017, **20**, 34–42.
- 20 L. Torrente-Murciano, D. Mattia, M. D. Jones and P. K. Plucinski, *J. CO<sub>2</sub> Util.*, 2014, **6**, 34–39.
- 21 S. Kar, J. Kothandaraman, A. Goeppert and G. K. S. Prakash, *J. CO<sub>2</sub> Util.*, 2018, **23**, 212–218.
- 22 W. Wang, S. Wang, X. Ma and J. Gong, *Chem Soc Rev*, 2011, **40**, 3703–3727.
- 23 G. Centi and S. Perathoner, *Catal. Today*, 2009, **148**, 191–205.
- 24 K. Jalama, *Catal. Rev. - Sci. Eng.*, 2017, **59**, 95–164.
- 25 M. Götz, J. Lefebvre, F. Mörs, A. McDaniel Koch, F. Graf, S. Bajohr, R. Reimert and T. Kolb, *Renew. Energy*, 2016, **85**, 1371–1390.
- 26 M. Lehner, R. Tichler, H. Steinmüller and M. Koppe, *Power-to-Gas: Technology and Business Models*, Springer International Publishing, Cham, 2014.
- 27 S. Gmbh and S. Rieke, in *Ecosummit*, Berlin, 2012.
- 28 O. Mohan, C. Muraleedharan and A. Palatel, *Int. J. Mod. Res. Eng. Technol.*, 2016, **1**, 1–8.
- 29 O. Mohan, S. Rupesh, C. Muraleedharan and P. Arun, in *2015 IEEE International Conference on Signal Processing, Informatics, Communication and Energy Systems (SPICES)*, IEEE, 2015, pp. 1–5.
- 30 W. Wang, S. Wang, X. Ma and J. Gong, *Chem Soc Rev*, 2011, **40**, 3703–3727.
- 31 M. Daryanavard, H. Hadadzadeh, H. Farrokhpour and M. Weil, *J. CO<sub>2</sub> Util.*, 2018, **26**, 612–622.
- 32 H. Wang, X. Nie, Y. Chen, X. Guo and C. Song, *J. CO<sub>2</sub> Util.*, 2018, **26**, 160–170.
- 33 H. Wang, X. Nie, X. Guo and C. Song, *J. CO<sub>2</sub> Util.*, 2016, **15**, 107–114.
- 34 Y. M. Liu, J. T. Liu, S. Z. Liu, J. Li, Z. H. Gao, Z. J. Zuo and W. Huang, *J. CO<sub>2</sub> Util.*, 2017, **20**, 59–65.
- 35 X. Nie, H. Wang, W. Li, Y. Chen, X. Guo and C. Song, *J. CO<sub>2</sub> Util.*, 2018, **24**, 99–111.
- 36 A. Solis-Garcia and J. C. Fierro-Gonzalez, *J. Nanosci. Nanotechnol.*, 2019, **19**, 3110–3123.
- 37 W. Wang and J. Gong, *Front. Chem. Eng. China*, 2011, **5**, 2–10.
- 38 P. Frontera, A. Macario, M. Ferraro and P. Antonucci, *Catalysts*, 2017, **7**, 59.
- 39 Energy Market Authority, 2015, 110.
- 40 M. Younas, L. Loong Kong, M. J. K. Bashir, H. Nadeem, A. Shehzad and S. Sethupathi,

- Energy and Fuels*, 2016, **30**, 8815–8831.
- 41 E. Perry Murray, T. Tsai and S. A. Barnett, *Nature*, 1999, **400**, 649–651.
  - 42 S. Park, *J. Electrochem. Soc.*, 1999, **146**, 3603.
  - 43 K. Stangeland, D. Kalai, H. Li and Z. Yu, *Energy Procedia*, 2017, **105**, 2022–2027.
  - 44 D. Pakhare and J. Spivey, *Chem. Soc. Rev.*, 2014, **43**, 7813–7837.
  - 45 A. W. Budiman, S. H. Song, T. S. Chang, C. H. Shin and M. J. Choi, *Catal. Surv. from Asia*, 2012, **16**, 183–197.
  - 46 M. Götz, J. Lefebvre, F. Mörs, A. McDaniel Koch, F. Graf, S. Bajohr, R. Reimert and T. Kolb, *Renew. Energy*, 2016, **85**, 1371–1390.
  - 47 C. Mebrahtu, F. Krebs, S. Abate, S. Perathoner, G. Centi and R. Palkovits, in *Studies in Surface Science and Catalysis*, Elsevier B.V., 1st edn., 2019, vol. 178, pp. 85–103.
  - 48 K. IWAMOTO, Singapore aims to be Asia LNG hub as demand soars.
  - 49 S. Basu Das, Ed., *Enhancing ASEAN's Connectivity*, ISEAS–Yusof Ishak Institute Singapore, Singapore, 2012.
  - 50 J. Luther and T. Reindl, 2013, 75.
  - 51 T. K. Doshi, N. Sebastian D'Souza, L. Nguyen, H. G. Teo and N. Bin Zahur, *GSTF J. Eng. Technol.*, , DOI:10.5176/2251-3701\_2.1.33.
  - 52 A. Quindimil, U. De-La-Torre, B. Pereda-Ayo, A. Davó-Quiñonero, E. Bailón-García, D. Lozano-Castelló, J. A. González-Marcos, A. Bueno-López and J. R. González-Velasco, *Catal. Today*, 2020, **356**, 419–432.
  - 53 S. Hwang, J. Lee, U. G. Hong, J. G. Seo, J. C. Jung, D. J. Koh, H. Lim, C. Byun and I. K. Song, *J. Ind. Eng. Chem.*, 2011, **17**, 154–157.
  - 54 Y. Wang, Y. Su, M. Zhu and L. Kang, *Int. J. Hydrogen Energy*, 2015, **40**, 8864–8876.
  - 55 T. Van Herwijnen, H. Van Doesburg and W. A. De Jong, *J. Catal.*, 1973, **28**, 391–402.
  - 56 H. Yuan, X. Zhu, J. Han, H. Wang and Q. Ge, *J. CO<sub>2</sub> Util.*, 2018, **26**, 8–18.
  - 57 P. Bousquet, P. Ciais, J. B. Miller, E. J. Dlugokencky, D. A. Hauglustaine, C. Prigent, G. R. Van Der Werf, P. Peylin, E. G. Brunke, C. Carouge, R. L. Langenfelds, J. Lathière, F. Papa, M. Ramonet, M. Schmidt, L. P. Steele, S. C. Tyler and J. White, *Nature*, 2006, **443**, 439–443.
  - 58 U. S. G. Survey and M. Park, 1988, **2**, 299–327.
  - 59 Natural Gas left in the world (BOE), <https://www.worldometers.info/gas/>.

- 60 B. Wang, S. Albarracín-Suazo, Y. Pagán-Torres and E. Nikolla, *Catal. Today*, 2017, **285**, 147–158.
- 61 R. Horn and R. Schlögl, *Catal. Letters*, 2015, **145**, 23–39.
- 62 B. Abdullah, N. A. Abd Ghani and D.-V. N. Vo, *J. Clean. Prod.*, 2017, **162**, 170–185.
- 63 W. Tu, M. Ghoussoub, C. V. Singh and Y. H. C. Chin, *J. Am. Chem. Soc.*, 2017, **139**, 6928–6945.
- 64 C. Fan, Y. A. Zhu, M. L. Yang, Z. J. Sui, X. G. Zhou and D. Chen, *Ind. Eng. Chem. Res.*, 2015, **54**, 5901–5913.
- 65 H. Ay and D. Üner, *Appl. Catal. B Environ.*, 2015, **179**, 128–138.
- 66 D. Pakhare and J. Spivey, *Chem. Soc. Rev.*, 2014, **43**, 7813–7837.
- 67 J. R. Petit, J. Jouzel, D. Raynaud, J. M. Barnola, I. Basile, M. Bender, J. Chappellaz, M. Davis, G. Delaygue, M. Delmotte, V. M. Kotlyakov, M. Legrand, V. Y. Lipenkov, C. Lorius, L. Pepin, C. Ritz, E. Saltzman and M. Stievenard, *Futur. Nat. Doc. Glob. Chang.*, 2013, 348–358.
- 68 Z. Liu, D. C. Grinter, P. G. Lustemberg, T.-D. Nguyen-Phan, Y. Zhou, S. Luo, I. Waluyo, E. J. Crumlin, D. J. Stacchiola, J. Zhou, J. Carrasco, H. F. Busnengo, M. V. Ganduglia-Pirovano, S. D. Senanayake and J. A. Rodriguez, *Angew. Chemie Int. Ed.*, 2016, **55**, 7455–7459.
- 69 J. He, Z. Yang, C. Ding, L. Zhang, Y. Yan and X. Du, *Fuel*, 2018, **226**, 400–409.
- 70 P. Ferreira-Aparicio, A. Guerrero-Ruiz and I. Rodríguez-Ramos, *Appl. Catal. A Gen.*, 1998, **170**, 177–187.
- 71 J. Wei and E. Iglesia, *J. Catal.*, 2004, **224**, 370–383.
- 72 A. Abdulrasheed, A. A. Jalil, Y. Gambo, M. Ibrahim, H. U. Hambali and M. Y. Shahul Hamid, *Renew. Sustain. Energy Rev.*, 2019, **108**, 175–193.
- 73 V. C. H. Kroll, H. M. Swaan, S. Lacombe and C. Mirodatos, *J. Catal.*, 1996, **164**, 387–398.
- 74 J. Li, E. Croiset and L. Ricardez-Sandoval, *Appl. Surf. Sci.*, 2014, **311**, 435–442.
- 75 J. Juan-Juan, M. C. Román-Martínez and M. J. Illán-Gómez, *Appl. Catal. A Gen.*, 2006, **301**, 9–15.
- 76 M. M. Barroso-Quiroga and A. E. Castro-Luna, *Int. J. Hydrogen Energy*, 2010, **35**, 6052–6056.

- 77 H. S. Bengaard, I. Alstrup, I. Chorkendorff, S. Ullmann, J. R. Rostrup-Nielsen and J. K. Nørskov, *J. Catal.*, 1999, **187**, 238–244.
- 78 P. Kratzer, B. Hammer and J. K. Nørskov, *J. Chem. Phys.*, 1996, **105**, 5595–5604.
- 79 S. M. De Lima and J. M. Assaf, *Catal. Letters*, 2006, **108**, 63–70.
- 80 J. Xu and M. Saeys, *Chem. Eng. Sci.*, 2007, **62**, 5039–5041.
- 81 J. Xu, L. Chen, K. F. Tan, A. Borgna and M. Saeys, *J. Catal.*, 2009, **261**, 158–165.
- 82 J. Xu and M. Saeys, *J. Phys. Chem. C*, 2009, **113**, 4099–4106.
- 83 K. Hassan-legault, O. Mohan and S. H. Mushrif, *Curr. Opin. Chem. Eng.*, 2019, **26**, 38–45.
- 84 Z. Han, Z. Yang and M. Han, *Appl. Surf. Sci.*, 2019, **480**, 243–255.
- 85 J. Li, E. Croiset and L. Ricardez-Sandoval, *Chem. Phys. Lett.*, 2015, **639**, 205–210.
- 86 M. Zhang, K. Yang, X. Zhang and Y. Yu, *Surf. Sci.*, 2014, **630**, 236–243.
- 87 Y.-A. Zhu, D. Chen, X.-G. Zhou and W.-K. Yuan, *Catal. Today*, 2009, **148**, 260–267.
- 88 S. G. Wang, D. B. Cao, Y. W. Li, J. Wang and H. Jiao, *J. Phys. Chem. B*, 2006, **110**, 9976–9983.
- 89 W. Zhen, B. Li, G. Lu and J. Ma, *RSC Adv.*, 2014, **4**, 16472–16479.
- 90 Q. Liu, B. Bian, J. Fan and J. Yang, *Int. J. Hydrogen Energy*, 2018, **43**, 4893–4901.
- 91 S. Valinejad Moghaddam, M. Rezaei, F. Meshkani and R. Daroughegi, *Int. J. Hydrogen Energy*, 2018, **43**, 16522–16533.
- 92 Z. Hou, O. Yokota, T. Tanaka and T. Yashima, *Appl. Surf. Sci.*, 2004, **233**, 58–68.
- 93 V. Talanquer, *J. Chem. Educ.*, 2018, **95**, 1905–1911.
- 94 A. A. Gokhale, J. A. Dumesic and M. Mavrikakis, *J. Am. Chem. Soc.*, 2008, **130**, 1402–1414.
- 95 A. B. Mhadeshwar and D. G. Vlachos, *J. Catal.*, 2005, **234**, 48–63.
- 96 J. K. Nørskov, F. Abild-Pedersen, F. Studt and T. Bligaard, *Proc. Natl. Acad. Sci.*, 2011, **108**, 937–943.
- 97 J. K. Nørskov, T. Bligaard, J. Rossmeisl and C. H. Christensen, *Nat. Chem.*, 2009, **1**, 37–46.
- 98 H. Yuan, X. Zhu, J. Han, H. Wang and Q. Ge, *J. CO<sub>2</sub> Util.*, 2018, **26**, 8–18.
- 99 X. Dong, X. Liu, Y. Chen and M. Zhang, *J. CO<sub>2</sub> Util.*, 2018, **24**, 64–72.
- 100 Q. T. Trinh, J. Yang, J. Y. Lee and M. Saeys, *J. Catal.*, 2012, **291**, 26–35.



- 101 P. N. Amaniampong, Q. T. Trinh, B. Wang, A. Borgna, Y. Yang and S. H. Mushrif, *Angew. Chemie - Int. Ed.*, 2015, **54**, 8928–8933.
- 102 Q. T. Trinh, A. Banerjee, Y. Yang and S. H. Mushrif, *J. Phys. Chem. C*, 2017, **121**, 1099–1112.
- 103 M. S. Tameh, A. K. Dearden and C. Huang, *J. Phys. Chem. C*, 2018, **122**, acs.jpcc.8b06498.
- 104 P. J. Feibelman, B. Hammer, J. K. Nørskov, F. Wagner, M. Scheffler, R. Stumpf, R. Watwe and J. Dumesic, *J. Phys. Chem. B*, 2001, **105**, 4018–4025.
- 105 D. S. Sholl and J. a Steckel, *Density Funct. Theory*, 2009, 35–48.
- 106 L. C. Grabow and M. Mavrikakis, *ACS Catal.*, 2011, **1**, 365–384.
- 107 Y. F. Zhao, Y. Yang, C. Mims, C. H. F. Peden, J. Li and D. Mei, *J. Catal.*, 2011, **281**, 199–211.
- 108 G. C. Wang, L. Jiang, Y. Morikawa, J. Nakamura, Z. S. Cai, Y. M. Pan and X. Z. Zhao, *Surf. Sci.*, 2004, **570**, 205–217.
- 109 S. G. Wang, D. B. Cao, Y. W. Li, J. Wang and H. Jiao, *J. Phys. Chem. B*, 2005, **109**, 18956–18963.
- 110 K. Czelej, K. Cwieka, T. Wejrzanowski, P. Spiewak and K. J. Kurzydowski, *Catal. Commun.*, 2016, **74**, 65–70.
- 111 X. Ding, L. De Rogatis, E. Vesselli, A. Baraldi, G. Comelli, R. Rosei, L. Savio, L. Vattuone, M. Rocca, P. Fornasiero, F. Ancilotto, A. Baldereschi and M. Peressi, *Phys. Rev. B - Condens. Matter Mater. Phys.*, 2007, **76**, 1–12.
- 112 S. Rangarajan, C. T. Maravelias and M. Mavrikakis, *J. Phys. Chem. C*, 2017, **121**, 25847–25863.
- 113 S. H. Mushrif, V. Vasudevan, C. B. Krishnamurthy and B. Venkatesh, *Chem. Eng. Sci.*, 2015, **121**, 217–235.
- 114 V. G. S. Box, *Mol. Model. Annu.*, 1997, **3**, 124–141.
- 115 Frank Jensen, *Introduction to Computational Chemistry, 3rd Edition*, Wiley, 2016.
- 116 D. Marx and J. Hutter, *Ab initio molecular dynamics: Theory and implementation*, 2000, vol. 1.
- 117 A. C. T. Van Duin, *ReaxFF User Man.*, 2002, 1–39.
- 118 E. Schrödinger, *Phys. Rev.*, 1926, **28**, 1049–1070.

- 
- 119 M. Born, *Zeitschrift für Phys.*, 1926, **37**, 863–867.
- 120 W. Kohn and L. J. Sham, *Phys. Rev.*, DOI:10.1103/PhysRev.140.A1133.
- 121 P. Hohenberg and W. Kohn, *Phys. Rev.*, 1964, **136**, B864–B871.
- 122 P. Ziesche, S. Kurth and J. P. Perdew, *Comput. Mater. Sci.*, 1998, **11**, 122–127.
- 123 G. Wilson and A. Liberman, 1995, **54**, 857–878.
- 124 J. P. Perdew, K. Burke and M. Ernzerhof, *Phys. Rev. Lett.*, 1996, **77**, 3865–3868.
- 125 J. P. Perdew and Y. Wang, 1992, **45**, 244–249.
- 126 J. Klimeš, D. R. Bowler and A. Michaelides, *J. Phys. Condens. Matter*, 2010, **22**, 022201.
- 127 Y. Zhang and W. Yang, *Phys. Rev. Lett.*, 1998, **80**, 890–890.
- 128 B. Hammer, L. Hansen and J. Nørskov, *Phys. Rev. B*, 1999, **59**, 7413–7421.
- 129 a. D. Becke, *J. Chem. Phys.*, 1986, **84**, 4524.
- 130 J. Klimeš, D. R. Bowler and A. Michaelides, *J. Phys. Condens. Matter*, 2010, **22**, 022201.
- 131 G. Kresse and J. Furthmüller, *Comput. Mater. Sci.*, 1996, **6**, 15–50.
- 132 G. Kresse and J. Furthmüller, *Phys. Rev. B*, 1996, **54**, 11169–11186.
- 133 J. P. Perdew and Y. Wang, *Phys. Rev. B*, 1992, **45**, 244–249.
- 134 D. Cheng, F. R. Negreiros, E. Aprà and A. Fortunelli, *ChemSusChem*, 2013, **6**, 944–965.
- 135 Y. Hori, R. Takahashi, Y. Yoshinami and A. Murata, *J. Phys. Chem. B*, 1997, **101**, 7075–7081.
- 136 Y. Hori, A. Murata, R. Takahashi and S. Suzuki, *J. Am. Chem. Soc.*, 1987, **109**, 5022–5023.
- 137 H. Xiao, T. Cheng, W. A. Goddard and R. Sundararaman, *J. Am. Chem. Soc.*, 2016, **138**, 483–486.
- 138 P. J. Feibelman, B. Hammer, J. K. Nørskov, F. Wagner, M. Scheffler, R. Stumpf, R. Watwe and J. Dumesic, *J. Phys. Chem. B*, 2001, **105**, 4018–4025.
- 139 F. Studt, F. Abild-Pedersen, J. B. Varley and J. K. Nørskov, *Catal. Letters*, 2013, **143**, 71–73.
- 140 J. Wellendorff, T. L. Silbaugh, D. Garcia-Pintos, J. K. Nørskov, T. Bligaard, F. Studt and C. T. Campbell, *Surf. Sci.*, 2015, **640**, 36–44.
- 141 J. B. Miller, H. R. Siddiqui, S. M. Gates, J. N. Russell, J. T. Yates, J. C. Tully and M. J. Cardillo, *J. Chem. Phys.*, 1987, **87**, 6725–6732.
- 142 P. E. Blöchl, *Phys. Rev. B*, 1994, **50**, 17953–17979.

- 143 C. L. A, R. Krishnan and D. J. L, *Comput. Thermochem.*, 1998, **677**, 176–196.
- 144 J. L. C. Fajín, J. R. B. Gomes and M. N. D. S. Cordeiro, *J. Phys. Chem. C*, 2015, **119**, 16537–16551.
- 145 B. Hammer and J. K. Norskov, *Adv. Catal.*, 2000, **45**, 71–129.
- 146 D. S. Sholl and J. a Steckel, *Density Funct. Theory*, 2009, 35–48.
- 147 L. Köhler and G. Kresse, *Phys. Rev. B*, 2004, **70**, 165405.
- 148 Q. T. Trinh, K. F. Tan, A. Borgna and M. Saeys, *J. Phys. Chem. C*, 2013, **117**, 1684–1691.
- 149 A. Kokalj, T. Makino and M. Okada, *J. Phys. Condens. Matter*, 2017, **29**, 194001.
- 150 O. Skibbe, D. Vogel, M. Binder, A. Pucci, T. Kravchuk, L. Vattuone, V. Venugopal, A. Kokalj, M. Rocca, O. Skibbe, D. Vogel, M. Binder, A. Pucci, T. Kravchuk, L. Vattuone, V. Venugopal, A. Kokalj and M. Rocca, , DOI:10.1063/1.3159736.
- 151 C. Dri, A. Peronio, E. Vesselli, C. Africh, M. Rizzi, A. Baldereschi, M. Peressi and G. Comelli, *Phys. Rev. B - Condens. Matter Mater. Phys.*, 2010, **82**, 1–6.
- 152 H. H. Madden, *J. Chem. Phys.*, 1973, **58**, 3401.
- 153 G. Peng, S. J. Sibener, G. C. Schatz and M. Mavrikakis, *Surf. Sci.*, 2012, **606**, 1050–1055.
- 154 P. J. Feibelman, B. Hammer, J. K. Nørskov, F. Wagner, M. Scheffler, R. Stumpf, R. Watwe and J. Dumesic, *J. Phys. Chem. B*, 2001, **105**, 4018–4025.
- 155 J. Wellendorff, K. T. Lundgaard, A. Møgelhøj, V. Petzold, D. D. Landis, J. K. Nørskov, T. Bligaard and K. W. Jacobsen, *Phys. Rev. B - Condens. Matter Mater. Phys.*, 2012, **85**, 32–34.
- 156 Y. P. G. Chua, G. T. K. K. Gunasooriya, M. Saeys and E. G. Seebauer, *J. Catal.*, 2014, **311**, 306–313.
- 157 A. Banerjee, A. P. Van Bavel, H. P. C. E. Kuipers and M. Saeys, *ACS Catal.*, 2015, **5**, 4756–4760.
- 158 R. Christensen, H. A. Hansen and T. Vegge, *Catal. Sci. Technol.*, 2015, **5**, 4946–4949.
- 159 T. Engel, *Quantum Chemistry and Spectroscopy*, 2013.
- 160 T. Shimanouchi, *Tables of molecular vibrational frequencies, consolidated volume i*, Gaithersburg, MD, 1972.
- 161 M. Roiaz, E. Monachino, C. Dri, M. Greiner, A. Knop-Gericke, R. Schlögl, G. Comelli and E. Vesselli, *J. Am. Chem. Soc.*, 2016, **138**, 4146–4154.

- 162 H. Yang, C. Zhang, P. Gao, H. Wang, X. Li, L. Zhong, W. Wei and Y. Sun, *Catal. Sci. Technol.*, 2017, **7**, 4580–4598.
- 163 W. Li, H. Wang, X. Jiang, J. Zhu, Z. Liu and X. Guo, 2018, 7651–7669.
- 164 F. Muttaqien, Y. Hamamoto, I. Hamada, K. Inagaki, Y. Shiozawa, K. Mukai, T. Koitaya, S. Yoshimoto, J. Yoshinobu and Y. Morikawa, *J. Chem. Phys.*, , DOI:10.1063/1.4994149.
- 165 P. B. Rasmussen, P. A. Taylor and I. Chorkendorff, *Surf. Sci.*, 1992, **269–270**, 352–359.
- 166 J. Ren, H. Guo, J. Yang, Z. Qin, J. Lin and Z. Li, *Appl. Surf. Sci.*, 2015, **351**, 504–516.
- 167 J. Huang, X. Li, X. Wang, X. Fang, H. Wang and X. Xu, *J. CO<sub>2</sub> Util.*, 2019, **33**, 55–63.
- 168 S. T. Zhang, H. Yan, M. Wei, D. G. Evans and X. Duan, *RSC Adv.*, 2014, **4**, 30241–30249.
- 169 W. Zhen, F. Gao, B. Tian, P. Ding, Y. Deng, Z. Li, H. Gao and G. Lu, *J. Catal.*, 2017, **348**, 200–211.
- 170 I. Chiorescu, J. Arce-Ramos, W. qing Li, A. Genest and N. Rösch, *Surf. Sci.*, 2019, **681**, 54–58.
- 171 M. Marwood, R. Doepper and A. Renken, *Appl. Catal. A Gen.*, 1997, **151**, 223–246.
- 172 S. Ewald, M. Kolbeck, T. Kratky, M. Wolf and O. Hinrichsen, *Appl. Catal. A Gen.*, 2019, **570**, 376–386.
- 173 B. Mutz, P. Sprenger, W. Wang, D. Wang, W. Kleist and J. D. Grunwaldt, *Appl. Catal. A Gen.*, 2018, **556**, 160–171.
- 174 T. Avanesian, G. S. Gusmão and P. Christopher, *J. Catal.*, 2016, **343**, 86–96.
- 175 J. Li, E. Croiset, L. Ricardez-Sandoval, L. Foppa, M. C. Silaghi, K. Larmier, A. Comas-Vives, L. li Xu, H. Wen, X. Jin, Q. ming Bing and J. yao Liu, *Appl. Surf. Sci.*, 2016, **443**, 196–207.
- 176 S.-G. Wang, D.-B. Cao, Y.-W. Li, J. Wang and H. Jiao, *J. Phys. Chem. B*, 2005, **109**, 18956–18963.
- 177 K. Czelej, K. Cwieka, T. Wejrzanowski, P. Spiewak and K. J. Kurzydowski, *Catal. Commun.*, 2016, **74**, 65–70.
- 178 O. Mohan, Q. T. Trinh, A. Banerjee and S. H. Mushrif, *Mol. Simul.*, 2019, **45**, 1163–1172.
- 179 L. Vitos, A. V. Ruban, H. L. Skriver and J. Kollár, *Surf. Sci.*, 1998, **411**, 186–202.
- 180 A. J. Medford, J. Wellendorff, A. Vojvodic, F. Studt, F. Abild-Pedersen, K. W. Jacobsen, T. Bligaard and J. K. Nørskov, *Science (80-. )*, 2014, **345**, 197–200.

- 181 T. P. De Carvalho, R. C. Catapan, A. A. M. Oliveira and D. G. Vlachos, *Ind. Eng. Chem. Res.*, 2018, **57**, 10269–10280.
- 182 A. B. Mhadeshwar and D. G. Vlachos, *Catal. Today*, 2005, **105**, 162–172.
- 183 M. Maestri, D. G. Vlachos, A. Beretta, G. Groppi and E. Tronconi, *J. Catal.*, 2008, **259**, 211–222.
- 184 C. T. Campbell, *J. Catal.*, 2001, **204**, 520–524.
- 185 C. A. Wolcott, A. J. Medford, F. Studt and C. T. Campbell, *J. Catal.*, 2015, **330**, 197–207.
- 186 C. Stegelmann, A. Andreasen and C. T. Campbell, *J. Am. Chem. Soc.*, 2009, **131**, 8077–8082.
- 187 C. T. Campbell, *ACS Catal.*, 2017, **7**, 2770–2779.
- 188 T. Choksi and J. Greeley, *ACS Catal.*, 2016, **6**, 7260–7277.
- 189 J. N. Dew, R. R. White and C. M. Sliepcevich, *Ind. Eng. Chem.*, 1955, **47**, 140–146.
- 190 S. Rönsch, J. Schneider, S. Matthischke, M. Schlüter, M. Götz, J. Lefebvre, P. Prabhakaran and S. Bajohr, *Fuel*, 2016, **166**, 276–296.
- 191 M. A. Vannice, *Catal. Rev.*, 1976, **14**, 153–191.
- 192 T. D. Gould, A. Izar, A. W. Weimer, J. L. Falconer and J. W. Medlin, *ACS Catal.*, 2014, **4**, 2714–2717.
- 193 T. D. Gould, M. M. Montemore, A. M. Lubers, L. D. Ellis, A. W. Weimer, J. L. Falconer and J. W. Medlin, *Appl. Catal. A Gen.*, 2015, **492**, 107–116.
- 194 S. Chen, J. Zaffran and B. Yang, *ACS Catal.*, 2020, **10**, 3074–3083.
- 195 K. Delgado, L. Maier, S. Tischer, A. Zellner, H. Stotz and O. Deutschmann, *Catalysts*, 2015, **5**, 871–904.
- 196 M. Dion, H. Rydberg, E. Schröder, D. C. Langreth and B. I. Lundqvist, *Phys. Rev. Lett.*, 2004, **92**, 22–25.
- 197 J. A. Dumesic, *J. Catal.*, 1999, **185**, 496–505.
- 198 M. C. J. BRADFORD and M. A. VANNICE, *Catal. Rev.*, 1999, **41**, 1–42.
- 199 H. Arandiyani, Y. Wang, J. Scott, S. Mesgari, H. Dai and R. Amal, *ACS Appl. Mater. Interfaces*, 2018, **10**, 16352–16357.
- 200 Z. Ou, C. Qin, J. Niu, L. Zhang and J. Ran, *Int. J. Hydrogen Energy*, 2019, **44**, 819–834.
- 201 H. Yuan, X. Zhu, J. Han, H. Wang and Q. Ge, *J. CO<sub>2</sub> Util.*, 2018, **26**, 8–18.
- 202 J. Ren, X. Qin, J.-Z. Yang, Z.-F. Qin, H.-L. Guo, J.-Y. Lin and Z. Li, *Fuel Process.*

- Technol.*, 2015, **137**, 204–211.
- 203 J. Sehested, K. E. Larsen, A. L. Kustov, A. M. Frey, T. Johannessen, T. Bligaard, M. P. Andersson, J. K. Nørskov and C. H. Christensen, *Top. Catal.*, 2007, **45**, 9–13.
- 204 A. Erhan Aksoylu and Z. I. Önsan, *Appl. Catal. A Gen.*, 1998, **168**, 399–407.
- 205 L. R. Winter, E. Gomez, B. Yan, S. Yao and J. G. Chen, *Appl. Catal. B Environ.*, 2018, **224**, 442–450.
- 206 D. Pandey, K. Ray, R. Bhardwaj, S. Bojja, K. V. R. Chary and G. Deo, *Int. J. Hydrogen Energy*, 2018, **43**, 4987–5000.
- 207 K. Ray and G. Deo, *Appl. Catal. B Environ.*, 2017, **218**, 525–537.
- 208 P. E. D. Le Thien An, Kim Jieun, Jeong Yu Ri, *Catalysts*, 2019, **9**, 599–611.
- 209 T. Burger, F. Koschany, O. Thomys, K. Köhler and O. Hinrichsen, *Appl. Catal. A Gen.*, 2018, **558**, 44–54.
- 210 J. K. Nørskov, F. Abild-Pedersen, F. Studt and T. Bligaard, *Proc. Natl. Acad. Sci.*, 2011, **108**, 937–943.
- 211 K. Hassan-Legault, O. Mohan and S. H. Mushrif, *Curr. Opin. Chem. Eng.*, 2019, **26**, 38–45.
- 212 L. Xu, F. Wang, M. Chen, J. Zhang, K. Yuan, L. Wang, K. Wu, G. Xu and W. Chen, *ChemCatChem*, 2016, **8**, 2536–2548.
- 213 W. J. Cai, L. P. Qian, B. Yue and H. Y. He, *Chinese Chem. Lett.*, 2014, **25**, 1411–1415.
- 214 K. Li, M. Li, Y. Wang and Z. Wu, *Fuel*, 2020, **274**, 117849.
- 215 J. Horlyck, S. Lewis, R. Amal and J. Scott, *Top. Catal.*, 2018, **61**, 1842–1855.
- 216 Y. Song, E. Ozdemir, S. Ramesh, A. Adishev, S. Subramanian, A. Harale, M. Albuali, B. A. Fadhel, A. Jamal, D. Moon, S. H. Choi and C. T. Yavuz, *Science (80-. )*, 2020, **367**, 777–781.
- 217 P. Kratzer, B. Hammer and J. K. Nørskov, *J. Chem. Phys.*, 1996, **105**, 5595–5604.
- 218 J. Niu, J. Ran, X. Du, W. Qi, P. Zhang and L. Yang, *Mol. Catal.*, 2017, **434**, 206–218.
- 219 K. Li, F. He, H. Yu, Y. Wang and Z. Wu, *J. Catal.*, 2018, **364**, 248–261.
- 220 G. Sun, Z.-J. Zhao, R. Mu, S. Zha, L. Li, S. Chen, K. Zang, J. Luo, Z. Li, S. C. Purdy, A. J. Kropf, J. T. Miller, L. Zeng and J. Gong, *Nat. Commun.*, 2018, **9**, 4454.
- 221 G. Giannakakis, M. Flytzani-Stephanopoulos and E. C. H. Sykes, *Acc. Chem. Res.*, 2019, **52**, 237–247.

- 222 A. Trimpalis, G. Giannakakis, S. Cao and M. Flytzani-Stephanopoulos, *Catal. Today*, 2020, **355**, 804–814.
- 223 M. T. Darby, R. Réocreux, E. C. H. Sykes, A. Michaelides and M. Stamatakis, *ACS Catal.*, 2018, **8**, 5038–5050.
- 224 M. T. Darby, E. C. H. Sykes, A. Michaelides and M. Stamatakis, *Top. Catal.*, 2018, **61**, 428–438.
- 225 M. D. Marcinkowski, M. T. Darby, J. Liu, J. M. Wimbale, F. R. Lucci, S. Lee, A. Michaelides, M. Flytzani-Stephanopoulos, M. Stamatakis and E. C. H. Sykes, *Nat. Chem.*, 2018, **10**, 325–332.
- 226 M. T. Darby, M. Stamatakis, A. Michaelides and E. C. H. Sykes, *J. Phys. Chem. Lett.*, 2018, **9**, 5636–5646.
- 227 J. L. C. Fajín, J. R. B. Gomes and M. N. D. S. Cordeiro, *J. Phys. Chem. C*, 2015, **119**, 16537–16551.
- 228 Y. Yang, M. G. White and P. Liu, *J. Phys. Chem. C*, 2012, **116**, 248–256.
- 229 K. Yang and B. Yang, *Phys. Chem. Chem. Phys.*, 2017, **19**, 18010–18017.
- 230 F. R. Lucci, J. Liu, M. D. Marcinkowski, M. Yang, L. F. Allard, M. Flytzani-Stephanopoulos and E. C. H. Sykes, *Nat. Commun.*, 2015, **6**, 1–8.
- 231 J. Shan, J. Liu, M. Li, S. Lustig, S. Lee and M. Flytzani-Stephanopoulos, *Appl. Catal. B Environ.*, 2018, **226**, 534–543.
- 232 D. A. Patel, R. T. Hannagan, P. L. Kress, A. C. Schilling, V. Çlnar and E. C. H. Sykes, *J. Phys. Chem. C*, 2019, **123**, 28142–28147.
- 233 M. D. Marcinkowski, J. Liu, C. J. Murphy, M. L. Liriano, N. A. Wasio, F. R. Lucci, M. Flytzani-Stephanopoulos and E. C. H. Sykes, *ACS Catal.*, 2017, **7**, 413–420.
- 234 C. Liu, T. R. Cundari and A. K. Wilson, *J. Phys. Chem. C*, 2012, **116**, 5681–5688.
- 235 K. Blaziak, D. Tzeli, S. S. Xantheas and E. Uggerud, *Phys. Chem. Chem. Phys.*, 2018, **20**, 25495–25505.
- 236 J. Ko, B. K. Kim and J. W. Han, *J. Phys. Chem. C*, 2016, **120**, 3438–3447.
- 237 L. Dietz, S. Piccinin and M. Maestri, *J. Phys. Chem. C*, 2015, **119**, 4959–4966.
- 238 J. S. Yoo, Z.-J. Zhao, J. K. Nørskov and F. Studt, *ACS Catal.*, 2015, **5**, 6579–6586.
- 239 J. S. Choi, K. I. Moon, Y. G. Kim, J. S. Lee, C. H. Kim and D. L. Trimm, *Catal. Letters*, 1998, **52**, 43–47.

- 240 S. H. Seok, H. C. Sun, E. D. Park, H. H. Sung and S. L. Jae, *J. Catal.*, 2002, **209**, 6–15.
- 241 T. Burger, F. Koschany, O. Thomys, K. Köhler and O. Hinrichsen, *Appl. Catal. A Gen.*, 2018, **558**, 44–54.
- 242 N. A. Pechimuthu, K. K. Pant, S. C. Dhingra and R. Bhalla, *Ind. Eng. Chem. Res.*, 2006, **45**, 7435–7443.
- 243 A. A. B. Padama, H. Kasai and H. Kawai, *Surf. Sci.*, 2012, **606**, 62–68.
- 244 J. M. Sanchez, F. Ducastelle and D. Gratias, *Phys. A Stat. Mech. its Appl.*, 1984, **128**, 334–350.
- 245 J. R. Kitchin, *Phys. Rev. B - Condens. Matter Mater. Phys.*, 2009, **79**, 1–6.
- 246 A. Bajpai, K. Frey and W. F. Schneider, *Langmuir*, 2020, **36**, 465–474.
- 247 J. Lym, G. H. Gu, Y. Jung and D. G. Vlachos, *J. Phys. Chem. C*, 2019, **123**, 18951–18959.
- 248 J. R. Boes and J. R. Kitchin, *Mol. Simul.*, 2017, **43**, 346–354.
- 249 S. Deshpande, T. Maxson and J. Greeley, *npj Comput. Mater.*, 2020, **6**, 1–6.
- 250 J. Li, E. Croiset and L. Ricardez-Sandoval, *Appl. Surf. Sci.*, 2014, **311**, 435–442.
- 251 S. G. Wang, D. B. Cao, Y. W. Li, J. Wang and H. Jiao, *Surf. Sci.*, 2009, **603**, 2600–2606.
- 252 T. Ogura, D. W. Blaylock, G. J. O. Beran and W. H. Green, *ACS Natl. Meet. B. Abstr.*, 2008, 4898–4908.
- 253 D. W. Blaylock, Y. A. Zhu and W. H. Green, *Top. Catal.*, 2011, **54**, 828–844.
- 254 T. Ogura, D. W. Blaylock, G. J. O. Beran and W. H. Green Jr., *ACS Natl. Meet. B. Abstr.*, 2008, 4898–4908.
- 255 F. Che, J. T. Gray, S. Ha and J. S. McEwen, *ACS Catal.*, 2017, **7**, 551–562.
- 256 L. Maier, B. Schädel, K. H. Delgado, S. Tischer and O. Deutschmann, *Top. Catal.*, 2011, **54**, 845–858.
- 257 G. Collinge, S. F. Yuk, M. T. Nguyen, M. S. Lee, V. A. Glezakou and R. Rousseau, *ACS Catal.*, 2020, **10**, 9236–9260.
- 258 E. Suárez, N. Díaz and D. Suárez, *J. Chem. Theory Comput.*, 2011, **7**, 2638–2653.
- 259 C. T. Campbell and J. R. V. Sellers, *J. Am. Chem. Soc.*, 2012, **134**, 18109–18115.
- 260 C. T. Campbell and J. R. V. Sellers, *Chem. Rev.*, 2013, **113**, 4106–4135.
- 261 C. T. Campbell, L. Árnadóttir and J. R. V. Sellers, *Zeitschrift für Phys. Chemie*, , DOI:10.1524/zpch.2013.0395.



- 262 P. J. Dauenhauer and O. A. Abdelrahman, *ACS Cent. Sci.*, 2018, **4**, 1235–1243.
- 263 R. D. Cortright and J. A. Dumesic, in *Advances in Catalysis*, 2001, pp. 161–264.
- 264 S. Wang, *Ind. Eng. Chem. Res.*, 1999, **38**, 2615–2625.
- 265 A. Nandini, K. K. Pant and S. C. Dhingra, *Appl. Catal. A Gen.*, 2006, **308**, 119–127.